THE UNIVERSITY OF MICHIGAN

ANALYSIS OF CROSSED-FIELD SPACE-CHARGE FLOWS

TECHNICAL REPORT NO. 74

ELECTRON PHYSICS LABORATORY
Department of Electrical Engineering

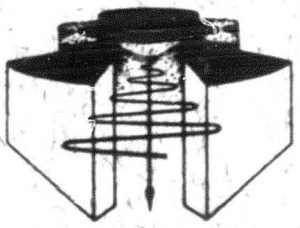

By: N. A. Masnari

Approved by: J. E. Rowe

July, 1964

CONTRACT WITH:

ELECTRONIC TECHNOLOGY DIVISION OF THE AIR FORCE AVIONICS LABORATORY, RESEARCH AND TECHNOLOGY DIVISION, AIR FORCE SYSTEMS COMMAND WRIGHT-PATTERSON AIR FORCE BASE, OHIO. CONTRACT NO. AF33(615)-1553.

Qualified requesters may obtain copies of this report from the Defense Documentation Center, Cameron Station, Alexandria, Virginia.

THE UNIVERSITY OF MICHIGAN
ANN ARBOR, MICHIGAN

ANALYSIS OF CROSSED-FIELD SPACE-CHARGE FLOWS

TECHNICAL REPORT NO. 74

Electron Physics Laboratory
Department of Electrical Engineering

By

Nino A. Masnari

Approved by: J. E. Rowe

J. E. Rowe, Director
Electron Physics Laboratory

Project 06349

CONTRACT NO. AF-33(615)-1553
ELECTRONIC TECHNOLOGY DIVISION
AIR FORCE AVIONICS LABORATORY
RESEARCH AND TECHNOLOGY DIVISION
AIR FORCE SYSTEMS COMMAND
WRIGHT-PATTERSON AIR FORCE BASE, OHIO

July, 1964

This report has also been submitted as a dissertation in partial fulfillment of the requirements for the degree of Doctor of Philosophy in The University of Michigan, 1964.

ABSTRACT

The purpose of this dissertation is to investigate the characteristics of space-charge flows in crossed d-c electric and magnetic fields. The investigations include theoretical considerations of rectilinear laminar space-charge flow, analog and digital computer analyses of electron injection systems and experimental studies of beam characteristics. In general the results provide a better understanding of the operation of injected-beam crossed-field devices.

The performance of a crossed-field device is optimum when the electron beam satisfies the conditions of rectilinear Brillouin flow. For any given circuit voltage, beam current and magnetic field there is a unique beam which satisfies the Brillouin conditions. This leads to a theoretical limitation in the perveance and electronic efficiency. The analysis of various theoretical electron gun systems indicates that the beam characteristics invariably differ from the ideal conditions.

Digital and analog computer techniques have been used to determine the space-charge flow produced by various electron injection systems. The studies indicate that the electron beam characteristics for various Kino gun configurations differ noticeably from the theoretical results. In particular, the emission from the cathode is nonuniform and the beam nonlaminar. However, with appropriate electrode modifications it is possible to improve both the uniformity of the emission and the beam laminarity.

The digital computer analysis of initial velocity effects indicates that variations in the normal emission velocity component produce essentially no change in the electron motion. However, any change in the initial tangential velocity results in significantly different electron trajectories.

The nonlaminar injection of electron streams into the anode-sole region was investigated by means of the digital computer. The general results indicate that crossed-field space-charge flows are extremely sensitive to transverse forces. Consequently beams which are improperly injected are observed to undulate, vary in thickness and become increasingly nonlaminar.

The experimental investigations were undertaken in an attempt to evaluate both the gross and microscopic characteristics of the space-charge flow. The experiments involved the use of an interception system to probe the beam at various cross-sections in the anode-sole region. Generally the beam experienced variations in thickness and undulated with approximately the cyclotron period. The space-charge densities at various points in the beam were found to be between 0.5 and 1.5 times the Brillouin value. The results also indicate that the space-charge flow in crossed-field devices is generally nonlaminar with appreciable intersecting of electron trajectories.

ACKNOWLEDGMENTS

The author wishes to express his gratitude to his doctoral committee and especially to his Chairman, Professor Joseph E. Rowe, for his guidance and encouragement during the course of this work. Appreciation is extended to the administrative staff of the laboratory for their assistance in the preparation of the text. Messrs. J. Murray and J. Boers should also be thanked for their efforts in obtaining the Poisson cell and digital computer results. Finally, the author is grateful to Mr. H. O. Wagner for his conscientious efforts during the construction and assembly of the experimental device.

TABLE OF CONTENTS

LIST OF ILLUSTRATIONS

Figure		Page
4.1	Comparison of Digital Computer and Poisson Cell Trajectories for the Original Kino Short Gun.	89
4.2	Comparison of Digital Computer and Poisson Cell Trajectories for the Modified Kino Short Gun.	91
4.3	Trajectories Obtained from the Digital Computer Investigation of the Extended Kino Short Gun.	92
4.4	Cathode Current Density Distribution Obtained from the Extended Kino Short Gun Investigations.	93
4.5	Theoretical Trajectories for the Abbreviated Kino Gun.	96
4.6	Digital Computer Results for the Theoretical Abbreviated Kino Gun Configuration.	97
4.7	Electron Trajectories and Cathode Current Density Distribution with Focusing Anode Parallel to the Cathode.	99
4.8	Electron Trajectories and J_c Distribution for Abbreviated Kino Gun with Modified Ramp Electrodes.	101
4.9	Electron Trajectories and J_c Distribution for 8° Front Ramp Electrode.	102
4.10a	Modified Version of Abbreviated Kino Gun Illustrating Nearly Laminar Flow.	104
4.10b	Velocity Variation Across the Beam at Planes B-B, C-C and D-D.	105
4.11	Modification of the Front and Rear Ramp Electrodes Resulting in Nearly Uniform Emission from the Cathode.	106
4.12	Electron Trajectories When the Front Edge of the Cathode Is not Emitting.	108
4.13	Electron Trajectories When the Rear Edge of the Cathode Is not Emitting.	109
4.14a	Trajectories in the Potential Minimum Region for Electrons Emitted Normal to the Cathode with Initial Energy as the Parameter.	112
4.14b	Trajectories in the Gun Region After Passage Through the Potential Minimum.	113
4.15	Trajectories of Electrons Emitted from the Cathode in Different Directions but with the Same Energy. (φ_o = 0.12 Volt)	115

Figure		Page
7.11b	Location of Maximum Current Interception at Various z-Positions. (V_c = -1425, V_f = -500, B = 352 Gauss)	190
7.12a	Currents Intercepted by the Grid Wires at Various Cross Sections in the Interaction Region. (V_c = -1890, B = 409 Gauss)	191
7.12b	Location of Maximum Current Interception at Various z-Positions. (V_c = -1890, B = 409 Gauss)	192
7.13a	Currents Intercepted by the Grid Wires at Various Cross Sections in the Interaction Region. (V_c = -2210, V_f = -850, B = 590 Gauss)	193
7.13b	Location of Maximum Current Interception at Various z-Positions. (V_c = -2210, V_f = -850, B = 590 Gauss)	194
7.14a	Currents Intercepted by the Grid Wires at Various Cross Sections in the Interaction Region. (V_c = -1450, V_f = -500, B = 335)	196
7.14b	Location of Maximum Current Interceptions at Various z-Positions. (V_c = -1450, V_f = -500, B = 335)	197
7.15a	Currents Intercepted by the Grid Wires at Various Cross Sections. (V_c = -1765, V_f = -660, B = 465)	199
7.15b	Location of Maximum Current Interception at Various z-Positions. (V_c = -1765, V_f = -660, B = 465)	200
7.16a	Currents Intercepted by the Grid Wires at Various Cross Sections. (V_c = -2000, V_f = -750, B = 578)	201
7.16b	Location of Maximum Interception at Various z-Positions. (V_c = -2000, V_f = -750, B = 578)	202
7.17a	Currents Intercepted by the Grid Wires at Various Cross Sections of the Interaction Region with Wire No. 4 Disconnected. (V_c = -1490, V_f = -500, B = 352 Gauss)	203
7.17b	Location of Maximum Current Interception at Various z-Positions with Wire No. 4 Disconnected. (V_c = -1490, V_f = -500, B = 352)	204
7.18	Comparison of the Currents Intercepted by Wire 3 When Wire 4 Is Connected and Disconnected. (V_c = -1490, V_f = -500, B = 352 Gauss)	206
7.19	Illustration of the Manner in Which a Grid Wire Intercepts Various Parts of a Cycloiding Beam as the Grid Assembly Is Moved in the z-Direction. The Distance from A to C Corresponds to One Period of the Beam Variation.	207

Figure		Page

LIST OF TABLES

CHAPTER I. INTRODUCTION

1.1 Preliminary Remarks

The general class of electron tubes commonly referred to as crossed-field devices involves the motion of electrons through orthogonal electric and magnetic fields. These devices are ideally suited for many microwave applications. Figure 1.1 illustrates three crossed-field electrode configurations which have been investigated and used in the past. Figure 1.1a shows a cylindrical magnetron in which electrons are emitted from the entire cathode. Figure 1.1b is essentially a linear version of the cylindrical device since it also involves the emission of electrons from the entire low potential electrode. It differs in the sense that the beam is not re-entrant as in the cylindrical magnetron. Figure 1.1c, however, involves the formation of a well defined beam from a relatively narrow cathode and, thus, is significantly different from the preceding devices. The first two classes involve the saturation of the cathode-anode space with a large number of electrons whereas the third device requires the injection of a strip type electron beam into a parallel plane anode-sole region. The electrode beneath the beam is referred to as the sole and that above the beam as the anode. It is the injected-beam family of devices which forms the basis of this dissertation.

One of the primary requirements for the successful operation of an injected-beam crossed-field device is the establishment of a well defined laminar electron beam in the anode-sole region. The great importance of the space-charge flow characteristics can be demonstrated by considering the fundamental objective of the device. Figure 1.2

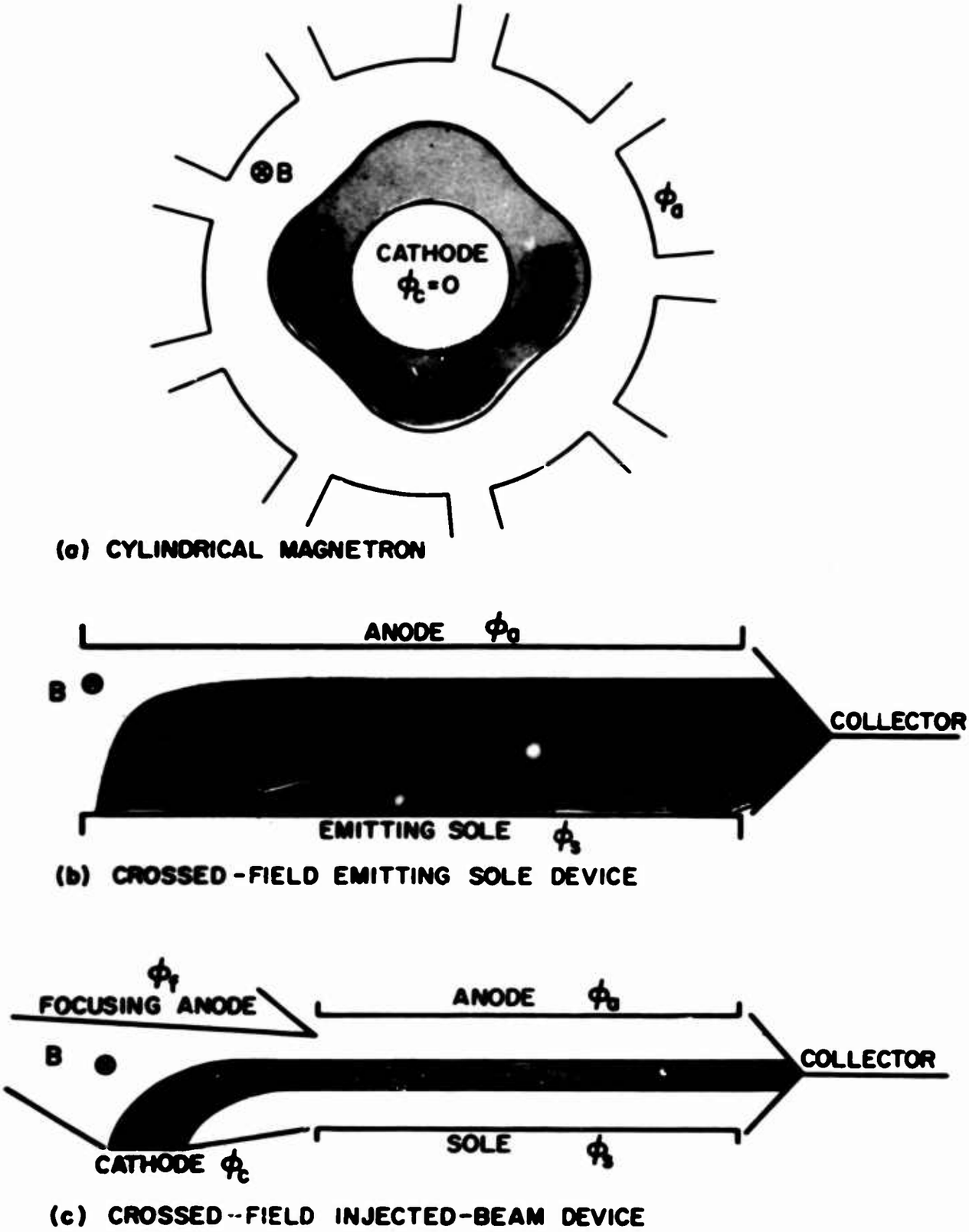

FIG 1.1 EXAMPLES OF VARIOUS CROSSED-FIELD ELECTRON DEVICE CONFIGURATIONS.

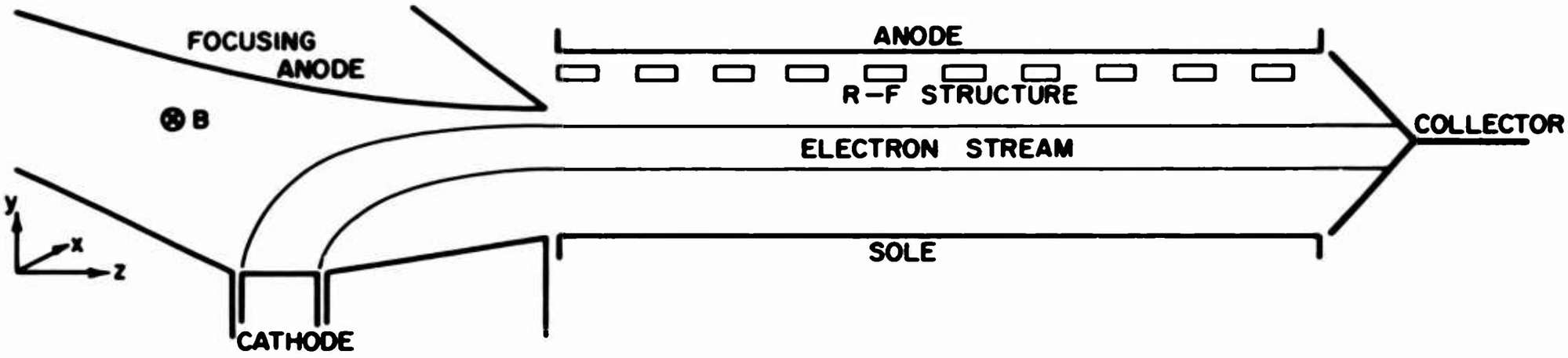

FIG. 1.2 BASIC CONFIGURATION OF AN INJECTED-BEAM CROSSED-FIELD DEVICE.

illustrates a typical tube including the slow-wave structure which is located adjacent to the anode. The structure is designed so that the applied r-f signal propagates in the z-direction with a velocity approximately equal to the velocity of the electrons in the beam. Under these conditions the electrons remain in phase with the r-f signal and are able to exchange energy continuously with the wave. As the electrons lose energy to the wave they maintain the same z-component of velocity but move closer to the structure and hence to higher potentials. Thus, the energy conversion mechanism is the transference of potential energy from the beam to the r-f signal with little change in the electron kinetic energy. Since favorable electrons stay in phase with the wave until they strike the slow-wave structure, the efficiency of such devices should be quite high.

The ideal electron beam for such a device is one in which all of the electrons have the same velocity as the r-f wave. This velocity must also satisfy

$$\dot{z} = \frac{E_o}{B} \tag{1.1}$$

which is the condition required for balance between the transverse electric and magnetic fields (E_o and B respectively) acting on the electron. However, for a uniform magnetic field it is impossible, even in theory, to have a finite thickness univelocity beam which is capable of linear motion in the anode-sole region. (This assumes that the electrons are all emitted from a unipotential cathode.) Consequently, there must be a velocity variation across the beam. Those electrons whose velocities are less than the r-f wave phase velocity abstract energy from the wave and are detrimental to the interaction process.

Fortunately these electrons continuously move away from the structure until they are collected on the sole.

Obviously the characteristics of the space-charge flow in the interaction region exert a great influence on the performance of a crossed-field device. Since the electrons at a given cross section must have different velocities, the optimum beam is one in which the d-c electrons exhibit rectilinear laminar flow characterized by non-intersecting trajectories. This is referred to as a rectilinear Brillouin beam[1,2] in which case the space-charge density is constant and the electron velocity varies linearly across the beam. This velocity variation is required to provide a balance between the transverse electric and magnetic forces acting on the individual particles. Various investigations[3] have indicated that the Brillouin beam provides the optimum space-charge flow conditions for the operation of crossed-field amplifiers and oscillators. Consequently, rectilinear laminar electron beams have usually been the objective in the design of crossed-field injection systems.

As indicated above, the successful operation of any crossed-field device requires an electron injection system which is capable of producing an acceptable beam. In O-type devices an axial magnetic field can be applied to constrain the electrons within a reasonably small cross-sectional area. In crossed-field devices there is no comparable constraint and any imperfection in the beam as it enters the interaction region will necessarily result in curvilinear motion of the electrons.

The evaluation of crossed-field injected-beam devices requires a fundamental understanding of the formation of electron beams as well as a thorough knowledge of their d-c behavior. Thus, it is necessary to consider the beam characteristics in both the gun region and in the

interaction space. Although there have been many investigations which are pertinent to the formation and behavior of electron beams in crossed-field devices, the following sections will describe only a few of the more important studies.

1.2 Crossed-Field Electron Injection Systems

1.2.1 Theoretical Gun Designs. In recent years there have been numerous attempts to design electron injection systems capable of forming laminar beams. One of the earliest investigations resulted in the French short gun or Charles gun[4], illustrated in Fig. 1.3. The design is based on the space-charge-free trajectory of an electron emitted from a cathode located in a parallel plane gun region. The electric field is assumed to be uniform in the gun region so that the electron follows a cycloidal path and reaches the exit plane at the apogee of its trajectory. The electric field in the interaction region is also considered to be uniform and twice as great as the gun region field. Thus, the electron should theoretically be capable of maintaining linear motion through the anode-sole region.

Dain and Lewis[5] have applied Ehrenfest's principle of adiabatic invariance to the investigation of electron motion through crossed electric and magnetic fields. In essence the adiabatic principle states that if a parameter which appears in the Hamiltonian of a conditionally periodic system changes slowly and continuously, the action variables remain invariant in the limit of an infinitesimally slow change. For the particular application to the electron guns this means that the behavior of the beam in the interaction region can be obtained without considering the details of the electron motion through the transition region provided the fields in this region vary sufficiently slowly.

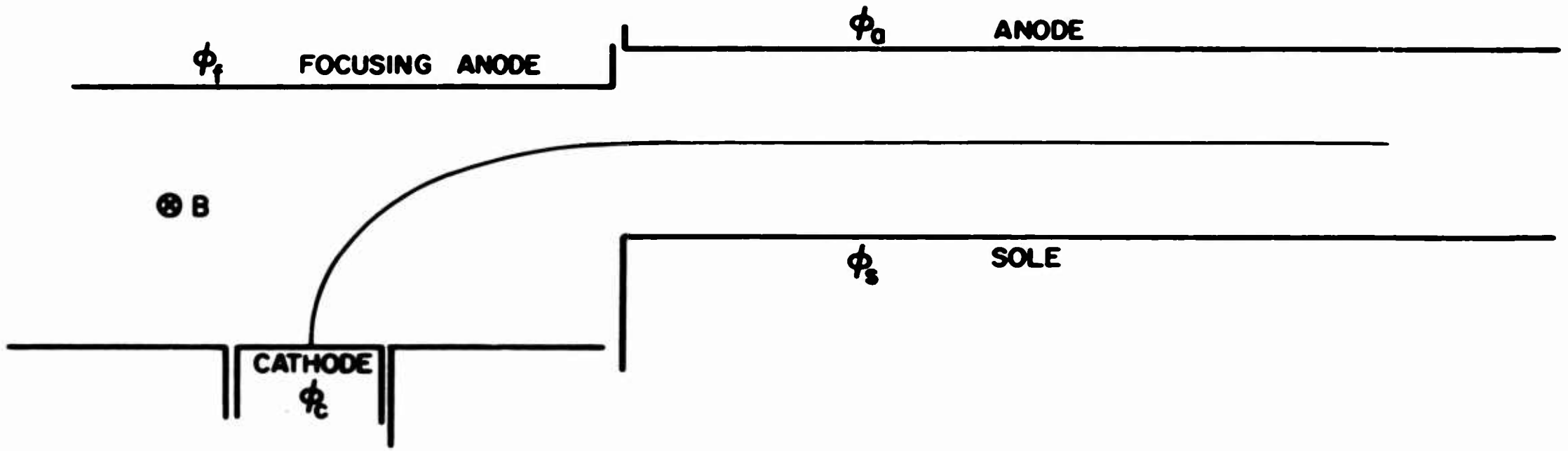

FIG. 1.3 IDEAL TRAJECTORY IN A FRENCH SHORT GUN.

Thus, by properly selecting the electric and magnetic field values in the cathode and interaction regions it is possible to obtain a converged beam in the sense that the beam width is less than the cathode width. However, the flow is not that of a rectilinear laminar beam, but rather, consists of electrons cycloiding between rectilinear boundaries.

Bartram and Pease[6] also applied the adiabatic principle to the design of an electron injection system. Their device was termed a "ramp gun" and is illustrated in Fig. 1.4. The nomenclature results from the fact that the transition region is comprised of various overlapping ramp electrodes biased at intermediate potentials. The electron flow was assumed to be that of the single trajectory beam (not necessarily laminar) described by Brillouin[1] and Slater[2]. Unlike the Dain and Lewis work, the effects of space charge were included in this analysis. The ramp electrode configurations were obtained by computing the equipotentials outside of the beam region and placing the properly designed electrodes along these curves.

The so-called Kino guns[7] illustrated in Fig. 1.5a and 1.5b also were developed on the assumption of a single trajectory electron beam. The electrons are assumed to leave the cathode in the normal direction and this component of current density (J_y) is considered to remain constant throughout the space-charge flow. The electric field and electron velocity have no variation in the z-direction and the field is further restricted to have only a y-component. Under these conditions the beam is composed of identical electron trajectories.

The appropriate electrode configurations for producing the assumed flow are obtained by utilizing a method of complex variables derived independently by Kirstein[8] and Lomax[9]. The method consists of transforming the problem to the complex plane and solving for the complex

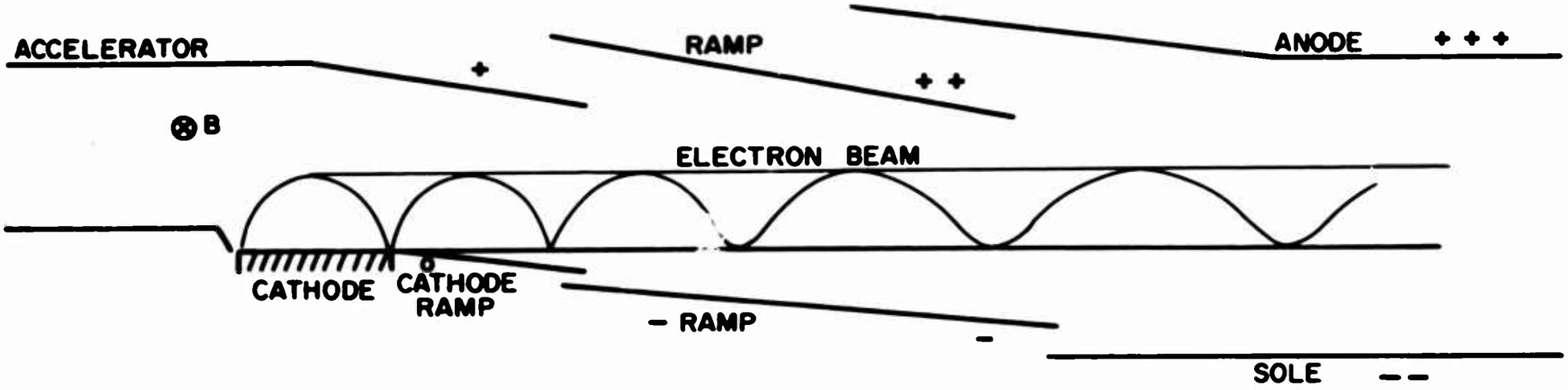

FIG. 1.4 CROSSED-FIELD RAMP GUN.

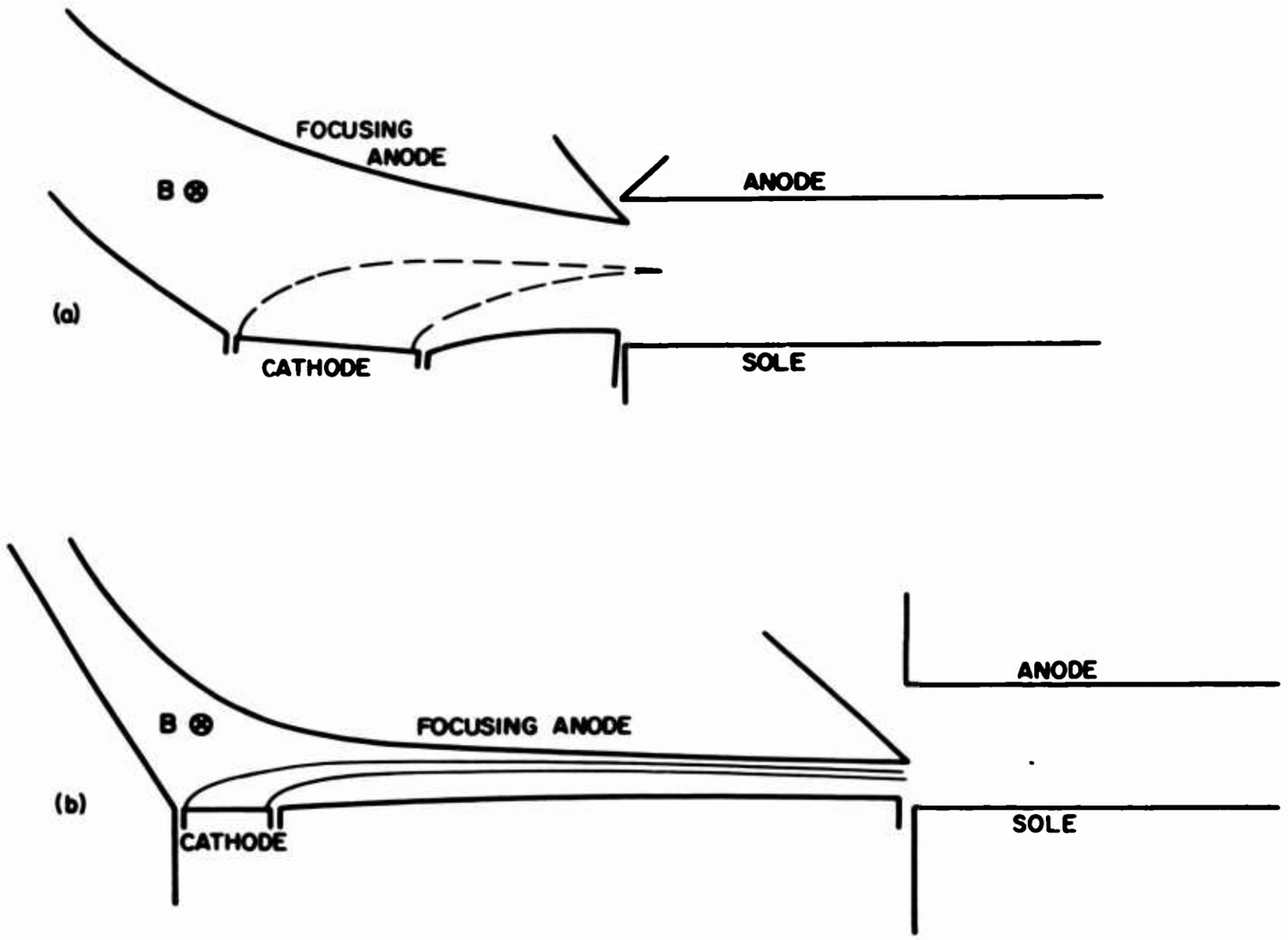

FIG. 1.5 THEORETICAL KINO ELECTRON GUN CONFIGURATIONS.

(a) KINO SHORT GUN.

(b) KINO LONG GUN.

potential function required to provide the proper voltage and electric field variation along the boundary of the beam in the complex plane. The inverse transformation then gives the equipotentials outside of the beam in the y-z plane. Although the operation is complicated it can be performed on a digital computer. In Fig. 1.5 one of these equipotentials has been selected as the focusing anode while the two zero potential curves become the cathode ramp electrodes.

The Kino short gun is derived on the basis of space-charge-limited operation and zero emission velocity from the catnode. One of the difficulties of the short gun flow is the infinite space-charge density which occurs at the $\omega_c t = 2\pi$ point along a trajectory. Another is the fact that the electron velocity vectors are nonparallel in any volume element of thickness Δz, thus making it impossible to inject the beam into the anode-sole region in the desired manner.

The Kino long gun configuration is obtained if the electrons are assumed to leave the cathode with a small initial y-component of velocity. The theoretical velocity variation and space-charge density in the beam are found to be closely related to the Brillouin values. The major objection to this type of flow is the severe restriction that all the electrons leaving the cathode normal to the surface must do so with the same value of initial velocity.

The magnetically shielded gun illustrated in Fig. 1.6 was developed by Hoch[10]. The electron beam is formed within the shielded gun and then injected into the magnetic field region. The beam leaves the shield with essentially a uniform velocity and travels through a transition region in which both the electric and magnetic fields vary. The electrons are then injected into the anode-sole region. The objective of the gun

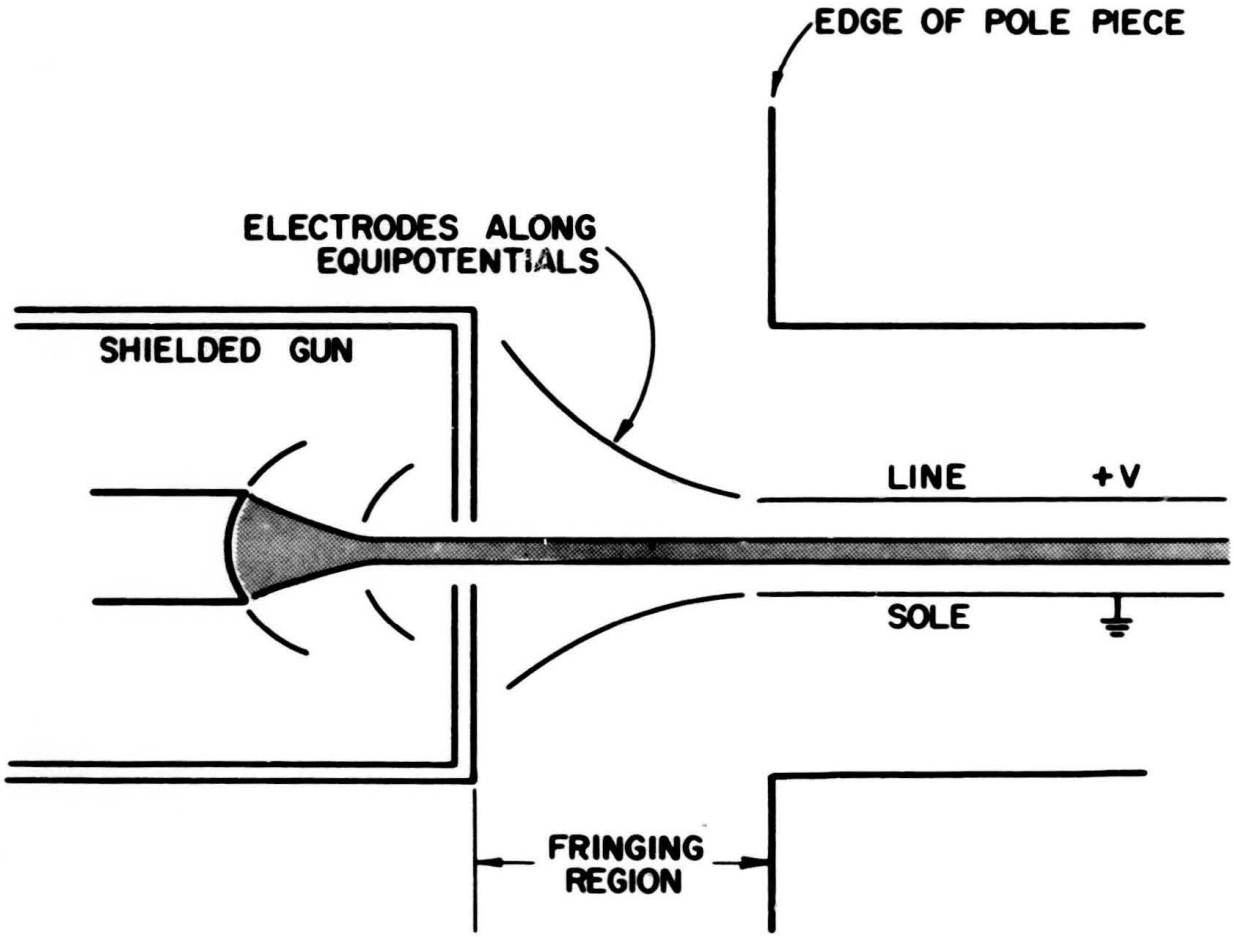

FIG. 1.6 MAGNETICALLY SHIELDED INJECTED-BEAM GUN CONFIGURATION.

is to converge the beam within the shield and taper B and E_y to maintain the same beam thickness through the transition region. This differs from the usual crossed-field injection systems in which the orthogonal electric and magnetic fields are simultaneously used to converge the beam.

The difficulty with the shielded gun is the fact that the electrons leave the shield with the same velocity but must reach the anode-sole entrance with a linear velocity variation across the beam. This requires the careful design of the electric and magnetic fields in the transition region so that the upper electrons are accelerated more than the lower ones. At the same time the electrons must be restricted to linear motion along the z-direction with no transverse displacement. The design of a system capable of producing such a transition appears to be extremely difficult.

Other types of crossed-field electron injection systems have been developed but in general they are similar to those described above. The objective is always the same; the formation of a beam whose characteristics are nearly identical to Brillouin flow. Except for the shielded gun, these designs deal with electrons which are emitted from a unipotential cathode and are then rotated by approximately 90° before injection into the anode-sole region. Experimental investigations of various injection systems clearly demonstrate the difficulty associated with the formation of laminar crossed-field electron beams.

1.2.2 Previous Evaluations of Injection Systems. The Charles-type gun has been used extensively in the construction of crossed-field devices. It is still employed frequently despite the fact that it cannot be used with a wide cathode. This limitation is a direct consequence of the manner in which the gun is designed. That is, the design is

based on electrons leaving just one point on the cathode. Thus, those electrons emitted from different locations along the cathode will enter the anode-sole region in a nonlaminar fashion.

Dain and Lewis did not construct an adiabatic gun and, hence, no experimental data is available. However, a beam tester model of the adiabatic ramp gun of Bartram and Pease was operated and evaluated. The electron beam was observed by introducing hydrogen into the system and noting the ionization pattern due to the collisions with the electrons. The results indicated that the device generated essentially the predicted current, beam thickness and location.

The Kino short gun was investigated by Midford[11] and found to behave in many respects as predicted by the theory. For example, the current and beam location were approximately as expected. However, investigation of the beam after leaving the gun indicated that the flow became nonlaminar. This can be attributed to the nonideal characteristics of the beam near the $\omega_c t = 2\pi$ plane. Furthermore, the emission from the cathode appeared to be quite nonuniform. In particular, photographs of the beam indicated suppressed emission from the rear of the cathode.

Despite the apparent ideal nature of the space-charge flow in the Kino long gun, experiments[11] have suggested undesirable characteristics. In particular, extremely high noise figures and r-f instabilities have been observed[12]. This behavior is thought to be caused by the occurrence of diocotron interactions during the motion of the beam through the long transition region. The existence of the diocotron effect is observed by the presence of extremely large sole currents even when the sole is at a negative potential relative to the cathode. These results suggest that the traversal of any long transition region at low

velocities will increase the nonlaminarity of the beam. Thus, it appears that any tube utilizing an adiabatic transition region will result in high noise level operation.

The shielded gun experiments of Hoch indicated 20 to 30 percent interception of the beam within the shielded region. Four different tubes were built and tested with the investigations indicating that 75 to 95 percent of the current leaving the shield was capable of reaching the collector although the beam profile on the collector suggested that the beam position between the plates was somewhat different than that predicted. However, there was no way of determining the complete beam configuration throughout the interaction region.

1.3 Previous Investigations of Crossed-Field Electron Beam Characteristics

To the author's knowledge the generation of a Brillouin beam has never been achieved in practice. It can, in fact, be shown[13] that it is impossible to achieve Brillouin flow even in theory if the thermal-velocities of the electrons emitted from the cathode are taken into account. Consequently, in any practical device the space-charge flow must necessarily be nonlaminar.

Rectilinear laminar flow is a special case of the single trajectory beam illustrated in Fig. 1.7. In this situation the beam boundaries are rectilinear but the individual trajectories are cycloidal. It has been shown that such a flow possesses exactly the same potential distribution and current as the rectilinear laminar beam.

Waters[14] has investigated theoretically the behavior of a beam which was subjected to small amplitude deviations from the Brillouin flow conditions. He developed a paraxial approach to the problem and

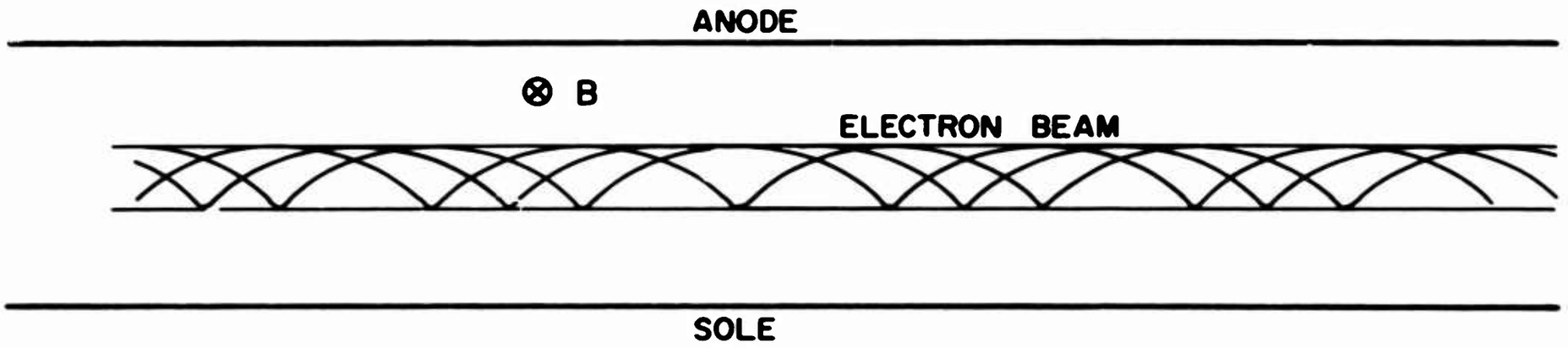

FIG. 1.7 ELECTRON BEAM COMPOSED OF IDENTICAL TRAJECTORIES.

his results indicated scalloped beams whose thicknesses varied periodically through the interaction region. Figure 1.8 illustrates several types of beam undulations obtained from Waters' analysis.

Midford[11] has considered briefly the types of flow which result when the beam is injected improperly into the interaction region. Figure 1.9a and 1.9b illustrate two particular situations wherein the entire beam undulates but maintains a constant thickness. The investigation involved a d-c small-signal analysis restricted to a thin beam but including the effects of space charge. Midford concluded that under no condition was the beam subjected to growth or decay in space and, hence, it should not exhibit d-c transverse cyclotron instabilities. This conclusion is in agreement with Pierce[15] who predicted that planar crossed-field beams were not subject to d-c instabilities. The experimental works of Midford and Anderson indicated that the electron beams did undulate as they moved through the interaction region.

One of the characteristics of crossed-field space-charge flows which has been subjected to a great deal of investigation is the diocotron phenomenon. As mentioned above, the diocotron effect refers to the collection of current on the sole even when that electrode is biased at a large negative potential relative to the cathode. The effect implies an appreciable energy increase by certain electrons during their motion from the cathode to the sole. Åstrom[16] suggested that the process causing the energy increase occurred during the motion of the electrons through the anode-sole region and was essentially independent of the conditions near the cathode.

Miller[17] found that excess energy electrons were already present in the beam as it entered the anode-sole region thus indicating that the diocotron process was occurring even in the gun. In general he operated

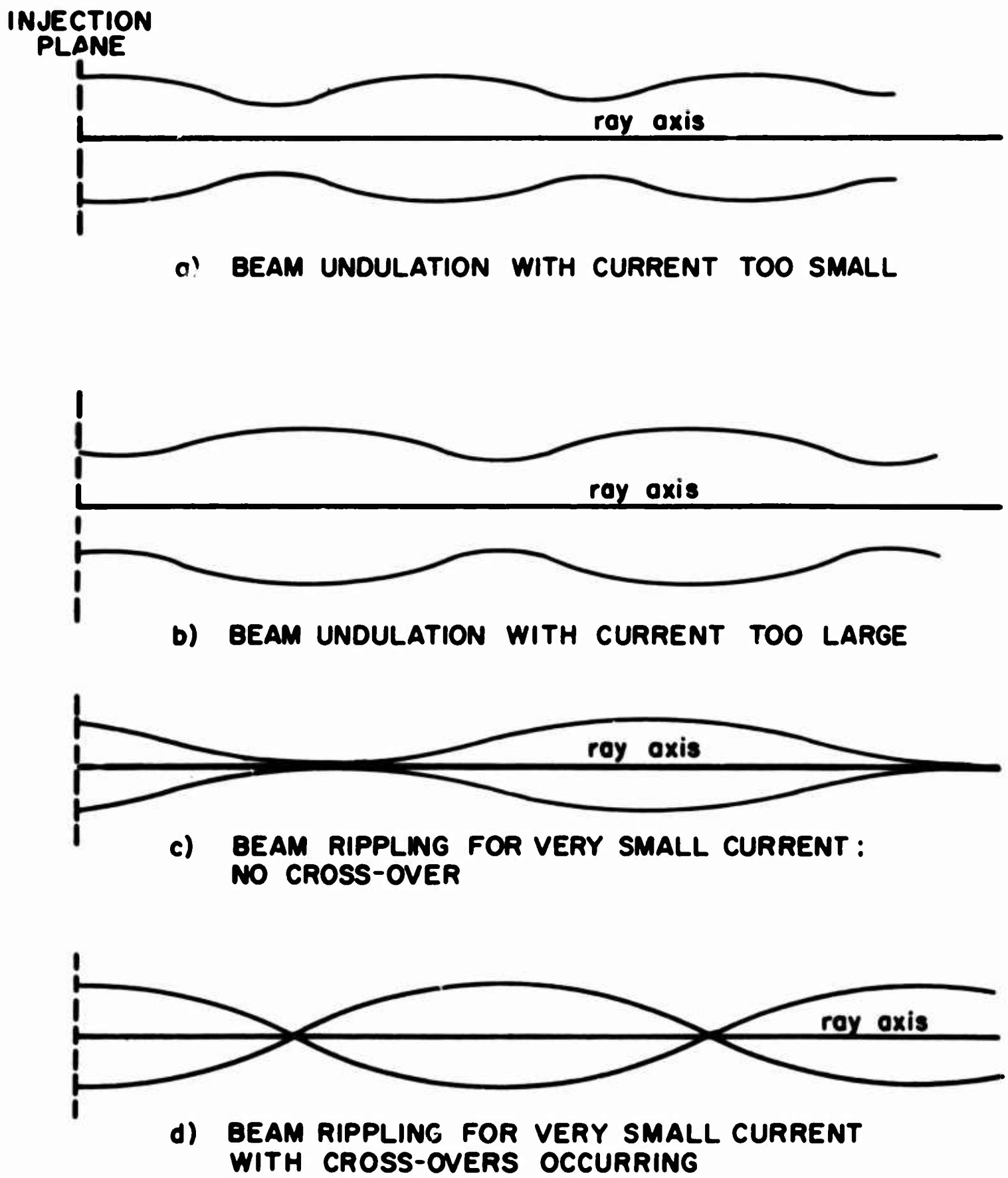

FIG. 1.8 THEORETICAL ELECTRON BEAM CONFIGURATIONS OBTAINED FROM PARAXIAL ANALYSIS.

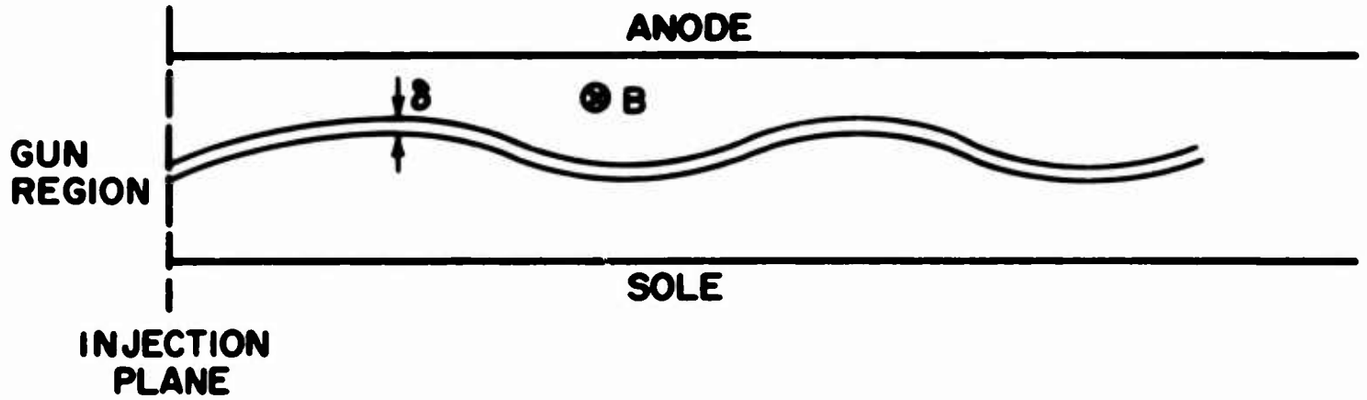

(a) BEAM INJECTION AT AN ANGLE INTO ANODE-SOLE REGION

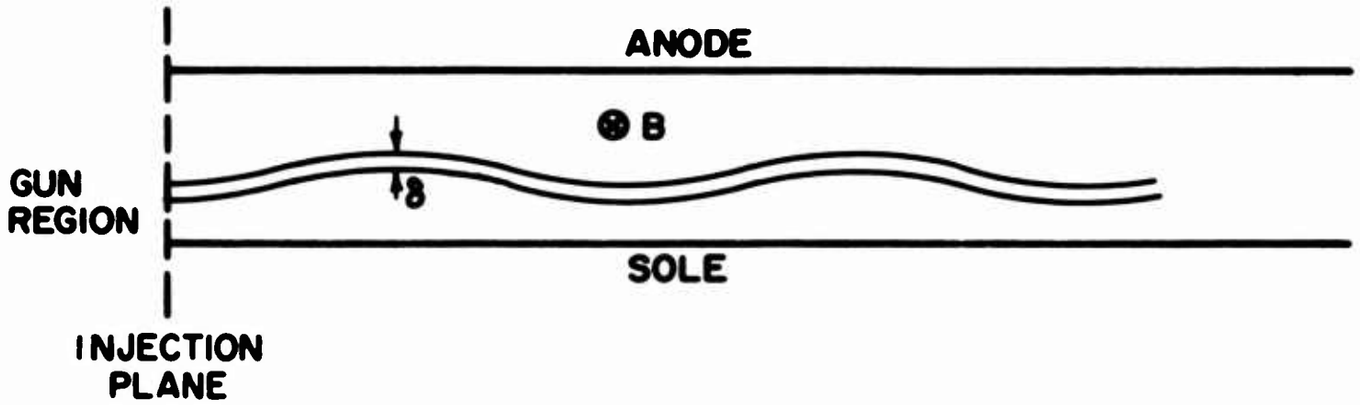

(b) DISCONTINUITY IN ELECTRIC FIELD BETWEEN GUN AND INTERACTION REGION

FIG. 1.9 UNDULATION OF ELECTRON BEAM DUE TO IMPROPER CONDITIONS AT THE GUN EXIT PLANE.

at extremely high magnetic fields so that the electrons performed a series of tight loops in the gun region. The geometry was such that a low voltage region or potential well existed between the edge of the cathode and the sole. Electrons were frequently "trapped" in this region and required long time intervals before reaching the anode-sole region. Consequently Miller concluded that the diocotron phenomenon resulted from the exchange of energy between electrons during their travel through a low voltage region such as the potential well.

The experimental results of Midford[11] indicated the existence of diocotron gain in the gun region even though no potential well existed. He concluded that the effect was due to instabilities associated with the formation of the potential minimum near the cathode under space-charge-limited conditions. Substantiating proof for this conclusion was experimentally observed by Guenard and Huber[18], and Epsztein and Maillart[19]. In each investigation the sole current was observed to be greatly reduced when changing from space-charge-limited to temperature-limited operation.

Warnecke, Huber, Guenard and Doehler[20] also encountered the diocotron phenomenon during their study of carcinotrons. They attributed the negative sole current to a growing-wave electron interaction process. Such a process would occur everywhere along the beam.

Another characteristic of crossed-field devices is the situation in which the anode of a cylindrical magnetron continues to draw current even after the critical magnetic field has been exceeded. This indicates a process whereby certain electrons arrive at electrodes which in theory are impossible to reach. Similarly, space charge is found to exist in regions of the magnetron where theoretically there should be no electrons.

Lindsay[21] has suggested that the excess anode current is attributable to the presence of tangential initial velocities at the cathode; i.e., although the normal thermal velocities are not sufficient to explain the phenomenon, the presence of tangential emission velocities is capable of allowing an appreciable fraction of the current to reach the anode. Horsley and Sims[22] have devised a special planar diode geometry to test the Lindsay theory by accurately determining the cut-off curves.

The presence of space charge outside of the theoretical Brillouin radius was predicted by Hok[23] in a statistical analysis of magnetron operation. Independent experimental investigations were carried out by Reverdin[24] and Peterson[25] in which the cathode-anode space was probed by means of an axially directed electron beam. The beam passed through the space-charge region and the pattern was displayed on a flourescent screen which indicated space charge present outside of the Brillouin limit. Mathias[26], using a cesium flouride molecular beam, and Nedderman[27], using helium and hydrogen probes, obtained results similar to the Reverdin and Peterson data.

The investigations described above indicate quite clearly the many problems involved in crossed-field space-charge flows. These problems involve the formation of well-defined electron beams and an understanding of the many strange characteristics which have been observed in experimental crossed-field devices.

1.4 Outline of the Investigations

The preceding investigations were concerned with various aspects of the space-charge flow in crossed-field devices. These include the study of theoretical electron guns, the experimental evaluation of

electron injection systems, and the general characteristics of electron beams in crossed-field regions. The investigations which follow are intended to provide a better understanding of the electron beams formed by crossed-field injection systems. To do this it is necessary to treat the problem in its entirety beginning with the formation of the beam in the gun and continuing to the analysis of the electron flow characteristics in the anode-sole region.

In Chapter II some of the theoretical space-charge flow limitations are discussed. The analyses are concerned with the limitations of electron injection systems and the beam restrictions which exist in the interaction region.

Chapter III describes the results of analog computer investigations of specific electron injection systems. The Kino short gun is analyzed in detail and the effects of various electrode modifications are indicated.

Chapter IV involves similar gun studies carried out by digital computer methods. The effects of initial velocities and potential minimum regions are also considered.

The properties of beams in the crossed-field interaction region are carried out in Chapter V. Special emphasis is given to the electron beam configurations which are possible in planar crossed-field regions. The result of improper injection of the beam into the anode-sole region is also discussed.

Chapter VI describes the experimental beam analyzer equipment which was designed to allow analysis of electron beam characteristics. A description is also given of the extended Kino short gun which was used as the beam launching system.

Chapter VII describes the operating characteristics of the extended Kino gun and the analyses of electron beams in the anode-sole region. The latter investigations are concerned with both the gross characteristics of the beam (e.g., beam profile, location of beam, variations in space, etc.) and with the detailed characteristics of the individual electrons comprising the flow (e.g., electron velocity and space-charge density).

Chapter VIII summarizes the results of the investigations and the conclusions derived therefrom. Suggestions are also made as to possible future investigations which would be pertinent to these studies.

CHAPTER II. THEORETICAL LIMITATIONS ON SPACE-CHARGE FLOW IN CROSSED-FIELD DEVICES

2.1 Preliminary Remarks

The prime objective of a crossed-field injection system is to produce a high-density electron beam which is properly located to interact with the r-f wave propagating along the slow-wave structure. However, as mentioned in Chapter I, there are many difficulties associated with the formation of high current density, laminar electron beams. Although much effort has been devoted to the solution of this problem, the generation of laminar space-charge flow has not yet been successfully achieved in static crossed fields.

Superficially the achievement of high current densities appears to be relatively simple. One possibility would be to use a wide cathode operating at a reasonable current density and then converge the beam to a small cross-sectional area. Thus the desired density would be achieved by simply using the correct gun system to produce the necessary convergence of the beam. However, there are two fundamental obstacles which exist:

1. At the present time there is no electron gun design which is capable of forming extremely high-density beams in crossed-field devices.

2. Even if such a high-convergence gun did exist it can be easily shown that electron beams which have a density exceeding the Brillouin value are incapable of laminar flow. Thus for any crossed-field electron gun system there is a maximum convergence which can be imposed on the beam and still allow the flow to be compatible with the restriction of laminarity.

There are several conditions which must be satisfied to maintain a rectilinear laminar beam in a planar anode-sole region. For example, the location and thickness of a laminar beam are directly dependent on the current, voltage, and magnetic field.

It is the extremely critical balance between the electric and magnetic forces acting on the electrons which limits the space-charge density that can be achieved. Attempts to exceed the Brillouin density will reduce the electric field which acts on the electrons. This results in an imbalance between the electric and magnetic forces and hence leads to nonlaminar flow. This, of course, is in contrast to O-type flows wherein the density of the beam can be increased quite appreciably by introducing an axial magnetic field to confine the beam to a given diameter.

2.2 Brillouin Beam Conditions

A Brillouin beam involves the laminar, unidirectional flow of electrons. For crossed-field devices the beam moves between planar anode and sole electrodes as illustrated in Fig. 2.1. The beam is assumed to be formed in an arbitrary electron gun system, the difficulty of such a formation being of no concern at this time. The linear motion in the anode-sole region is obtained by the proper balancing of electric and magnetic forces acting on the electrons. The analysis of the problem is carried out in Appendix A where the following relations for the beam quantities are obtained:

$$\varphi_2 = \frac{\omega_c^2}{2\eta}(y + 2a)^2 \quad , \tag{2.1}$$

$$E_2 = -\frac{\omega_c^2}{\eta}(y + 2a) \quad , \tag{2.2}$$

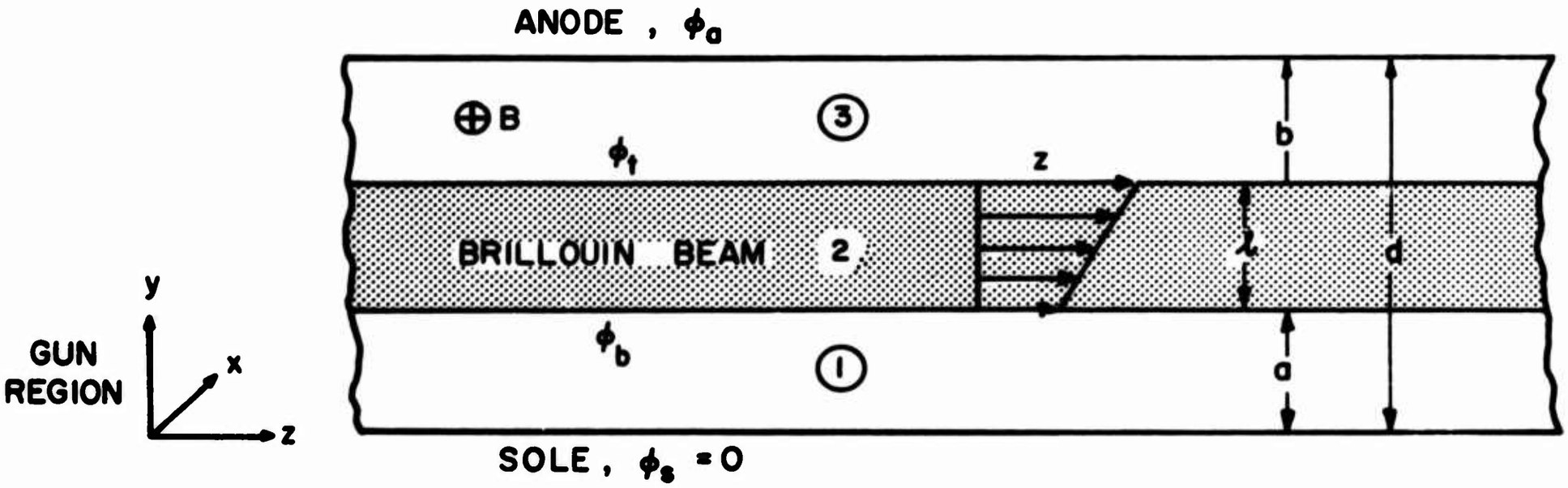

FIG. 2.1 BRILLOUIN BEAM MOVING THROUGH THE ANODE-SOLE REGION.

$$\frac{dz}{dt} = \omega_c (y + 2a) \quad , \tag{2.3}$$

$$\rho_o = -\frac{\epsilon_o \omega_c^2}{\eta} \quad , \tag{2.4}$$

and

$$J_z = -\frac{\epsilon_o \omega_c^3}{\eta} (y + 2a) \quad . \tag{2.5}$$

The subscripts 2 refer to quantities within the beam, $\eta \triangleq |q|/m$ is the electron charge-to-mass ratio, $\omega_c \triangleq \eta B$ is the radian cyclotron frequency, and the distance y is measured relative to the lower edge of the beam. If the beam is assumed to have a width h in the x-direction, the total current is given by

$$I = h \int_{y=0}^{y=\ell} J_z \, dy \quad , \tag{2.6}$$

which upon integration becomes

$$I = \frac{h \, \epsilon_o \omega_c^3}{\eta} \left(\frac{\ell^2}{2} + 2a\ell \right) \quad . \tag{2.7}$$

Equations 2.1 through 2.7 provide a complete description of a Brillouin beam moving through the anode-sole region of a crossed-field device at a distance "a" above the sole.

2.3 Limitations of Brillouin Flow

The restriction to rectilinear laminar flow imposes certain conditions on the beam in the anode-sole region. The relation between the thickness and location of the beam and the current which it carries is of particular interest. From Eq. 2.2 the electric field at any point in the beam can be written as

$$E_2 = -\frac{\omega_c^2}{\eta}\left[y + 2\,(d - b - \ell)\right] \quad . \tag{2.8}$$

The constant electric field which exists in the region above the beam is given by

$$E_3 = -\frac{\varphi_a - \varphi_2\big|_{y=\ell}}{b} \quad . \tag{2.9}$$

Evaluating E_2 at $y = \ell$ and equating to E_3 gives

$$b = (d - \ell/2) - \frac{\eta\varphi_a}{\omega_c^2\,(2d - \ell)} \quad . \tag{2.10}$$

Thus for a given anode-sole spacing (d) and magnetic field (B), the location of the beam as specified by b, the distance between the anode and upper beam boundary, is dependent only on the beam thickness (ℓ) and anode voltage (φ_a).

The total current can be expressed as

$$I = \frac{h\,\epsilon_o\,\omega_c^3\,\ell}{\eta}\left[(2d - 2b - \ell) - \ell/2\right] \quad , \tag{2.11}$$

where a has been replaced by $(d - b - \ell)$. From Eq. 2.10 it is obvious that

$$(2d - 2b - \ell) = \frac{2\eta\varphi_a}{\omega_c^2\,(2d - \ell)} \quad , \tag{2.12}$$

so that the current becomes

$$I = \frac{h\,\epsilon_o\,\omega_c^3\,\ell}{\eta}\left[\frac{2\eta\varphi_a}{\omega_c^2\,(2d - \ell)} - \ell/2\right] \quad . \tag{2.13}$$

The implications of this equation are quite significant. If an electron gun is generating a beam of total current I for a given magnetic field, the injection of this beam into an anode-sole region where the anode potential is φ_a will result in laminar flow only if the beam has the thickness specified by Eq. 2.13 and enters at the location given by Eq. 2.10. The equation for ℓ is a cubic equation for which two of the roots are physically unrealizable. Thus there is but one value of ℓ which is compatible with Brillouin flow. In general, therefore, for specified I, φ_a, and B values the beam location (b) and thickness (ℓ) for laminar flow are uniquely determined.

The requirements for laminar beams indicate that there are maximum theoretical limits on the perveance and electronic efficiency of a crossed-field tube. To analyze the perveance, consider the current carried by an elementary filament of width dy,

$$dI = \frac{h\,\epsilon_o\,\omega_c^3}{\eta}\,(y + 2a)\,dy \quad . \tag{2.14}$$

The differential perveance for such a filament can be defined as

$$\Delta\ \text{Perv.} \triangleq \frac{dI}{\varphi^{3/2}} \ , \tag{2.15}$$

where φ is the voltage of the strip of current and is given by Eq. 2.1. The total perveance of the beam can thus be written as

$$\text{Perv.}_{\text{Br.}} = \int_{y=0}^{y=\ell} \frac{dI}{\varphi^{3/2}} = \int_{y=0}^{y=\ell} \frac{h\,\epsilon_o\,\omega_c^3\,(y + 2a)dy}{[\omega_c^2/2\,(y + 2a)^2]^{3/2}} \quad . \tag{2.16}$$

Performing the integration gives

$$\text{Perv.}_{\text{Br.}} = h\,\epsilon_o \sqrt{2\eta}\;\frac{\ell}{a\,(\ell + 2a)} \tag{2.17}$$

as the perveance of a Brillouin beam.

In the same manner as Dunn[28] the perveance per square is defined as the perveance divided by the beam width to beam thickness ratio,

$$\text{Perv.}_{\square} \triangleq \frac{\text{Perv.}_{\text{Br.}}}{(h/\ell)} = \frac{\epsilon_o \sqrt{2\eta}\;\ell^2}{a(\ell + 2a)} \;. \tag{2.18}$$

The evaluation of efficiency can be carried out in a similar manner. This is done by considering that the electrons which leave a zero potential cathode carry a total power given by

$$P_o = I\,\varphi_a \;, \tag{2.19}$$

where I and φ_a are the beam current and anode voltage as previously defined. However, since the electrons enter the interaction region with some velocity, not all of the electron energy is available for conversion to the propagating r-f wave. To determine how much energy is available, consider the maximum power which can be extracted from a differential current element of the Brillouin beam. This can be written as

$$dP = (\varphi_a - \varphi)\,dI \;, \tag{2.20}$$

where φ = voltage of the current strip. Thus the total power which could be extracted from a Brillouin beam entering the interaction region is given by

$$P_{\text{Br.}} = h \int_{y=0}^{y=\ell} (\varphi_a - \varphi)\,J_z\,dy \;. \tag{2.21}$$

Substituting for φ and J and integrating gives

$$P_{Br.} = \frac{h\,\epsilon_o\,\omega_c^3\,\ell\,(\ell + 4a)}{2\eta}\left\{\varphi_a - \frac{\omega_c^2}{4\eta}\left[\ell^2 + 4a\ell + 8a^2\right]\right\} . \qquad (2.22)$$

Since $P_{Br.}$ is the maximum power which can be extracted from a Brillouin beam while P_o is the power contained by the beam as it leaves the cathode, it is possible to define a maximum Brillouin electronic efficiency (similar to the usual electronic efficiency of a planar crossed-field device) as

$$\eta_{Br} \triangleq \frac{P_{Br.}}{P_o} . \qquad (2.23)$$

Substituting for P_o from Eq. 2.19 and $P_{Br.}$ from Eq. 2.22 the efficiency becomes

$$\eta_{Br.} = 1 - \frac{\omega_c^2}{4\eta\varphi_a}\left[\ell^2 + 4a\ell + 8a^2\right] . \qquad (2.24)$$

This can also be written as

$$\eta_{Br.} = 1 - \frac{\varphi_m}{\varphi_a} , \qquad (2.25)$$

where $\varphi_m = 1/2(\varphi_{top} + \varphi_{bottom})$ is the mean value of the voltage within the beam. Notice that this expression is very similar to the electronic efficiency of a thin beam[2] in a planar region as given by

$$\eta_{e\ell} = 1 - \frac{\varphi}{\varphi_a} , \qquad (2.26)$$

where φ is the potential at the beam location. Since the presence of the beam depresses the potential in the interaction region, it is obvious

that for the same beam location the theoretical Brillouin efficiency is greater than the electronic efficiency when space charge is neglected.

The restriction to laminar flow requires that the following conditions be satisfied:

1. The beam has unique thickness,
2. The beam has unique location,
3. The perveance is given by Eq. 2.18, and
4. The maximum possible efficiency is given by Eq. 2.24.

The equations can be simplified by defining

$$\bar{I} \triangleq \frac{\eta I}{\epsilon_o \omega_c^3 d^2 h} , \tag{2.27}$$

$$\bar{\Phi}_a \triangleq \frac{2\eta\varphi_a}{\omega_c^2 d^2} , \tag{2.28}$$

$$\bar{l} \triangleq l/d , \tag{2.29}$$

$$\bar{a} \triangleq a/d , \tag{2.30}$$

and

$$\bar{b} \triangleq b/d . \tag{2.31}$$

($\bar{I}$ and $\bar{\Phi}_a$ are different from the normalized parameters used in the Kino theory.) With these definitions the pertinent equations become

$$\bar{I} = \bar{l}\left[\frac{\bar{\Phi}_a}{(2 - \bar{l})} - \frac{\bar{l}}{2}\right] , \tag{2.32}$$

$$\bar{b} = \frac{1}{2}\left[(2 - \bar{l}) - \frac{\bar{\Phi}_a}{(2 - \bar{l})}\right] , \tag{2.33}$$

$$\text{Perv.}_{\square} = \frac{\epsilon_o \sqrt{2\eta}\ (\bar{\ell})^2}{(\bar{a})\ (\bar{\ell} + 2\bar{a})} \quad , \tag{2.34}$$

and

$$\eta_{Br.} = 1 - \frac{1}{4\bar{\Phi}_a} [(\bar{\ell})^2 + 4(\bar{a})\ (\bar{\ell}) + 8(\bar{a})^2] \quad . \tag{2.35}$$

$\bar{I}$ is plotted vs. $\bar{\ell}$ in Fig. 2.2 for different values of the parameter $\bar{\Phi}_a$. For low values of $\bar{\Phi}_a$ (e.g. $\bar{\Phi}_a = .40$) the curves display a relative maximum and then become negative at some $\bar{\ell} < 1$. This of course is physically impossible. A more thorough investigation reveals that points on the curve beyond the maximum $\bar{I}$ value correspond to the physically unobtainable roots of $\bar{\ell}$. As $\bar{\Phi}_a$ is increased, the curves become steeper indicating that the current is being carried by a thinner beam.

The curves of $\bar{b}$ vs. $\bar{\ell}$ are shown in Fig. 2.3. This figure indicates that as the beam becomes thinner, it must be located farther from the anode to maintain laminar flow. As $\bar{\Phi}_a$ is increased, the necessary beam thickness at a fixed distance from the anode is reduced. Thus a thin beam situated close to the anode is possible only for extremely high $\bar{\Phi}_a$ values which requires either high φ_a or low magnetic field. The diagonal $\bar{b} = \bar{\ell}$ line represents the dividing line between those situations which are physically realizable and those which are impossible. In other words, any point to the right of this line corresponds to a situation wherein part of the beam is being intercepted by the sole since in this region

$$(\bar{b} + \bar{\ell}) > 1 \quad . \tag{2.36}$$

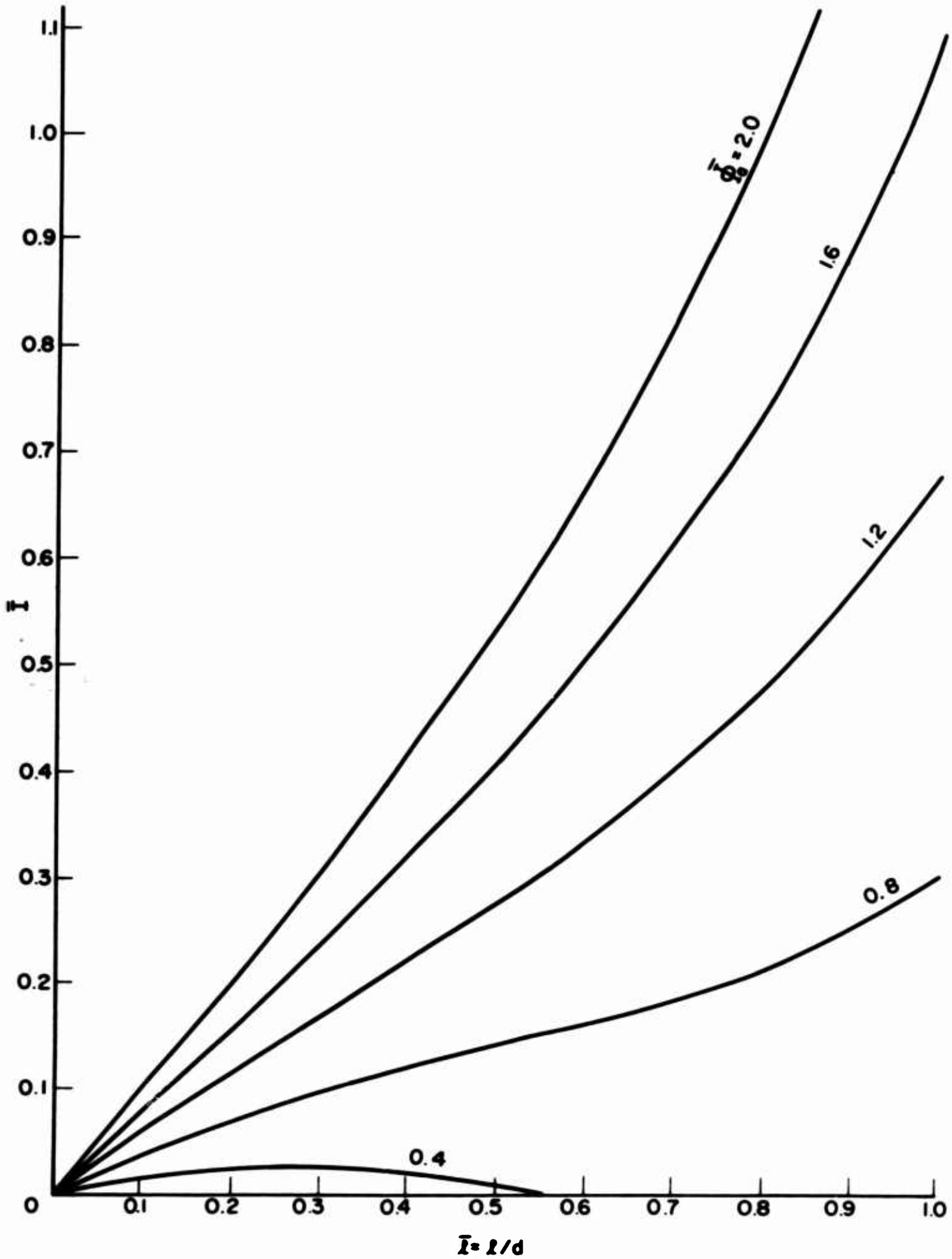

FIG. 2.2 VARIATION OF $\bar{I}$ WITH $\bar{l}$ FOR DIFFERENT $\bar{\phi}_a$ VALUES.

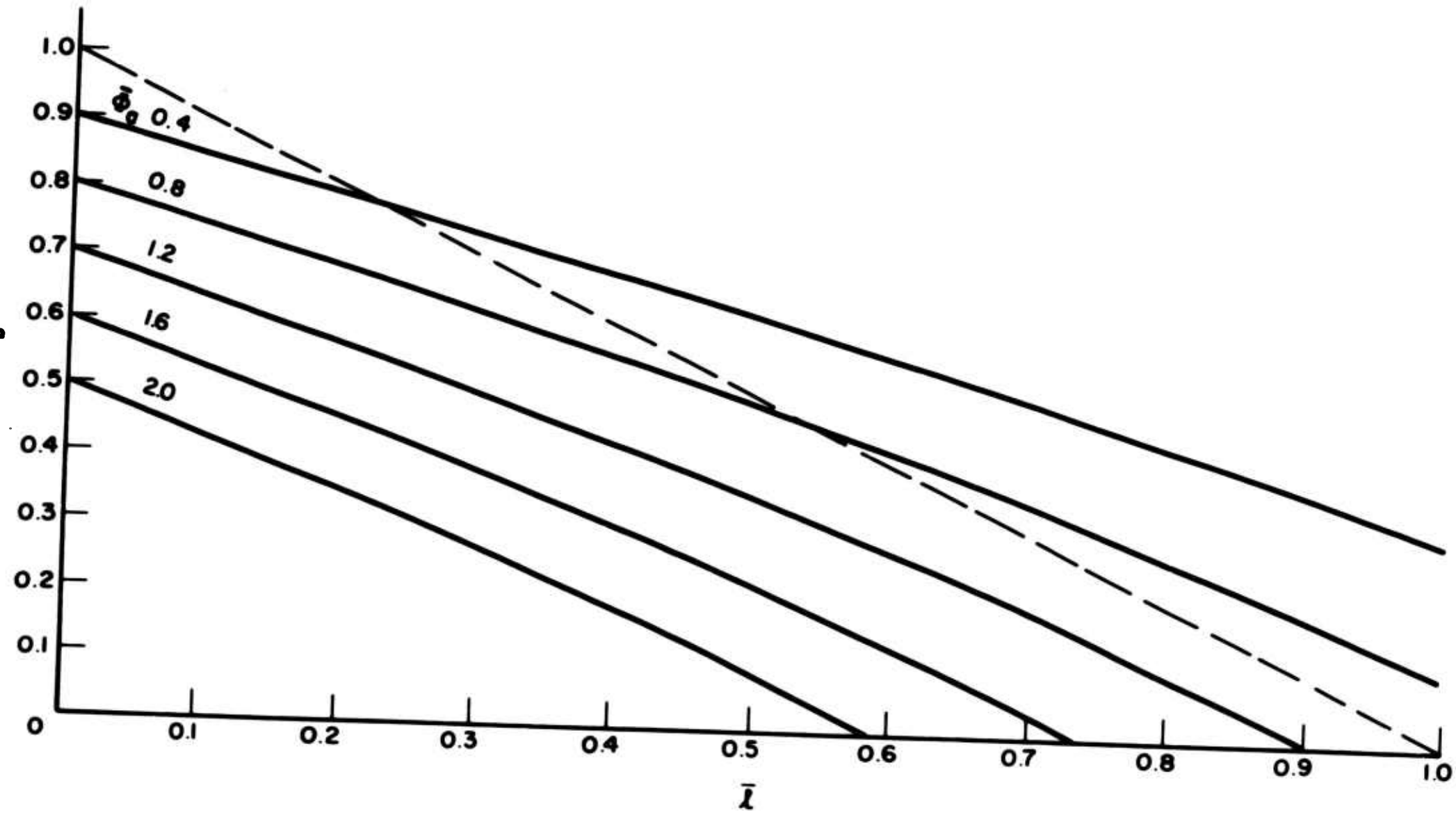

FIG. 2.3 VARIATION OF $\bar{b}$ WITH $\bar{l}$ FOR DIFFERENT $\bar{\Phi}_a$ VALUES.

Notice also that the point at which the $\bar{\Phi}_a = 0.40$ curve intercepts the $\bar{b} = \bar{l}$ line is precisely that $\bar{l}$ value at which $\bar{I}$ has its maximum value. Thus it is obvious that the above statement concerning the physical impossibility of having any $\bar{l}$ values beyond the value at maximum $\bar{I}$ is correct.

Figure 2.4 illustrates the variation of perveance with current. The interesting feature here is that increases in current require similar increases in the perveance. This comes about because increases in Brillouin current require an increase in $\bar{l}$ which in turn requires the beam to be located closer to the anode. Consequently the beam potential is increased and, in fact, is sufficiently larger so that it more than compensates for the reduction in Perv.$_{\square}$ brought about by the increase in current.

Finally Fig. 2.5 indicates the variation of efficiency as a function of the beam to anode spacing. The curves indicate that for each $\bar{\Phi}_a$ value there is one $\bar{b}$ at which $\eta_{Br.}$ is maximum. For example, the $\bar{\Phi}_a = 1.2$ case has a maximum theoretical efficiency of approximately 97 percent at $\bar{b} \approx 0.4$. Notice that there can be no situation wherein points can exist to the right of the diagonal line since in this region $\bar{l} < 0$. In general, the efficiencies are quite high with values in excess of 90 percent being available for various $\bar{\Phi}_a$. Furthermore, the minimum theoretical Brillouin efficiency is 50 percent which occurs at $\bar{b} = 0$; i.e., when the beam is adjacent to the anode. This suggests that if Brillouin flow could be achieved in practice, the electronic efficiency should be quite high. Of course the major problem would then be that of providing an effective means of coupling between the beam and the r-f circuit wave.

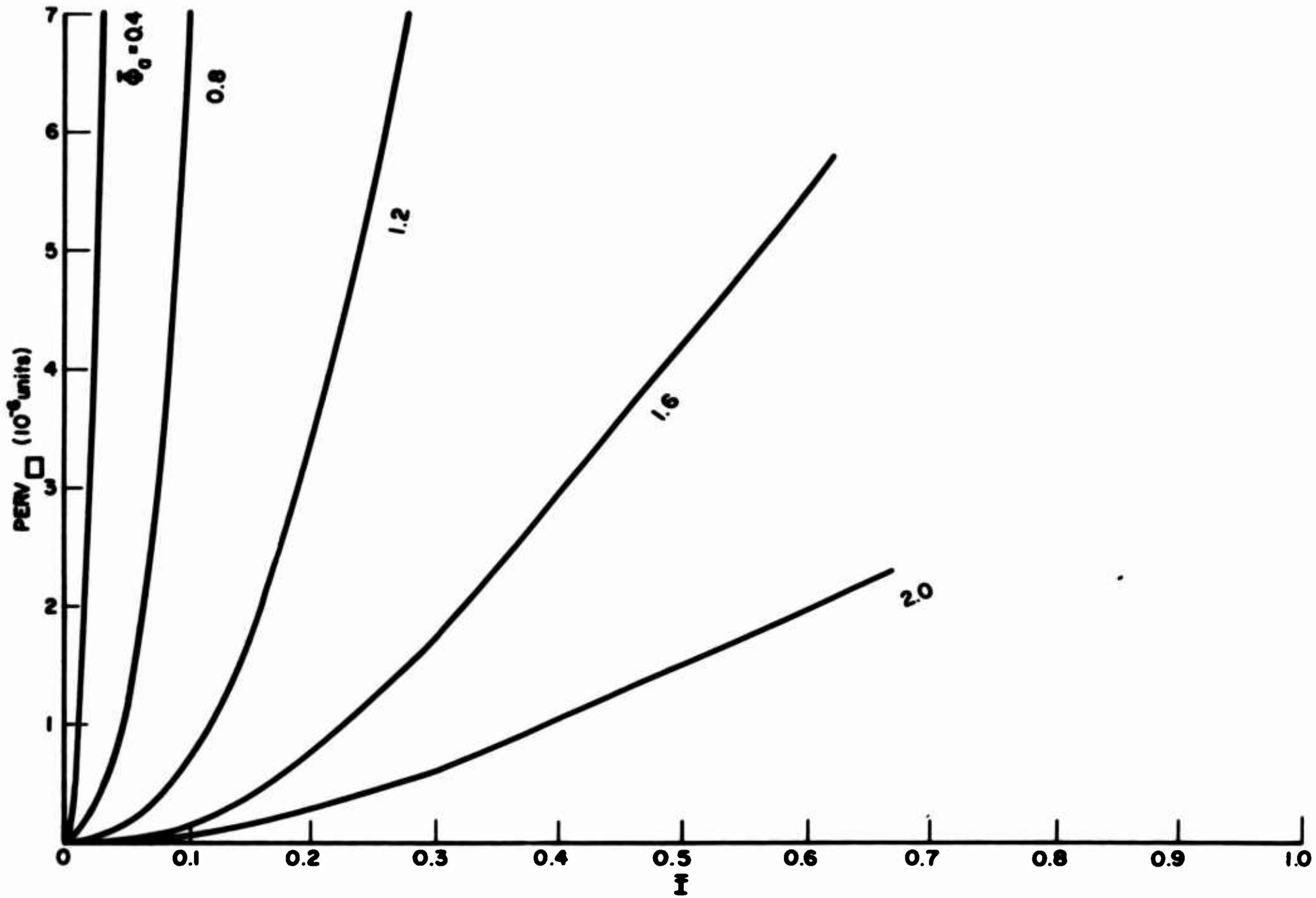

FIG. 2.4 VARIATION OF PERVEANCE WITH $\bar{I}$ FOR DIFFERENT $\bar{\Phi}_a$ VALUES.

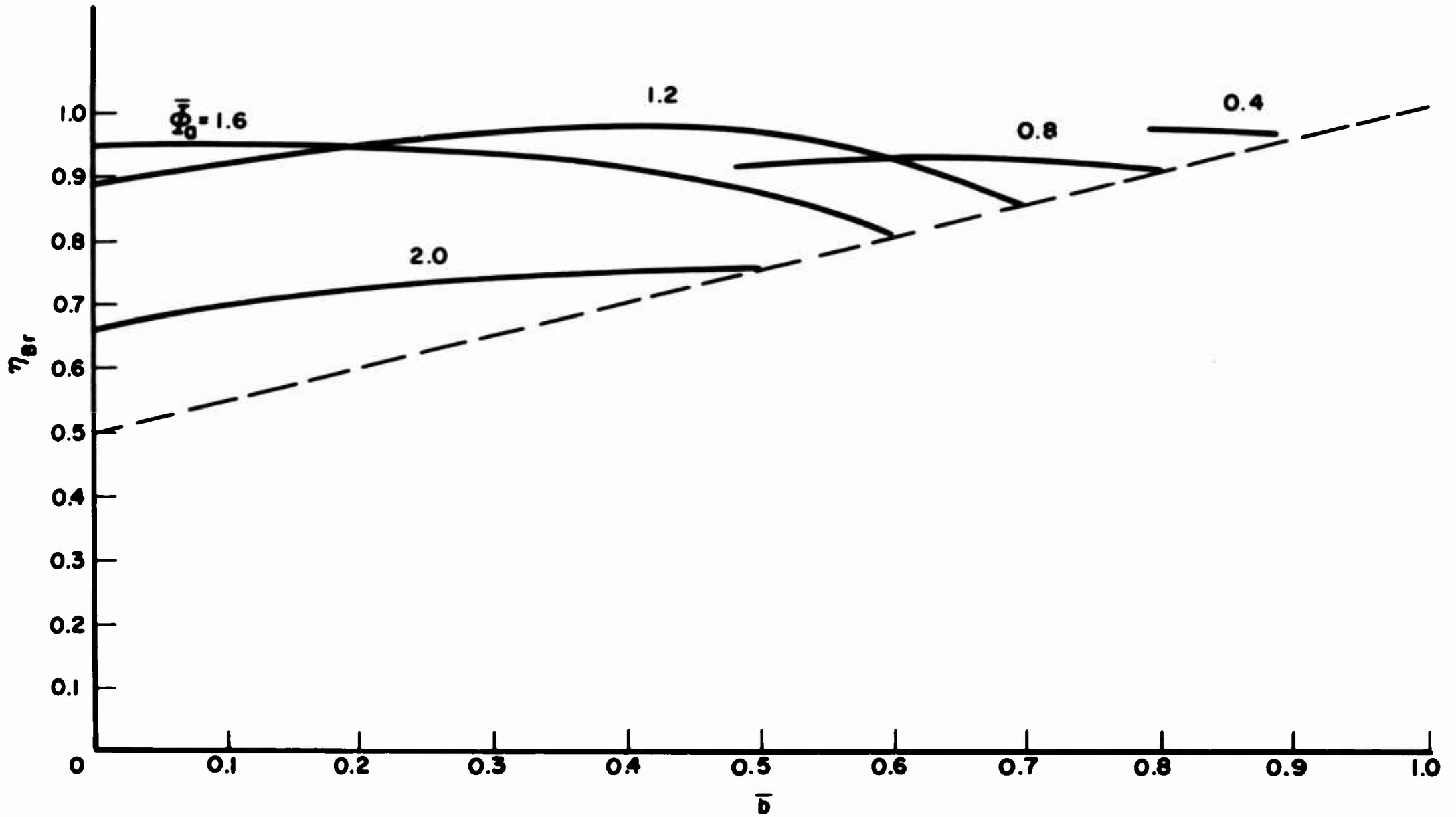

FIG. 2.5 VARIATION OF EFFICIENCY WITH $\bar{b}$ FOR DIFFERENT $\bar{\Phi}_a$ VALUES.

2.4 Practical Convergence Limitations for Electron Guns

With reference to Fig. 2.1 again, consideration will now be extended to the required gun properties necessary for the formation of a Brillouin beam. Of principal importance is the question of whether there exists a limitation on the magnitude of convergence which can be imposed on a beam by the gun system. If W is the width of the cathode from which the electrons originate, the convergence of the beam can be defined as

$$K \triangleq \frac{W}{\ell} \quad . \tag{2.37}$$

The assumption of uniform emission from the cathode allows the total beam current to be written as

$$I = h\, W\, J_c \quad , \tag{2.38}$$

where J_c is the uniform cathode current density. But from Eq. 2.7 it is also known that the Brillouin beam current is

$$I = \frac{h\, \epsilon_o\, \omega_c^3}{\eta} \left(\frac{\ell^2}{2} + 2a\ell \right) \quad . \tag{2.7}$$

Continuity requires that these two expressions be the same thus resulting in the relation

$$\ell^2 + 4a\ell = \frac{2\eta\, W\, J_c}{\epsilon_o\, \omega_c^3} \quad . \tag{2.39}$$

Replacement of ℓ by W/K results in a quadratic equation for K whose solution is

$$K = \frac{a\, \epsilon_o\, \omega_c^3}{\eta J_c} \left\{ 1 + \sqrt{1 + \frac{\eta\, J_c\, W}{2a^2\, \epsilon_o\, \omega_c^3}} \right\} \quad . \tag{2.40}$$

Thus for a given magnetic field and cathode current density this equation gives the convergence which must be achieved in order to generate a laminar beam which leaves the gun at a distance "a" above the sole.

For a fixed cathode width the only alternative for increasing the beam current is, of course, to increase the cathode current density. Therefore, if the magnetic field and beam location are fixed, the net effect of the increased J_c is to decrease the convergence. In other words, since the space-charge density for a Brillouin beam is given by

$$\rho_o = -\frac{\epsilon_o \omega_c^2}{\eta} , \tag{2.41}$$

it is obvious that the only way to increase the beam current for a fixed magnetic field and beam voltage is to increase the beam thickness. Consequently the convergence of the beam is determined by J_c which in turn is determined by the voltage applied to the gun accelerator electrode. If higher convergence values are desired, it is necessary to resort to increased magnetic field values. However, increases in B also require increased voltages in order to maintain the electron trajectories approximately the same.

As mentioned earlier one of the reasons for wanting high beam convergence is to produce high current density space-charge flow. However, in the previous section the current density for laminar flow was shown to be

$$J_z = -\frac{\epsilon_o \omega_c^3}{\eta} (y + 2a) . \tag{2.42}$$

Thus there exists only three possibilities for increasing the average Brillouin current density.

1. Increase the magnetic field. This is simply the same as increasing the Brillouin space-charge density.

2. Increase the distance of the beam above the sole. This is equivalent to increasing the velocity of the beam.

3. Increase the beam thickness. This is the condition of increased current flow from the gun region either by increasing the cathode area or the cathode current density.

There has been no discussion of the gun systems which are assumed to generate the Brillouin beams. The only objective here is to present some of the limitations which exist even if laminar flow could be generated. The design of electron injection systems capable of forming laminar beams is a formidable task which has not been satisfactorily achieved as of the present time. The following section discusses a few gun configurations and the limitations of their beam forming capabilities.

2.5 Limitations of Typical Electron Gun Configurations

The preceding parts of this chapter have indicated some of the limitations which exist for rectilinear, laminar electron beams. These can be considered as the fundamental limitations which are inherent in space-charge flow through crossed electric and magnetic fields. In actual electron injection systems, however, the beam invariably differs from the laminar flow model. Although some gun systems are better than others, none has yet been found which is capable of forming an ideal Brillouin beam. A few examples will illustrate the problems encountered in practical configurations.

2.5.1 Charles Gun[4]. The first gun will be the so-called Charles or French Short Gun which is shown in Fig. 2.6. The electric fields in the two regions are assumed to be constant and uniform. An electron

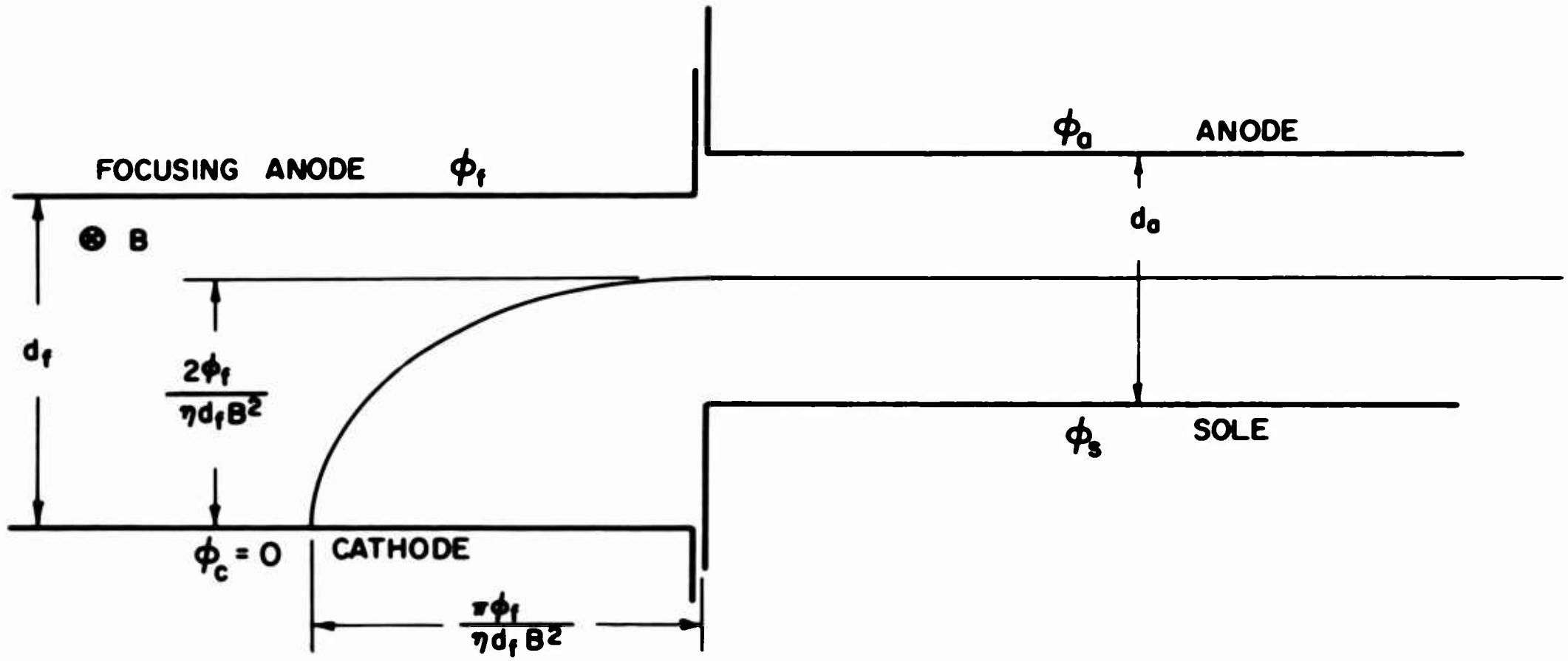

FIG. 2.6 FRENCH SHORT GUN ELECTRODE CONFIGURATION.

emitted from the cathode will undergo cycloidal motion in region 1 and pass into region 2 at the apogee of its trajectory. In the cathode region the coordinates of the electron at any time are given by

$$y_1 = \frac{\varphi_f}{\eta\, d_f\, B^2} (1 - \cos \omega_c t) \quad , \tag{2.43}$$

and

$$z_1 = \frac{\varphi_f}{\eta\, d_f\, B^2} (\omega_c t - \sin \omega\, t) \quad . \tag{2.44}$$

If the electron is to undergo linear motion through region 2 it should enter at $y_f = 2\, \varphi_f/\eta\, d_f\, B^2$, $z_f = \pi\, \varphi_f/\eta\, d_f\, B^2$ with a velocity

$$\dot{z} = \frac{2\varphi_f}{d_f\, B} = \frac{\varphi_a - \varphi_s}{d_a\, B} \quad , \tag{2.45}$$

where φ_a and φ_s are the anode and sole voltages respectively. Obviously any electron which leaves the cathode at $z \neq z_f$ will reach the entrance plane with $\dot{y} \neq 0$ so that it will be incapable of linear motion through the anode-sole region. Thus it is obvious that the Charles gun is restricted to fairly narrow cathodes in order to have a reasonably thin rectilinear beam in the interaction region. In fact the thickness and nonlaminarity of the beam are directly related to the cathode width from which electrons are emitted. This particular characteristic is illustrated in Fig. 2.7 where the center trajectory is nearly linear in region 2 but those electrons leaving from different points along the cathode undergo undulatory motion in the anode-sole region. The transverse amplitudes of these undulations are proportional to the distance between the

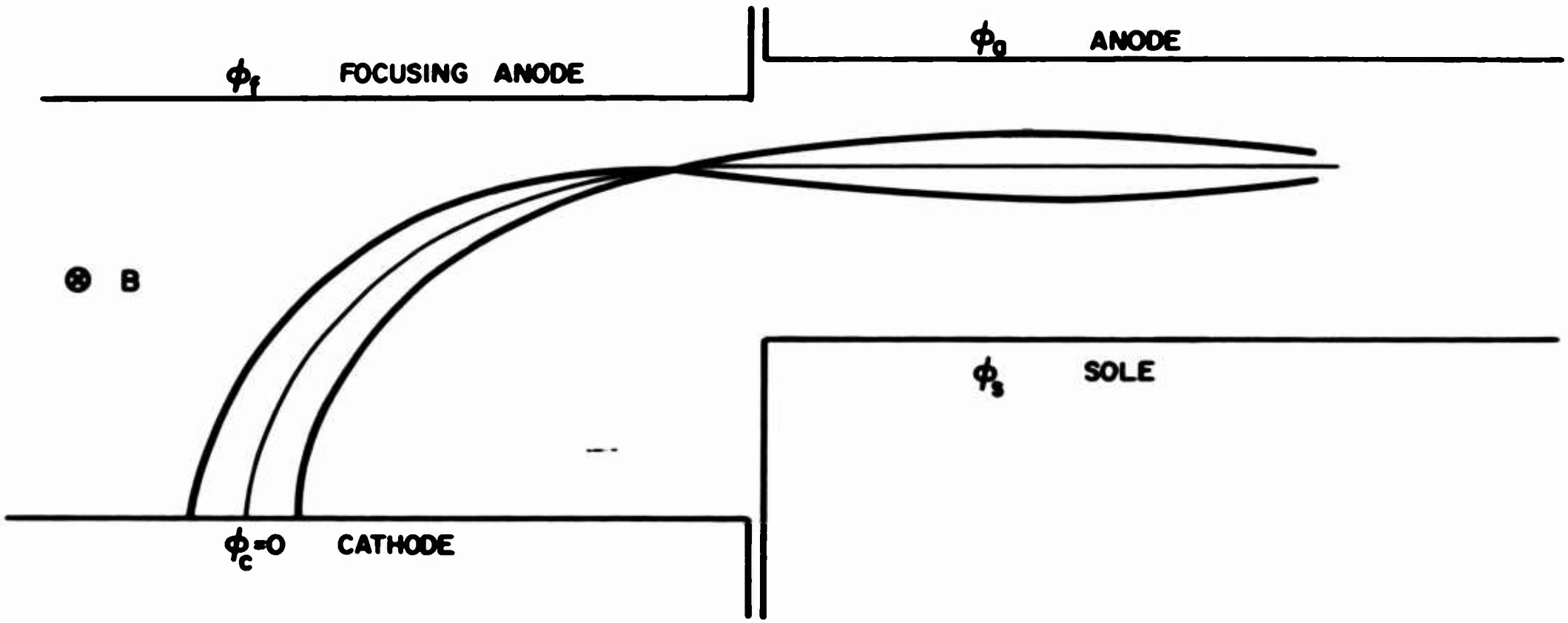

FIG. 2.7 ELECTRON TRAJECTORIES ILLUSTRATING NONLAMINARITY OF THE BEAM PRODUCED BY THE FRENCH SHORT GUN.

point at which the electron leaves the cathode and the emission point of the center trajectory electron.

These results were obtained from a space-charge-free Poisson cell analysis similar to those described in the following chapter. The effect of space charge is such as to actually decrease the turbulent nature of the beam. However, it is still true that the useful cathode width for such a gun is quite restricted.

2.5.2 Kino Short Gun. The design of the crossed-field Kino gun is based on a particular two-dimensional space-charge-flow condition for which the electric field is always in the y-direction (i.e., $E_z = 0$). In addition it is assumed that all electrons flow in parallel paths with the current density, space-charge density and electron velocity independent of the z-coordinate. For this situation the J_y component of current density is constant.

The theory is based on the additional assumption that the electrons are emitted perpendicular to the cathode with zero initial velocity. (This is contrasted with the long gun flow where a nonzero emission velocity is assumed.) The trajectory equations thus take the from

$$(z - z_o) = \frac{\eta J_y}{\epsilon_o \omega_c^3} \left[\frac{(\omega_c t)^2}{2} + \cos \omega_c t - 1 \right] \tag{2.46}$$

and

$$y = \frac{\eta J_y}{\epsilon_o \omega_c^3} \left[\omega_c t - \sin \omega_c t \right] . \tag{2.47}$$

The direction in which the electrons are traveling at any point is given by

$$\tan \psi = \frac{dy}{dz} = \frac{1 - \cos \omega_c t}{\omega_c t - \sin \omega_c t} \quad . \tag{2.48}$$

The potential and space-charge density observed at any time during the electron motion are

$$\varphi = \frac{\eta J_y^2}{\epsilon_o^2 \omega_c^4} \left[1 - \cos \omega_c t + \frac{(\omega_c t)^2}{2} - \omega_c t \sin \omega_c t \right] \tag{2.49}$$

and

$$\rho = \frac{\rho_o}{1 - \cos \omega_c t} \quad , \tag{2.50}$$

where $\rho_o = -\frac{\epsilon_o \omega_c^2}{\eta}$ is the Brillouin density.

Although Eq. 2.47 describes the y-location of an electron at various times, it can also be considered as the y-location of different electrons at a fixed z-plane (exit plane). For the latter case, different y values imply that the electrons were emitted from the cathode at different z_o positions and hence arrived at the exit plane at different values of $\omega_c t$. Viewing the problem in this manner it is then possible to determine the variation of ρ and ψ across the exit plane. Restricting the investigation to those electrons which reach the plane with $\omega_c t \leq 2\pi$ results in the trajectories shown in Fig. 2.8. Thus the upper electron reaches the exit plane at $\omega_c t = 2\pi$ and has an angle $\psi = 0$. All the other electrons lie below this and have $\omega_c t < 2\pi$ and $\psi > 0$ at the exit.

In order to simplify the equations, z and y are normalized as follows:

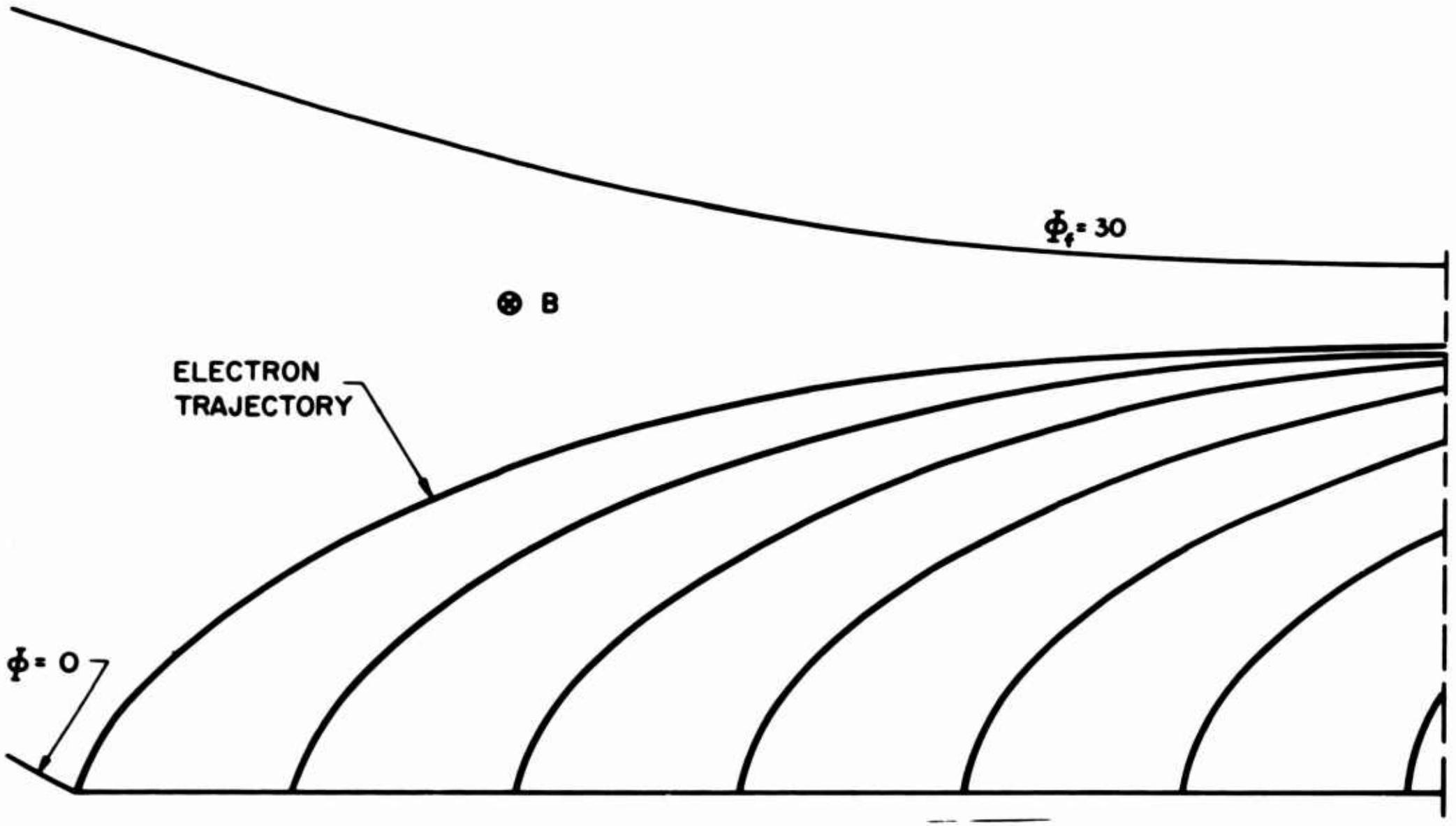

FIG. 2.8 THEORETICAL TRAJECTORIES IN THE KINO SHORT GUN.

$$Z \triangleq \frac{\epsilon_o \omega_c^3}{\eta J_y}(z - z_o) = \frac{(\omega_c t)^2}{2} + \cos \omega_c t - 1 \quad , \tag{2.51}$$

and

$$Y \triangleq \frac{\epsilon_o \omega_c^3}{\eta J_y} y = \omega_c t - \sin \omega_c t \quad . \tag{2.52}$$

Defining

$$\xi \triangleq 2\pi - Y \quad , \tag{2.53}$$

results in the upper trajectory having $\xi = 0$ at the exit plane. Thus all the other trajectories have $\xi > 0$ at this plane.

These relations allow ρ/ρ_o and ψ to be plotted vs. ξ as shown in Fig. 2.9. The space-charge density is infinite at the top of the beam and decays rapidly with ξ until reaching the Brillouin value at $\xi = 0.571$ ($\omega_c t = 3\pi/2$). ρ remains less than ρ_o until $\xi = 5.782$ ($\omega_c t = \pi/2$) when the Brillouin density is again achieved. The minimum density is $0.5\rho_o$ at $\xi = \pi$ ($\omega_c t = \pi$). At $\xi = 2\pi$ the space-charge density again becomes infinite. Notice that this point corresponds to the cathode location where the condition of space-charge-limited operation requires $\rho = \infty$. Finally, the directions in which the electrons travel as they pass the exit plane vary from $\psi = 0$ at the top of the beam to $\psi = 90°$ at the bottom (i.e., at the cathode).

Figure 2.10 illustrates the normalized velocity (U) and current density (S) variations across the beam where

$$U \triangleq \frac{\epsilon_o \omega_c^3}{\eta J_y} v = \sqrt{(\omega_c t - \sin \omega_c t)^2 + (1 - \cos \omega_c t)^2} \quad , \tag{2.54}$$

and

$$S \triangleq \frac{\epsilon_o \omega_c^2}{\eta J_y \rho_o} J = \sqrt{1 + \left(\frac{\omega_c t - \sin \omega_c t}{1 - \cos \omega_c t}\right)^2} \quad . \tag{2.55}$$

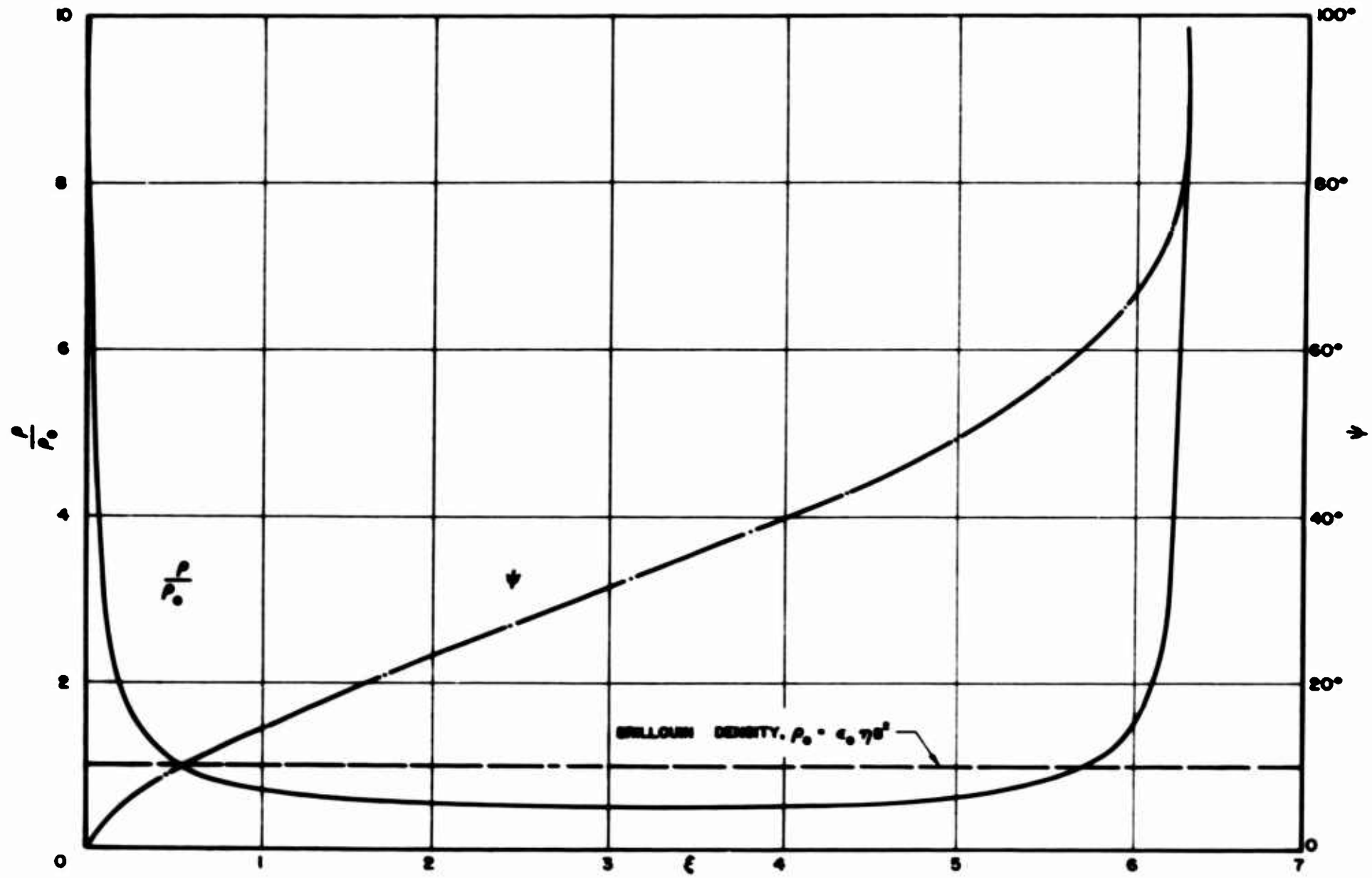

FIG. 2.9 VARIATION OF SPACE-CHARGE DENSITY AND TRAJECTORY ANGLE IN A THEORETICAL KINO SHORT GUN BEAM. $[\xi = 2x - (\epsilon_0 \omega_c^3/\eta J_y)\, y]$

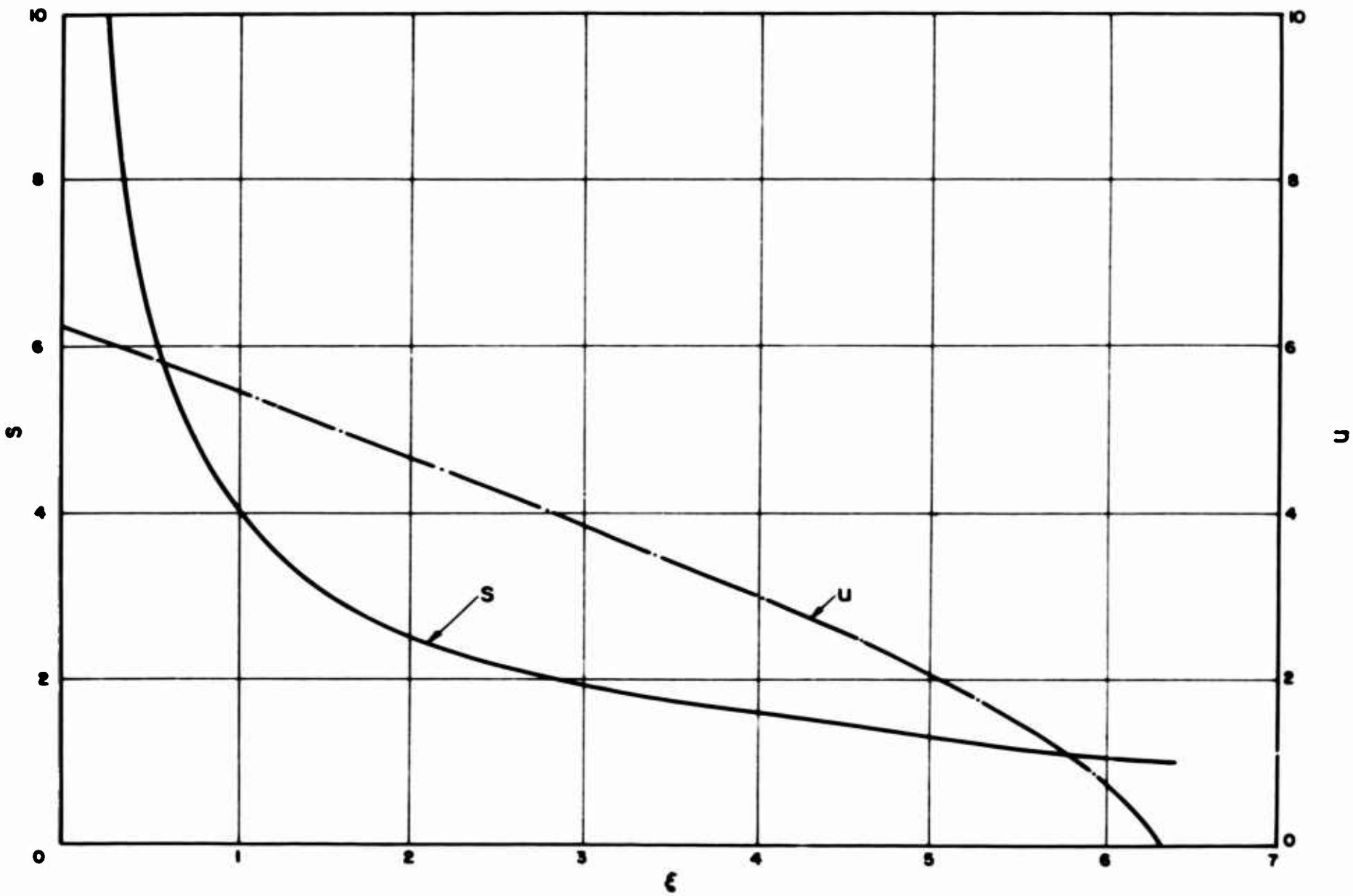

FIG. 2.10 VARIATION OF VELOCITY AND CURRENT DENSITY IN A THEORETICAL KINO SHORT GUN BEAM.

$[\xi = 2\pi - (\epsilon_o\omega_c^3/\eta J_y)y,\ S = (\epsilon_o\omega_c^2/\eta J_y\rho_o)J,\ U = (\epsilon_o\omega_c^2/\eta J_y)v]$

Except near the cathode, the velocity varies almost linearly across the beam thus indicating some resemblance to the Brillouin velocity variation. However, the current density changes rapidly near the top of the beam ($\omega_c t = 2\pi$) as a result of the rapid ρ variation in that region. Consequently the current density differs appreciably from the linear Brillouin requirement.

In view of the above results it is obvious that two fundamental problems exist which prevent the achievement of laminar flow from a theoretical Kino short gun. First, the space-charge density undergoes a rapid variation near the $\omega_c t = 2\pi$ point. This is contradictory to the desired $\rho = \rho_o$ for Brillouin flow. The second problem involves the different directions in which the electrons are moving as they pass the exit plane. In other words, the wider the beam is at the exit plane the greater is the difference between the ψ of the top and bottom trajectories. The combination of these two problems make it impossible to achieve laminar flow, even on a theoretical basis, from the Kino short gun.

However, the use of a narrow cathode located so that the upper electron reaches the exit plane prior to $\omega_c t = 2\pi$ should help in improving the beam. The restriction of the cathode width is necessary to minimize the ψ variation across the exit beam. Of course the gun should also be tilted with respect to the circuit-sole structure at an angle which is half the difference between the ψ of the upper and lower electron trajectories in the beam. Figure 2.11 illustrates the theoretical trajectories of a Kino short gun which is terminated prior to the $\omega_c t = 2\pi$ point for the upper trajectory. The behavior of such a gun will be discussed in more detail in Chapter IV.

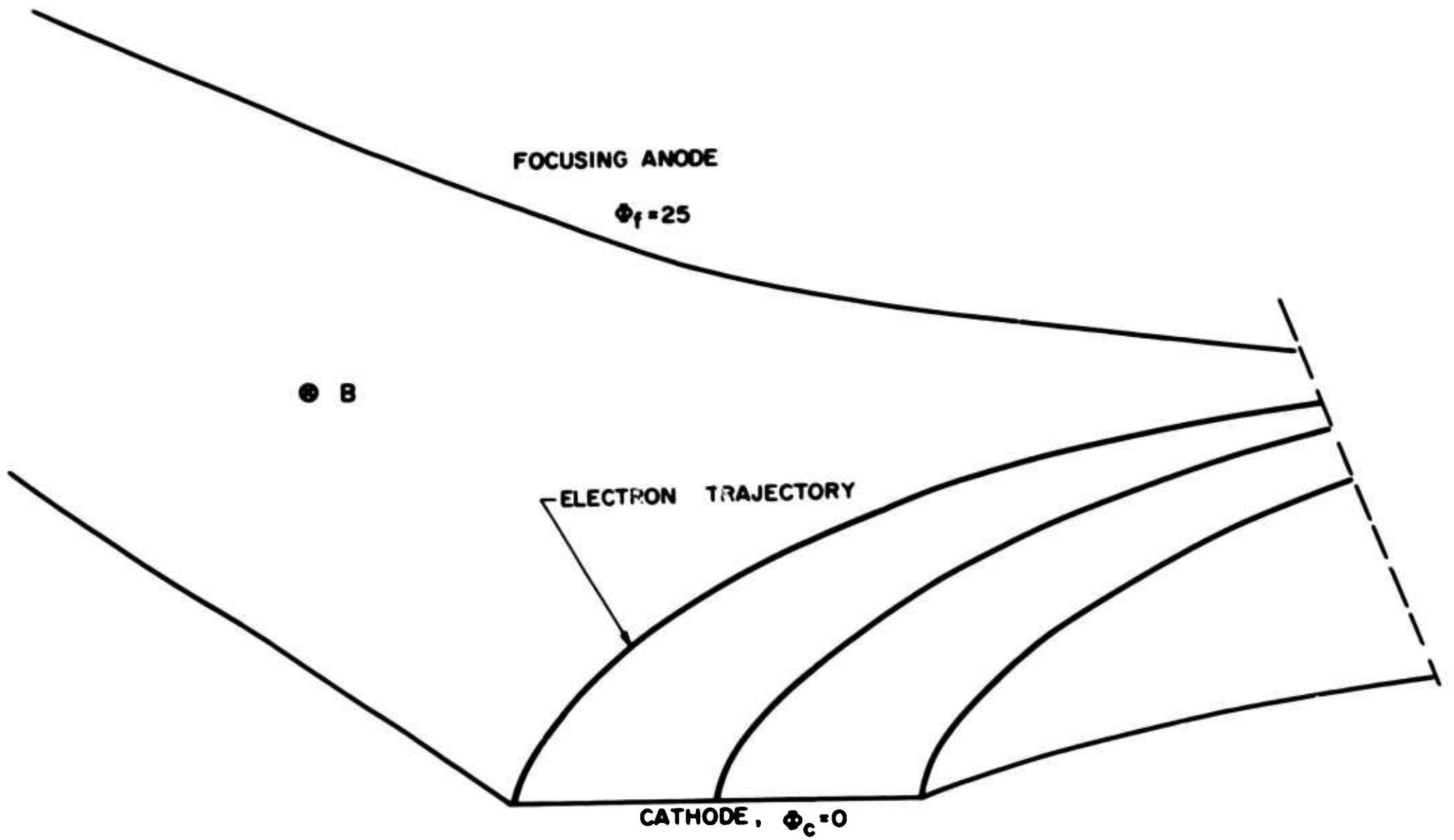

FIG. 2.11 KINO SHORT GUN TRAJECTORIES WITH GUN EXIT PLANE LOCATED PRIOR TO THE $\omega_c t = 2\pi$ POINT.

The results of the above investigation indicate that the Kino space-charge flow solution produces a beam which is similar to the Brillouin beam in some respects but differs radically in others, i.e., ρ and J. In theory, therefore, it is not possible to achieve exact Brillouin flow by means of a Kino short gun. The nonlaminarity of the beam in the anode-sole region will be a function of the cathode width and the transit time of the electrons through the gun region.

2.5.3 Kino Long Gun[7]. The Kino long gun configuration, including the theoretical trajectories, is shown in Fig. 2.12. The flow is derived using the assumption that all of the electrons leave the cathode with the same normal velocity component given by

$$\dot{y}_o = \frac{\eta J_y}{\epsilon_o \omega_c^2} . \tag{2.56}$$

For this situation the trajectory equations are

$$(z - z_o) = \frac{\eta J_y}{\epsilon_o \omega_c^3} \frac{(\omega_c t)^2}{2} \tag{2.57}$$

and

$$y = \frac{\eta J_y}{\epsilon_o \omega_c^3} (\omega_c t) . \tag{2.58}$$

The potential variation along a trajectory is

$$\varphi = \frac{\eta J_y^2}{2\epsilon_o^2 \omega_c^4} (\omega_c t)^2 , \tag{2.59}$$

while the space-charge density is

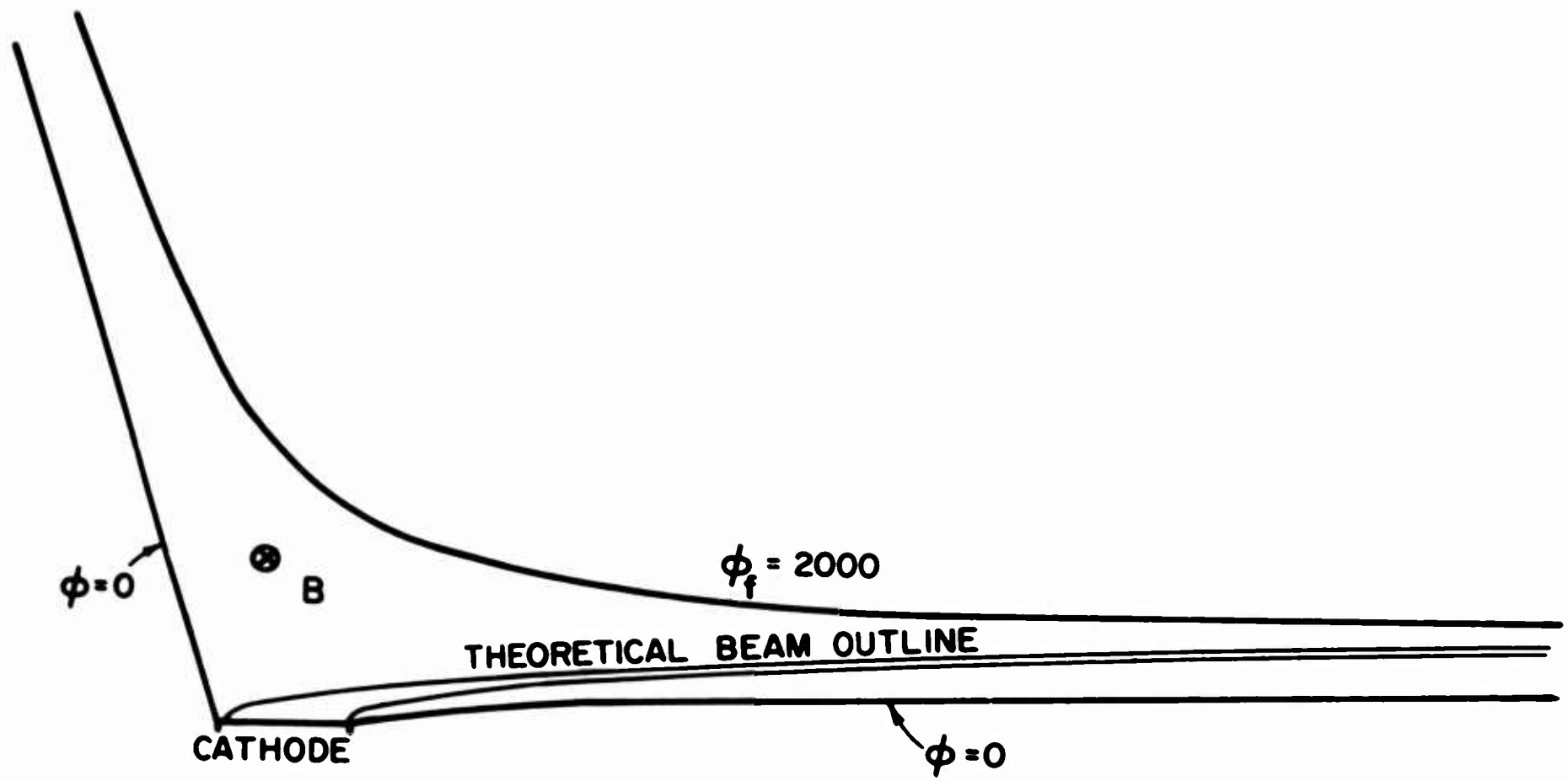

FIG. 2.12 THEORETICAL TRAJECTORIES IN THE KINO LONG GUN.

$$\rho = -\frac{\epsilon_o \omega_c^2}{\eta} , \tag{2.60}$$

which is precisely the Brillouin value. Thus the theoretical flow from the Kino long gun is characterized by the Brillouin density at every point in the beam.

The trajectory angle is

$$\tan \psi = \frac{dy}{dz} = \frac{1}{\omega_c t} , \tag{2.61}$$

while the velocity components are

$$\dot{z} = \frac{\eta J_y}{\epsilon_o \omega_c^2} (\omega_c t) = \omega_c y , \tag{2.62}$$

and

$$\dot{y} = \frac{\eta J_y}{\epsilon_o \omega_c^2} = \dot{y}_o . \tag{2.63}$$

Hence the flow is such as to maintain the y-component of velocity constant at every point within the beam. Furthermore, the z-component of velocity is such that its y-derivative is

$$\frac{\partial \dot{z}}{\partial y} = \omega_c , \tag{2.64}$$

which is exactly the velocity gradient across a rectilinear Brillouin beam. If the magnetic field is very large $\dot{y}_o$ is observed to be exceedingly small and the total velocity is essentially given by

$$v \approx \dot{z} = \omega_c y . \tag{2.65}$$

Thus the long gun produces a theoretical beam whose velocity and space-charge density are essentially those of Brillouin flow.

These results suggest that the Kino long gun should be capable of generating laminar electron beams. Unfortunately, experimental investigations[11,12] of such a gun have not substantiated the theoretically predicted desirable characteristics. They have, in fact, indicated highly nonlaminar and unstable flow. The principal problems appear to be:

1. In actual thermionic emission the electrons do not leave the cathode with the same velocity.

2. The electrons require a fairly long time to pass through the gun region. This allows a significant interval during which undesirable forces (primarily the diocotron phenomenon) may affect the beam. The first difficulty is related to the fact that any discrepancy in initial velocities from the $\dot{y}_o$ value will result in different trajectories and hence in a different beam configuration. Any nonuniform emission will also increase the possibility of diocotron-type phenomena occurring in the gun region and hence will lead to greater beam nonlaminarity. Whatever the reasons may be, experiments have indicated that instead of the excellent beam characteristics predicted by the theory the actual flow is unstable and extremely noisy. One explanation for the undesirable behavior appears to lie in the emission characteristics of electrons leaving from a thermionic cathode; i.e., the assumption of a single emission velocity is not valid.

<u>2.5.4</u> <u>Other Types of Guns</u>. Dain and Lewis[5] and Bartram and Pease[6] have described guns which are derived on the basis of the adiabatic principle as discussed in the first chapter. They essentially involve the emission of electrons from a cathode located in a uniform field region after which the beam is subjected to a slowly varying transition

and then injected into the anode-sole region. The long transition region makes these guns similar to the Kino long gun but with less ideal theoretical characteristics. In particular the theoretical trajectories in the anode-sole region are characterized by cycloidal variations. There is no need to consider these adiabatic guns in any more detail since their theoretical beams are no improvement over those generated by Kino-type guns.

All of the crossed-field electron gun systems which have been devised involve basically the same principle. That is, the electrons are emitted from a unipotential cathode after which the gun must act on the beam and rotate it by approximately 90° and inject it into the interaction region. The success of the injection system is measured by the laminarity of the beam as it leaves the gun.

The above examples illustrate some of the theoretical limitations which exist for various types of crossed-field injection systems. The following two chapters involve computer investigations of the beam characteristics derived from specific crossed-field electron gun configurations.

CHAPTER III. ANALOG COMPUTER INVESTIGATION OF ELECTRON INJECTION SYSTEMS

3.1 Introduction

A comprehensive evaluation of the beam-forming capability of an electron injection system requires the determination of the electron trajectories through the gun region. The motion of an electron through d-c electric and magnetic fields is described by the Lorentz force equation

$$\frac{d\vec{v}}{dt} = -\eta\,[\vec{E} + \vec{v} \times \vec{B}] \quad , \tag{3.1}$$

where $\vec{E}$ = electric field,

$\vec{B}$ = magnetic field, and

$\vec{v}$ = electron velocity.

For crossed-field devices the problem can be simplified if the variation in the magnetic field direction (x-direction) is neglected. The Lorentz equation can then be separated into the two component equations which are

$$\frac{d^2y}{dt^2} = \eta\frac{\partial\varphi}{\partial y} - \omega_c\dot{z} \quad , \tag{3.2}$$

and

$$\frac{d^2z}{dt^2} = \eta\frac{\partial\varphi}{\partial z} + \omega_c\dot{y} \quad , \tag{3.3}$$

where φ = the potential.

These equations are valid for any crossed electric and magnetic fields regardless of the space-charge density. The presence of

significant space charge manifests itself by affecting the potential distribution. In other words, with no space charge present the potential must satisfy Laplace's equation

$$\nabla^2\varphi(y,z) = 0 \quad . \tag{3.4}$$

Obviously in this situation the potential at any point is dependent only on the electrode configurations and the externally applied voltages. However, when space-charge effects become significant the potential distribution is modified according to Poisson's equation

$$\nabla^2\varphi(y,z) = -\frac{\rho(y,z)}{\epsilon_o} \quad . \tag{3.5}$$

where $\rho(y,z)$ is the space-charge density. Equation 3.5 indicates that the voltage is a superposition of the space-charge free value and the contribution due to the space-charge distribution.

The evaluation of electron trajectories requires the simultaneous solution of two problems. First it is necessary to determine the potential distribution including the effects of space charge. Then the two component force equations must be solved to yield the electron motion.

Numerous analog methods have been devised to evaluate the flow of electrons. Some of the more familiar methods involve the use of electrolytic tanks[29], resistance networks[30], and rubber membranes[31]. The system employed by the author involved the use of a Poisson cell[32], which is a solid conducting medium, and an analog computer. The system was developed under the Signal Corps Contract DA-36-039- sc-56714 and has been used extensively in analyzing crossed-field electron injection systems in the Electron Physics Laboratory at The University of Michigan. The basic theory of operation is presented in Appendix B.

3.2 Poisson Cell Investigation of a Kino Short Gun

Figure 3.1 illustrates a particular Kino short gun configuration as well as the space-charge free trajectories determined from the Poisson cell analysis. The gun utilized an extremely wide cathode which was found to be responsible for generating certain nonlaminarities in the space-charge flow. The theoretical design values were

φ_f = focusing anode voltage = 520 volts,

B = 141 gauss, and

J_c = cathode current density = 0.048 amp/cm^2.

The important dimensions were a cathode width of 0.305 inch and a circuit-sole spacing of 0.225 inch.

Figure 3.2 indicates the electron trajectories obtained, with space-charge effects included, under the assumption of a uniform emission of 0.048 amp/cm^2 over the cathode surface. It is readily apparent that the gun did not generate a laminar beam. The principal reason for the nonlaminarity was the manner in which the electrons from the rear portion of the cathode (section A-B) moved through the remainder of the beam before reaching the gun exit plane.

Figure 3.3 illustrates the beam configuration when the cathode was no longer considered to be emitting electrons uniformly across its surface. The cathode current density variation indicated greater emission from the center portion of the cathode than from any other region. However, the average cathode current density was still considered to be 0.048 amp/cm^2. The beam was still nonlaminar with the electrons in the upper part of the beam being responsible for most of the turbulence. Various other J_c distributions were considered but they all resulted in essentially the same type of nonlaminar flow behavior.

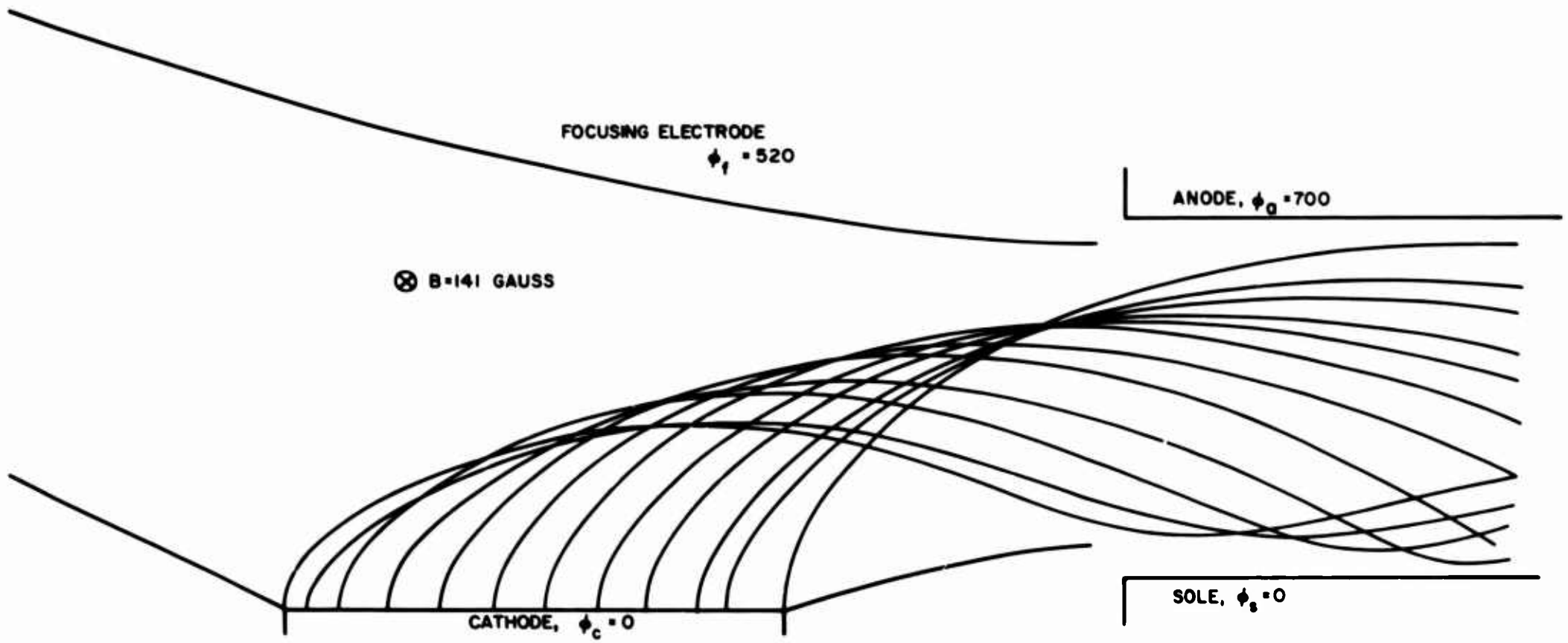

FIG. 5.1 SPACE-CHARGE-FREE TRAJECTORIES FOR THE KINO SHORT GUN.

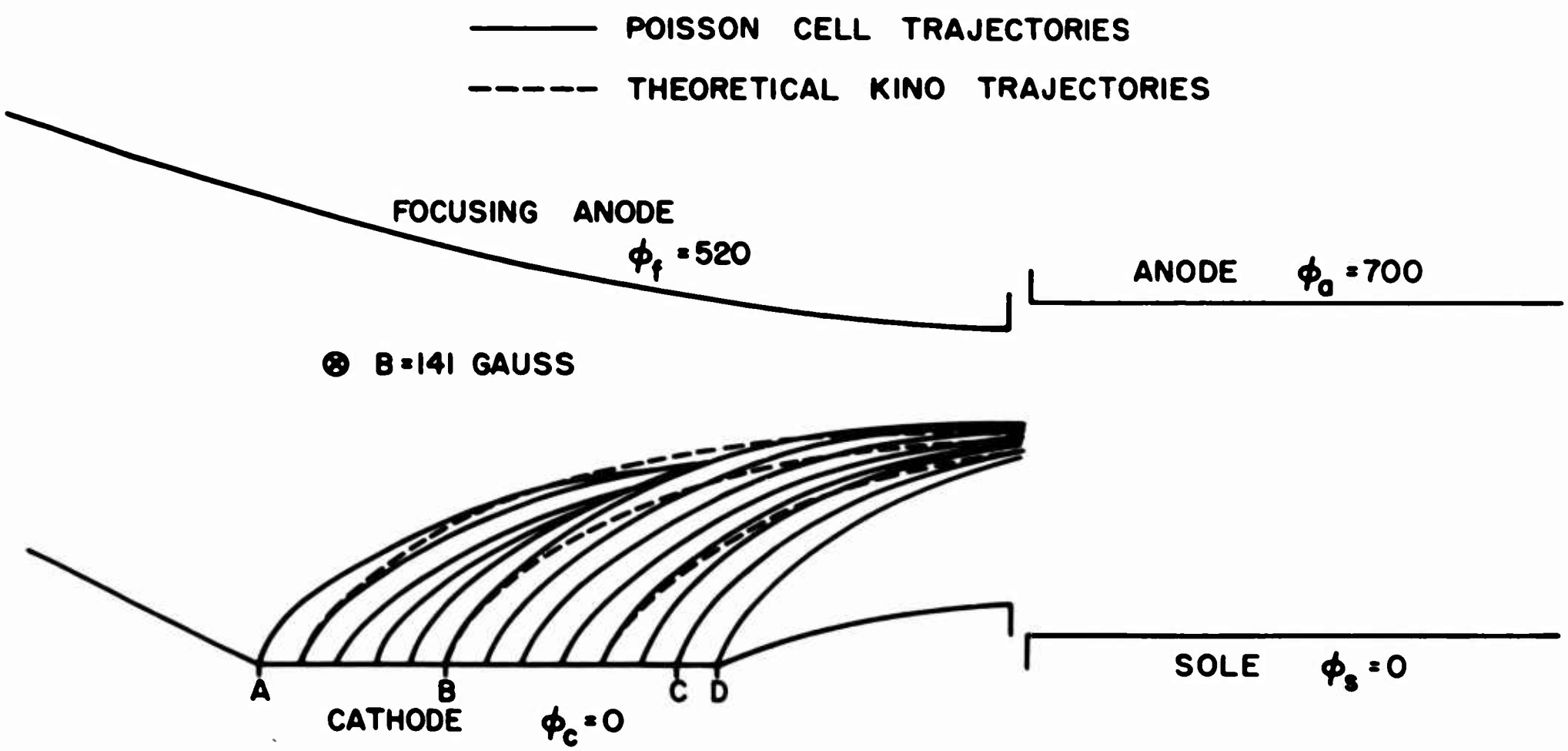

FIG. 3.2 FINAL TRAJECTORIES OBTAINED WITH CURRENTS INJECTED AS DETERMINED FROM THE THIRD RUN RESULTS.

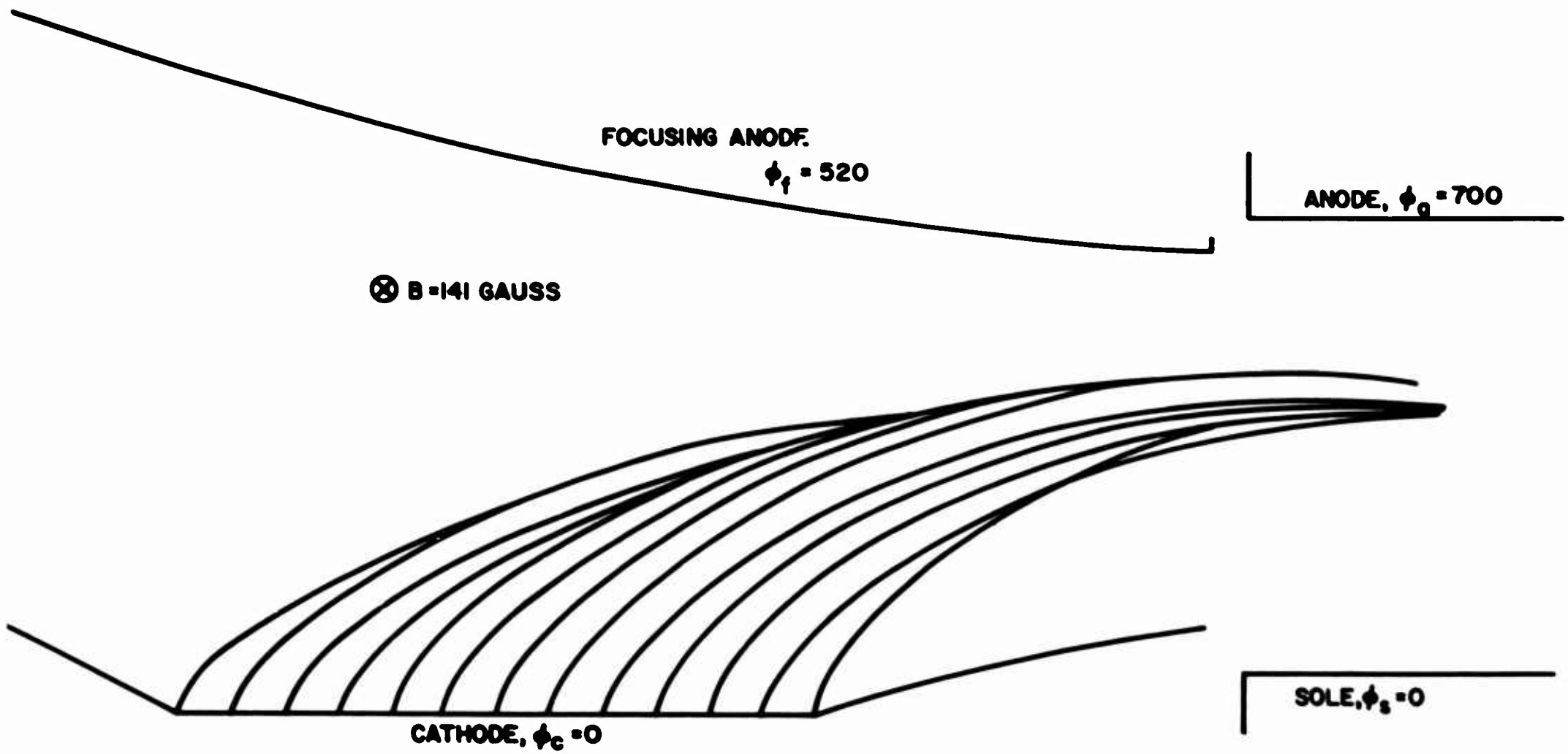

FIG. 3.3 TRAJECTORIES OBTAINED WITH NONUNIFORM EMISSION FROM THE CATHODE. MAXIMUM EMISSION ASSUMED TO EXIST NEAR THE CENTER OF THE CATHODE. ($J_{c\ avg}$ = 0.048 AMP/CM^2)

Investigation of Fig. 3.2 in greater detail indicates the possibility of achieving a relatively laminar beam by restricting emission to only a portion of the original cathode; e.g., the electrons emitted from section B-D apparently form a nearly laminar beam. However, if the space charge produced by those electrons emitted from section A-B were removed from the beam the B-D trajectories would be different unless the external electrodes could be modified to produce the same effect as the removed space charge.

Figure 3.4 illustrates the electron flow when emission was restricted to only section B-C of the cathode. The removal of the space charge contributed by those electrons emitted from sections A-B and C-D required a decrease in focusing anode voltage and magnetic field to 315 volts and 107 gauss respectively. These modifications were necessary to prevent interception of the beam by the focusing anode. This reduction in cathode area resulted in the formation of a nearly laminar beam with a convergence of about 3.8 to 1. This flow was also based on a uniform emission of 0.048 amp/cm^2. Later in this chapter it will be shown that uniform emission from section B-C of the cathode corresponds to the space-charge-limited behavior of the Kino gun. That is, the space-charge-limited investigation indicates relatively uniform emission from the center portion of the cathode but not from the edges. Consequently the situation of Fig. 3.4 corresponds to a removal of the nonuniform emitting end sections of the cathode. This flow also has the physical interpretation that sections A-B and C-D of the cathode have been poisoned and are no longer capable of emission.

As suggested above, the beam formed by the reduced cathode was nearly laminar as it crossed plane A-A in the anode-sole region. The production of a Brillouin beam by the gun requires a convergence of

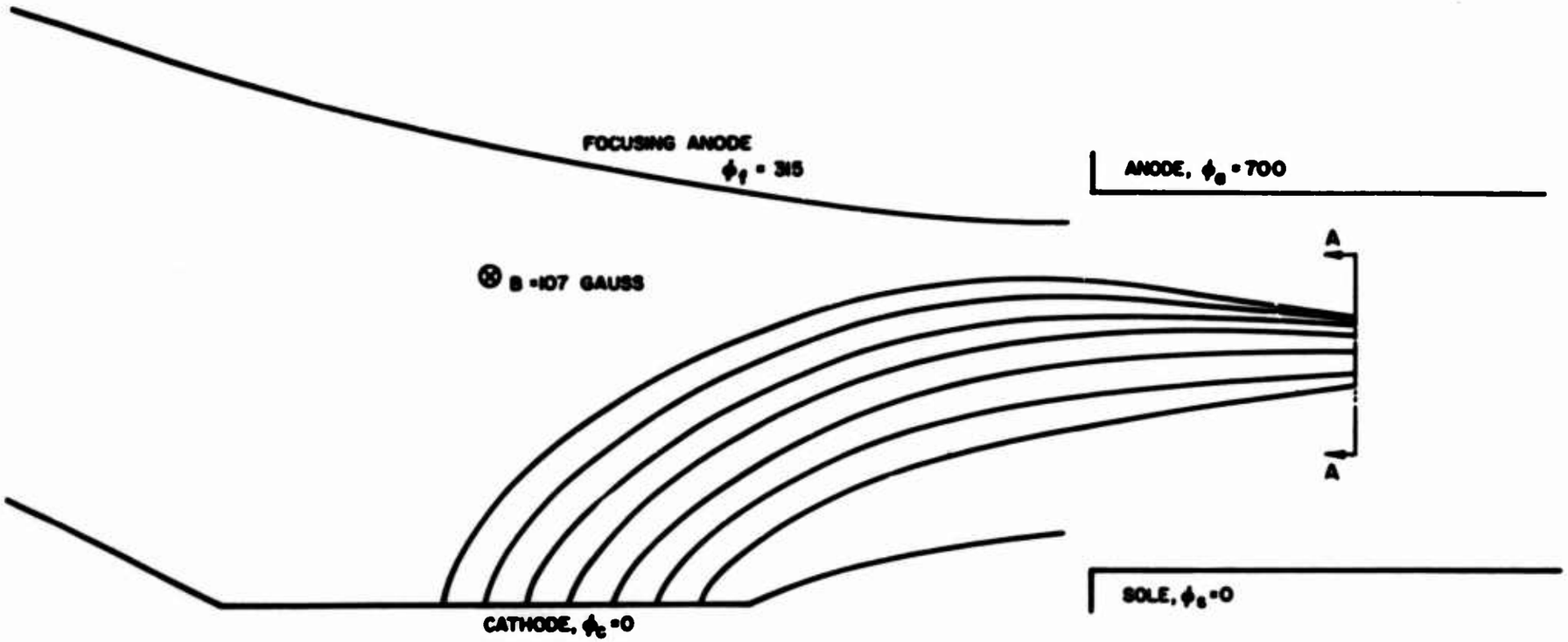

FIG. 3.4 FINAL TRAJECTORIES OBTAINED AFTER FOUR ITERATIONS OF THE SPACE-CHARGE SIMULATION PROCESS.

$$K = \frac{a\,\epsilon_o\,\omega_c^3}{\eta\,J_c}\left\{1 + \sqrt{1 + \frac{\eta\,J_c\,W}{2a^2\epsilon_o\,\omega_c^3}}\right\} \tag{3.6}$$

as indicated in Chapter II. For the conditions of Fig. 3.4,

J_c = 0.048 amp/cm^2,

ω_c = 1.88×10^9 radians/sec,

W = 3.80×10^{-8} meter, and

a = 2.80×10^{-3} meter.

Substitution of these values into Eq. 3.1 results in a convergence value of K = 4.2 which is close to the measured value of 3.8. This suggests that the gun is capable of producing nearly laminar flow if emission is restricted to the B-C portion of the cathode.

Any attempt to generate a decent beam from a wider cathode requires certain modifications of the electron gun configuration. Changes in the focusing anode seemed to offer the greatest possibility of increasing the cathode width without destroying the beam laminarity. As mentioned before, the nonlaminarity was created primarily by those electrons coming from the rear section of the cathode. The rapidity with which these electrons curved through the remainder of the beam indicated that the average electric field which these particles experienced was not sufficient to balance the magnetic force. Thus an increase in the electric field in this portion of the gun would seem to offer some advantage in improving the electron trajectories. The simplest procedure for increasing the electric field was to depress the rear portion of the focusing anode towards the cathode. Various modifications of this electrode were investigated. Figure 3.5 illustrates the optimum focusing anode configuration for increasing the useful emitting area of

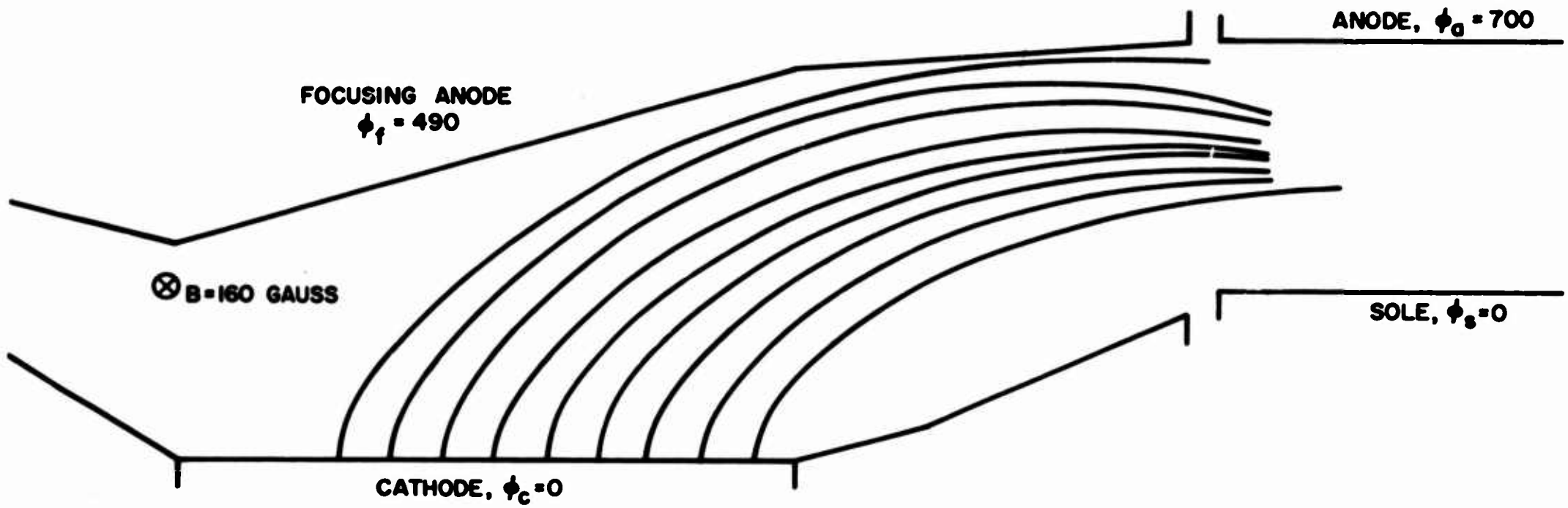

FIG. 3.5 TRAJECTORIES FOR A SITUATION IN WHICH THE FOCUSING ANODE AND MAGNETIC FIELD HAVE BEEN MODIFIED.

the cathode. Although there are no trajectory crossings in the gun region there is no doubt that the beam will be quite nonlaminar in the anode-sole region.

The above investigations indicate the existence of two fundamental limitations for crossed-field electron injection systems:

1. There is a maximum convergence which a gun can impose on an electron beam and still satisfy the conditions of laminar flow.

2. For a given injection system there is a maximum cathode width from which a Brillouin beam can be obtained.

Both of these conditions are direct consequences of the restriction of the space-charge density in a laminar beam to the Brillouin value, $\rho_o = - \epsilon_o \omega_c^2/\eta$. Any attempt to increase either the convergence or the cathode width beyond the limiting values will result in the generation of nonlaminar flow.

3.3 Investigation of the Extended Kino Short Gun

The experimental beam analyzer investigations described in Chapter VII involved the electron flow obtained from the gun shown in Fig. 3.6. This again is a Kino short gun except that the exit plane has been extended well beyond the theoretical $\omega_c t = 2\pi$ cut-off plane. This configuration will henceforth be referred to as the extended Kino short gun. The use of a narrow (0.050 inch wide) cathode presumably should simplify the achievement of laminar flow.

The Poisson cell analog of this configuration was investigated to determine the beam characteristics in the gun region and to correlate the results with the experimental beam analyzer data. The operating conditions were

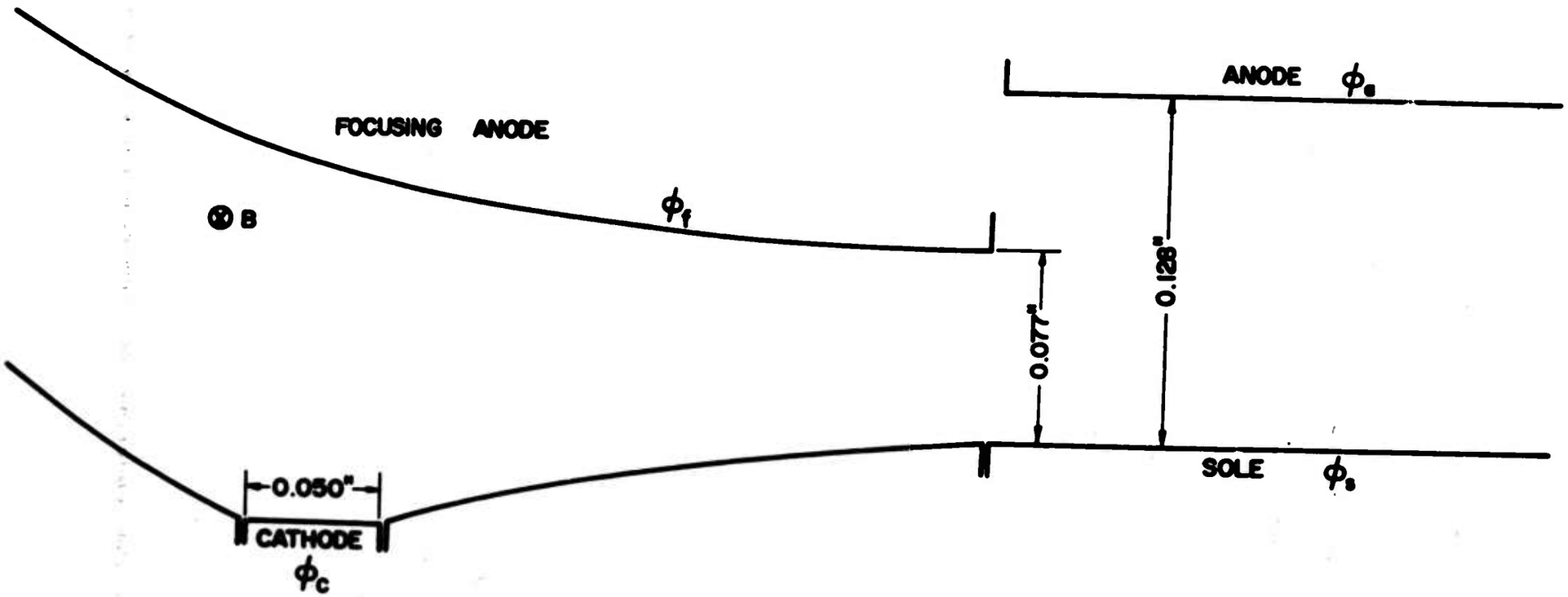

FIG. 3.6 ELECTRODE CONFIGURATION FOR THE EXTENDED KINO SHORT GUN.

φ_f = 1540 volts,

φ_a = 2500 volts, and

B = 368 gauss.

The space-charge-free trajectories are shown in Fig. 3.7. With the above voltages and magnetic field, the theoretical current density for this design should be 0.8 amp/cm^2.

The initial Poisson cell investigation was concerned with evaluating the effect of different cathode current densities on the resultant beam configuration. The analysis was carried out for uniform emission of 0.5, 1.0, 1.5, and 2.0 amp/cm^2. The corresponding space-charge flow patterns are illustrated in Figs. 3.8 through 3.11 respectively. The J_c = 0.5 beam indicated that the space-charge density was not sufficient to prevent the flow from becoming nonlaminar. The nonlaminarity of the beam is displayed by the manner in which the upper two electrons cross into the remainder of the space charge shortly after emission from the cathode.

When the cathode current density was increased to 1.0 amp/cm^2 the trajectories were improved and no severe cross-overs occurred. In fact the beam was nearly laminar in the region of the gun adjacent to the cathode. Comparison of the J_c = 0.5 and 1.0 trajectories indicates that the location and general configuration of the beams were essentially the same. This significant result indicates that the macroscopic or gross characteristics of the beam are not critically dependent on the behavior of the individual electrons which comprise the flow. In other words, for this particular case doubling the current has not altered the beam configuration to any great extent.

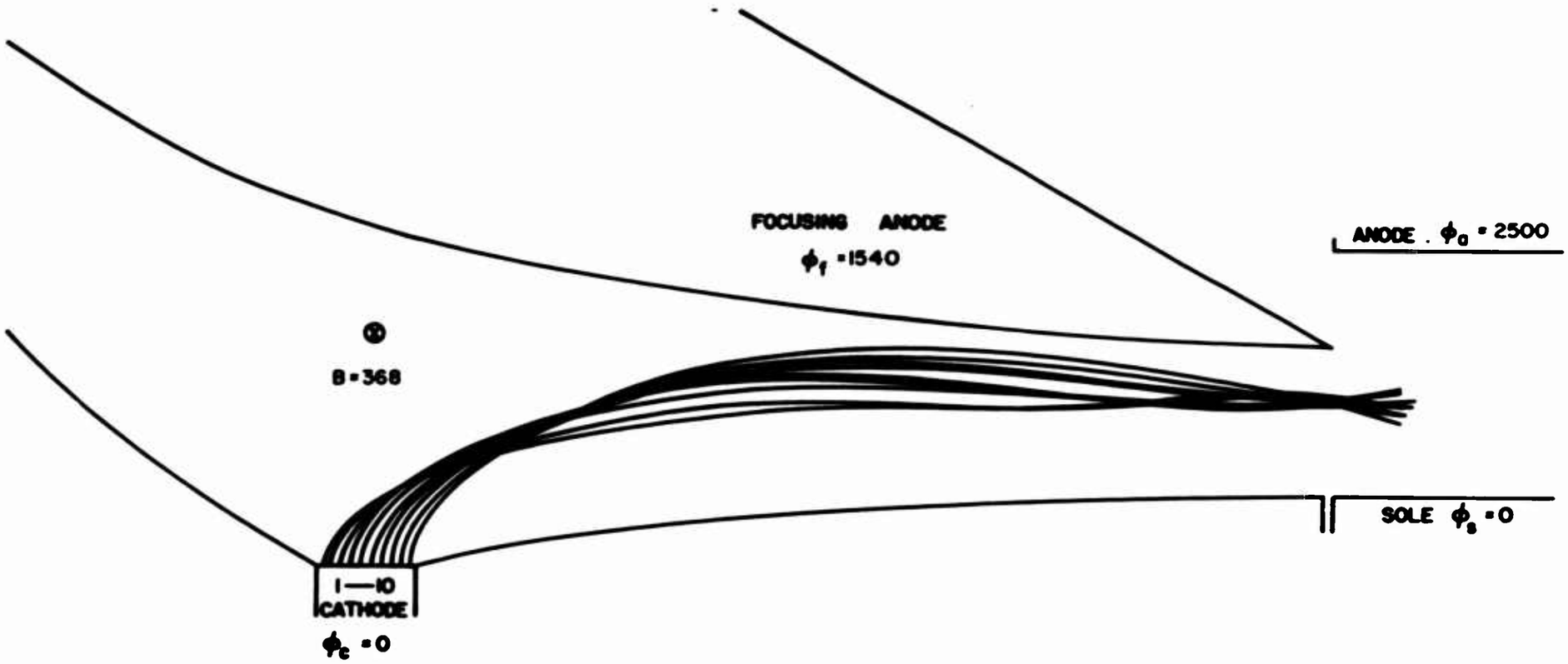

FIG. 3.7 SPACE-CHARGE-FREE TRAJECTORIES FROM THE POISSON CELL ANALOG OF THE EXPERIMENTAL KINO SHORT GUN.

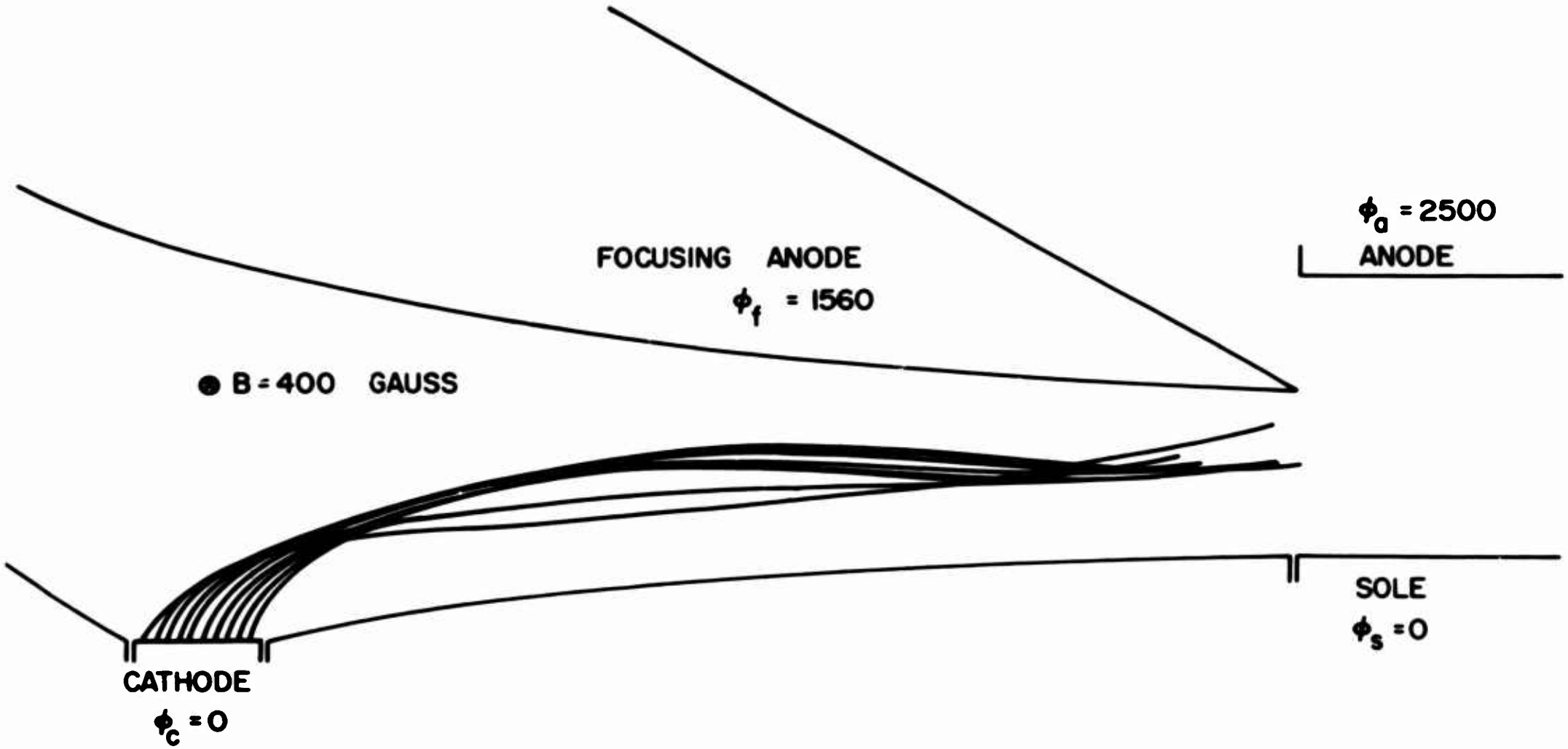

FIG. 3.8 POISSON CELL ELECTRON TRAJECTORIES FOR THE EXTENDED KINO SHORT GUN ASSUMING A UNIFORM EMISSION OF 0.5 AMP/CM^2.

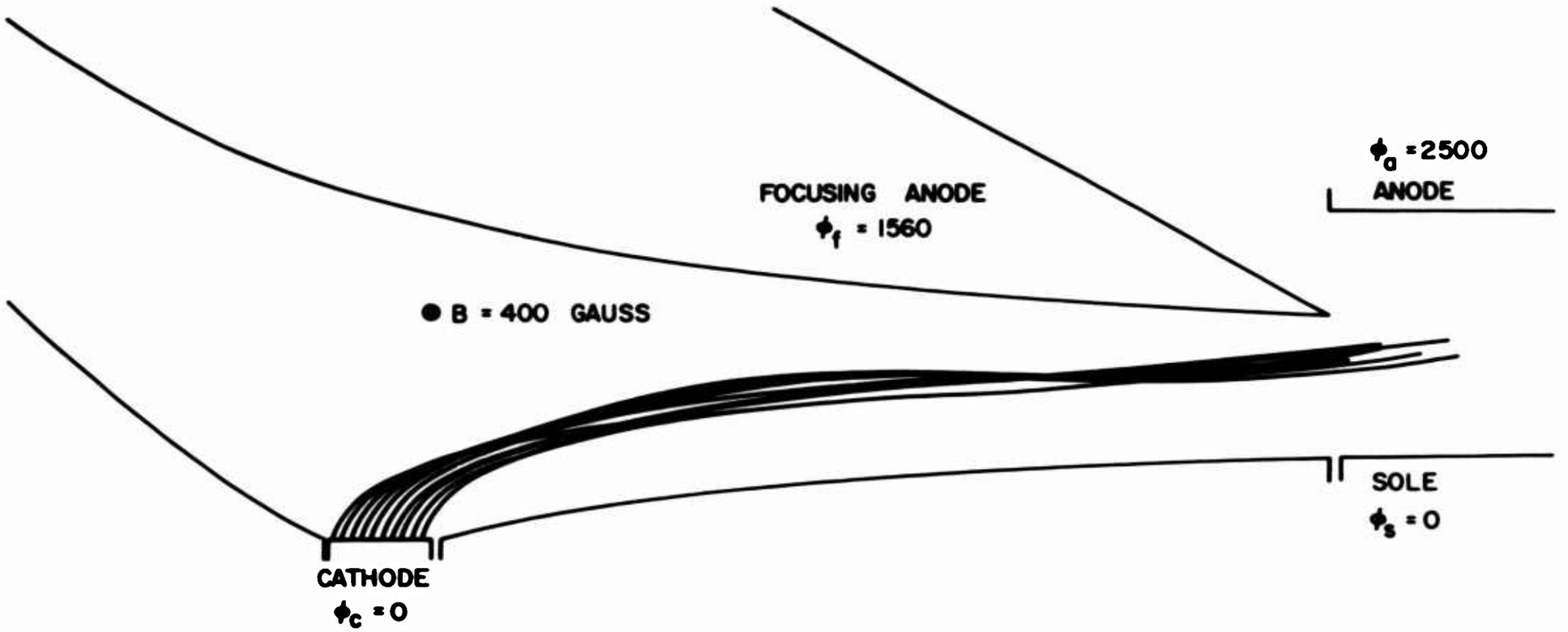

FIG. 3.9 POISSON CELL TRAJECTORIES ASSUMING A UNIFORM CATHODE EMISSION OF 1.0 AMP/CM^2.

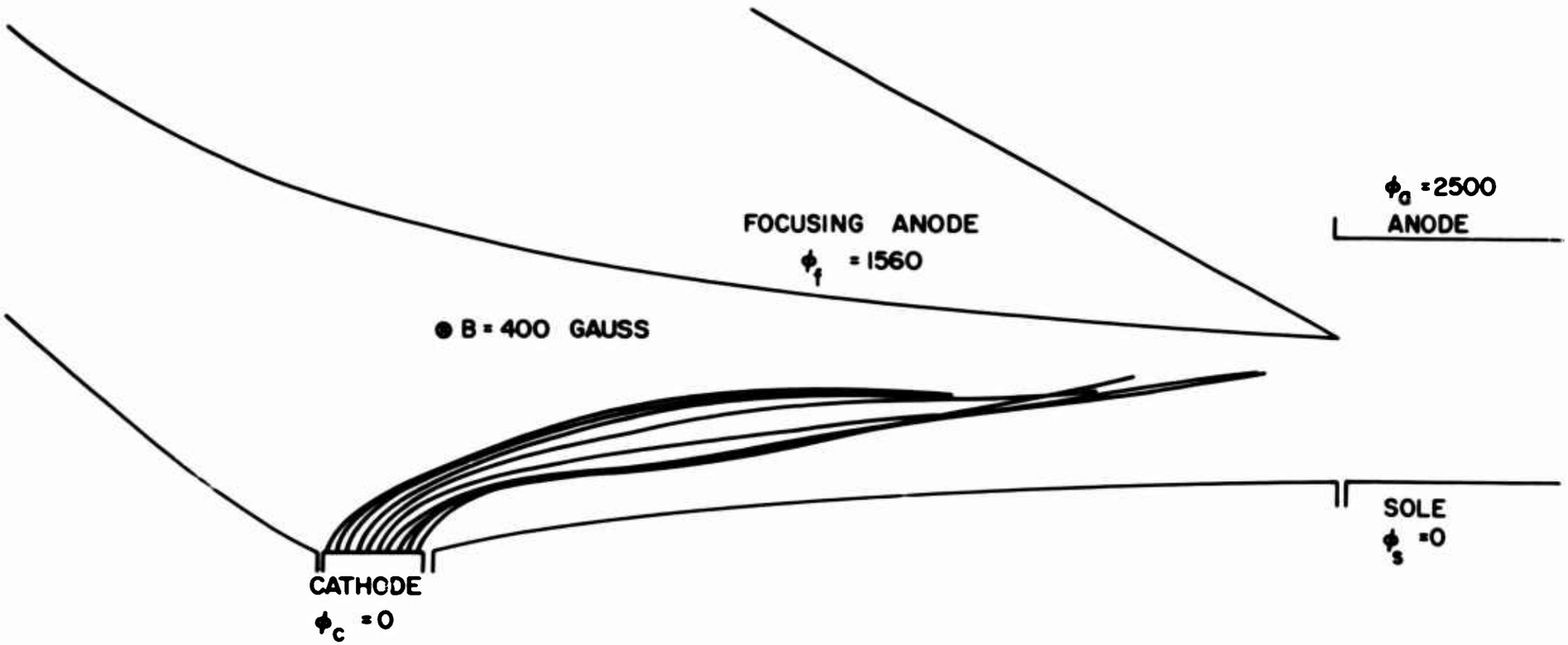

FIG. 3.10 POISSON CELL TRAJECTORIES ASSUMING A UNIFORM CATHODE EMISSION OF 1.5 AMPS/CM^2.

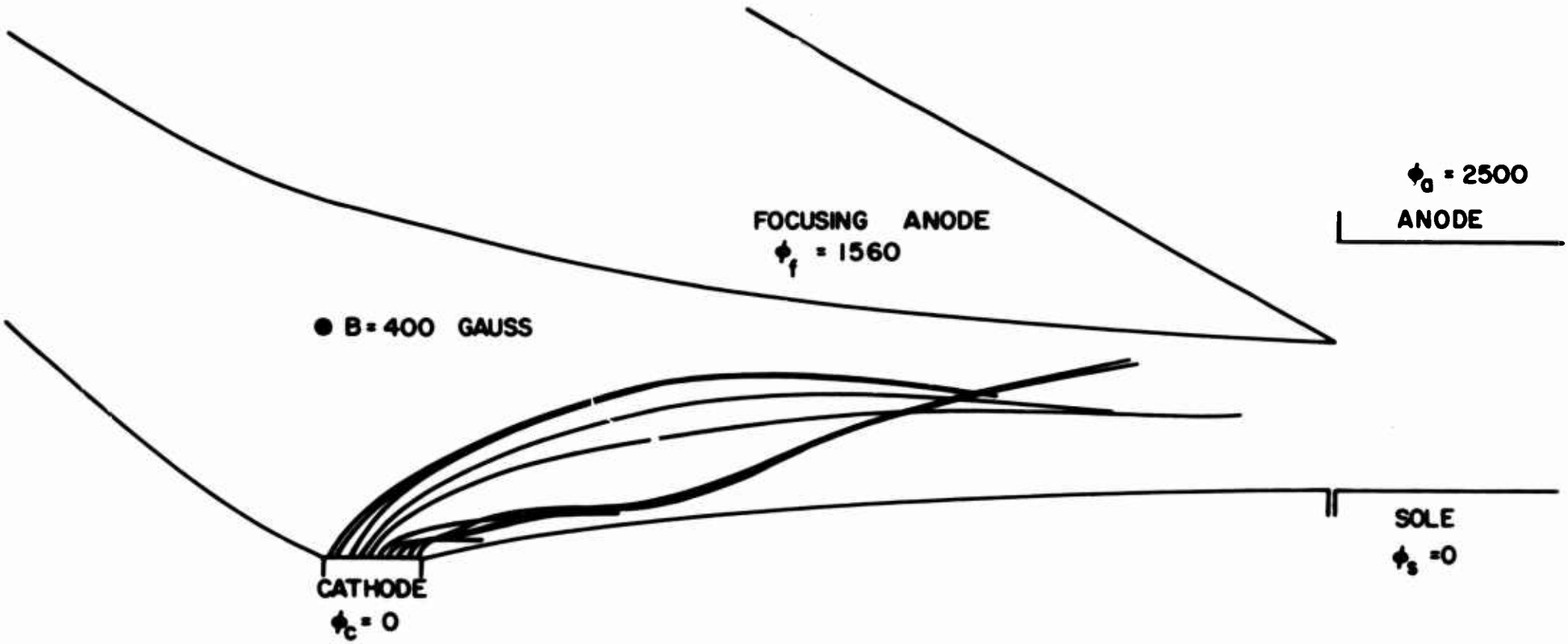

FIG. 3.11 POISSON CELL TRAJECTORIES ASSUMING A UNIFORM CATHODE EMISSION OF 2.0 AMPS/CM^2.

However, when J_c was increased to 1.5 amps/cm^2, the beam began to open up and became more nonlaminar. Nevertheless, the location of the beam was approximately the same as in the previous two cases.

The final situation of J_c = 2.0 amps/cm^2 resulted in an unfavorable situation wherein the trajectories spread apart rapidly and the beam became unstable. In other words, there was too much current and space charge in the beam thus causing the flow to become nonlaminar shortly after emission from the cathode.

These results suggest that the beam configuration was not directly dependent on the cathode current density as long as the value of J_c was not greatly different from the theoretical Kino value. The beam location was essentially the same in each case although the degree of laminarity was related to the cathode current density. The principal difference was that the beam width increased as J_c increased until the flow became unstable at approximately 2.0 amps/cm^2.

Each of the above investigations involved the properties of electron beams formed by assuming uniform emission from the cathode. This corresponds to the temperature-limited operation of the cathode; i.e., with fixed φ_f and B the total current leaving the emitting surface is determined by the cathode temperature. This is quite different from the space-charge-limited operation of a cathode where the emitted current is uniquely dependent on the focusing anode voltage and magnetic field. Nevertheless, the above results qualitatively describe the deviation from theoretical flow which results when the current density is slightly different from the theoretical design value.

The space-charge-limited behavior of a crossed-field gun requires a slightly more detailed investigation of the conditions near the cathode. In particular the emission from each point along the cathode must be

such as to result in a zero electric field value at the surface. Thus for specified φ_f and B values there is only one J_c distribution which will satisfy the requirement of space-charge-limited flow. The Poisson cell evaluation for this type of flow requires the introduction of certain conditions at the cathode. The proper cathode current density distribution is evaluated by assuming that the potential in the immediate vicinity of the cathode satisfies Child's law for a planar diode,

$$J = \frac{4\epsilon_o}{9} \sqrt{2\eta} \; \frac{\varphi^{3/2}}{y^2} \; . \qquad (3.7)$$

y is the distance from the cathode to the outer edge of the first row of space-charge-simulation sources while φ is the potential at this point. If for a given J_c there is disagreement between this theoretical φ value and the actual voltage as measured on the Poisson cell, a different J_c value is required. When a self-consistent solution is achieved, the voltages at the edge of the first row will be in agreement with the theoretical values obtained from Eq. 3.7. Since the electron beam in the Kino gun is derived on the assumption that the current density is uniform along the cathode, it is obvious that if the theoretical flow can not be achieved there must be a nonuniform emission from the cathode surface.

The analysis which follows is concerned with the space-charge-limited flow in the extended Kino short gun. The investigation was started by assuming a uniform cathode current density of 0.8 amp/cm^2 which was approximately the same value as prescribed by theory. After several iterations of the space charge simulation process it became obvious that space-charge-limited operation with uniform J_c was impossible. Various J_c distributions were considered until finally the

self-consistent trajectories of Fig. 3.12 were obtained. Comparison with earlier investigations indicated that the space-charge-limited beam configuration and location agreed reasonably well with the $J_c = 0.5$ and 1.0 amp/cm^2 results. Thus even with nonuniform emission from the cathode (see Fig. 3.13) the electron trajectories are similar to previous investigations in which uniform J_c conditions were assumed.

The nonuniform emission illustrated in Fig. 3.13 indicates that the cathode current density varied from a minimum of 0.55 amp/cm^2 on the left edge of the cathode to 1.03 amps/cm^2 on the right edge. This result is in agreement with the earlier investigation of the wide cathode Kino gun. In that case the electric field in the left region of the gun was observed to be too small to allow the electrons emitted from this section of the cathode to follow the proper trajectories. The extended Kino gun results indicate that this improper field is also responsible for reducing the emission from this part of the cathode.

The above results are contrary to the fact that one would expect a suppression of emission from the right side of the cathode rather than the left. In other words, the electrons emitted from the left side would pass over the rest of the cathode and hence would depress the potential and electric field in the right portion of the gun. It then follows that emission from this part of the cathode would be reduced. However, this interpretation implies a gun system in which the focusing electrode is planar and located parallel to the cathode surface. This results in the space-charge-free electric field being uniform along the cathode surface. Thus, with a beam present the space charge above the right part of the cathode combines with the space-charge-free field to produce a net electric field which is smaller than at the left edge of the cathode. Thus it is obvious that the emission must be reduced along

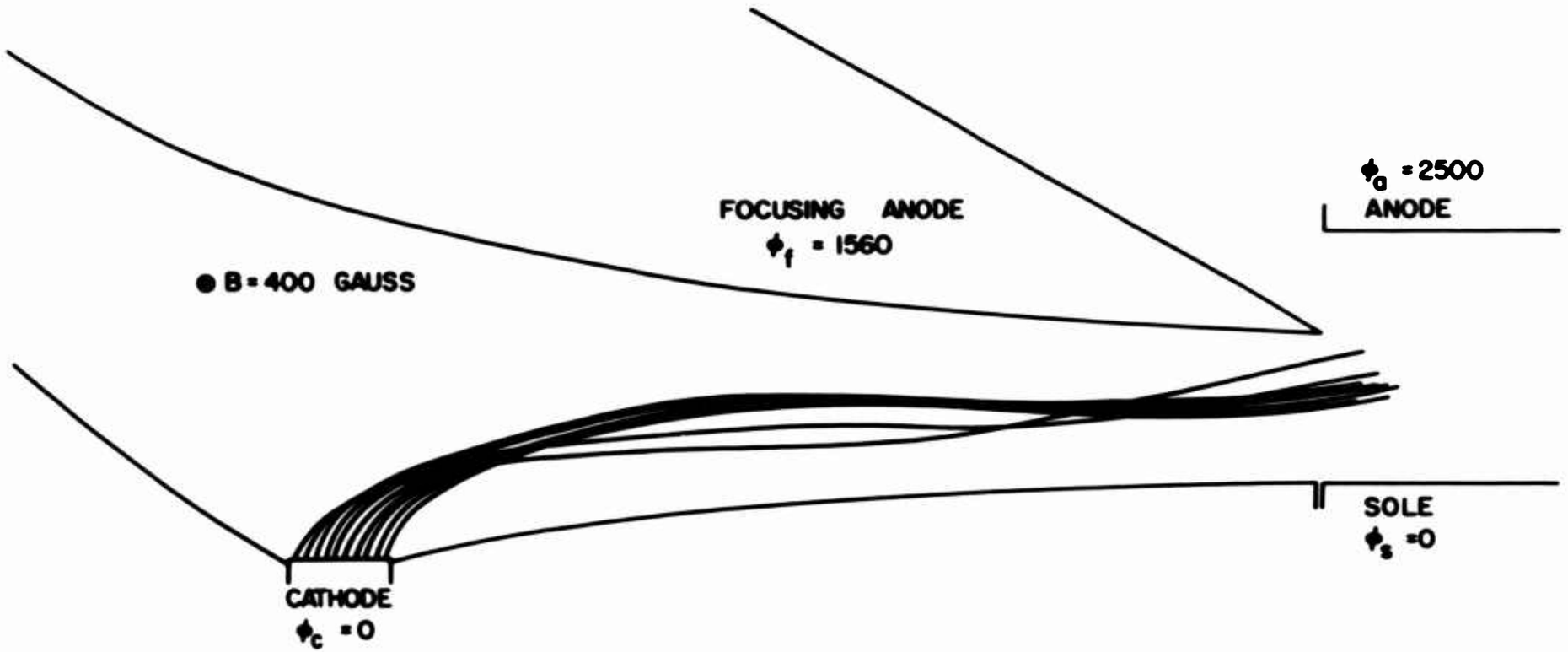

FIG. 3.12 POISSON CELL TRAJECTORIES ASSUMING SPACE-CHARGE-LIMITED EMISSION FROM THE CATHODE.

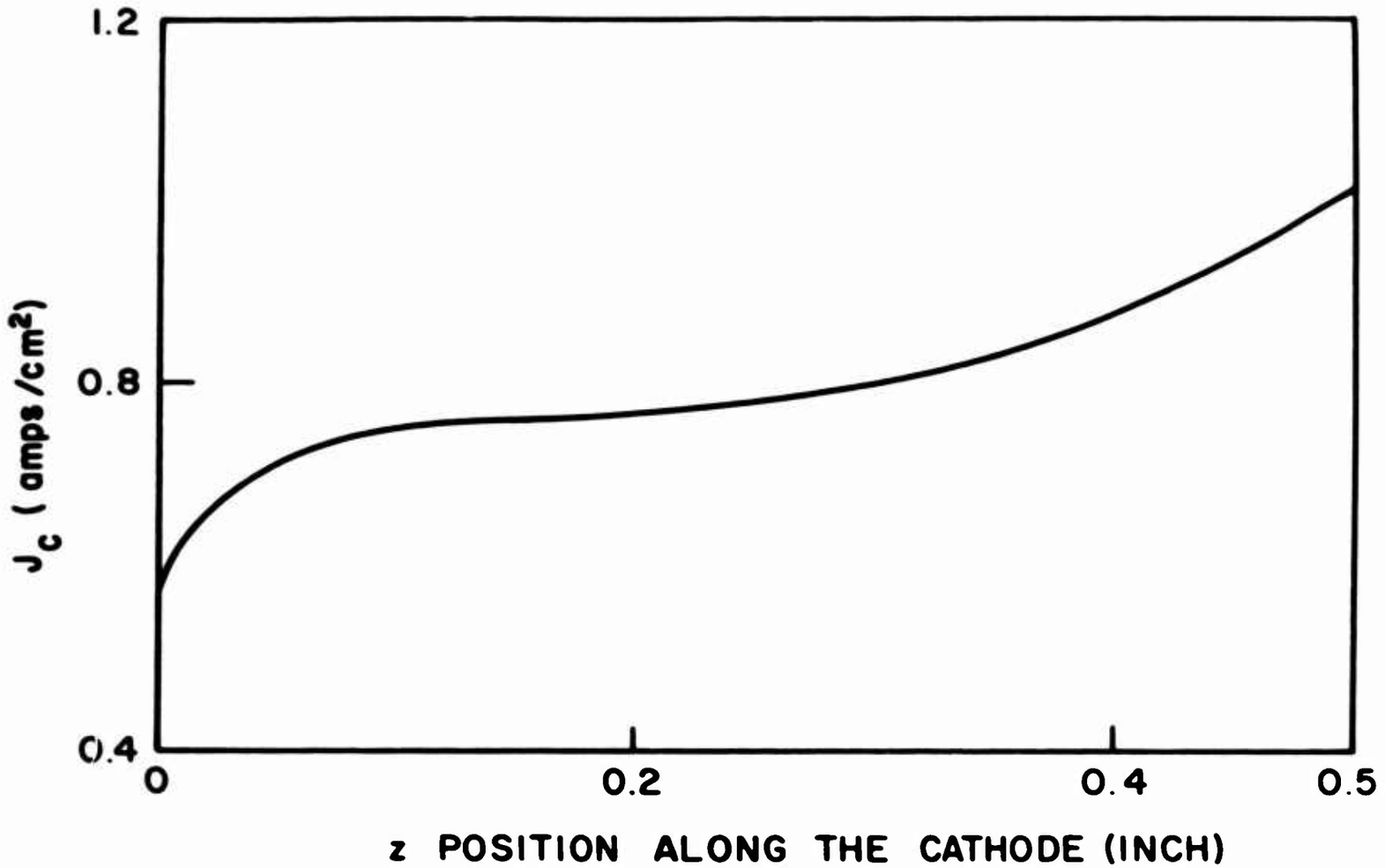

FIG 3.13 CATHODE CURRENT DENSITY VARIATION OBTAINED FROM THE POISSON CELL ANALYSIS OF THE EXTENDED KINO SHORT GUN.

the right edge in this situation. However, in the Kino gun the focusing anode is not equally displaced from each section of the cathode. In particular it is located much farther from the left side of the cathode than from the right side. Thus the charge-free field along the rear of the cathode is significantly less than on the front edge. As the electrons move through the gun they do tend to depress the field on the right more than on the left, but the results indicate that this depression is not sufficient to offset the greater field produced by the focusing anode on the front edge of the cathode. Consequently it should be expected that the investigation would indicate greater cathode current densities along the right edge.

The observation of nonuniform emission from the cathode of a Kino short gun has been substantiated by Midford[11] in his experimental investigations. Gas was introduced into his tube during its operation and photographs were then taken of the ionized beam. These photographs vividly illustrate a suppressed emission from the rear of the cathode thus agreeing with the Poisson cell results. The difference in the cathode emission characteristics of the Kino gun and the planar diode injection system is a result of different electrode configurations and is not indicative of contradictory behavior of the electron beams in the two situations.

The Poisson cell analysis of the extended Kino short gun indicated an average space-charge-limited cathode current density of 0.79 amp/cm^2. This was in good agreement with the theoretical uniform Kino value of 0.8 amp/cm^2 and suggested that the total beam current obtained by the Poisson cell was nearly identical to the Kino value for the selected φ_f and B values.

The above extended gun results suggested the possibility of improving the flow from the cathode by locating an auxiliary electrode closer to the left edge of the beam. Figure 3.14 illustrates the trajectories obtained when an auxiliary electrode is located along the $\varphi = 640$ volt theoretical equipotential. However, this electrode did not appear to affect the cathode current density distribution to any great extent although it did increase the average cathode current density from 0.79 to 0.87 amp/cm^2.

Figure 3.15 illustrates the situation when the auxiliary electrode voltage was increased to 850 volts. Once again the current distribution is unchanged except for increasing the average J_c value to 0.96 amp/cm^2. The current density distributions across the cathode for the auxiliary electrode investigations are shown in Fig. 3.16. These results indicate that the achievement of more uniform emission will not be possible unless the electric field in the rear portion of the gun can be increased. One possibility is the curvature of the rear of the focusing anode down towards the cathode, a situation considered earlier in this chapter. Another possibility is the modification of the cathode ramp electrodes. Such a study was carried out during a digital computer analysis of a shortened Kino gun and the results will be presented in Chapter IV.

3.4 General Conclusions of the Poisson Cell Investigation

The investigation of the various electron injection systems has resulted in the following observations:

1. There is a maximum convergence ratio which is compatible with the formation of a Brillouin beam.

2. There is a maximum cathode width from which Brillouin flow can be achieved.

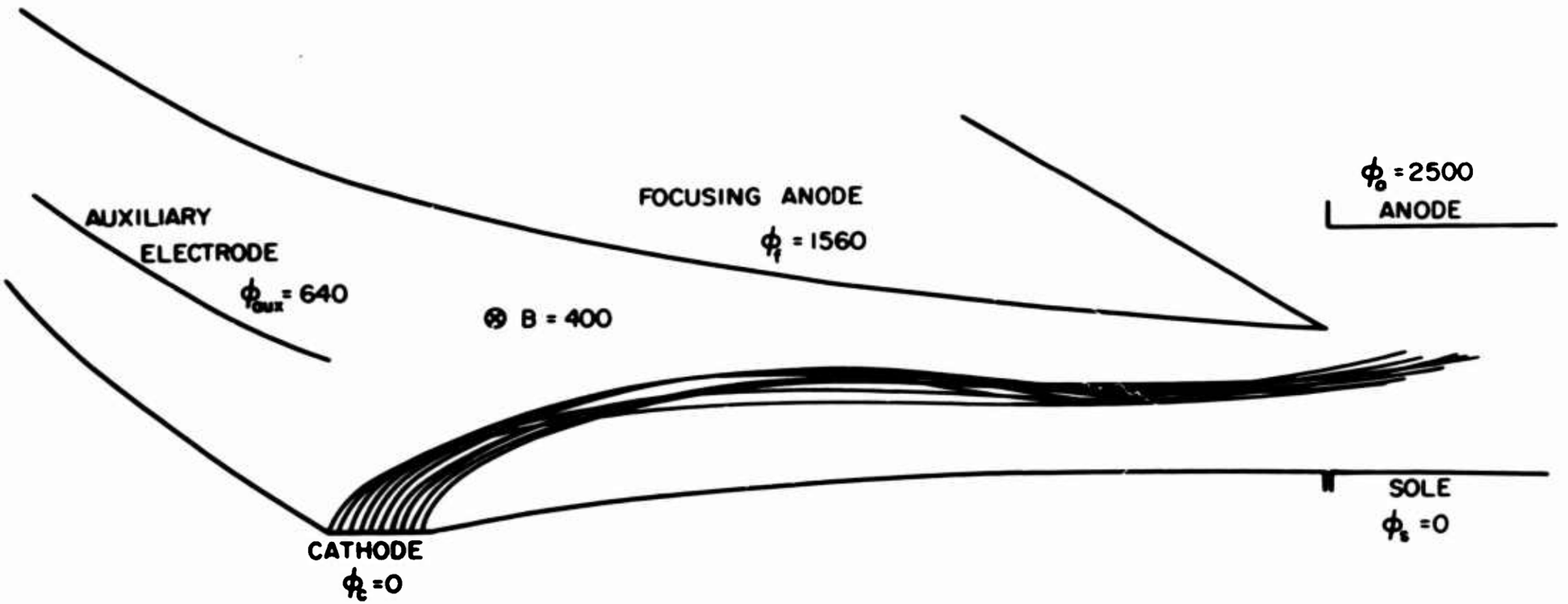

FIG. 3.14 ELECTRON TRAJECTORIES WHEN AN AUXILIARY ELECTRODE IS PLACED ALONG THE 640 VOLT EQUIPOTENTIAL CURVE IN THE KINO SHORT GUN.

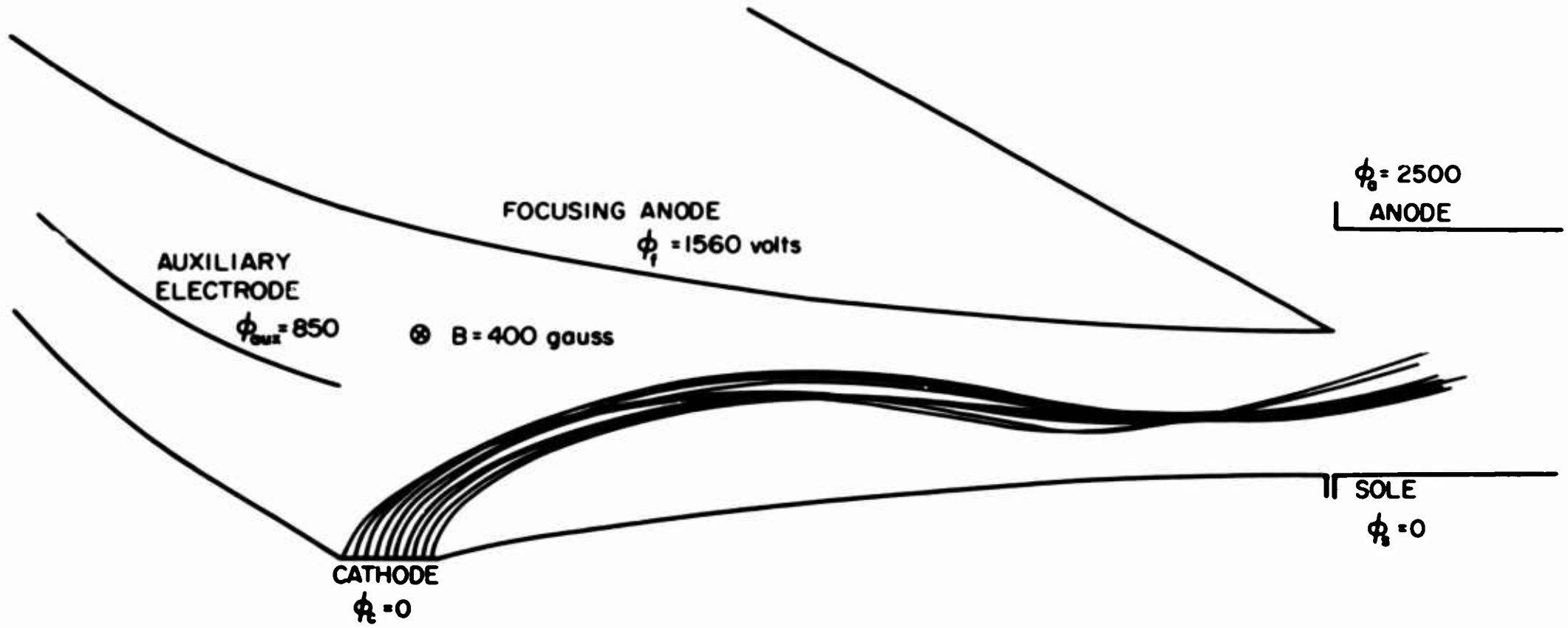

FIG. 3.15 TRAJECTORIES WITH AUXILIARY ELECTRODE POTENTIAL INCREASED TO 850 VOLTS.

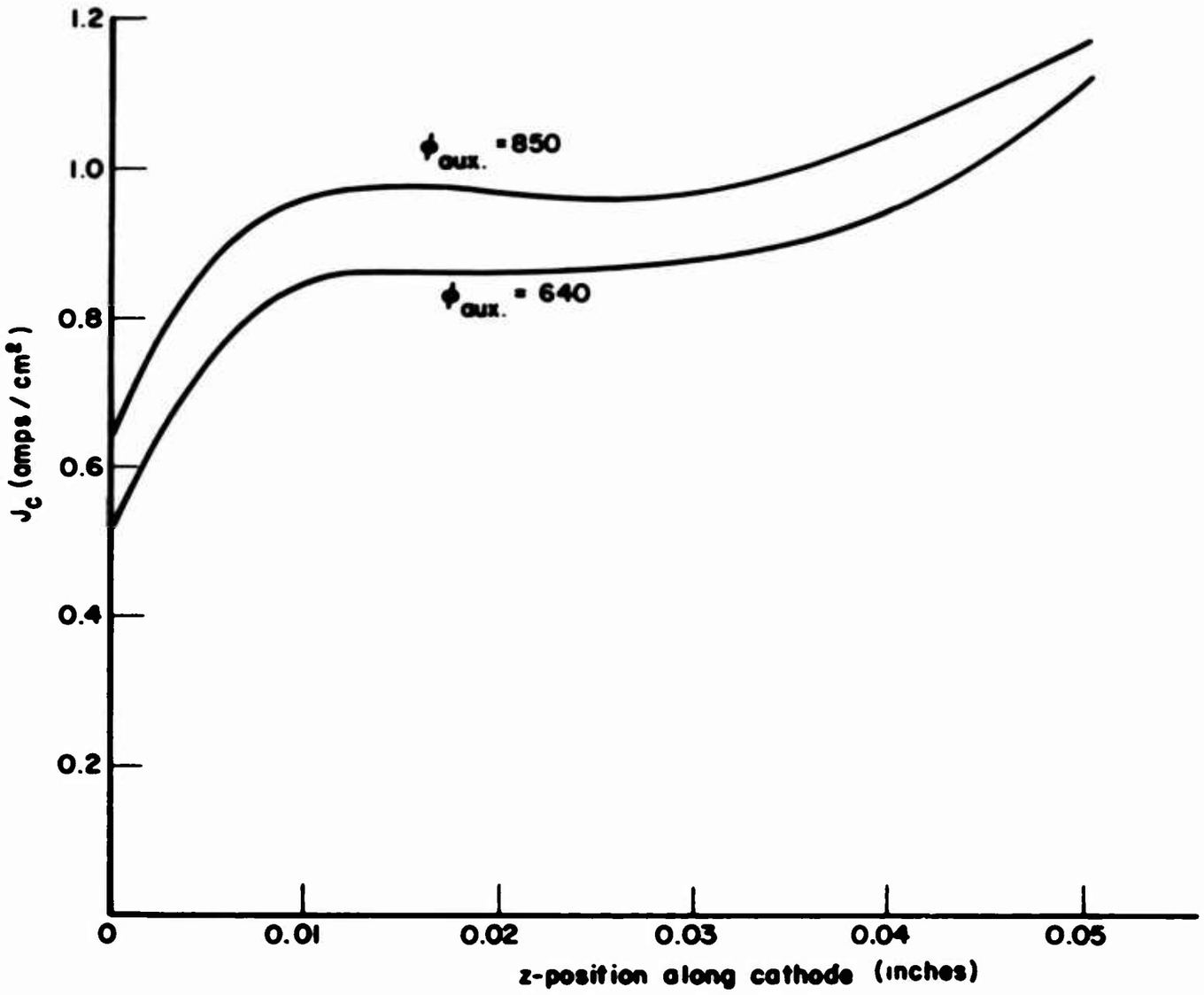

FIG. 3.16 CURRENT DENSITY VARIATION ACROSS THE CATHODE FOR THE VARIOUS AUXILIARY ELECTRODE POTENTIALS.

3. The beam location and configuration in the Kino gun is not critically dependent on the current unless operation is attempted for J_c values greatly exceeding the theoretical value.

4. The space-charge-limited behavior of the extended Kino short gun results in nonuniform emission from the cathode.

5. The average J_c value for space-charge-limited operation is approximately the same as the uniform value predicted by the theory. Further evidence substantiating some of these conclusions will be presented in the chapters which follow.

CHAPTER IV. DIGITAL COMPUTER INVESTIGATION OF CROSSED-FIELD ELECTRON GUNS

4.1 Introduction

A digital computer program has been developed by Boers[33] for the determination of electron trajectories in crossed-field devices. The program uses a 7200 point matrix to simulate the gun geometry and electric fields. The d-c electric field produced by the application of voltages to the various electrodes in the actual device is simulated by assigning the appropriate potentials to those matrix points which lie along a given electrode curve. Relaxation techniques are employed to evaluate the electric fields which act on the electrons during their motion. The magnetic field can be variable but for crossed-field analyses it has been assumed to be uniform.

The regular trajectory program begins by assigning initial conditions to the electrons at the edge of the first matrix row adjacent to the cathode. The electrons are assumed to have been emitted with zero velocity from a space-charge-limited cathode. Thus the potential distribution in the cathode region must satisfy Child's law

$$\varphi = \left(\frac{9J}{4\epsilon_o \sqrt{2\eta}}\right)^{2/3} y^{4/3} \quad , \tag{4.1}$$

and for a given cathode current density J_c the electrons at the first matrix point must have an initial energy prescribed by Eq. 4.1.

It is also possible to include the effects of a potential minimum near the cathode in which case it is necessary to introduce nonzero emission velocities for the electrons. The analysis requires a two-stage

process whereby the first step involves the simulation of the voltage distribution near the cathode. The electron trajectories are investigated in this potential minimum region and the velocity components are measured at the first matrix plane. This data is then used as the initial conditions for the regular computer program for determining the electron trajectories in the remainder of the gun region. The above results provide both a description of the electron beam configuration and an indication of the effect of initial velocities on the individual trajectories.

The digital computer program has been applied to the evaluation of space-charge flows produced by various Kino gun configurations. Some of these investigations involved the same type of guns as were used in the Poisson cell analyses and consequently will not be discussed in detail here. However, a comparison of the results obtained by the two methods is summarized below.

The investigations of a Kino short gun which is terminated prior to the $\omega_c t = 2\pi$ plane are described in detail. Changes in the ramp and focusing-anode electrodes were evaluated in terms of their effect on the electron trajectories and cathode current density distribution. This gun was also used as the model for studying the trajectories of electrons which had traversed a potential minimum region adjacent to the cathode.

4.2 Comparison with Poisson Cell Results

Figure 4.1 illustrates an electrode configuration which is identical to the Poisson cell model of the Kino gun described in Fig. 3.1. The solid curves are the trajectories obtained from the digital computer solution of the problem while the broken curves represent the

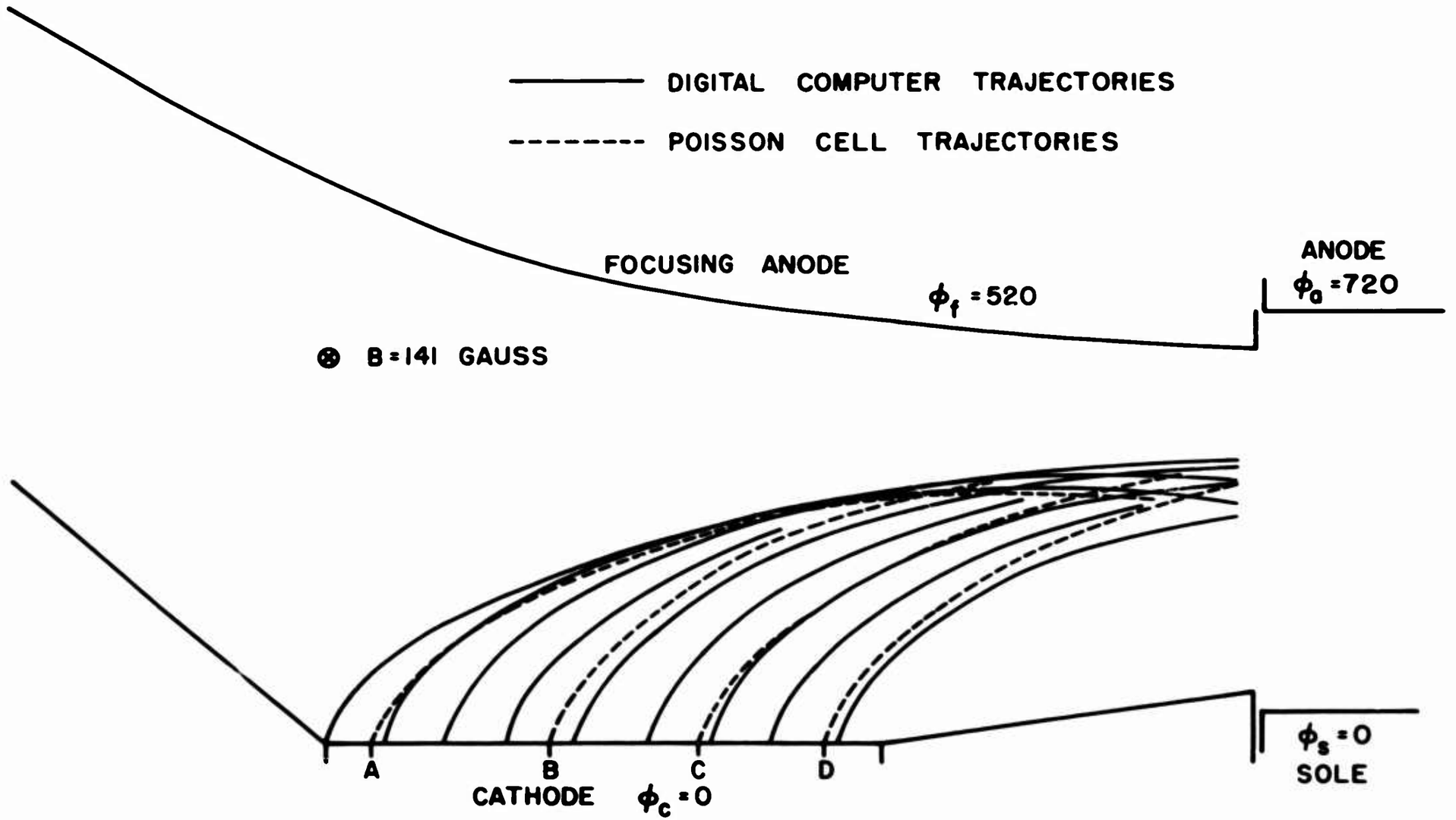

FIG 4.1 COMPARISON OF DIGITAL COMPUTER AND POISSON CELL TRAJECTORIES FOR THE ORIGINAL KINO SHORT GUN.

corresponding Poisson cell results. The trajectories obtained by the two methods are generally quite similar especially near the cathode. It is only when the trajectories approach points of intersection, indicating nonlaminar flow, that significant differences occur. Nevertheless, the general beam configurations are essentially the same. This was a space-charge-limited analysis in which the average cathode current density was found to be approximately 0.058 amp/cm^2 rather than the theoretical value of 0.048.

Figure 4.2 compares the Poisson cell and digital trajectories when the focusing anode configuration was modified. These results were both obtained under the assumption of a uniform cathode emission of 0.048 amp/cm^2. In each case it was quite apparent that the flow became nonlaminar as the beam approached the gun exit plane.

Figure 4.3 illustrates the digital computer trajectories for the extended Kino short gun of Fig. 3.12. As in the Poisson cell analysis, this investigation was concerned with space-charge-limited operation. The analog study described earlier indicated that the current density was variable across the cathode. The digital investigation also indicated nonuniform emission as is illustrated in Fig. 4.4 which compares the cathode current density distributions for both the Poisson cell and digital computer analyses. The results are similar except near the right edge of the cathode. Both results are derived by assuming the existence of a Child's law potential distribution between the cathode and some arbitrary plane a short distance away. For the Poisson cell analysis, the arbitrary plane was located only half as far from the cathode as it was in the digital analysis (0.005 inch as compared with 0.010 inch, actual tube dimensions). The manner in which the region immediately

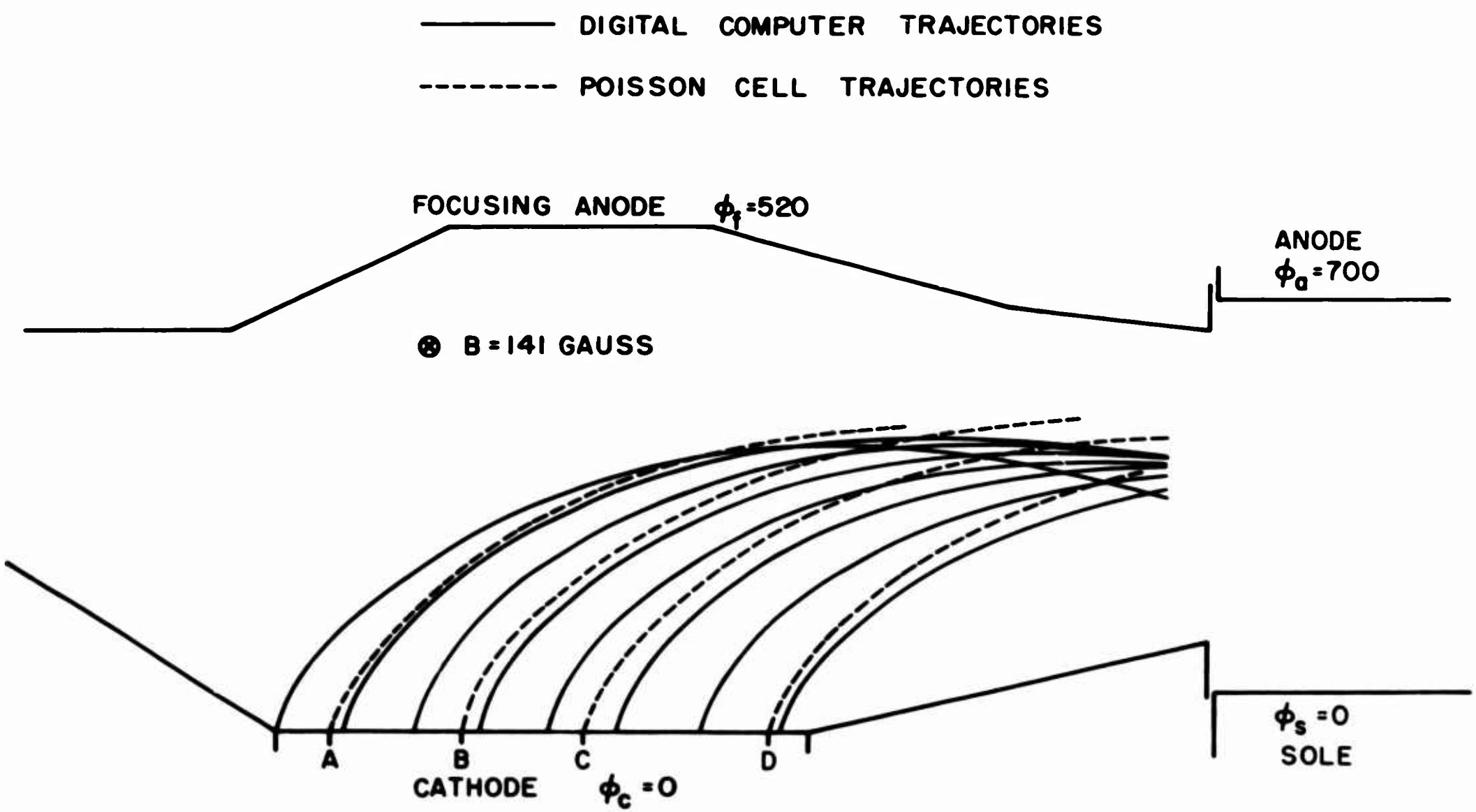

FIG. 4.2 COMPARISON OF DIGITAL COMPUTER AND POISSON CELL TRAJECTORIES FOR THE MODIFIED KINO SHORT GUN.

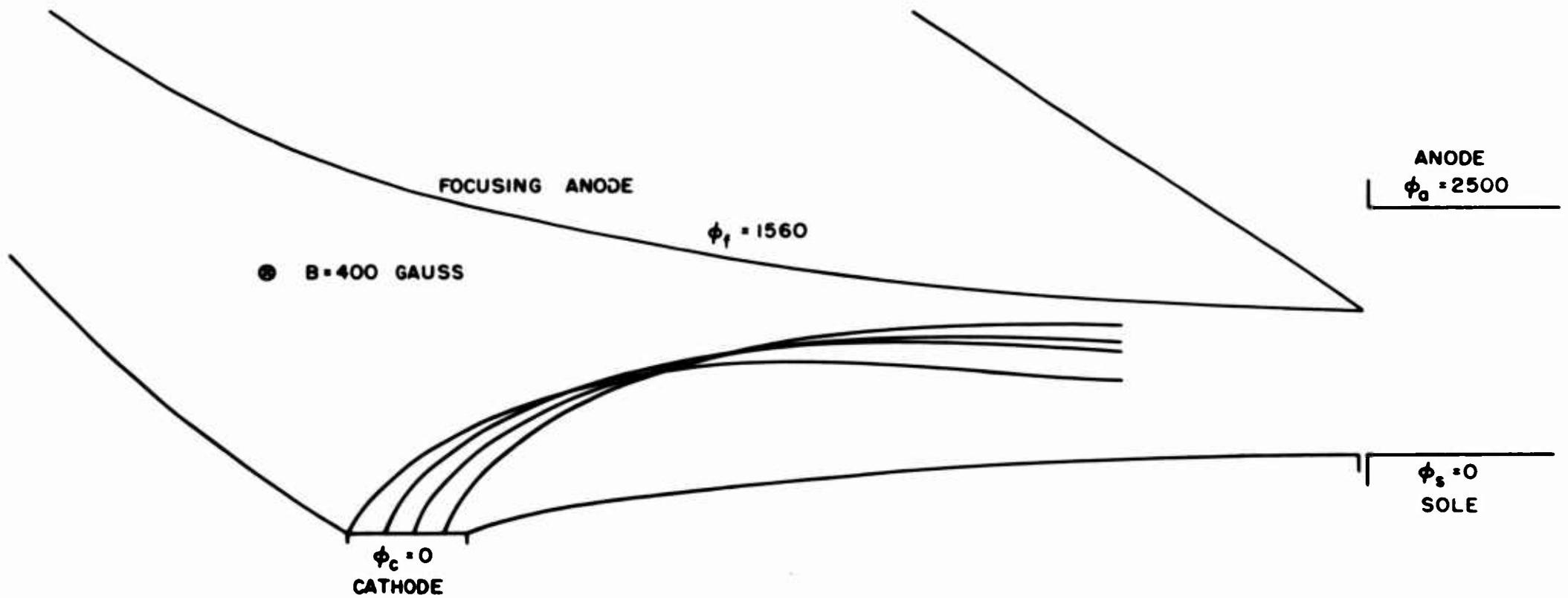

FIG. 4.3 TRAJECTORIES OBTAINED FROM THE DIGITAL COMPUTER INVESTIGATION OF THE EXTENDED KINO SHORT GUN.

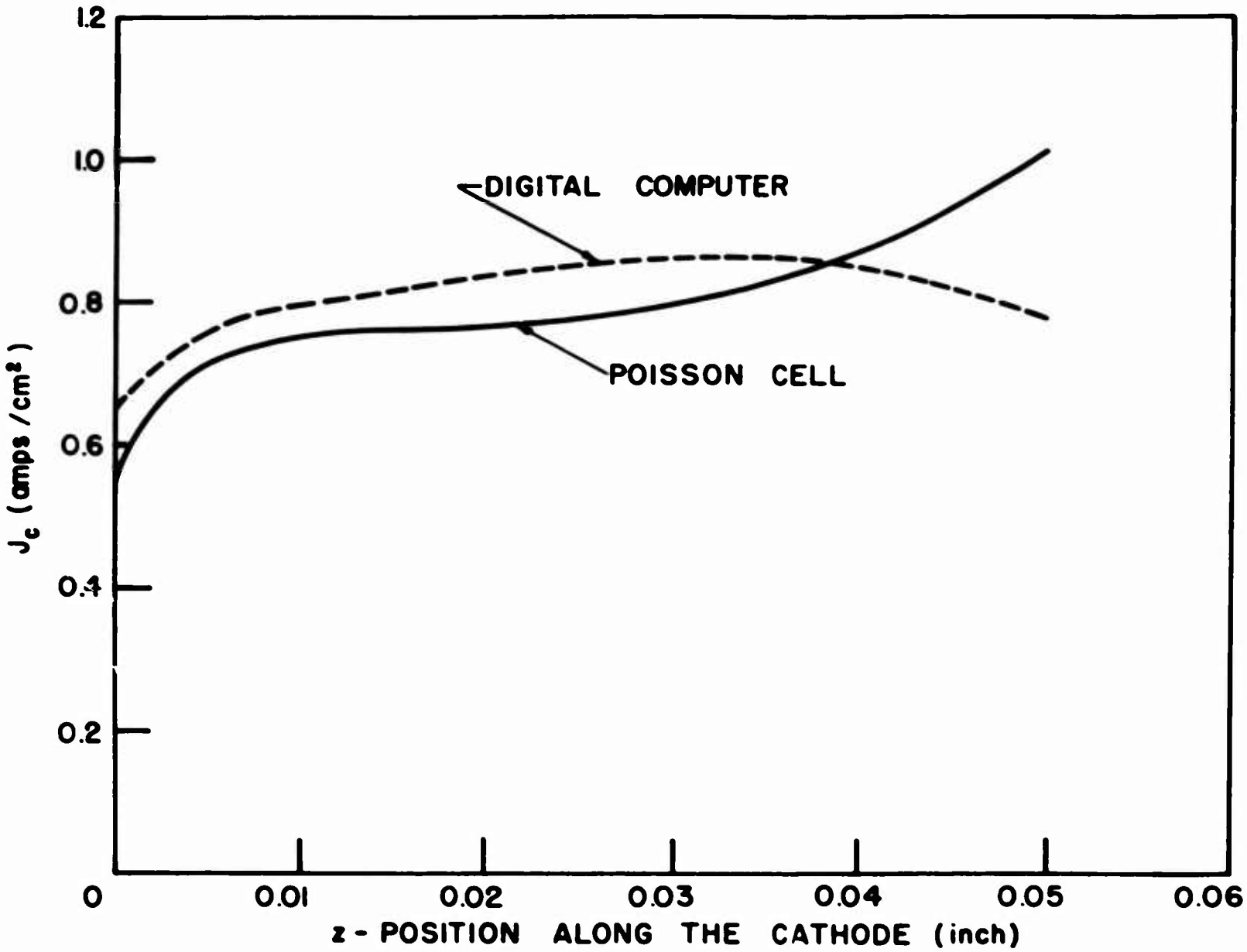

FIG. 4.4 CATHODE CURRENT DENSITY DISTRIBUTION OBTAINED FROM THE EXTENDED KINO SHORT GUN INVESTIGATIONS.

adjacent to the cathode is handled does not seem to influence the emission from the cathode to any great extent. This means that the solution to the problem should not be critically dependent on the manner in which the space charge is simulated near the cathode. However, the different location of the arbitrary plane probably is partially responsible for the discrepancy in the J_c values along the right edge of the cathode. (The ramp electrodes also greatly affect the edge emission from the cathode as will be illustrated in the following section.) The average digital computer value of cathode current density is approximately 0.82 amp/cm^2 which agrees favorably both with the Poisson cell result of 0.79 amp/cm^2 and the theoretical value of 0.80 amp/cm^2.

In general, comparison between the Poisson cell and digital computer results indicates that the trajectories are quite similar. The discrepancies which do exist are mostly attributable to the difficulty in simulating accurately the space-charge densities in regions where electron trajectories intersect. In such regions the manner in which the space charge is represented greatly affects the subsequent motion of the electrons. The difference in the initial conditions (i.e., initial position and velocity) which are used in the two methods generate some difference but as indicated in Fig. 4.1 and 4.2 these are not significant. At least this is true when the electrons are restricted to leave the cathode only in the normal direction.

4.3 Abbreviated Kino Gun Investigations

As described previously, the Kino short gun flow results in a theoretical infinite space-charge density at $\omega_c t = 2\pi$ along a trajectory.

Although such densities cannot be achieved in practice, it does indicate the possibility of beam instabilities in the vicinity of the 2π point. This difficulty can be circumvented by terminating the gun design prior to the critical region. Such an abbreviated Kino short gun is illustrated in Fig. 4.5 which also includes the theoretical trajectories. The upper beam boundary electron reaches the gun exit plane at $\omega_c t = 280°$ and the lower edge electron at $\omega_c t = 248°$.

The anode-sole region is designed to match as closely as possible the conditions in the exit beam with those required for rectilinear, Brillouin flow. The analysis of the theoretical gun and the matching conditions are presented in Appendix C. For the configuration of Fig. 4.5 the cathode width is 2.54×10^{-3} meter while the anode-sole spacing is 4.78×10^{-3} meter. The anode and sole are also tilted approximately 8.5° with respect to the cathode. The operating conditions are

$$B = 300 \text{ gauss},$$

$$\varphi_a = 3565 \text{ volts},$$

$$\varphi_f = 2850 \text{ volts},$$

$$\varphi_c = \varphi_s = 0,$$

and a theoretical current density of $J_c = 0.628$ amp/cm^2.

The electron trajectories obtained from the space-charge-limited operation of the abbreviated gun under the above conditions are illustrated in Fig. 4.6 which also includes a theoretical trajectory for comparison. Although the individual trajectories are similar to the theoretical path, the flow is still quite nonlaminar. The current density variation across the cathode is also illustrated in this figure and indicates that the emission from the rear edge is suppressed. The

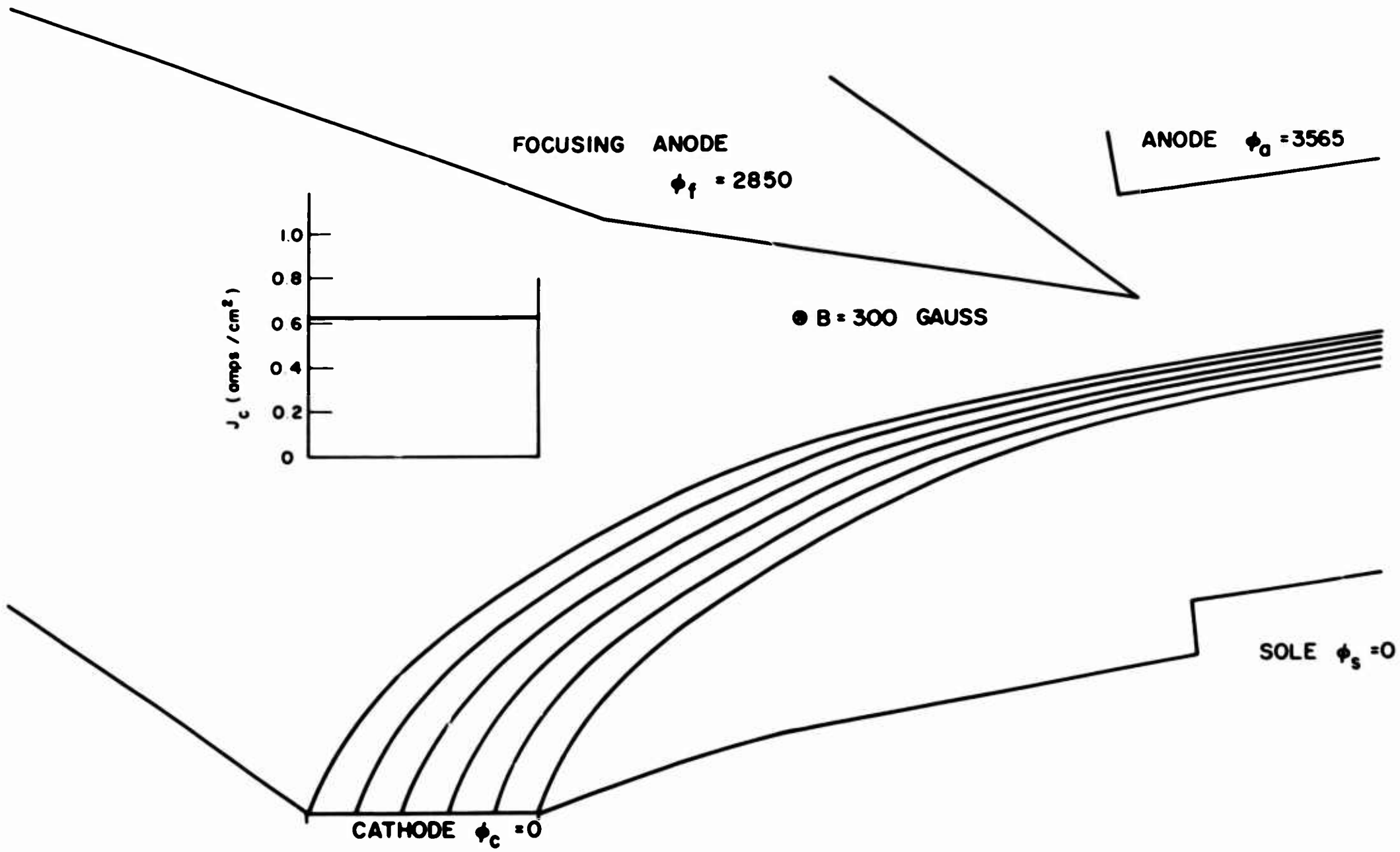

FIG. 4.5 THEORETICAL TRAJECTORIES FOR THE ABBREVIATED KINO GUN.

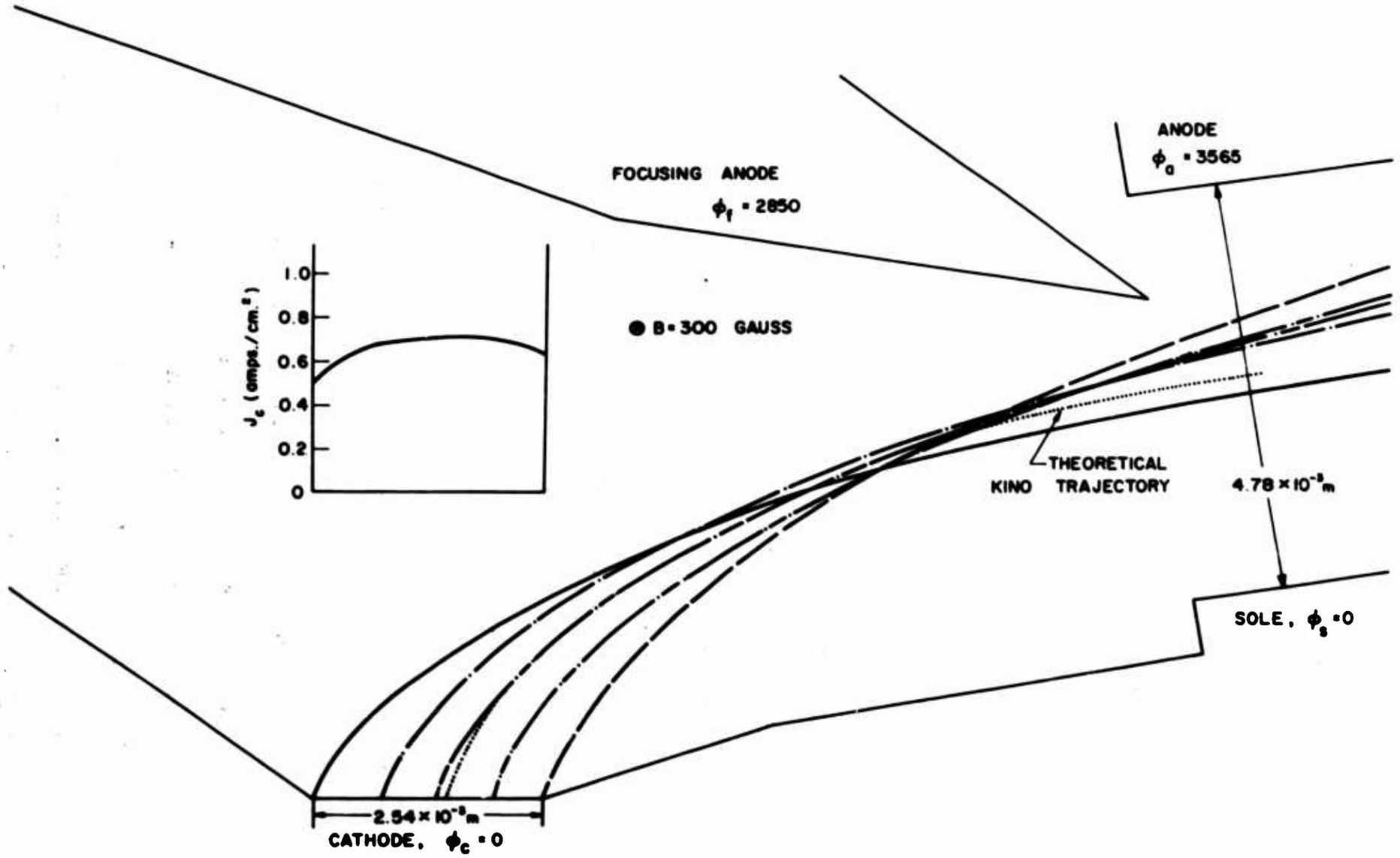

FIG. 4.6 DIGITAL COMPUTER RESULTS FOR THE THEORETICAL ABBREVIATED KINO GUN CONFIGURATION.

emission is greatest from the center portion of the cathode and drops off slightly at the front edge. However, the average J_c value is approximately 0.625 amp/cm^2 which is surprisingly close to the theoretical design value of 0.628 amp/cm^2.

The low J_c value at the rear of the cathode and the relatively sharp curvature of the trajectory for those electrons which are emitted from that region indicate that the average electric field in this region is insufficient to allow either the proper emission density or the desired electron motion. A similar type of behavior was also pointed out in Chapter III for the Poisson cell analysis of the extended Kino short gun.

Figure 4.7 illustrates the trajectories obtained when the focusing anode was extended back parallel to the cathode from the gun exit plane and the front ramp electrode was lowered slightly. The combined effect of these changes is threefold:

1. The trajectories in the beam are spread apart although the upper trajectory is still undesirable.

2. The beam passes much closer to the focusing anode.

3. The cathode current density distribution becomes extremely nonuniform with the emission from the rear being less than before and that from the front being greater.

The existence of nonuniform emission is not surprising but certainly the reduced emission from the rear of the cathode is unexpected; i.e., as mentioned earlier the operation of parallel-plane electron injection systems should result in reduced emission from the front of the cathode and not from the rear. This was attributed to the fact that the entire beam passes over the front portion of the cathode and thus

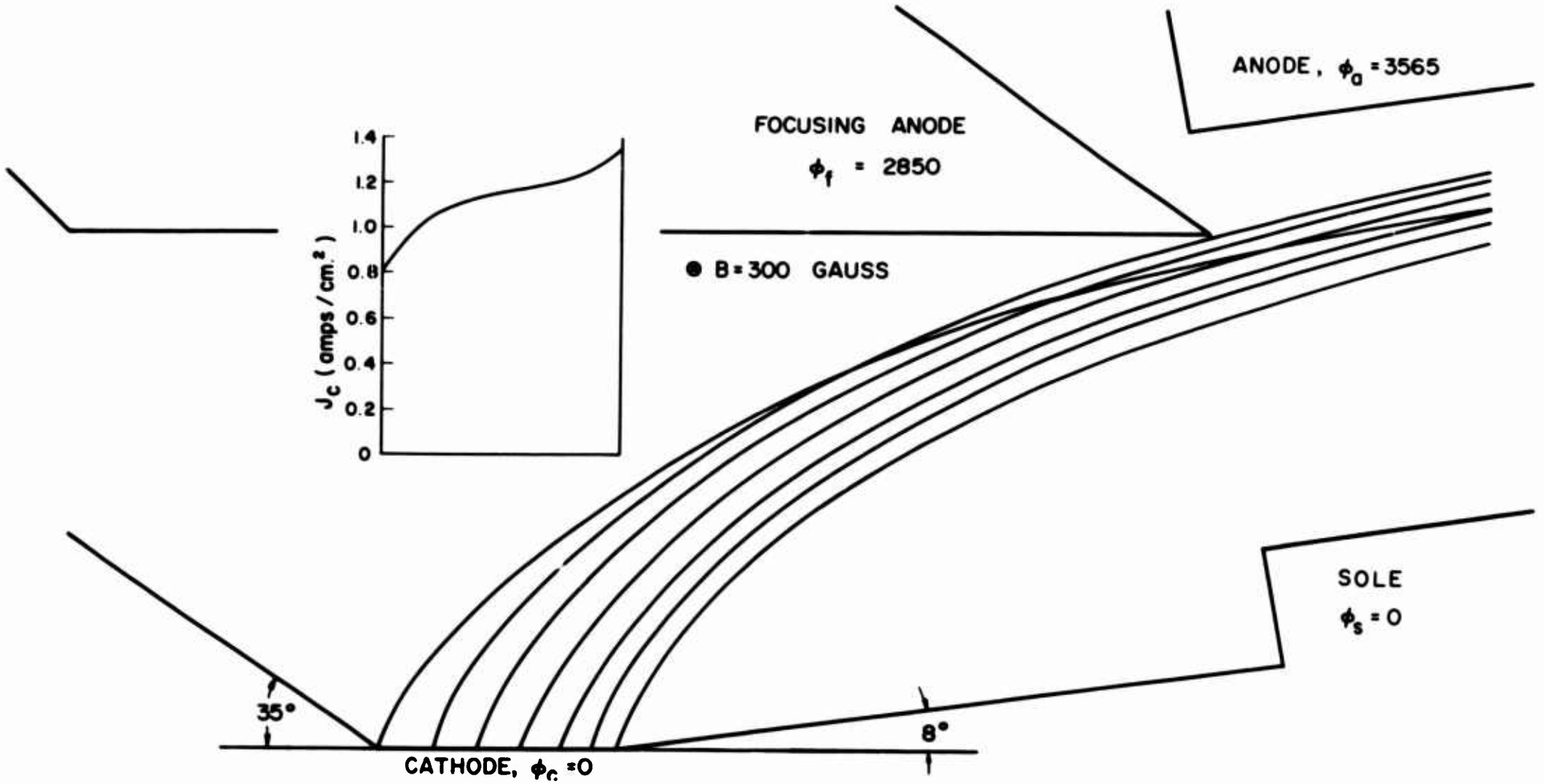

FIG. 4.7 ELECTRON TRAJECTORIES AND CATHODE CURRENT DENSITY DISTRIBUTION WITH FOCUSING ANODE PARALLEL TO THE CATHODE.

suppresses both the electric field and emission in that region. The contradictory effect observed in Fig. 4.7 clearly demonstrates that the ramp electrodes and not the focusing anode are the controlling factors in the uniformity of emission from the cathode. Consequently by lowering the rear ramp it should be possible to improve the emission from the rear of the cathode. The modification in trajectories caused by the change in the front ramp electrode indicates that the beam shape can also be controlled by the ramps.

Figure 4.8 illustrates the results when the focusing anode was returned to its original position, the front ramp angle was increased to 19° and the rear ramp angle was decreased to 18.5°. The change in the rear ramp greatly improved the trajectory of the electrons emitted from that edge of the cathode. However, the front ramp slope was too large and resulted in the lower electron entering the beam in a non-laminar manner. The most significant result, however, was the achievement of increased emission from the rear of the cathode. The larger J_c values in this region cause an increase in the amount of space-charge which passes over the front edge. This condition in conjunction with the increased slope of the front ramp results in decreased emission from the front edge of the cathode.

Figure 4.9 shows the effect of reducing the front ramp slope to 8°. The upper trajectories were essentially unaffected but the electrons emitted from the front of the cathode were significantly lower which indicated that the slope was now too small. The emission was still nonuniform but the current density distribution was such that J_c was greater along the edges than at the center of the cathode.

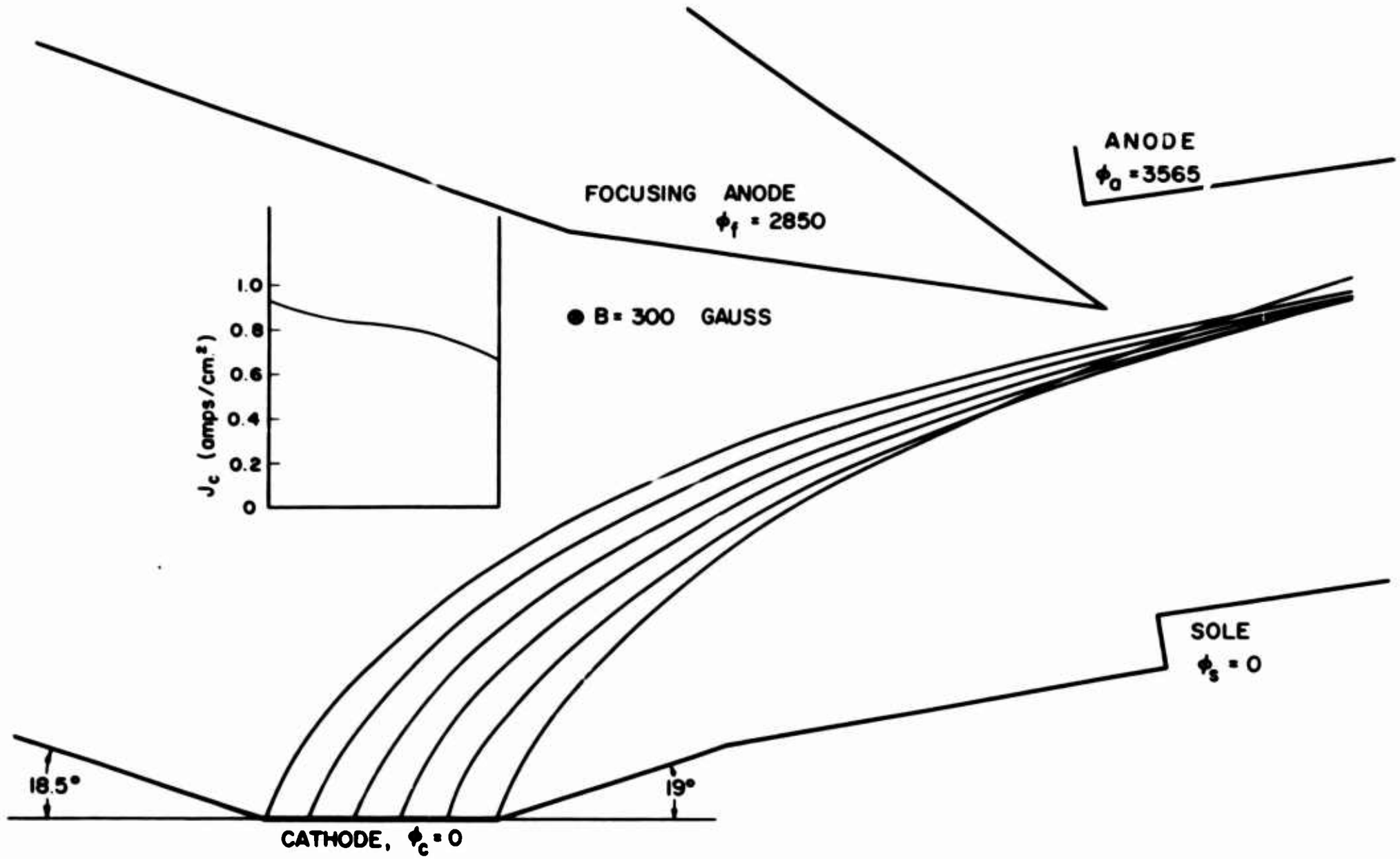

FIG. 4.8 ELECTRON TRAJECTORIES AND J_c DISTRIBUTION FOR ABBREVIATED KINO GUN WITH MODIFIED RAMP ELECTRODES.

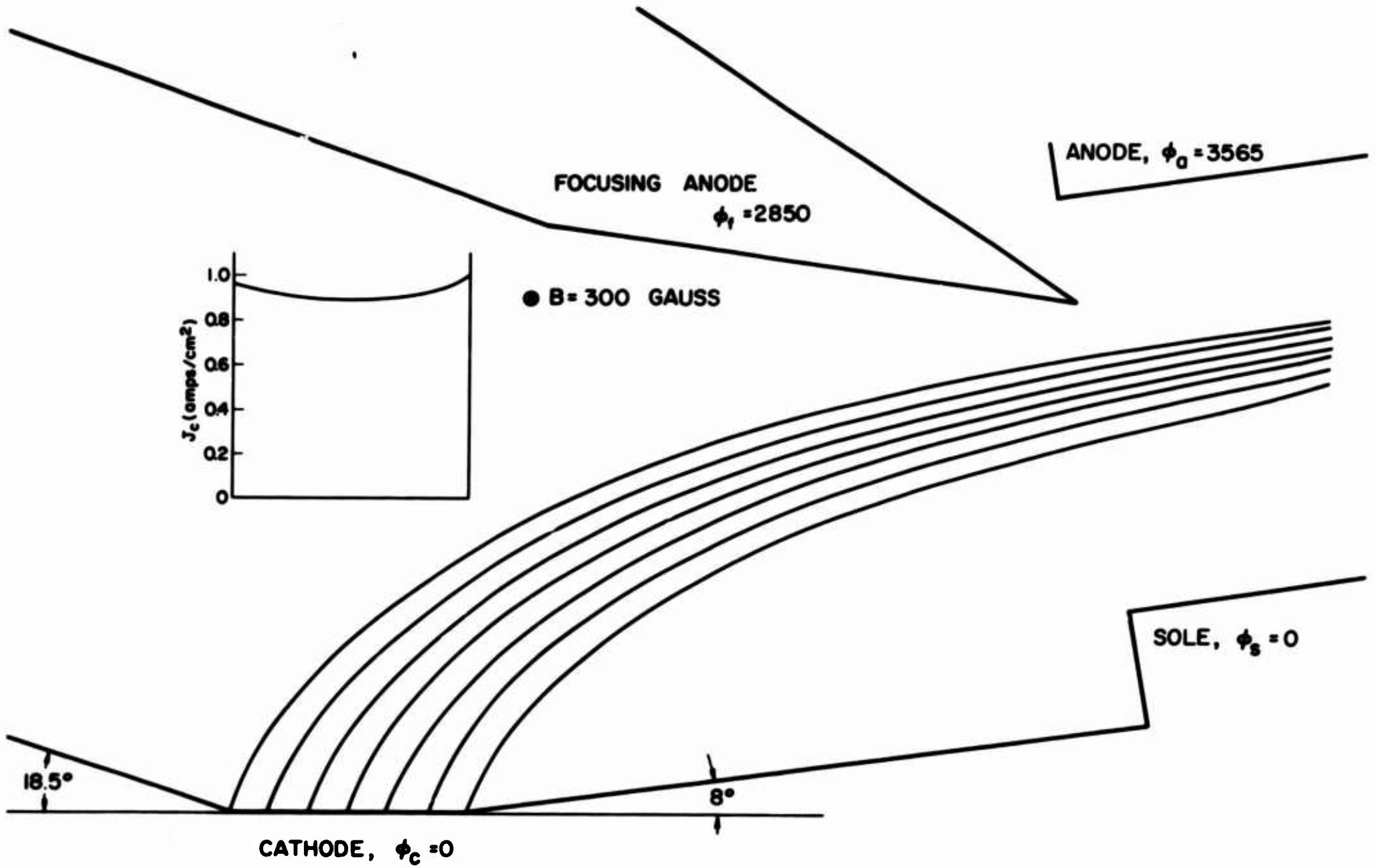

FIG. 4.9 ELECTRON TRAJECTORIES AND J_c DISTRIBUTION FOR 8° FRONT RAMP ELECTRODE.

Figure 4.10a illustrates a well-defined beam which was obtained by increasing the front ramp slope to 11°. The exit beam was slightly wider than the Brillouin beam which is compatible with the interaction region conditions. The cathode emission was still slightly nonuniform although it was an improvement over the preceding runs.

Figure 4.10b illustrates the variation in velocity across the beam at planes B-B, C-C, and D-D. If the beam were exactly laminar, then the velocity gradient across the beam would equal ω_c as indicated in the figure. As the beam leaves the gun region (plane B-B) the actual velocity gradient or beam slippage is approximately the desired Brillouin value. However, the beam thickness is greater than the Brillouin thickness indicating a deficiency of space charge within the beam. The velocity slip at two later cross-sections of the beam (C-C and D-D) is still approximately the same as the Brillouin value although the beam is becoming narrower. This is caused by the slight angle at which the beam is moving with respect to the sole and anode planes. The small space-charge density at the gun exit also is responsible for the decreasing beam thickness behavior.

The interesting feature is the apparent ability of the beam to maintain the same velocity gradient at any cross-section even though the beam thickness is changing. The above operating conditions satisfy the requirements of irrotational space-charge flow which will be discussed in the following chapter. It is shown there that the required behavior of irrotational flow is a velocity gradient of precisely ω_c across any transverse section of the beam. Thus the above results are not completely unexpected.

Figure 4.11 illustrates the results when the angles of the front and rear ramps were changed to 14° and 22.5° respectively. The

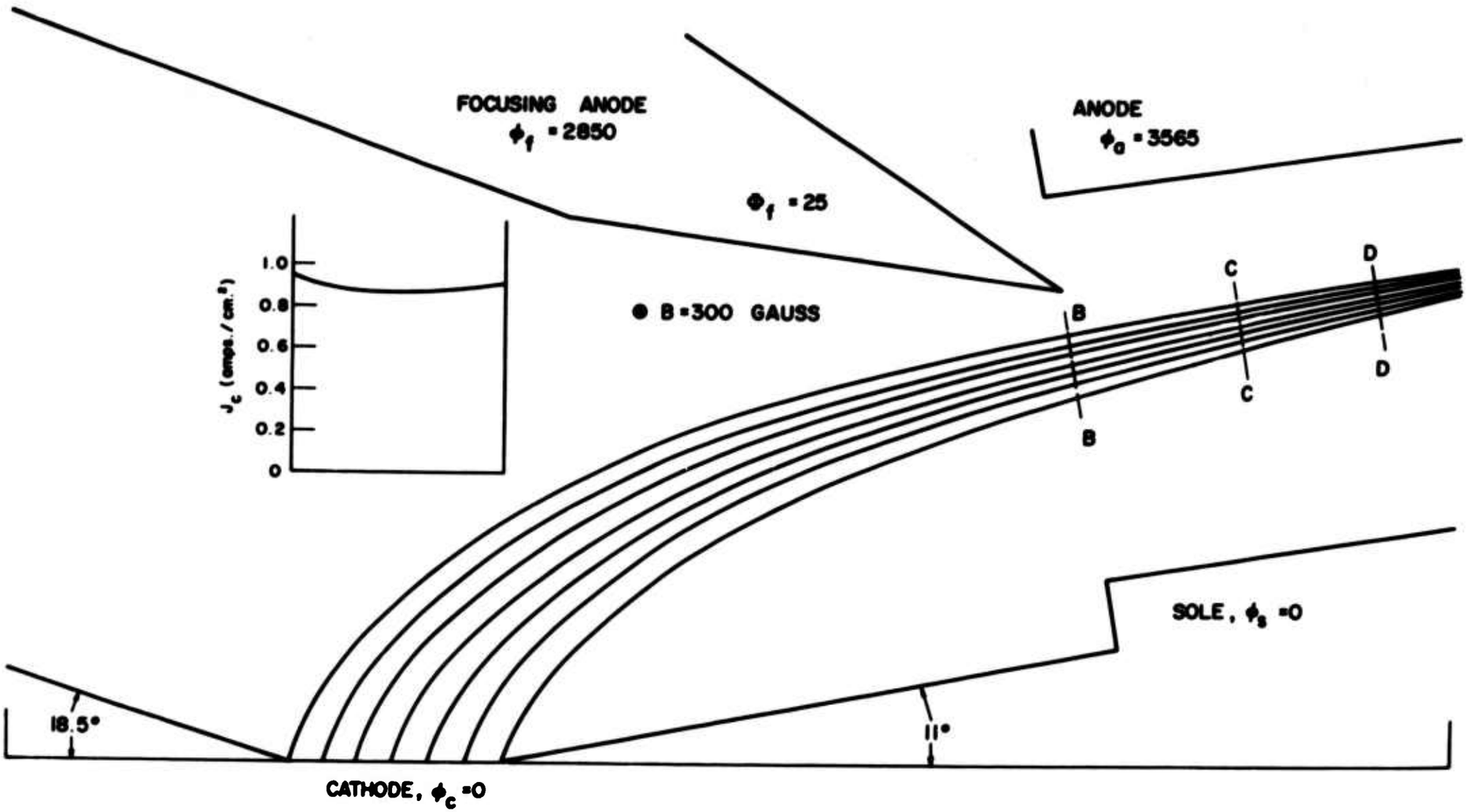

FIG. 4.10a MODIFIED VERSION OF ABBREVIATED KINO GUN ILLUSTRATING NEARLY LAMINAR FLOW.

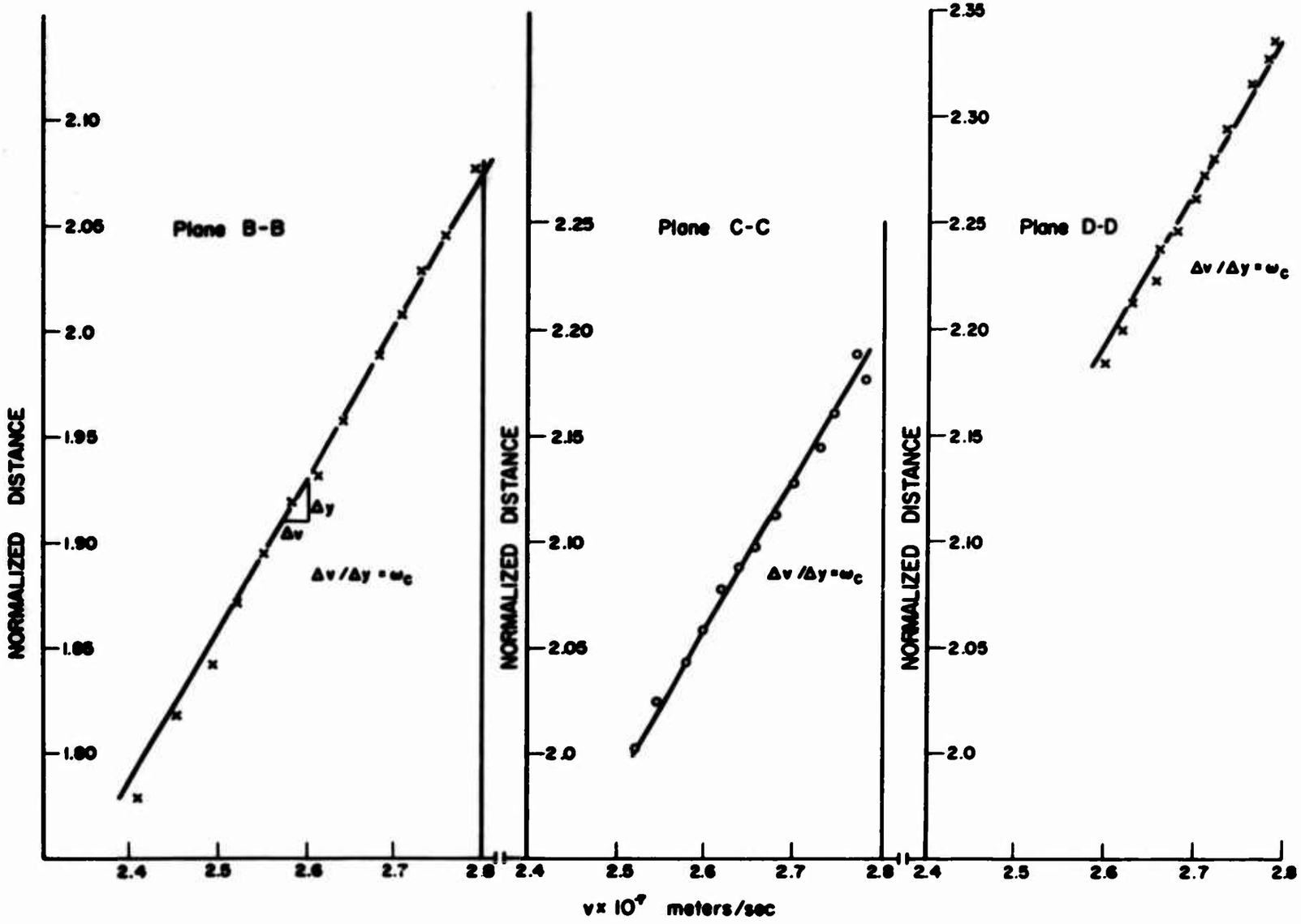

FIG. 4.10b VELOCITY VARIATION ACROSS THE BEAM AT PLANES B-B, C-C AND D-D.

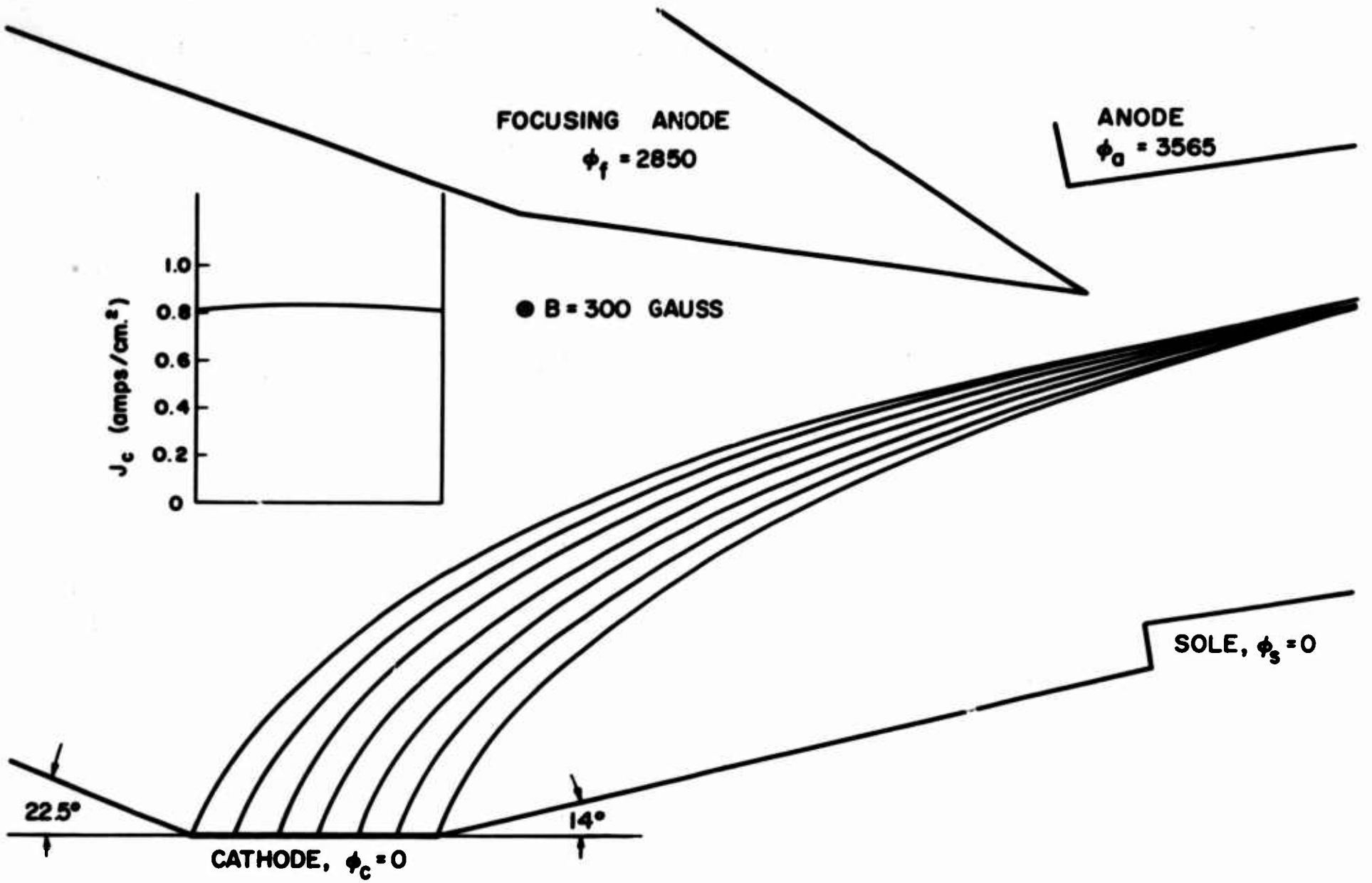

FIG. 4.11 MODIFICATION OF THE FRONT AND REAR RAMP ELECTRODES RESULTING IN NEARLY UNIFORM EMISSION FROM THE CATHODE.

trajectories were modified slightly resulting in a thinner, less laminar beam. The motion of the upper electron is such as to carry it into the beam at approximately the exit plane of the gun. The significant result of the modification, however, is the achievement of nearly uniform emission from the entire cathode. As indicated in Fig. 4.11 this current density is 0.820 amp/cm^2.

The above investigations clearly indicate that the space-charge-flow characteristics are strongly dependent on the shape of the ramp electrodes. In particular, it is possible to obtain either uniform cathode emission or nearly laminar flow simply by modifying the ramps. However, the simultaneous achievement of uniform emission and laminar flow is not possible without additional modifications involving the focusing anode structure.

One of the questions which frequently arises concerning the operation of thermionic cathodes is the effect on the electron beam when a portion of the cathode becomes incapable of emission. Utilizing the geometry of Fig. 4.10 this problem was analyzed by first considering zero emission from the front edge of the cathode (Fig. 4.12) and then from the rear edge (Fig. 4.13). In Fig. 4.12 the absence of emission from the front edge has not affected either the trajectories or the J_c values along the rear of the cathode. However, those electrons which leave the front portion of the reduced cathode are significantly modified with the trajectories being lower and the J_c values appreciably greater. Both of these results are a direct consequence of the absence of space charge from the lower edge of the original beam.

When emission from the rear edge disappears, the trajectories and cathode current densities are affected throughout the beam. This, of

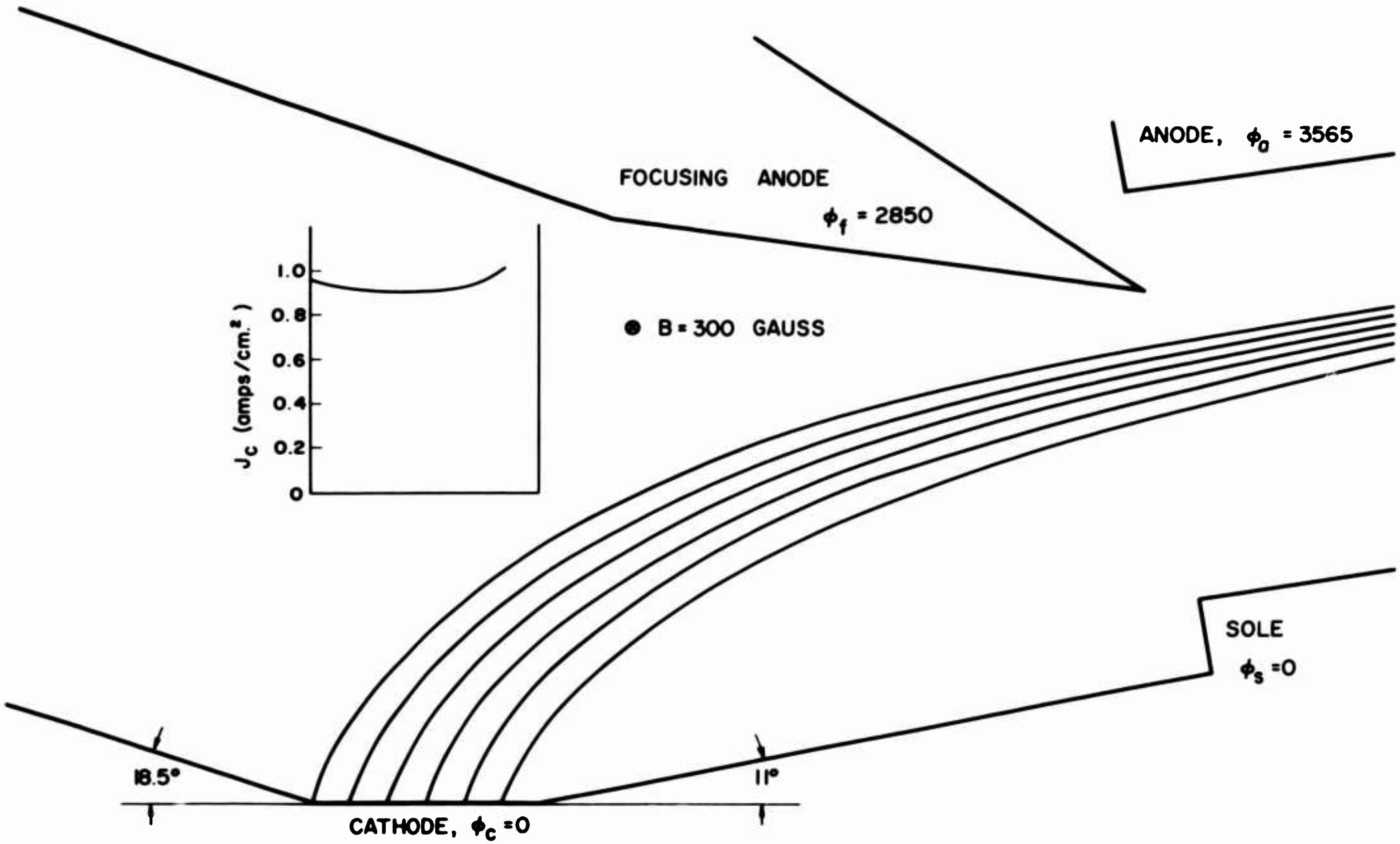

FIG. 4.12 ELECTRON TRAJECTORIES WHEN THE FRONT EDGE OF THE CATHODE IS NOT EMITTING.

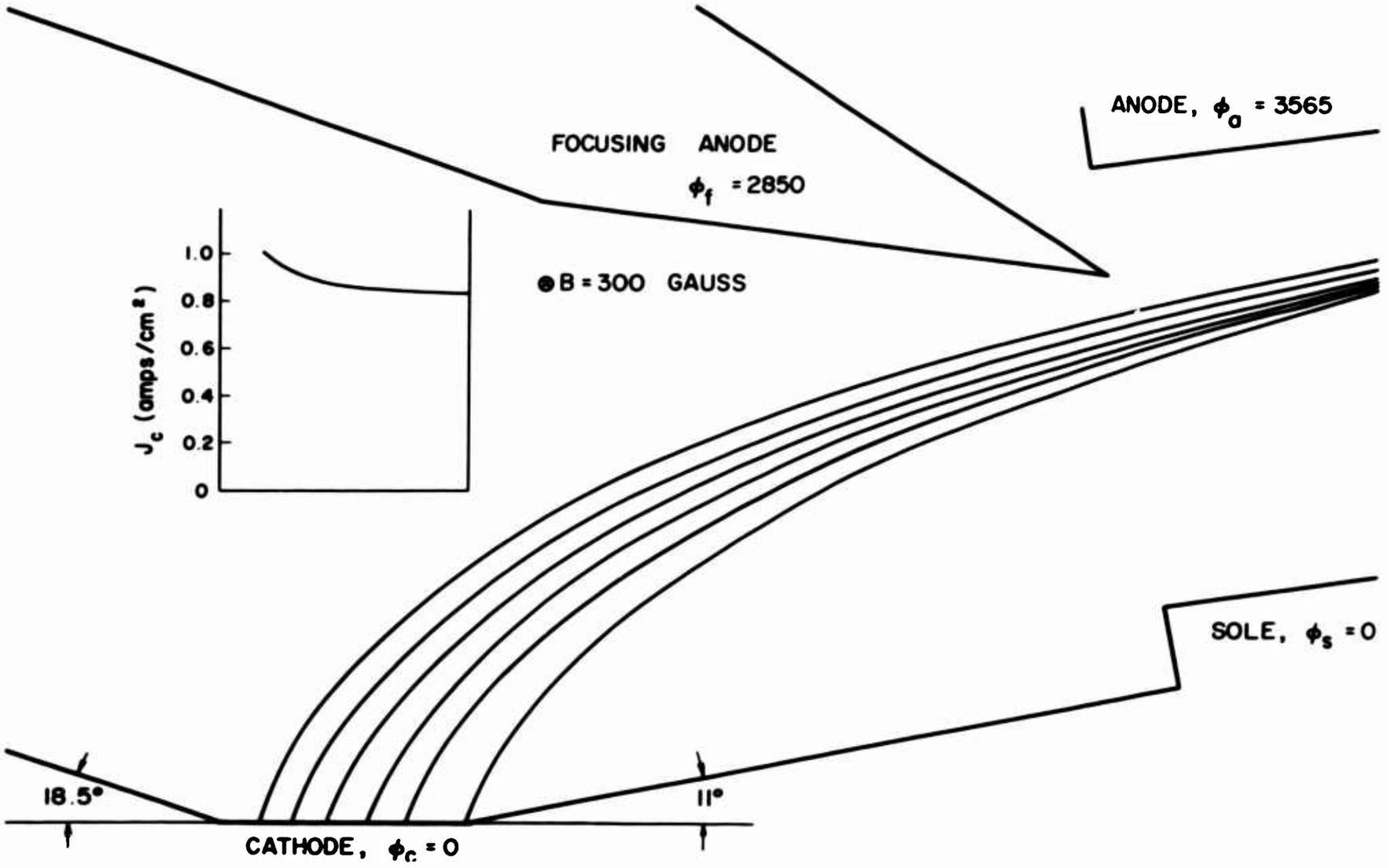

FIG. 4.13 ELECTRON TRAJECTORIES WHEN THE REAR EDGE OF THE CATHODE IS NOT EMITTING.

course, results from the fact that those electrons from the rear of the original cathode passed over the entire emitting surface. Consequently their absence causes the trajectories to be somewhat higher and more closely spaced and forces J_c to assume a maximum value on the left and decrease to a minimum on the right. However, in both Fig. 4.12 and 4.13 the beam configurations are nearly the same as the Fig. 4.10 case thus indicating that the beam optics is not appreciably affected when certain portions of the cathode become inactive.

4.4 Potential Minimum Investigations

The preceding electron beam configurations generally have been obtained based on space-charge-limited conditions at the cathode. For this situation the electrons are assumed to be emitted normal to the surface with zero initial velocity. A more accurate representation of the true physical picture requires the consideration of a potential minimum region adjacent to the cathode. This is a much more difficult problem to handle and involves the emission of electrons with finite initial velocities. In general, the thermionic emission of electrons from a heated cathode is described in terms of a Maxwellian distribution function for the initial velocities.

A digital computer analysis of the above problem involves a two-step procedure. First, the motion of the various initial velocity electrons in the potential minimum region must be evaluated. The velocity components and relative z-displacements of the electrons at a given plane beyond the potential minimum are then used as the initial conditions for the computer program which determines the electron motion in the remainder of the gun region.

The potential minimum region is simulated by assuming a voltage distribution given by

$$\varphi = \varphi_m + \left(\frac{9J_c}{4\epsilon_o \sqrt{2\eta}}\right)^{2/3} |y_m - y|^{4/3} \qquad (4.2)$$

where φ_m = voltage at the potential minimum = -0.05 volt,

y_m = distance from cathode to minimum = 1.71×10^{-6} meter, and

J_c = cathode current density = 0.887 amp/cm^2.

The gun configuration of Fig. 4.10 was selected as the model for investigation with a magnetic field of 300 gauss.

The cathode temperature was assumed to be 1100°C which resulted in an equivalent voltage of 0.12 volt. The existence of a Maxwellian velocity distribution for the electrons leaving the cathode requires the analysis of various classes of initial energy electrons. The object of such an investigation is to evaluate the effect of initial velocity on the subsequent electron trajectory.

Consider now the evaluation of electron motion corresponding to emission from the cathode in a normal direction but with different initial velocities. Figure 4.14a illustrates the trajectories in the potential minimum region for those electrons with initial energies of 0.08, 0.10, 0.12, 0.14, 0.16, 0.18 and 0.20 electron volts. The velocity components at a fixed plane (not shown) beyond the minimum are used as the initial conditions for determining the trajectories in the gun region which are shown in Fig. 4.14b. Obviously the electrons follow essentially the same trajectory and hence have approximately the same kinetic energy at a given z-plane. The only major difference in the trajectories is the time required for the electrons to travel a given distance as indicated in Fig. 4.14b. The designated points (t_1, etc.) indicate the

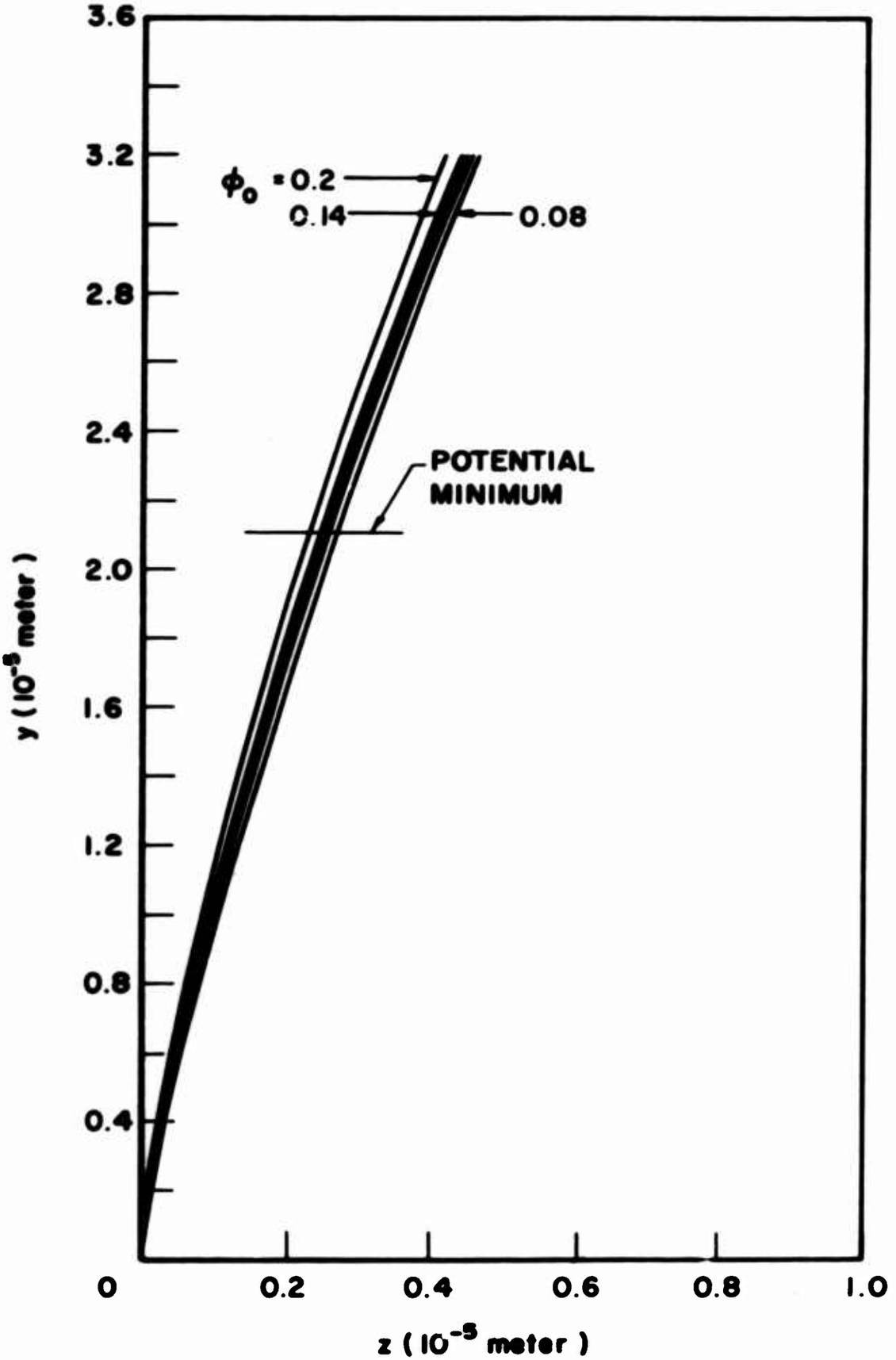

FIG. 4.14a TRAJECTORIES IN THE POTENTIAL MINIMUM REGION FOR ELECTRONS EMITTED NORMAL TO THE CATHODE WITH INITIAL ENERGY AS THE PARAMETER.

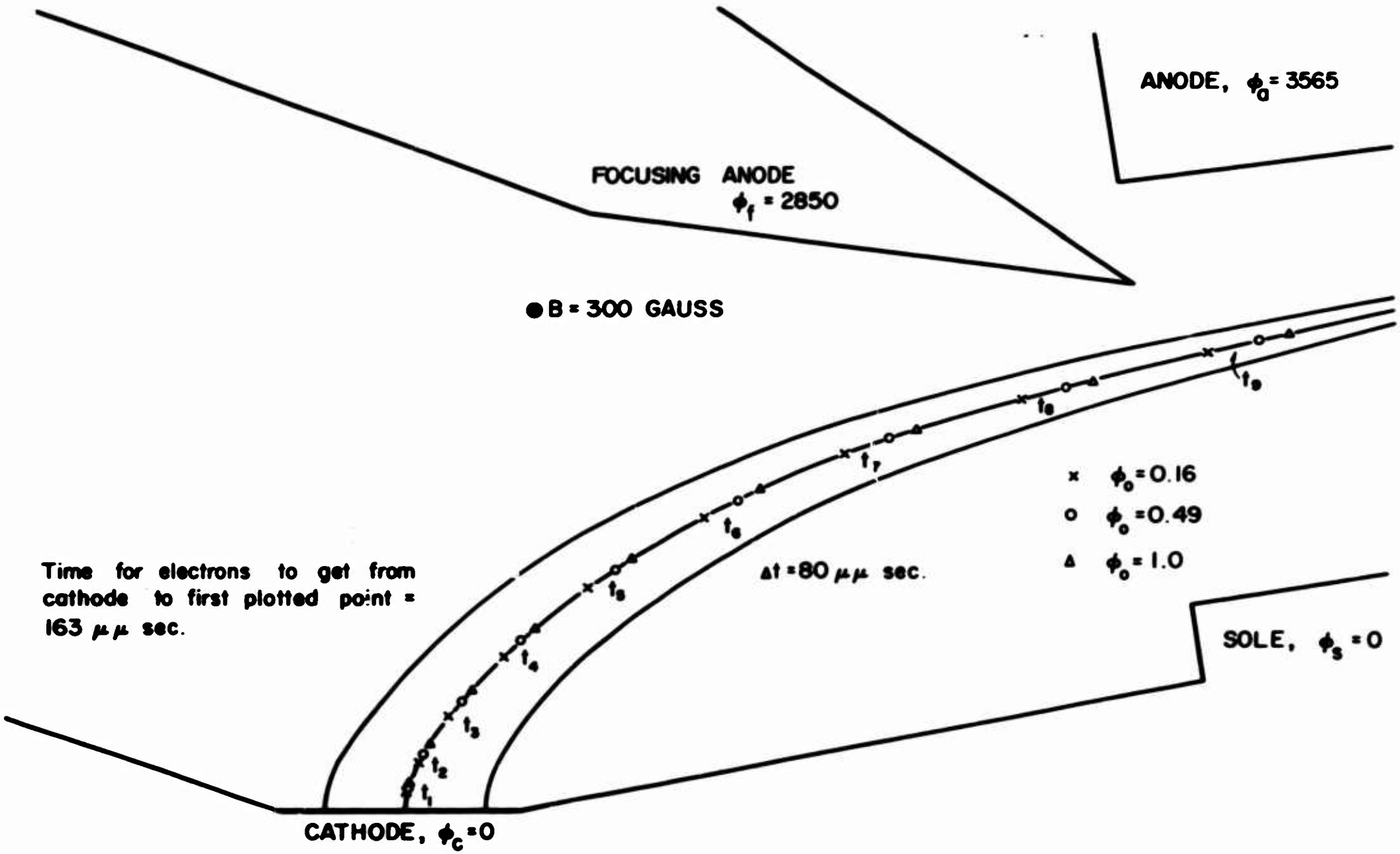

FIG. 4.14b TRAJECTORIES IN THE GUN REGION AFTER PASSAGE THROUGH THE POTENTIAL MINIMUM.

location of different initial velocity electrons at specified times after emission from the cathode. Neither the potential minimum by itself nor the existence of different normal initial velocities is capable of producing any significant changes in the electron trajectories, at least not for initial velocities which are within a factor of approximately ten times the thermal velocity.

The electrons emitted with the thermal energy of 0.12 electron volts but in different directions (-90°, -75°, -60°, -45°, -30°, -15°, 0, +15°, +30°, +45°, +60°, +75°) follow the potential minimum region trajectories indicated in Fig. 4.15. Seven of the electrons are capable of traversing the potential minimum region. In fact it is demonstrated in Appendix D that those electrons which are emitted in the range $-56° < \theta < 46°$ are all able to proceed beyond y_m. With the data obtained from the above potential minimum analysis as initial conditions (these conditions are evaluated at $y = 2.11 \times 10^{-4}$ meter which corresponds to the first matrix row of the regular gun program) the trajectories illustrated in Fig. 4.16 are obtained in the gun region. It is apparent that the presence of initial tangential velocity components is sufficient to force the electrons to travel along different trajectories. In particular, comparison of the electrons emitted in the -45° and +45° directions results in a difference of kinetic energy at plane B-B of approximately 140 volts. This is rather surprising in view of the fact that the electrons were emitted from the same cathode point and with the same value of initial kinetic energy. However, it should be emphasized that the difference in kinetic energy is due to the different location of the electrons and is not indicative of any energy exchange by the electrons.

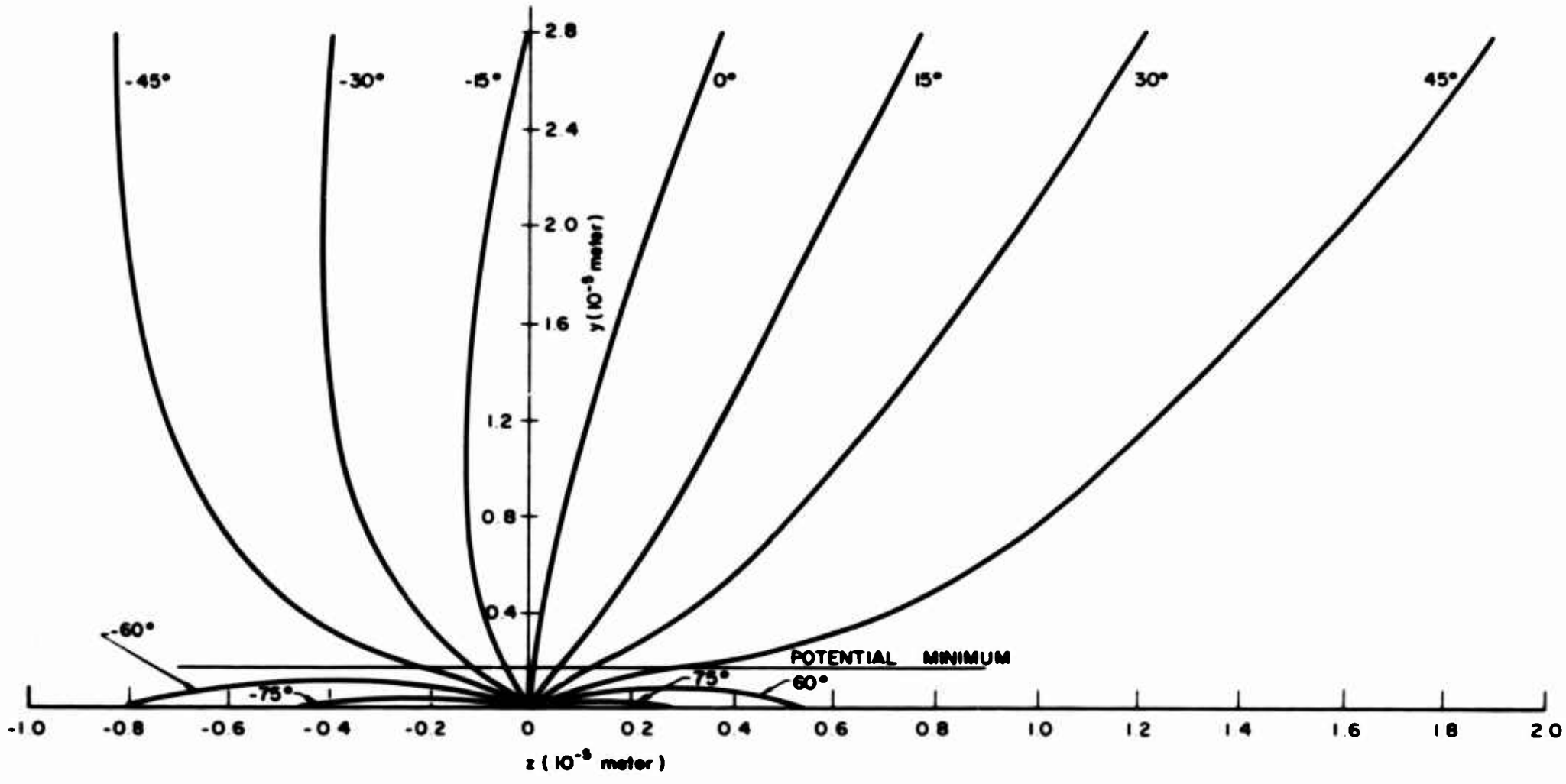

FIG. 4.15 TRAJECTORIES OF ELECTRONS EMITTED FROM THE CATHODE IN DIFFERENT DIRECTIONS BUT WITH THE SAME ENERGY. (φ_o = 0.12 VOLT)

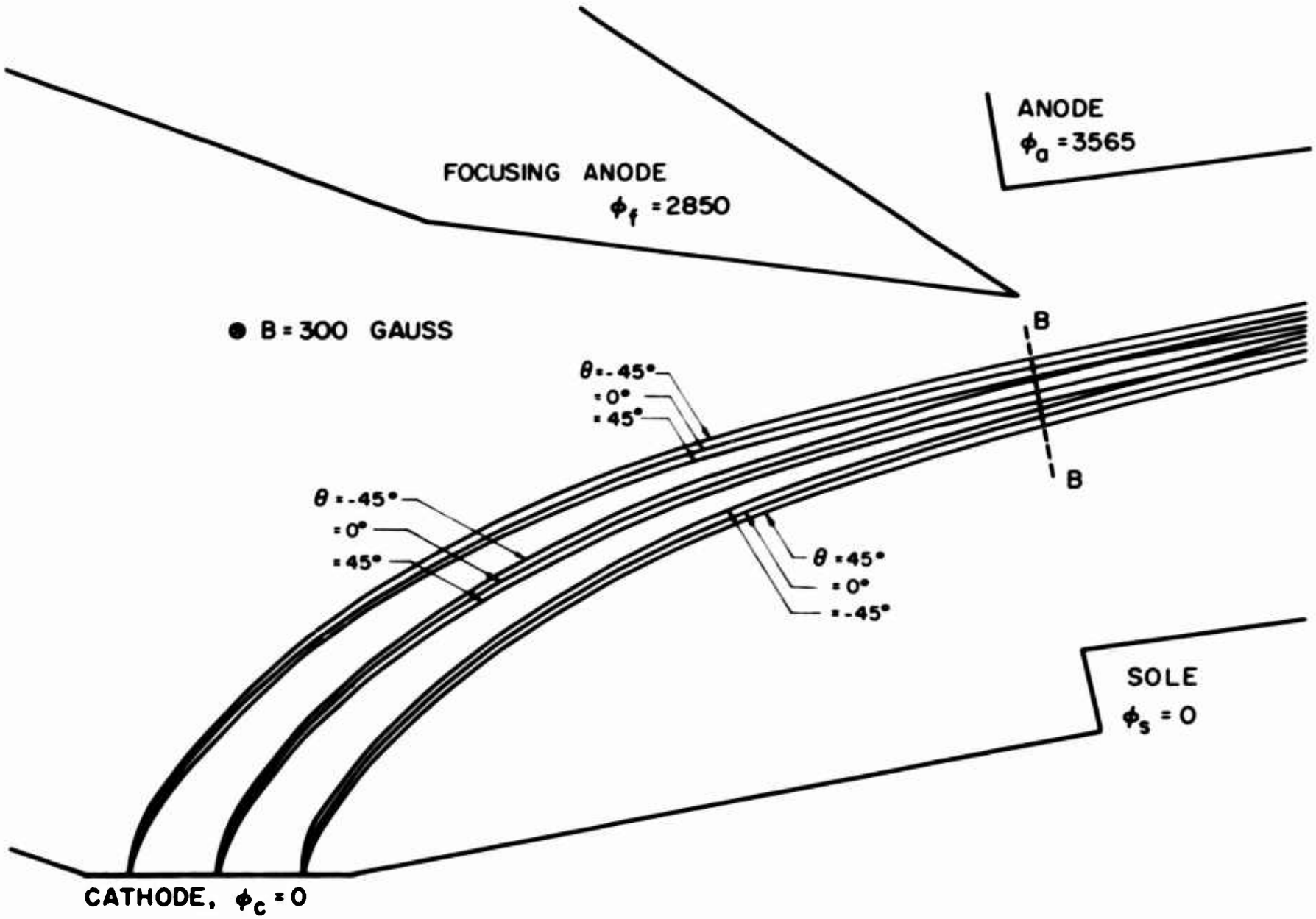

FIG 4.16 TRAJECTORIES IN THE GUN REGION FOR ELECTRONS EMITTED IN VARIOUS DIRECTIONS WITH φ_o = 0.12 VOLT.

The existence of initial tangential velocity components is also responsible for the generation of a wider beam. Comparison of the indicated beam width at plane B-B with that which would exist if only normal velocity components were present indicate that the width has been increased by nearly 35 percent.

Figures 4.17a and 4.17b illustrate the trajectories for electrons with initial energy of $\varphi_o = 0.23$ volts. The increased energy has resulted in a greater number of electrons passing through the potential minimum region. Consequently, the electrons follow even more diverse paths than in the preceding case. Calculations at plane B-B indicate that the -60° and +45° electrons now have a difference in kinetic energy of approximately 250 volts. The beam is also approximately 58 percent wider than it is when only normal initial velocity electrons are considered.

Figures 4.18a and 4.18b illustrate the effect of increasing the initial energy to $\varphi_o = 0.92$ volt. Although the trajectories are immensely different, it must be remembered that only a fraction of the electrons with a Maxwellian velocity distribution have an initial energy greater than 0.5 volt. Consequently, there are only a relatively few electrons capable of following such trajectories.

In general, as the initial energy of the electrons increases, the $\Delta\theta$ interval for which electrons can reach the potential minimum plane is increased. As the initial energy is reduced, $\Delta\theta$ decreases until only those electrons emitted in an optimum direction θ_{cr} are capable of reaching y_m when $\varphi_o = |\varphi_m|$. For the conditions being considered here, it is shown in Appendix D that $\theta_{cr} = -8.3°$.

The above results vividly demonstrate the tremendous influence of tangential emission velocity components on the electron trajectories.

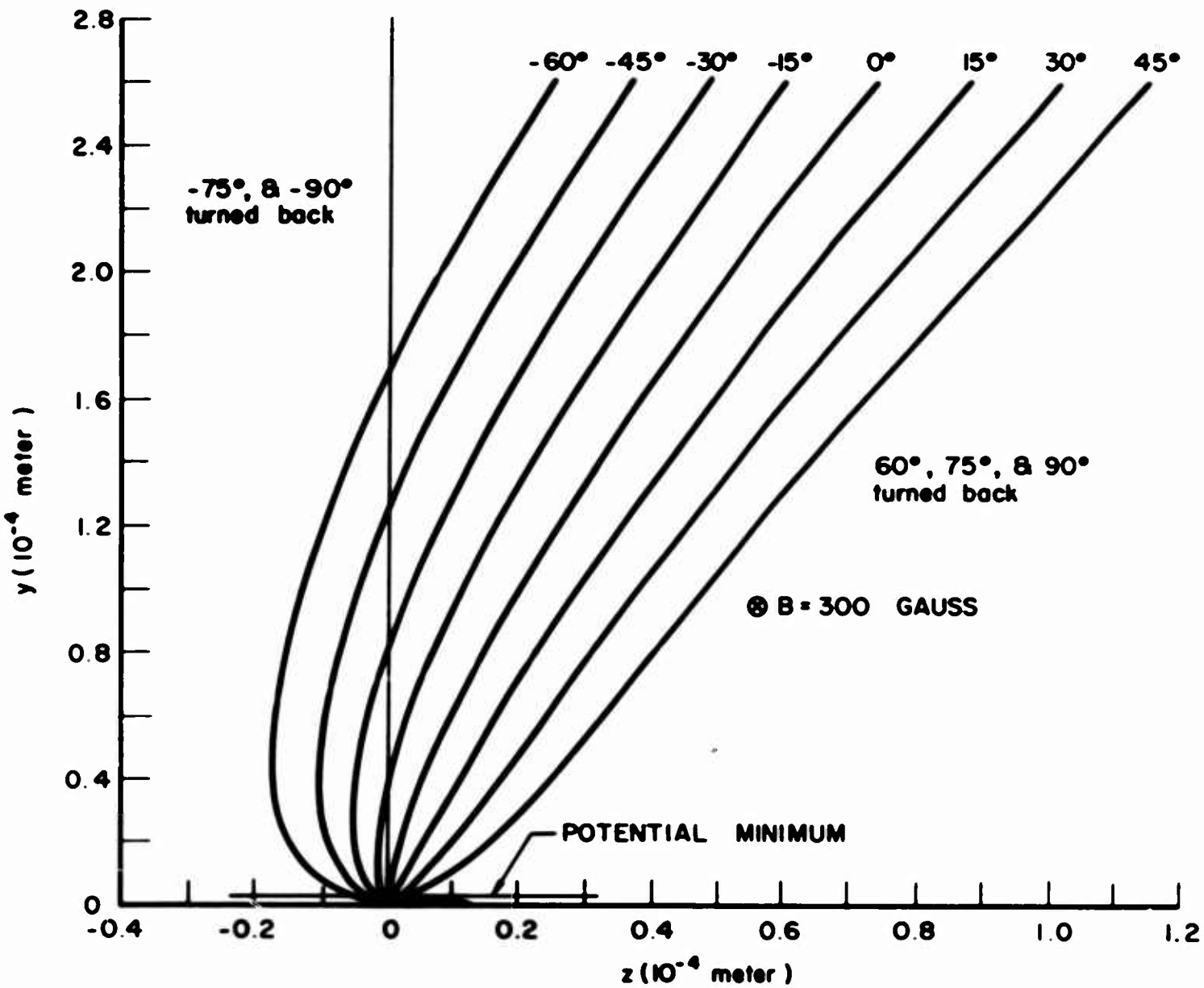

FIG. 4.17a TRAJECTORIES FOR ELECTRONS EMITTED IN DIFFERENT DIRECTIONS WITH THE ENERGY φ_o = 0.23 VOLT.

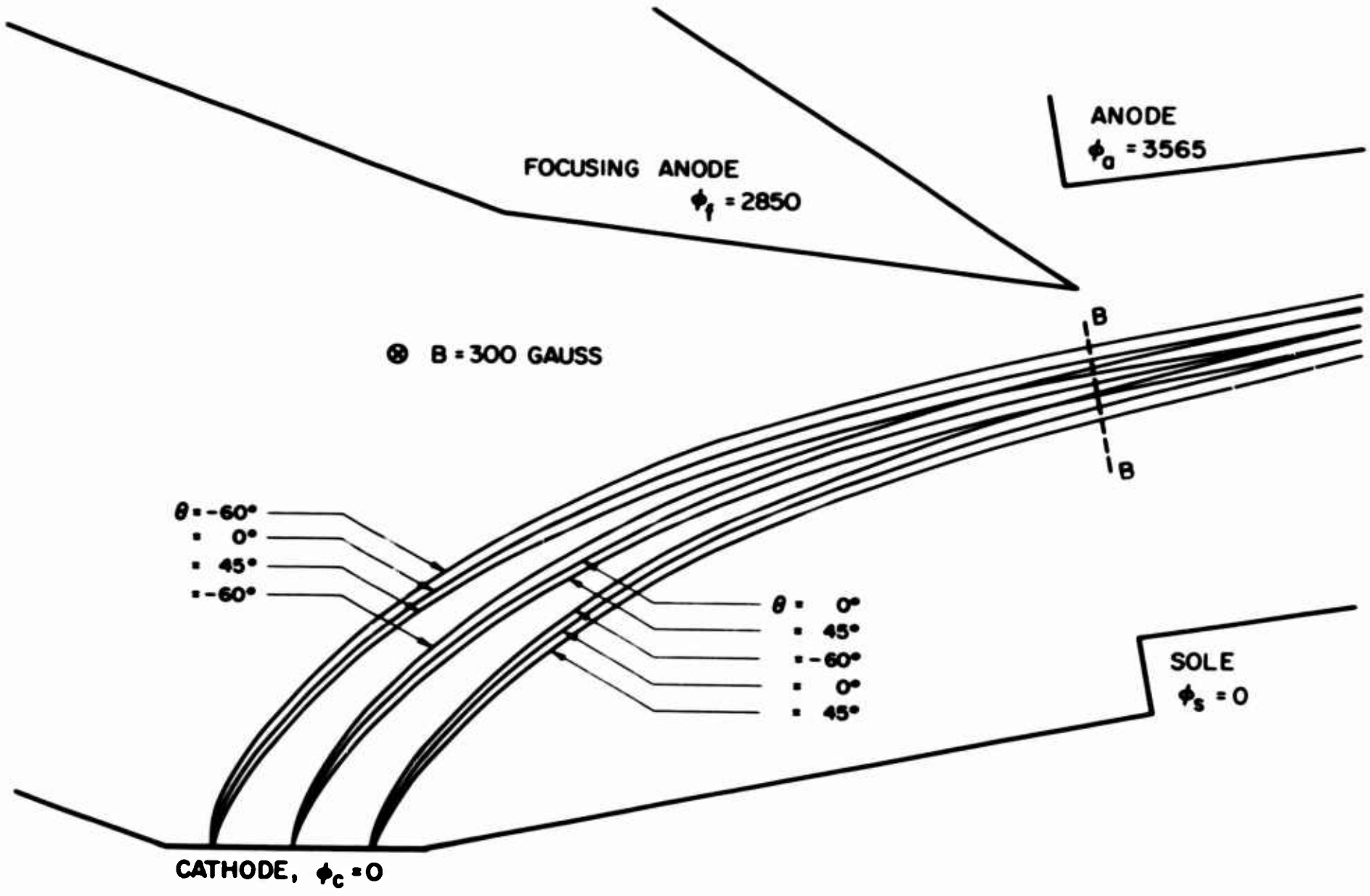

FIG. 4.17b TRAJECTORIES IN THE GUN REGION FOR ELECTRONS EMITTED IN VARIOUS DIRECTIONS WITH φ_o = 0.23 VOLT.

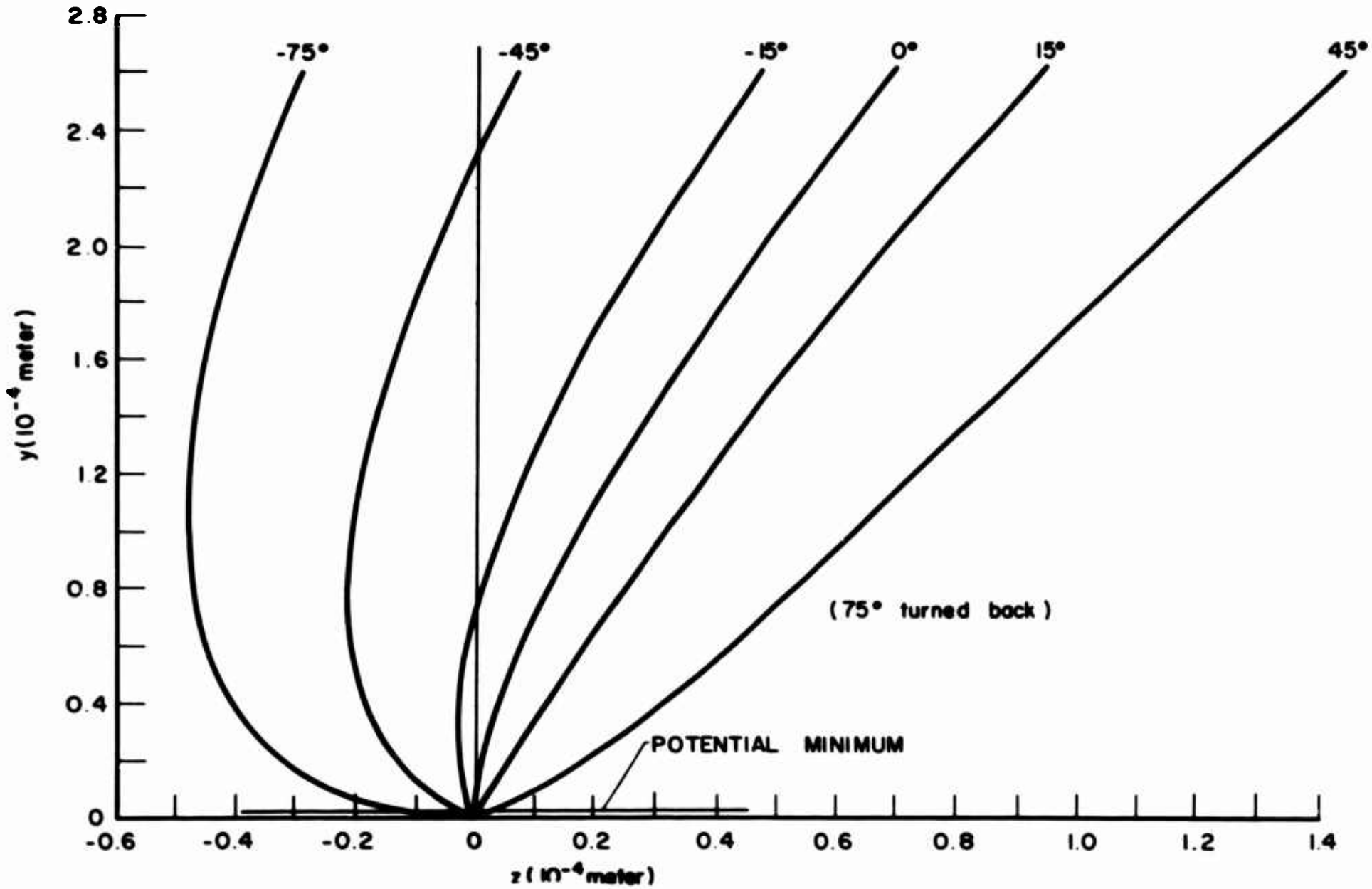

FIG. 4.18a TRAJECTORIES FOR ELECTRONS EMITTED IN DIFFERENT DIRECTIONS WITH φ_o = 0.92 VOLT.

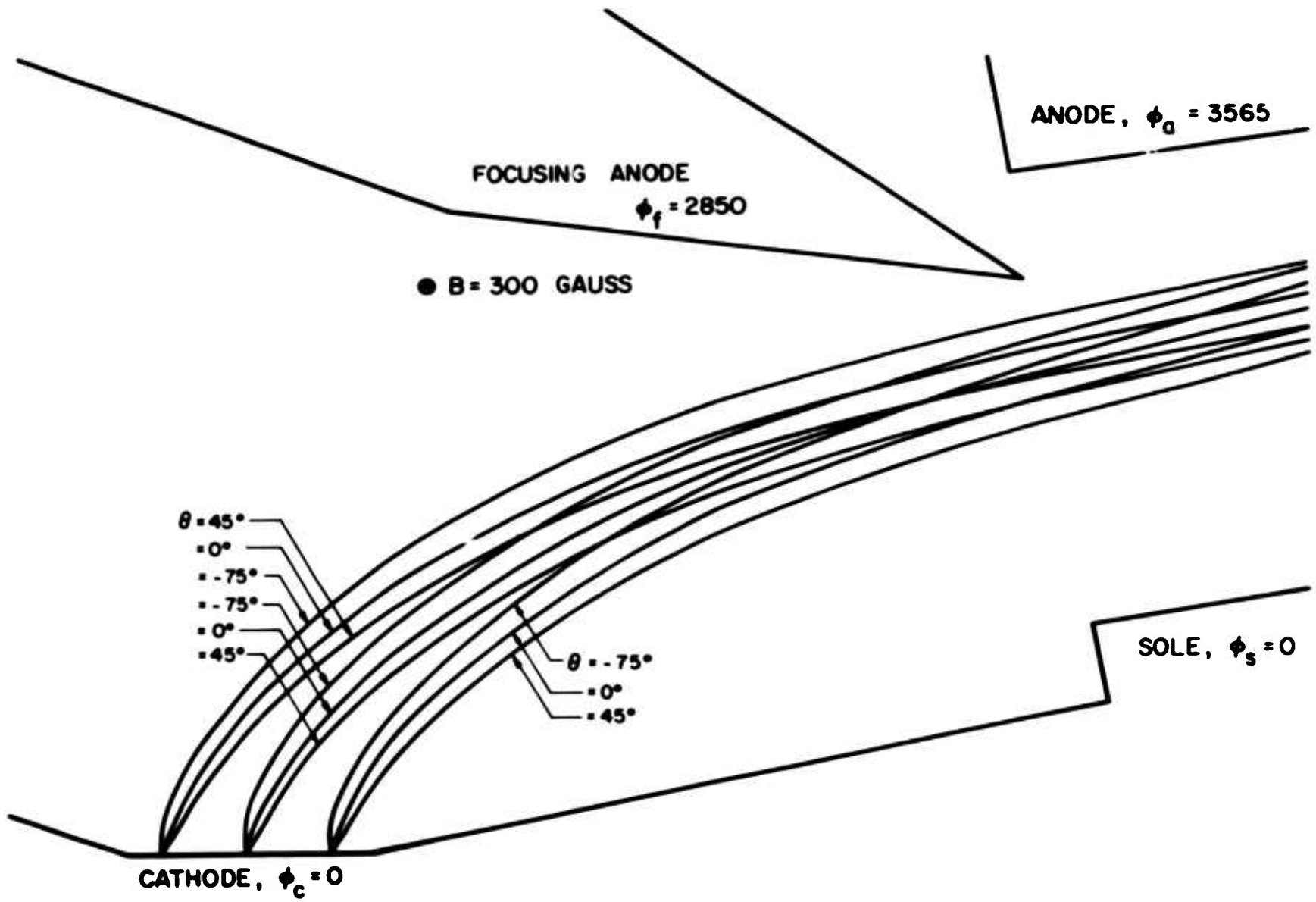

FIG. 4.18b TRAJECTORIES IN THE GUN REGION FOR ELECTRONS EMITTED IN VARIOUS DIRECTIONS WITH φ_o = 0.92 VOLT.

Whereas electrons emitted normal to the cathode all follow essentially the same trajectory (differing only in the time required to travel a given distance), those electrons with initial tangential components are capable of proceeding along completely different paths. And yet in each case, the total energy of the electron (potential energy minus kinetic energy) remains fixed at its initial value of ($|q|\varphi_o$). Thus, the difference in trajectories is not caused by an energy exchange mechanism, but rather comes about because of the difference in location and direction of motion of the different θ electrons when they reach the potential minimum plane. Of course, the spreading effect of the electron trajectories is also influenced by the depth of the potential minimum region.

A more quantitative description can be obtained if the potential in the beam is considered to be a function of the y-coordinate only (as in the Kino theory). Thus, it is possible to write

$$\frac{1}{2} m \dot{y}^2 = |q|\varphi(y) - \frac{1}{2} m \omega_c^2 y^2 + \frac{1}{2m} p_{y_o}^2 - \omega_c y \, p_{z_o} \quad , \qquad (4.3)$$

where p_{y_o} and p_{z_o} are the initial values of the linear momentum components at the cathode given by

$$p_{y_o} = m \dot{y}_o \quad ,$$

and

$$p_{z_o} = m \dot{z}_o \quad . \qquad (4.4)$$

Equation 4.3 is simply the energy equation which can be derived from the Hamiltonian formulation presented in Chapter V. The difference in the y-component of kinetic energy caused by initial tangential

velocities appears in the last term, $\omega_c\, y\, p_{z_o}$. Thus, at a fixed y-plane, electrons will have different $\dot{y}$ depending on the magnitude and sign of p_{z_o}. However, if one assigns typical values to y and p_{z_o} the results indicate very little difference in the corresponding $\dot{y}$ values. In fact, as mentioned above, the difference at any point will only be given by the difference in the φ_o of the electrons at the cathode. This is simply another statement of the fact that the initial thermal energy is inconsequential when compared with the total energy of an electron at a given point remote from the cathode. The true importance of the initial tangential velocity is the appreciable change which it imposes on the electron trajectory.

The significance of tangential emission velocity components has been pointed out by Twiss[34] and Lindsay[21] in earlier investigations. Twiss analyzed the linear magnetron and showed that the tangential velocities exerted a much greater influence on the electrons than did the normal velocity components. Lindsay has suggested that the excess anode current observed in a magnetron operating beyond cut-off can be at least partially explained in terms of the initial tangential velocity effects. In other words, he contends that it is not necessary for an electron to gain energy in order to reach the anode of a cut-off magnetron. This conclusion is supported by the above computer studies which show that electrons emitted in different directions are capable of reaching greater distances from the cathode. Thus, for the situation in Fig. 4.17, the electrons emitted in the -60° direction would be capable of reaching the anode of a magnetron which is appreciably beyond cut-off even though they would not have gained any energy beyond that which they had upon emission from the cathode. Consequently, as Lindsay suggests, it is indeed possible for a cut-off magnetron to theoretically

receive current even though energy is conserved. The mechanism which allows this is the sorting of electrons by the potential minimum region so that electrons are able to follow completely different trajectories. However, the magnitude of excess current which can be explained by this mechanism is difficult to predict.

The initial velocity effects also indicate why it is theoretically impossible to achieve a Brillouin beam from a thermionic cathode. In other words, electrons passing through a common point in the interaction region may have velocities which differ according to their thermionic emission energies. For emission normal to the cathode, however, the beam would still be very close to the theoretical Brillouin flow since the emission energies are small compared to the velocities in the beam. For this case, the electron trajectories are essentially the same. However, the presence of tangential components of initial velocity result in much wider beams because of the appreciable difference in electron trajectories. The space-charge density probably tapers off gradually from the value in the main body of the electron stream, thus resulting in poorly defined beam boundaries in the interaction region.

CHAPTER V. ELECTRON BEAM CHARACTERISTICS IN THE ANODE-SOLE REGION

5.1 Introduction

The d-c characteristics of an electron beam moving through the anode-sole region of a crossed-field device are dependent on the manner in which the electrons enter the region. For example, the achievement of rectilinear flow requires that the electrons enter moving parallel to the electrodes, and that there is a constant space-charge density in the beam as well as a linear velocity variation across the beam. It is also necessary that the beam be properly located with respect to the anode and sole electrodes.

When the ideal entrance conditions are not satisfied, the electrons deviate from linear trajectories. The more complicated motion is usually of an undulatory nature with variations occurring at approximately the cyclotron frequency. When space-charge effects are negligible, the motion of the electrons through the interaction region can be described analytically once the entrance conditions are specified. However, when space-charge effects are appreciable it is no longer possible, in general, to describe the motion of the individual particles. In many cases, however, it is possible to obtain a qualitative description of the beam in this region.

The purpose of this chapter is to present the basic equations which describe the behavior of charged particles in crossed electric and magnetic fields. These results are then applied to the investigation of theoretical electron beam configurations which can exist in the anode-sole region of a planar M-type device.

5.2 Electron Motion in the Anode-Sole Region

The motion of electrons can be conveniently expressed in terms of the Lagrangian for a charged particle in an electromagnetic field,

$$L = \frac{1}{2} m \vec{v} \cdot \vec{v} - q \varphi + q \vec{A} \cdot \vec{v} \quad , \tag{5.1}$$

where $\vec{v}$ = electron velocity,

φ = electric scalar potential, and

$\vec{A}$ = magnetic vector potential defined by $\nabla \times \vec{A} = \vec{B}$.

In the derivation of this expression it is assumed that the force field acting on the electrons is conservative.

The component equations of motion are derived from the Lagrange equations

$$\frac{d}{dt}\left(\frac{\partial L}{\partial \dot{q}_i}\right) - \frac{\partial L}{\partial q_i} = 0 \quad , \tag{5.2}$$

where q_i represents any one of the generalized coordinates. The present investigation is concerned with the behavior of electrons in the crossed-field device illustrated in Fig. 5.1. The analysis will be restricted to two dimensions so that the variation of quantities in the x-direction will be ignored. The magnetic field is uniform in the x-direction, $\vec{B} = \hat{x}\, B$, and thus

$$\vec{A} = \hat{z}\, B\, y \quad , \tag{5.3}$$

where A has been arbitrarily selected as zero at the cathode, $y = 0$. The expression for the electric potential (φ) depends on the space-charge density and generally is a function of both y and z. Therefore the Lagrangian is given by

$$L = \frac{1}{2} m (\dot{y}^2 + \dot{z}^2) - q\, \varphi(y,z) + q\, B\, y\, \dot{z} \tag{5.4}$$

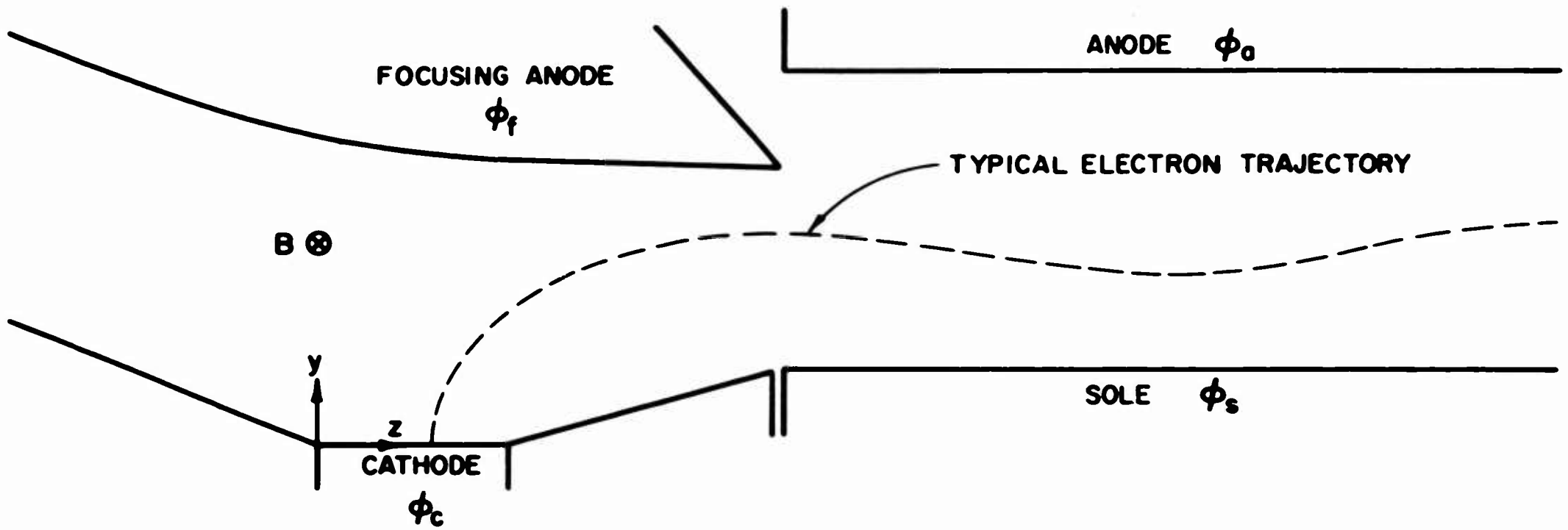

FIG. 5.1 TYPICAL CROSSED-FIELD INJECTED-BEAM DEVICE.

and Eq. 5.2 becomes

$$m\ddot{y} = -q\frac{\partial\varphi}{\partial y} + qB\dot{z} \tag{5.5}$$

and

$$m\ddot{z} = -q\frac{\partial\varphi}{\partial z} - qB\dot{y} \quad . \tag{5.6}$$

These are simply the components of the Lorentz force equation for an electron moving through a crossed electric and magnetic field region. The difficulty in obtaining analytic solutions arises because $\partial\varphi/\partial y$ and $\partial\varphi/\partial z$ cannot be evaluated until the problem is solved; i.e., φ depends on the space-charge density which in turn depends on the trajectories of the electrons comprising the flow. Consequently the solution to Eqs. 5.5 and 5.6 must be consistent with the potential distribution. In general this requires the use of a system similar to the Poisson cell described in Chapter III.

Although an analytic expression for the electron motion is not possible in most cases, it is possible to obtain a qualitative description of the beam by expressing the problem in the Hamiltonian formulation. The Hamiltonian is defined as

$$H(p_i, q_i, t) = \sum_i \dot{q}_i p_i - L(q_i, \dot{q}_i, t) \quad , \tag{5.7}$$

where p_i is the generalized momentum of the particle in the q_i direction and defined as

$$p_i \triangleq \frac{\partial L}{\partial \dot{q}_i} \quad .$$

Although the value of H is invariant, the proper formulation of the Hamiltonian requires that the $\dot{q}_i$ not appear explicitly but that they be

expressed in terms of p_i and q_i. A description of the electron motion is provided by the canonical equations of Hamilton

$$\dot{q}_i = \frac{\partial H}{\partial p_i} \tag{5.8}$$

and

$$-\dot{p}_i = \frac{\partial H}{\partial q_i} \quad . \tag{5.9}$$

Whereas the Lagrangian method gives n differential equations of the second order, the Hamiltonian formulation yields 2n equations of the first order. (For the two-dimensional case being considered here, n = 2.)

For the configuration of Fig. 5.1 the Hamiltonian can be written as

$$H = \frac{1}{2m}(p_y^2 + p_z^2) - \frac{q}{m} B\, y\, p_z + \frac{1}{2m}(q\, B\, y)^2 + q\, \varphi(y,z) \quad . \tag{5.10}$$

Differentiating according to Eqs. 5.8 and 5.9 gives

$$\dot{p}_y = -q \frac{\partial \varphi}{\partial y} + q\, B\, \dot{z} \quad , \tag{5.11}$$

$$\dot{p}_z = -q \frac{\partial \varphi}{\partial z} \quad , \tag{5.12}$$

$$\dot{y} = \frac{p_y}{m} \quad , \tag{5.13}$$

and

$$\dot{z} = \frac{p_z}{m} - \frac{q}{m} B\, y \quad . \tag{5.14}$$

Forming the square of Eqs. 5.13 and 5.14 and differentiating with respect to time gives

$$\frac{d}{dt}\left[(p_y)^2 + (p_z - q\, B\, y)^2\right] + \frac{d}{dt}(2\, q\, \varphi) = 0 \quad , \tag{5.15}$$

which implies

$$\frac{1}{2m}\,[p_y^2 + (p_z - q\,B\,y)^2] + q\,\varphi(y,z) \;=\; C_1 \quad , \tag{5.16}$$

where C_1 = constant.

The left-hand side of this last equation is simply H as given by Eq. 5.10. Thus for a conservative system

$$H\,(y,\,z,\,p_y,\,p_z,\,t) \;=\; \text{constant} \tag{5.17}$$

along any given trajectory. In this case it is also true that H is equal to the total energy of the electron at any point. (The equivalence of the Hamiltonian and total energy is valid in any case where the potential energy of the particle is independent of the velocity.)

If an electron enters the anode-sole region at y_o with $p_{y_o} \neq 0$ and $p_{z_o} \neq 0$, then

$$\frac{1}{2m}\,[p_y^2 + (p_z - q\,B\,y)^2] + q\,\varphi = C_1 \tag{5.18}$$

throughout this region. If the beam enters with exactly the Brillouin conditions, then $p_{y_o} = 0$ and the electron will move along the $y = y_o$ plane where the potential is φ_o. Thus the velocity becomes

$$\dot{z} \;=\; \omega_c y_o + \text{constant} \quad , \tag{5.19}$$

which is the familiar linear velocity variation across a rectilinear Brillouin beam.

If the beam does not enter with the proper conditions then the only statement which can be made is that the total energy (H) remains invariant along an electron trajectory. This implies that the beam

undergoes undulatory motion so that for each electron y, p_y, p_z, and φ vary along the trajectory.

Investigation of regular electron beams (i.e., those in which an electron at a given point can have only one velocity) leads to the Lagrange invariant

$$\oint \vec{p} \cdot d\vec{s} = \text{constant} \quad . \tag{5.20}$$

This states that the circulation of the total momentum around a closed path encircling the beam remains invariant along the beam. The most interesting consequence of this theorem is that of an irrotational electron beam in which

$$\nabla \times \vec{p} = 0 \quad . \tag{5.21}$$

Gabor[35] has shown that the only requirement for irrotationality is that there be no magnetic field normal to the cathode. If this condition is fulfilled, as it is in crossed-field devices, then at any point in the beam Eq. 5.21 will be valid.

For the injected-beam device this leads to the expression

$$\frac{\partial p_z}{\partial y} - \frac{\partial p_y}{\partial z} = 0 \quad , \tag{5.22}$$

or

$$\frac{\partial \dot{z}}{\partial y} - \frac{\partial \dot{y}}{\partial z} = \omega_c \quad . \tag{5.23}$$

Once again the Brillouin condition of $\dot{y} = 0$ gives a z-velocity variation of ω_c across the beam. However, when the beam is not rectilinear ($\dot{y} \neq 0$) it is the difference in the y-and z-velocity variations which equals ω_c. Thus the $\dot{z}$-variation across the beam will be either

greater or less than ω_c depending on whether the beam is decelerating or accelerating in the y-direction.

If Eq. 5.23 is written in vector notation it becomes

$$\nabla \times \vec{v} = \hat{x}\,\omega_c \quad . \tag{5.24}$$

If $\dot{y} = 0$, the situation is as shown in Fig. 5.2a where

$$\nabla \times \vec{v} = \nabla \times (\hat{z}\,\dot{z}) = \hat{x}\,\frac{\partial \dot{z}}{\partial y} \tag{5.25}$$

so that $\partial\dot{z}/\partial y = \omega_c$ as before. However, if $\dot{y} \neq 0$, then the situation is illustrated by Fig. 5.2b whereby

$$\nabla \times \vec{v} = \hat{x}\,\frac{\partial v}{\partial n} \tag{5.26}$$

and $\hat{n}$ is the unit vector normal to the velocity vector of the electron. Therefore $\partial v/\partial n = \omega_c$ and the condition of irrotational flow requires that the relative slip or velocity variation across the beam must be ω_c. This relationship has also been indicated by Buneman[36] in his work on crossed-field space-charge flows.

The force Eqs. 5.5 and 5.6 can be written as

$$\frac{d\dot{y}}{dt} = \eta\,\frac{\partial \varphi}{\partial y} - \eta\,B\,\dot{z} \tag{5.27}$$

and

$$\frac{d\dot{z}}{dt} = \eta\,\frac{\partial \varphi}{\partial z} + \eta\,B\,\dot{y} \quad . \tag{5.28}$$

Differentiation of Eqs. 5.27 and 5.28 with respect to y and z respectively, results in

$$\nabla \cdot \frac{d\vec{v}}{dt} = \eta\,\nabla^2\varphi + \omega_c\left(\frac{\partial \dot{y}}{\partial z} - \frac{\partial \dot{z}}{\partial y}\right) \quad . \tag{5.29}$$

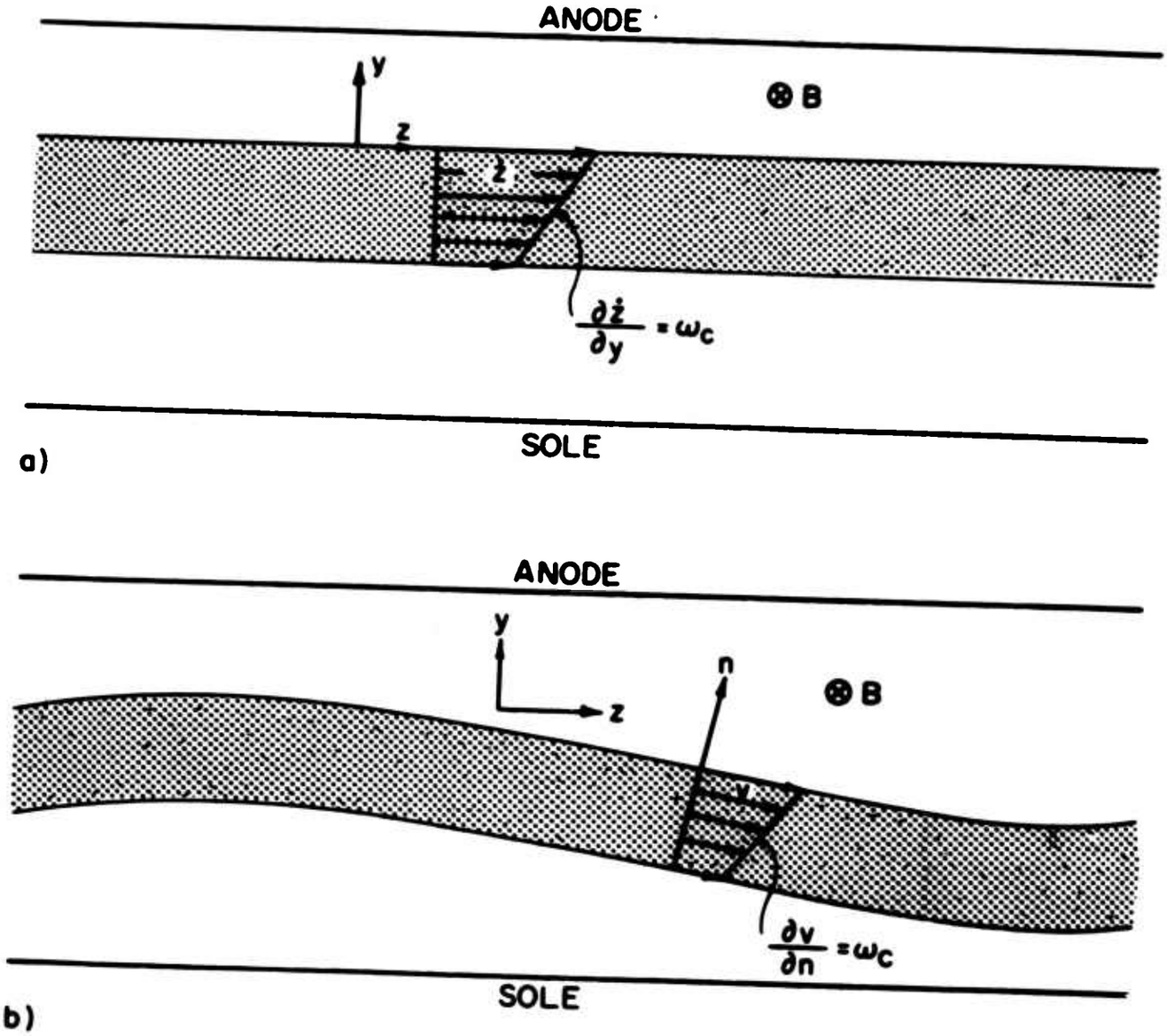

FIG. 5.2 ILLUSTRATIONS OF VELOCITY VARIATION ACROSS IRROTATIONAL ELECTRON STREAMS.

(a) RECTILINEAR FLOW.

(b) UNDULATING BEAM.

Equation 5.23 and Poisson's equation are then used to give

$$\rho = -\frac{\epsilon_o \omega_c^2}{\eta} - \nabla \cdot \frac{d\vec{v}}{dt} \quad . \tag{5.30}$$

This is the space-charge density which an observer moving with the electron sees at each point along the trajectory.

The current density is

$$\vec{J} = \rho \vec{v} \tag{5.31}$$

while the continuity equation requires

$$\nabla \cdot \vec{J} = 0 = \rho \nabla \cdot \vec{v} + \vec{v} \cdot \nabla \rho \quad . \tag{5.32}$$

Therefore

$$\nabla \cdot \vec{v} = -\frac{\vec{v} \cdot \nabla \rho}{\rho} \tag{5.33}$$

so that Eq. 5.30 becomes

$$\rho = -\frac{\epsilon_o \omega_c^2}{\eta} + \frac{d}{dt}\left(\frac{\vec{v} \cdot \nabla \rho}{\rho}\right) \quad . \tag{5.34}$$

If the space-charge density observed during the electron motion is constant, then the last term becomes zero and

$$\rho = -\frac{\epsilon_o \omega_c^2}{\eta} \quad . \tag{5.35}$$

Consequently, if the beam is to have a constant space-charge density throughout the interaction region (regardless of whether the beam moves linearly or undulates) its value must be precisely the Brillouin value as given by Eq. 5.35.

It should be emphasized that the preceding analysis has been concerned only with regular electron beams in which there is a unique

velocity associated with each point in the beam. Furthermore, the fields have been assumed to be conservative so that there is no energy gained or lost by individual electrons during their motion.

The analysis of multi-velocity electron streams (i.e., more than one velocity possible at a given point) requires the application of a method similar to the one utilized by Hok[37]. In his analysis the current density component in a given direction is given by

$$J_z = -q \int_u \rho \, u_z \, du = -q \, \rho_r \, \bar{u} \quad , \tag{5.36}$$

where $\rho(y,z,u_y,u_z,t) \triangleq$ electron density in 4 dimensional μ-space, (the variation in the x-direction has been assumed to be negligible and u_x has been chosen as zero),

$du = du_y \, du_z$ = velocity volume element,

$\bar{u}$ = expected value of electron velocity at (y,z,t), and

$\rho_r(y,z,t) = \int_u \rho \, du$ = space-charge density at (y,z,t).

This problem, of course, is much more difficult to handle. For example, the continuity equation of the single-velocity theory is replaced by the Boltzmann transport equation. It is not the intention to carry out the analysis, but only to indicate the procedure for such an investigation.

5.3 Electron Beam Configurations in the Anode-Sole Region

One of the problems of crossed-field devices is the determination of the various beam configurations which can exist in the anode-sole region. The following investigation qualitatively considers the possibility of achieving certain beam configurations.

Figure 5.3 illustrates two examples of scalloped beams moving through the interaction region. These beams have been analyzed by Waters[14] who applied a paraxial analysis based on small amplitude departures from the Brillouin flow conditions. In Fig. 5.3a the electrons all enter the region parallel to the anode and sole electrodes but with a space-charge density less than the Brillouin value. The paraxial method indicates that the beam boundary is scalloped such that the average space-charge density is equal to the Brillouin value, $\omega_p = \omega_c$. Figure 5.4 illustrates the potential variation across the beam at the planes of maximum and minimum thickness as well as the Brillouin potential distribution. The Brillouin beam would be located between planes y_2 and y_5 whereas the entering beam is located between y_1 and y_6 and the minimum thickness beam between y_3 and y_4. The electrons on the upper boundary of the entering beam have a velocity $\dot{z} = (2\eta\varphi_6)^{1/2}$ which is greater than the velocity of the corresponding electrons in the Brillouin beam $\dot{z} = (2\eta\varphi_5)^{1/2}$. Since the electric field at the upper edge of the entering beam is less than at the corresponding Brillouin beam boundary, these electrons must curve downward due to the greater magnetic force, $(q\,B\,\dot{z})$. The opposite conditions exist at the lower edge of the beam so that these electrons must move upward. Thus the beam is compressed until the space-charge density becomes great enough to spread the beam apart. This occurs at the minimum thickness where the potential distribution is such that the top electrons are forced up while the lower electrons move downward. The net result is the scalloped pattern described above.

The beam in Fig. 5.3b enters with an excess space-charge density and thus is forced to spread apart until reaching a maximum thickness.

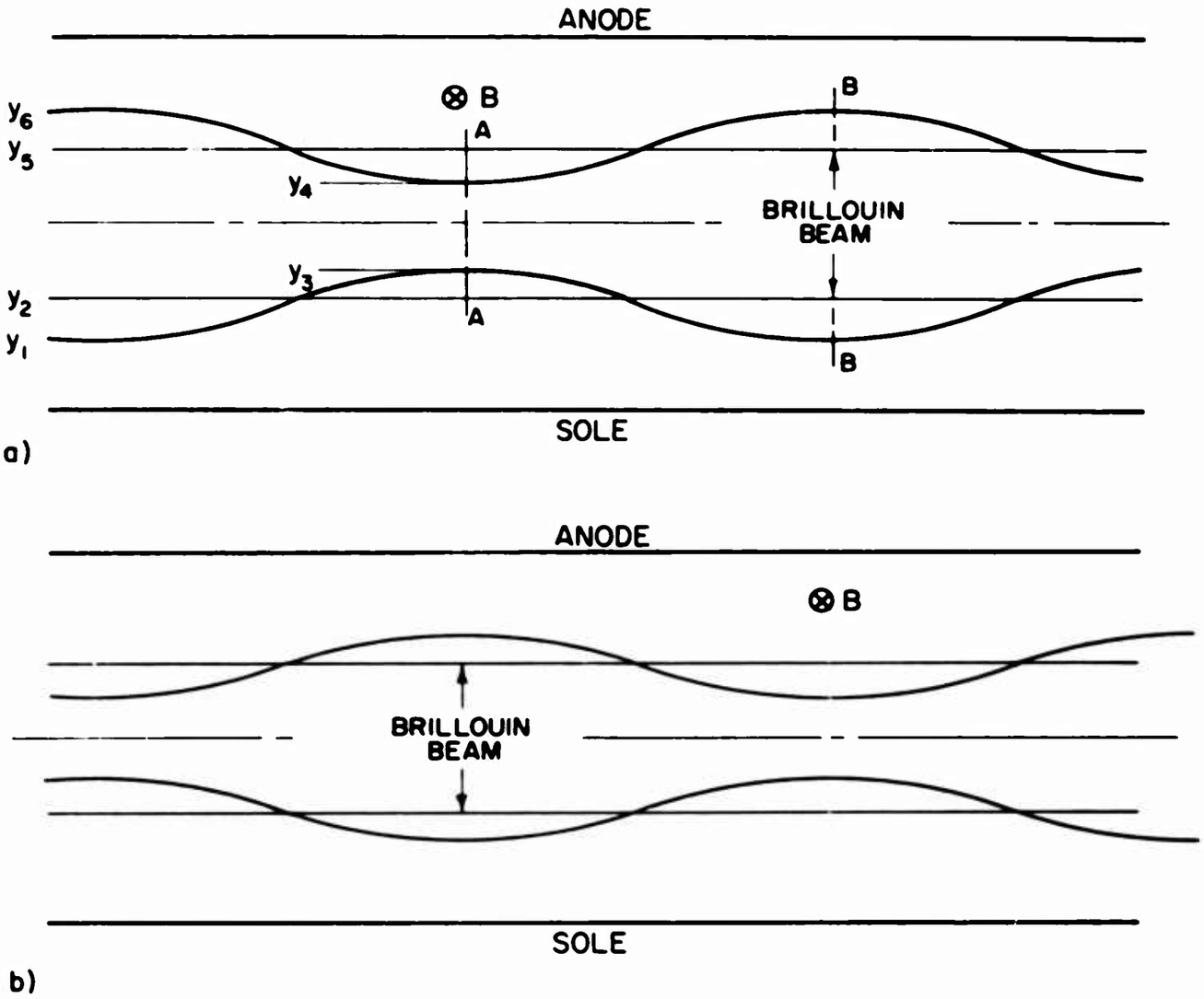

FIG. 5.3 SCALLOPED ELECTRON BEAM CONFIGURATIONS.

(a) CURRENT DENSITY AT INJECTION PLANE IS TOO SMALL.

(b) CURRENT DENSITY AT INJECTION PLANE IS TOO LARGE.

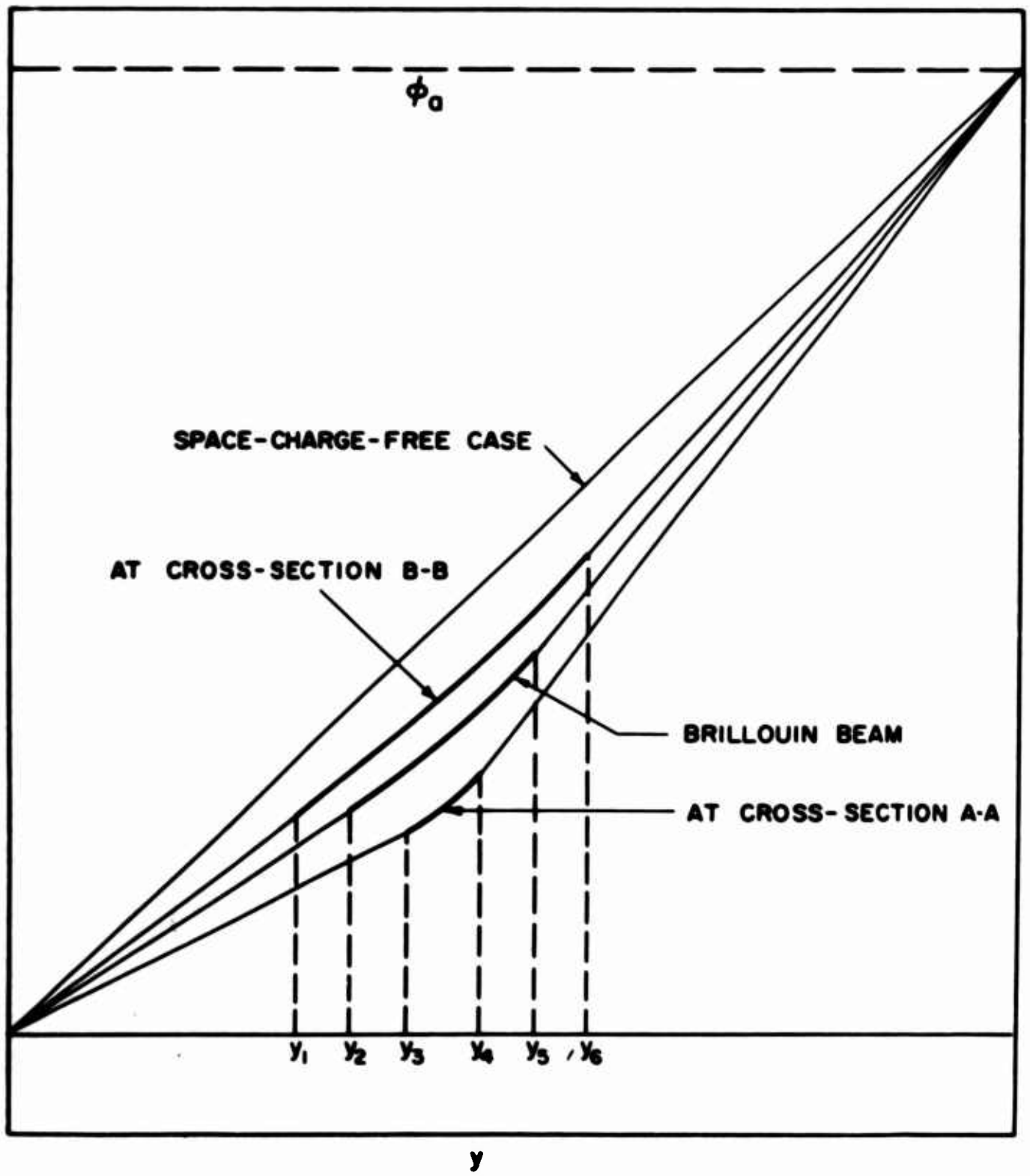

FIG. 5.4 POTENTIAL VARIATIONS FOR VARIOUS BEAM CONFIGURATIONS.

Consequently the beam thickness varies in the same manner as in the above case.

In the preceding section it was demonstrated that for irrotational beams,

$$\frac{\partial v}{\partial n} = \omega_c \quad . \tag{5.37}$$

Thus for cases (a) and (b) where the electrons enter with $\vec{v} = \hat{z}\, v_z$, it is necessary that

$$\frac{\partial v_z}{\partial y} = \omega_c \tag{5.38}$$

which leads to a voltage variation across the beam at the input plane of

$$\varphi = \frac{\omega_c^2}{2\eta} (y + \text{constant})^2 \quad . \tag{5.39}$$

This requires a space-charge density equal to the Brillouin value,

$$\rho = \frac{-\epsilon_o \omega_c^2}{\eta} \quad . \tag{5.40}$$

Consequently the scalloped beam patterns of Figs. 5.3a and 5.3b are theoretically impossible to achieve if the space-charge flow is irrotational. However, if the specified entrance conditions could be achieved in some manner, then one would expect to encounter the indicated type of behavior.

It should also be mentioned that the possibility of experimentally observing the situations described by Figs. 5.3a and 5.3b is extremely remote. Such configurations require that the electrons enter the anode-sole region parallel to one another which is the same requirement as for Brillouin flow. The only difference between the entering beams is

the space-charge density variation and hence the velocity slip across the beam. Consequently the establishment of the entrance conditions for the scalloped beams is just as difficult as the achievement of Brillouin flow itself. However, if a Brillouin beam could be achieved in practice, then the application of a perturbation might result in a scalloped type of beam.

The present investigation has been restricted to configurations in which the beam axis remains at a fixed plane while the thickness varies periodically between the maximum and minimum limits described above. If the investigations are restricted to laminar flow (i.e., nonintersecting trajectories) then there are additional beam configurations which are of interest:

1. The entire beam undulates through the interaction region and its motion is accompanied by a periodic variation of the beam thickness (Fig. 5.5).

2. The beam undulates but the thickness remains unchanged (Fig. 5.6). These configurations will be compared with the scalloped beams of Fig. 5.3.

<u>Case 1</u>: <u>Beam location and thickness undergo periodic variations</u>. The total current in the z-direction is given by

$$I = h \int_{y=0}^{y=\ell} \rho(y,z)\, \dot{z}(y,z)\, dy \quad . \tag{5.41}$$

Consider Fig. 5.5 and assume that the electrons at planes A-A and B-B have only z-directed motion. Furthermore, assume that the space-charge density is uniform across these planes so that

$$\rho_A \int_0^{\ell_A} \dot{z}_A\, dy = \rho_B \int_0^{\ell_B} \dot{z}_B\, dy \quad . \tag{5.42}$$

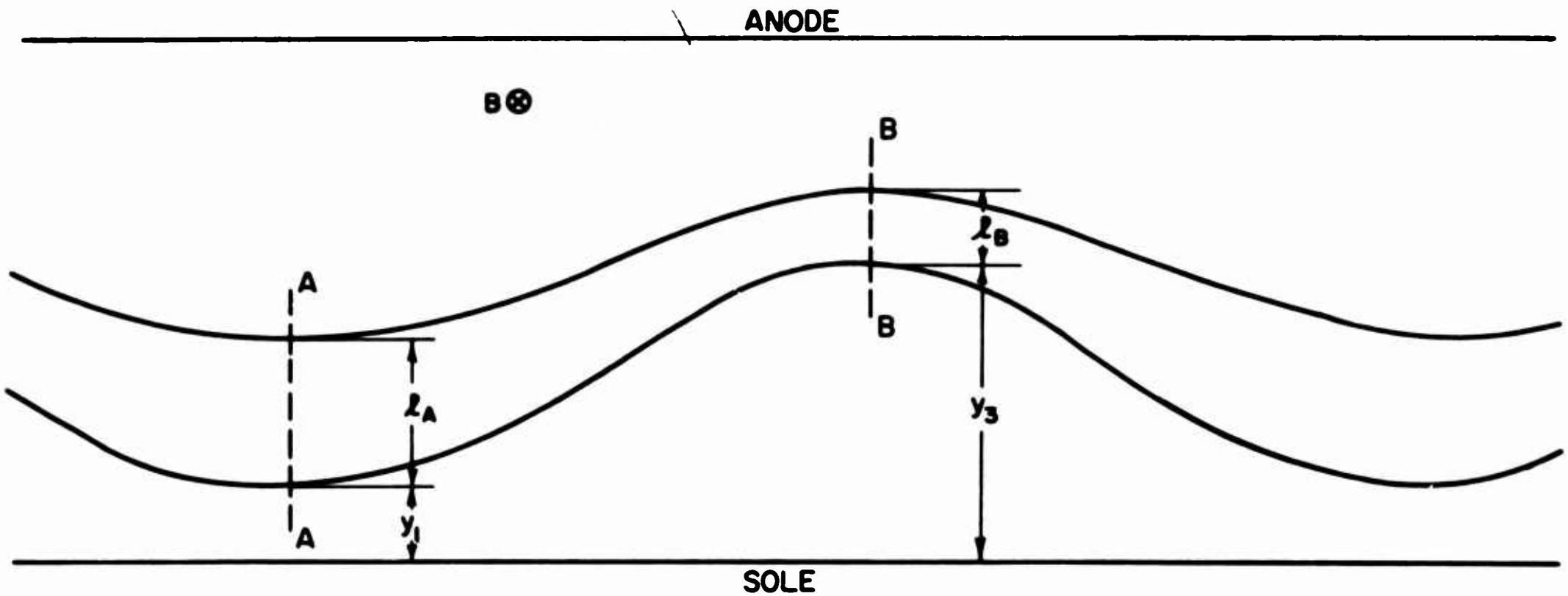

FIG. 5.5 SITUATION IN WHICH THE BEAM UNDULATES AND HAS PERIODIC VARIATIONS IN THICKNESS.

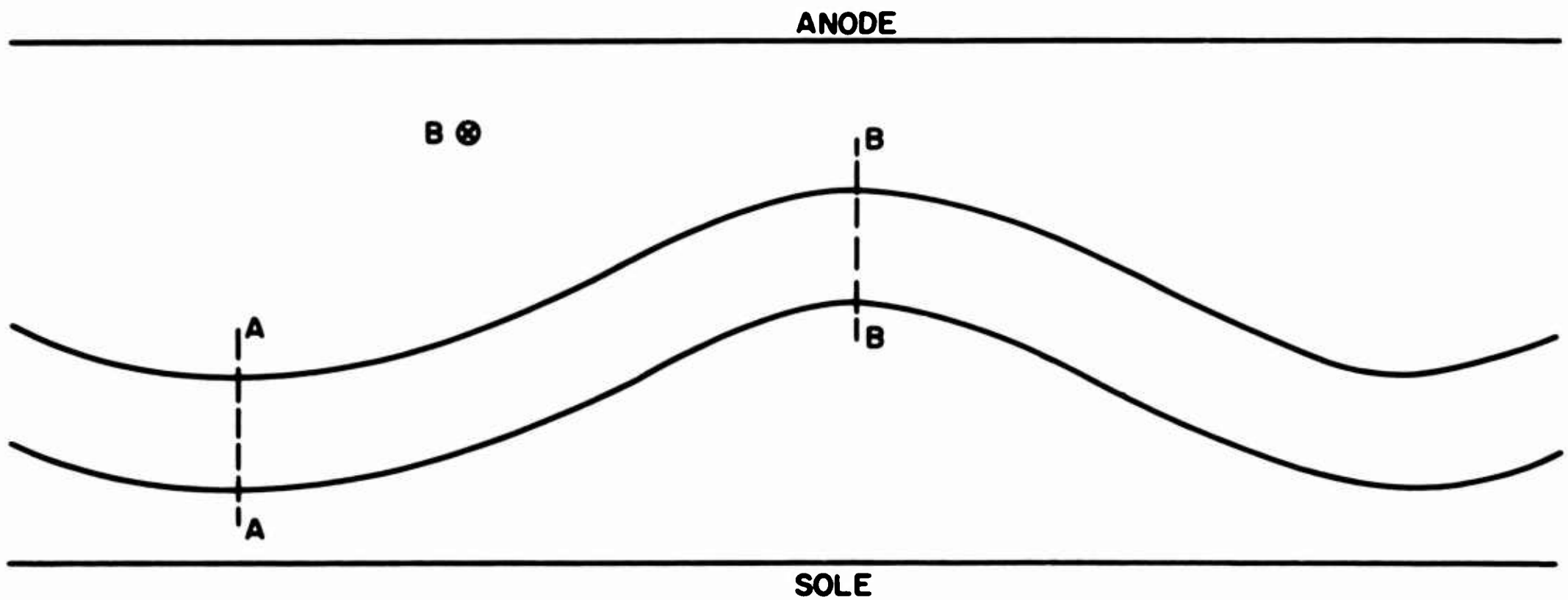

FIG. 5.6 SITUATION IN WHICH THE BEAM UNDULATES BUT MAINTAINS A CONSTANT THICKNESS.

For Brillouin flow the velocity is given by

$$\dot{z} = \omega_c (y + 2a) \quad , \tag{5.43}$$

where a is the distance between the lower beam boundary and the sole. Now assume that the electrons at A-A and B-B also have a linear velocity variation so that

$$\dot{z}_A = \omega_c (y + 2y_1) \tag{5.44}$$

and

$$\dot{z}_B = \omega_c (y + 2y_3) \quad . \tag{5.45}$$

Substituting these expressions into Eq. 5.42 yields

$$\frac{\rho_A}{\rho_B} = \frac{\ell_B (\ell_B + 4y_3)}{\ell_A (\ell_A + 4y_1)} \quad . \tag{5.46}$$

If $\rho_A = \rho_B$, then $\ell_B < \ell_A$ which implies that the configuration is similar to that displayed in Fig. 5.5; i.e., the beam has a minimum thickness at B-B and a maximum at A-A. If $\ell_B > \ell_A$, then $\rho_A > \rho_B$.

<u>Case 2</u>: <u>Constant thickness undulating beam</u>. This situation is illustrated in Fig. 5.6 and the result is

$$\frac{\rho_A}{\rho_B} = \frac{\ell + 4y_3}{\ell + 4y_1} \quad . \tag{5.47}$$

The above indicates that $\rho_A > \rho_B$ since $y_3 > y_1$. Notice that it is not possible for an undulating beam to have both constant thickness and constant space-charge density. Consequently it is not possible for

an undulating constant thickness beam to satisfy the requirements of irrotational flow.

Case 3: Scalloped beam at a fixed location. This case, described earlier in Fig. 5.3, has precisely the same equation as Case 1,

$$\frac{\rho_A}{\rho_B} = \frac{\ell_B\,(\ell_B + 4y_3)}{\ell_A\,(\ell_A + 4y_1)} \quad . \tag{5.48}$$

It is obvious that the space-charge density at the narrow part of the beam must be greater than at the wide part. Thus a scalloped configuration would always involve a varying space-charge density along the beam. As pointed out earlier, such a beam is not compatible with the requirements of irrotational flow.

5.4 Digital Computer Investigation of Injected Beams

The preceding section illustrates qualitatively the type of beam configurations which might be established under various operating conditions. To investigate this problem in more detail, a digital computer program was developed to analyze the situation wherein the beam conditions were prescribed at the anode-sole input plane. The computer solution provided a description of the beam during its anode-sole region motion.

The initial conditions were selected such that the beam location, thickness and current corresponded to the laminar flow conditions described in Chapter II except that it was assumed that the beam was injected into the anode-sole region at a slight angle. The operating parameters were selected as $\varphi_a = 1500$ volts, $d = 3.25 \times 10^{-3}$ m and $B = 350$ gauss. Figure 5.7 illustrates the case where the beam enters at 5° with respect to the z-axis (the y scale has been expanded to provide a clearer picture of the beam motion). It is apparent from the figure that the beam

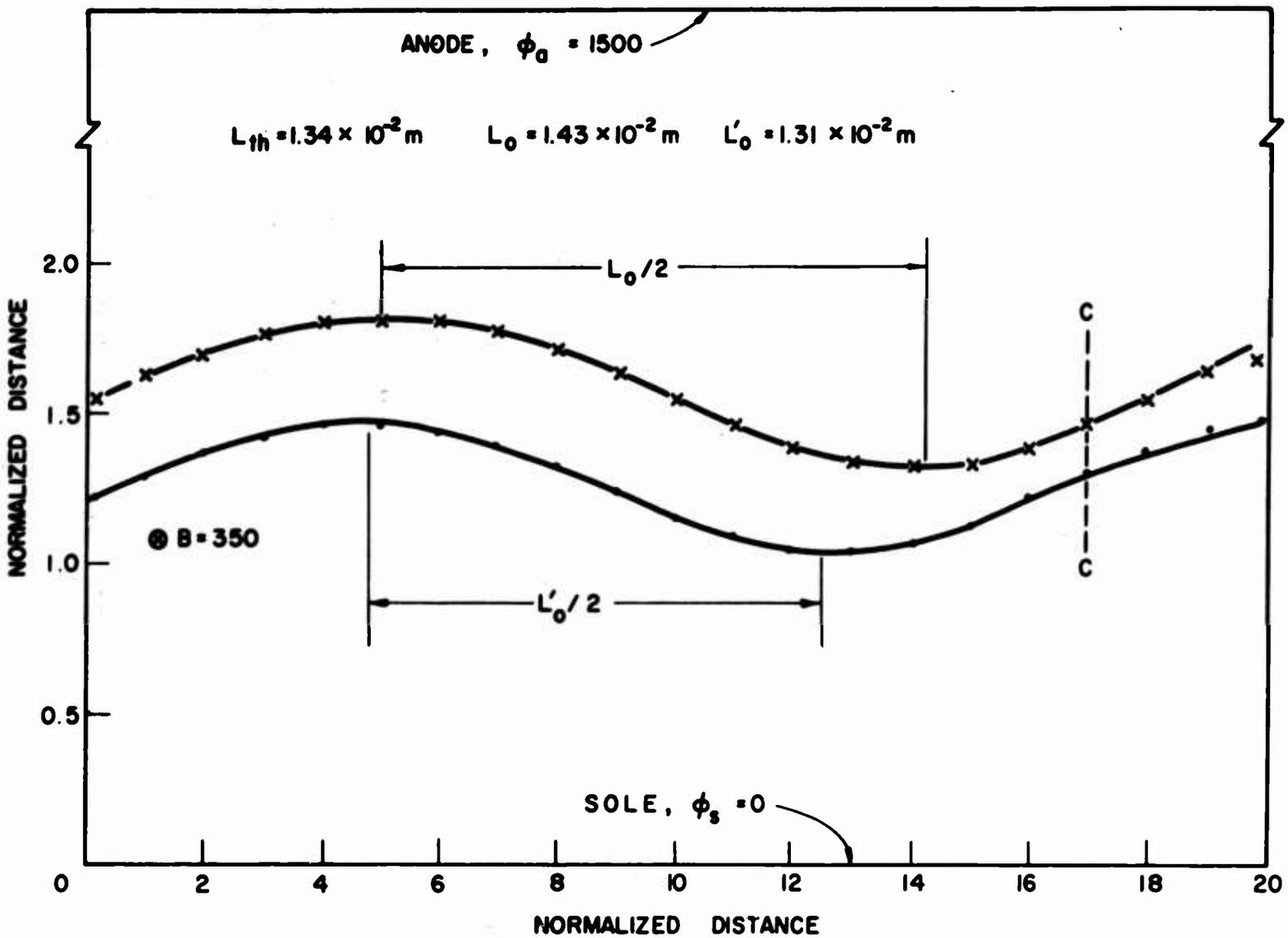

FIG. 5.7 ELECTRON BEAM CONFIGURATION AFTER INJECTION INTO THE ANODE-SOLE REGION AT AN ANGLE OF 5°.

undulates at some frequency and its thickness varies with distance. The theoretical variation of an electron trajectory in a space-charge-free field has a period

$$L_{th} = \frac{2\pi\varphi_a}{\eta d B^2} \tag{5.49}$$

which for the above values gives $L_{th} = 1.34 \times 10^{-2}$ m. The variations measured along the upper and lower beam boundaries respectively give

$$L_o = 1.49 \times 10^{-2} \text{ m}$$

and

$$L_o' = 1.25 \times 10^{-2} \text{ m} \quad .$$

Thus the upper boundary undergoes a slower spatial variation than the space-charge-free value while the lower boundary has a more rapid variation. The reason, of course, is the fact that the space charge causes the field on the upper boundary to be greater than the space-charge-free value (φ_a/d) while that along the lower boundary is less. This unequal variation of the boundaries causes the lower surface to move up after its minimum before the upper boundary does. Consequently there is a shearing action which occurs around plane C-C where the thickness is significantly reduced. Thus the variation in thickness is a direct consequence of the different periods associated with the upper and lower beam boundaries.

It is possible to obtain a fairly good estimate of the period for the beam boundaries by using Eq. 2.2 for the electric field in a Brillouin beam which is given by

$$E_2 = -\frac{\omega_c^2}{\eta}(y + 2a) , \tag{5.50}$$

where a is the distance from the sole to the lower boundary and y is measured relative to this surface. If Eq. 5.50 is assumed to be a good approximation for the beam of Fig. 5.7, then the average field encountered along the upper boundary can be written as

$$\bar{E}_{2+} = -\frac{\omega_c^2}{\eta} \left(\bar{l} + 2\bar{a} \right) \tag{5.51}$$

and along the lower boundary as

$$\bar{E}_{2-} = -\frac{\omega_c^2}{\eta} \left(2\bar{a} \right) , \tag{5.52}$$

where $\bar{a}$ and $\bar{l}$ are the values averaged over a complete period. Substituting these expressions into Eq. 5.49 gives

$$L_+ = 2\pi \left(\bar{l} + 2\bar{a} \right) \tag{5.53}$$

and

$$L_- = 2\pi \left(2\bar{a} \right) = 4\pi\bar{a} . \tag{5.54}$$

From Fig. 5.7 $\bar{a}$ and $\bar{l}$ are found to be 1.04×10^{-3} m and 0.23×10^{-3} m respectively which results in the values $L_+ = 1.45 \times 10^{-2}$ m and $L_- = 1.30 \times 10^{-2}$ m. The corresponding values in Fig. 5.7 are $L_o = 1.49 \times 10^{-2}$ m and $L_o' = 1.25 \times 10^{-2}$ m which indicates that the above approximations are fairly valid for predicting the period of variation of the upper and lower beam boundaries. Of course as the beam becomes more nonlaminar the approximations become less acceptable.

Figure 5.8 illustrates the case where the electrons enter at an angle of -5°. The shearing action occurs sooner because the minimum beam position is reached at an earlier time. However, for the same reason the shearing action is not as severe; i.e., the upper and lower boundaries have not had time to slip as much as in the 5° case. The corresponding

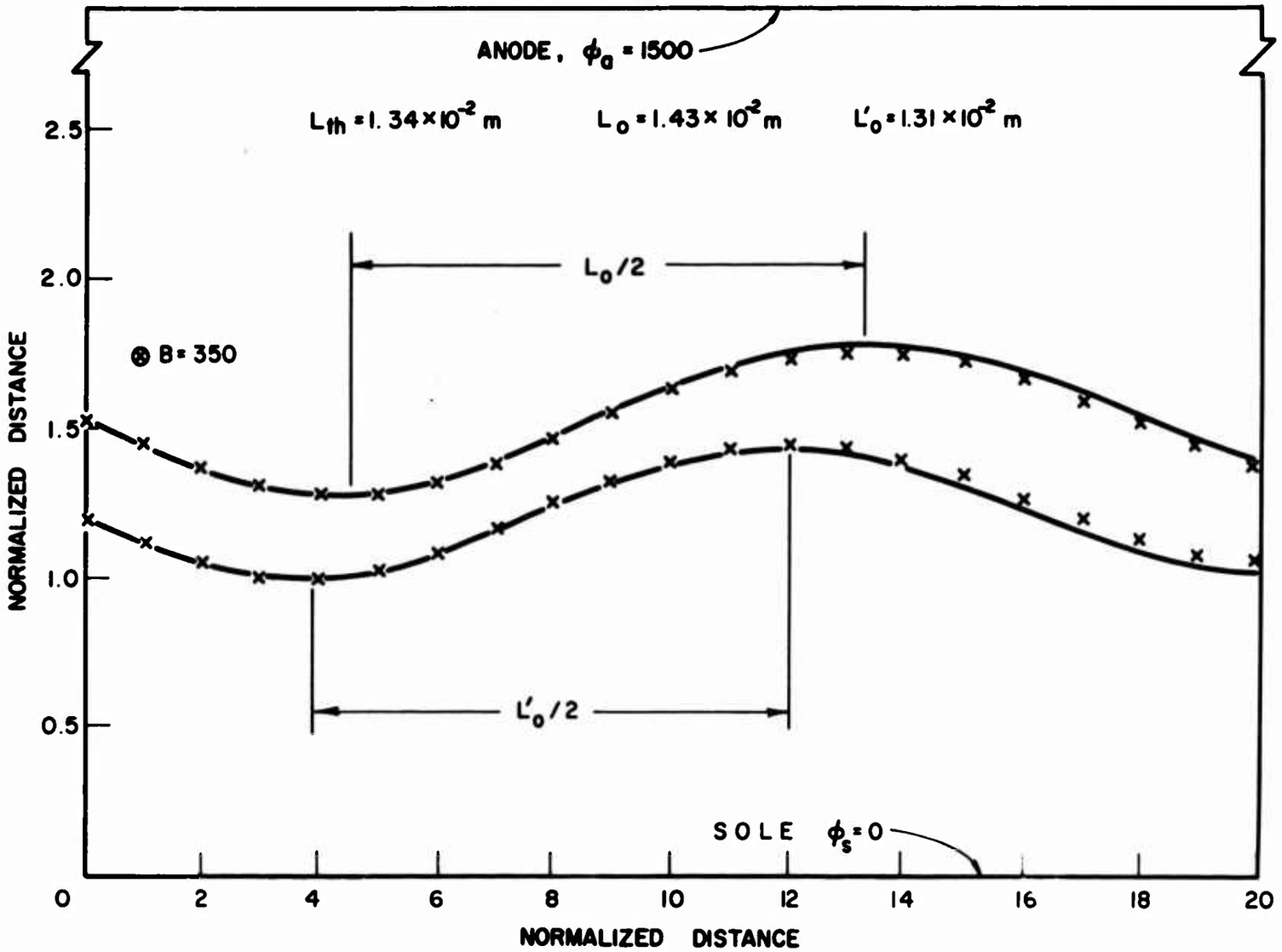

FIG. 5.8 ELECTRON BEAM CONFIGURATION AFTER INJECTION INTO THE ANODE-SOLE REGION AT AN ANGLE OF -5°.

boundary periods again lie above and below the theoretical space-charge-free value; i.e., $L_o = 1.43 \times 10^{-2}$ m and $L_o' = 1.31 \times 10^{-2}$ m. Calculations based on Eqs. 5.53 and 5.54 give $L_+ = 1.40 \times 10^{-2}$ m and $L_- = 1.24 \times 10^{-2}$ m which also are in fairly good agreement.

Figure 5.9 illustrates the beam configuration after a 10° entrance angle. The undulation is much more pronounced and results in a crossover point for the trajectories at the maximum shear plane C-C. At this point the electrons from the lower boundary cross through the beam and eventually form the upper boundary while the original upper boundary electrons proceed along the lower boundary. The boundary periods are $L_o = 1.44 \times 10^{-2}$ m and $L_o' = 1.30 \times 10^{-2}$ m which are consistent with the previous results. The calculated values are $L_+ = 1.51 \times 10^{-2}$ m and $L_- = 1.33 \times 10^{-2}$ which are reasonably close to the measured values despite the larger beam entrance angle.

Figure 5.10 shows the beam after injection at -10°. As explained before, the shearing action is not as severe because the electrons reach the shear plane sooner. Thus in this case there is not an inversion of the beam after plane C-C. However, if the analysis were carried further (i.e., beyond plane D-D) the beam would become completely nonlaminar just as in the preceding case.

The above results illustrate quite vividly the fact that the entrance conditions are extremely critical in affecting the laminarity of the beam in the interaction region. Injection with anything but the ideal Brillouin conditions will result in an undulating beam which is subjected to a strong shearing force. The result is a nonlaminar flow with the degree of nonlaminarity being determined by the injected beam's

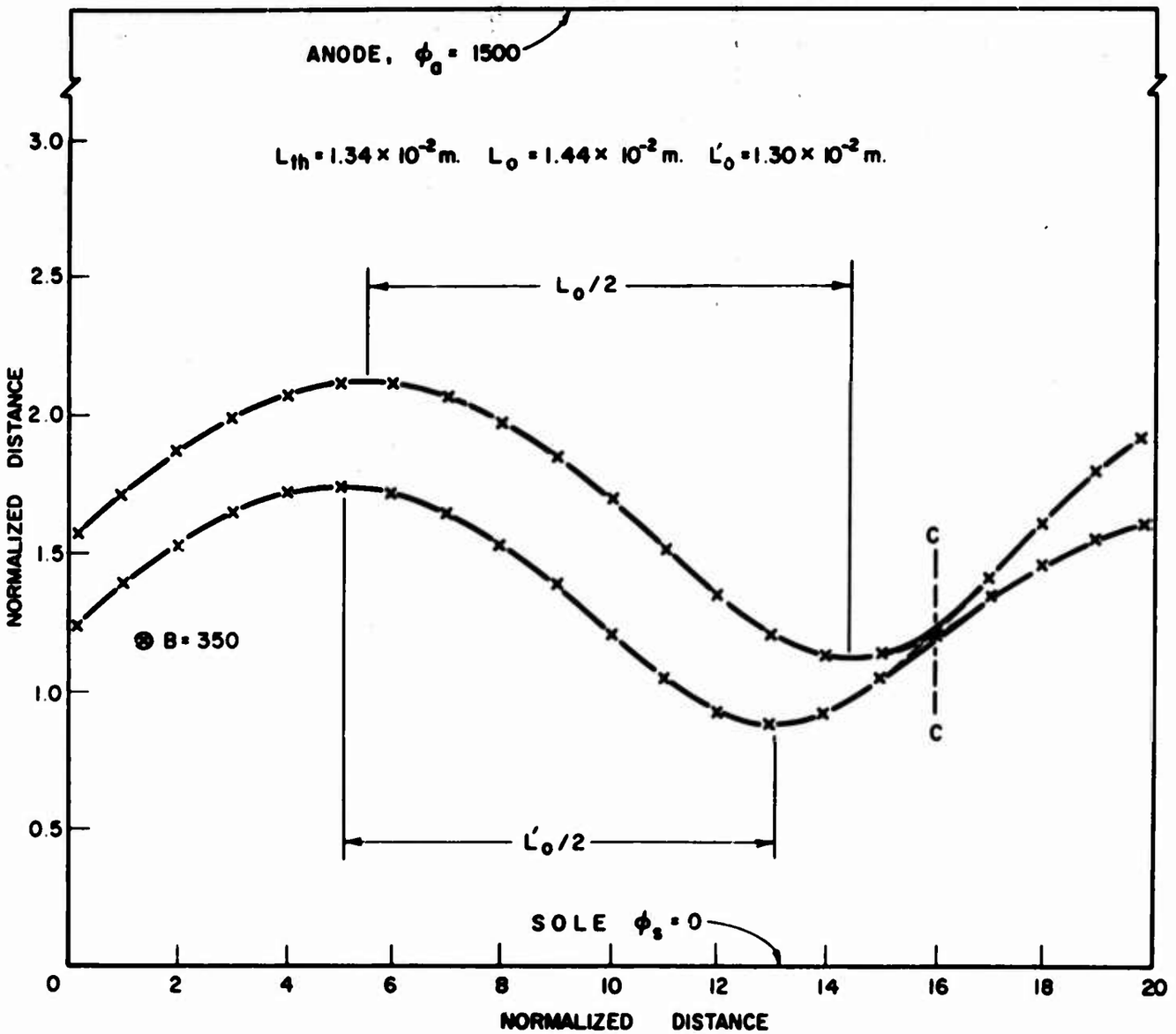

FIG. 5.9 ELECTRON BEAM CONFIGURATION AFTER INJECTION INTO THE ANODE-SOLE REGION AT AN ANGLE OF 10°.

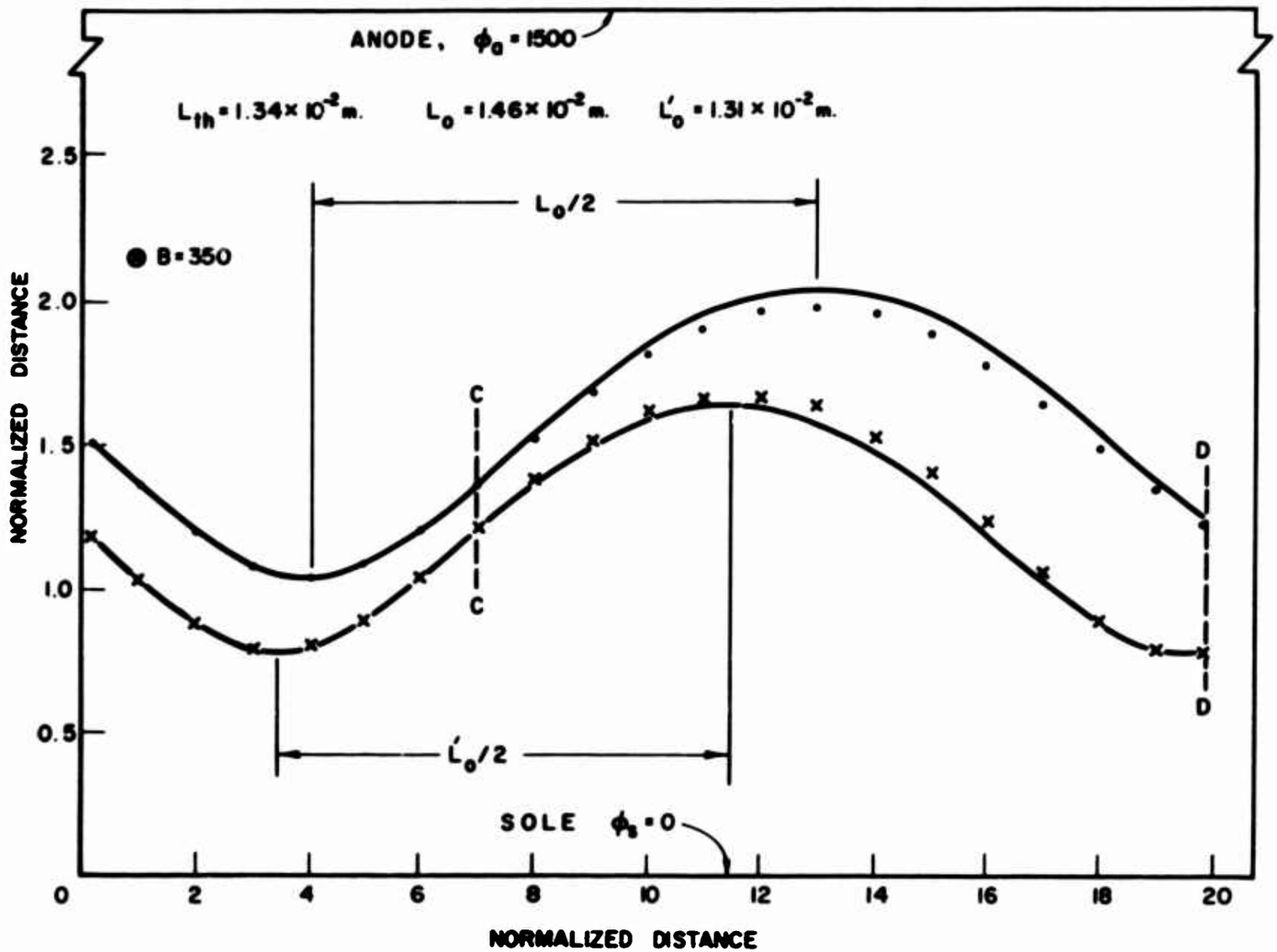

FIG. 5.10 ELECTRON BEAM CONFIGURATION AFTER INJECTION INTO THE ANODE-SOLE REGION AT AN ANGLE OF -10°.

deviation from the ideal conditions at the entrance plane. In many cases the experimental data of Chapter VII indicate beam configurations which have a strong resemblance to the above computer profiles.

CHAPTER VI. EXPERIMENTAL ELECTRON BEAM ANALYZING SYSTEM

6.1 Introduction

The electron beam analyzer was designed for the experimental investigation of the space-charge-flow characteristics in electron tubes. The analyzer has been used to study the beam forming capabilities of electron injection systems, the gross characteristics of electron beams, and the detailed properties of the electron trajectories which comprise the flow. The system has proven to be extremely valuable both in the design of electron guns and in improving the understanding of crossed-field space-charge flows.

A description of the various components of the beam analyzing unit is presented below. Since a majority of the crossed-field studies involved the experimental investigation of electron beams formed by the extended Kino short gun, a discussion of its construction is also included.

6.2 Crossed-Field Electron Beam Analyzer

Any system whose function is to investigate the characteristics of electron beams requires four basic units:

1. A pumping system capable of achieving a good vacuum,
2. A base plate and bell jar unit within which the experimental device is located,
3. A movable electron beam analyzing unit, and
4. A mechanical system for driving the analyzing unit.

Each of these units is indispensable for the investigation of space-charge flows.

The pumping system illustrated in Fig. 6.1 consists of a 180 liter/sec ion pump, sorption pump, mechanical fore pump, and associated valves. The system is connected to a base plate which is actually a box-type enclosure. Valves A and B are high vacuum bellows valves used to isolate the ion pump from the roughing system while valves C, D and E are used to provide an air inlet into the bell jar and to bypass the fore pump in order to process the sorption pump. Valve F is a high vacuum valve which allows the ion pump to continue operating even when the bell jar has been removed from the base plate. Viton gaskets are used in the high vacuum valves and for the bell jar seal. Most of the experimental investigations were carried out at pressures of less than 5×10^{-7} torr.

Figure 6.2 illustrates the relative arrangement of the bell jar, base enclosure and mechanical system. The experimental tube, which consists of an electron gun and planar anode and sole electrodes, is attached to the stationary base plate. The measuring system is mounted on the movable center pedestal which is brought into the base through a 2-1/2 inch flexible bellows. The mechanical stage is capable of 3 inches of motion in the z-direction, 2 inches in the x- and y-directions, and rotation about the x- and y-axes.

Three sides of the base enclosure are used for mounting eight high current feed throughs and two 7-pin feed throughs. The system is pumped through a 6-inch diameter pipe coming out of the fourth side of the base.

Figure 6.3 is a photograph of the entire assembly. The ion pump supply is mounted in the top left hand panel while the a-c supply for the cathode heater filaments is located in the center panel. The control

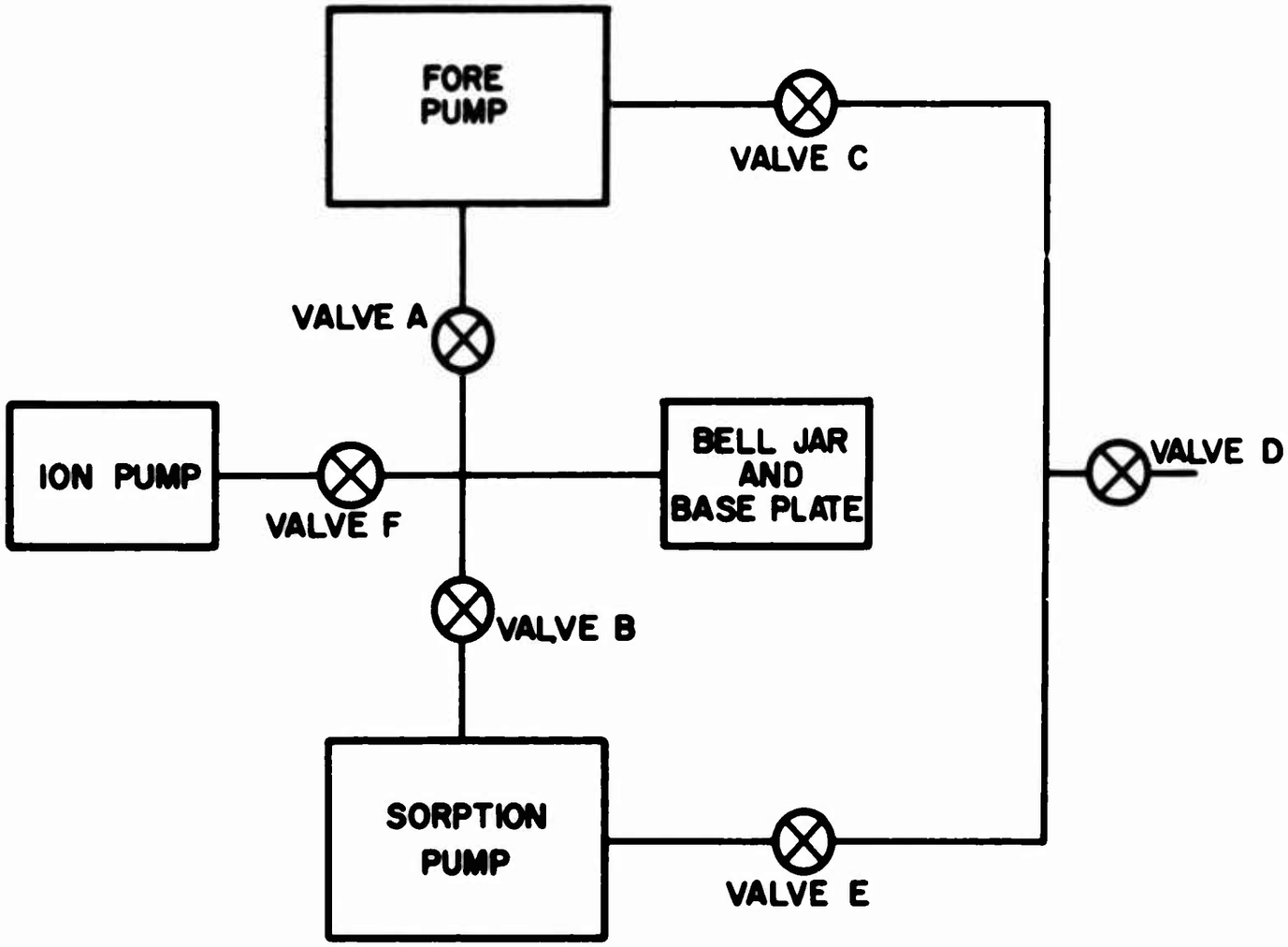

FIG. 6.1 BLOCK DIAGRAM OF PUMPING SYSTEM.

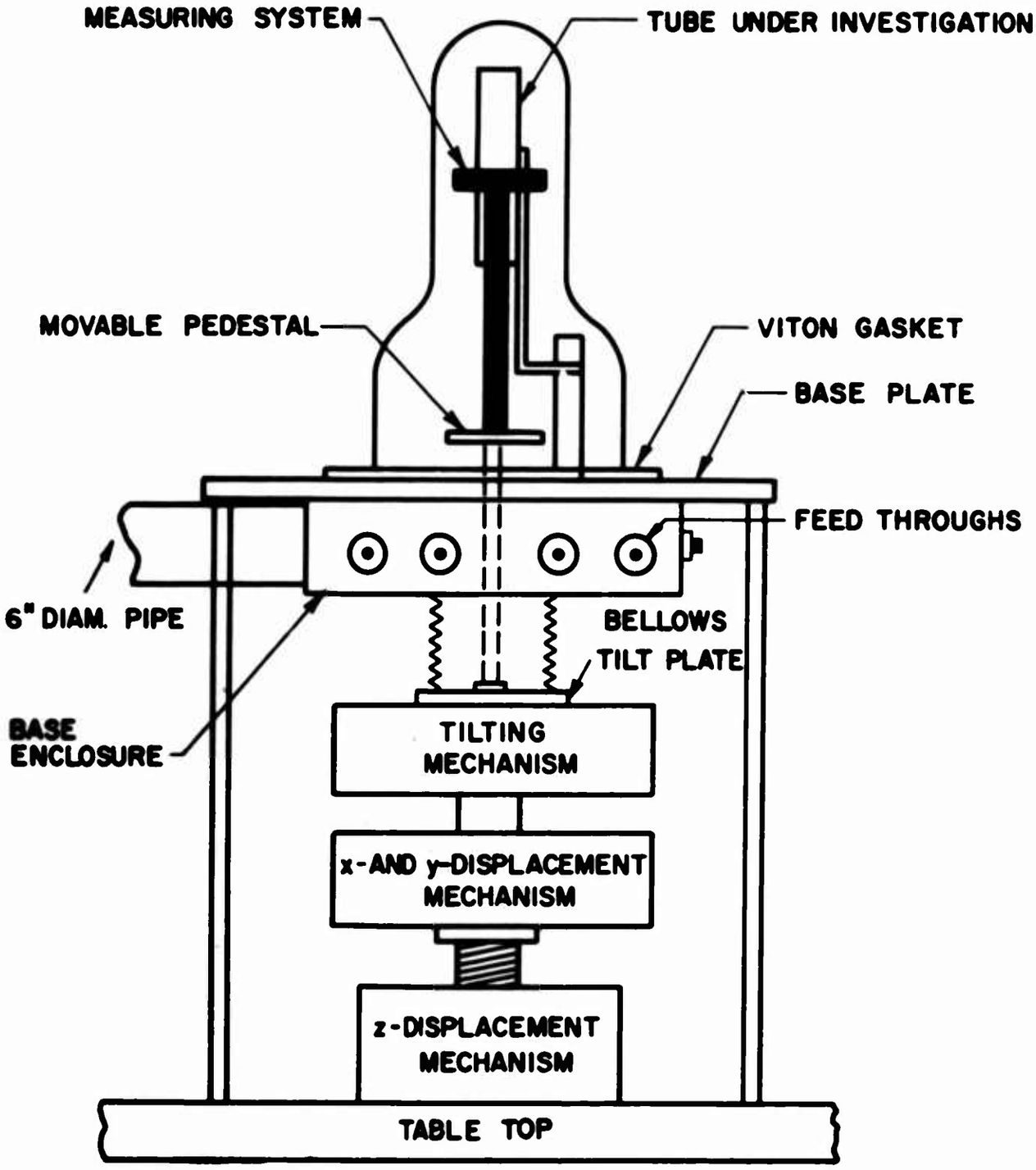

FIG. 6.2 DIAGRAM ILLUSTRATING THE RELATIVE LOCATION OF THE VARIOUS COMPONENTS.

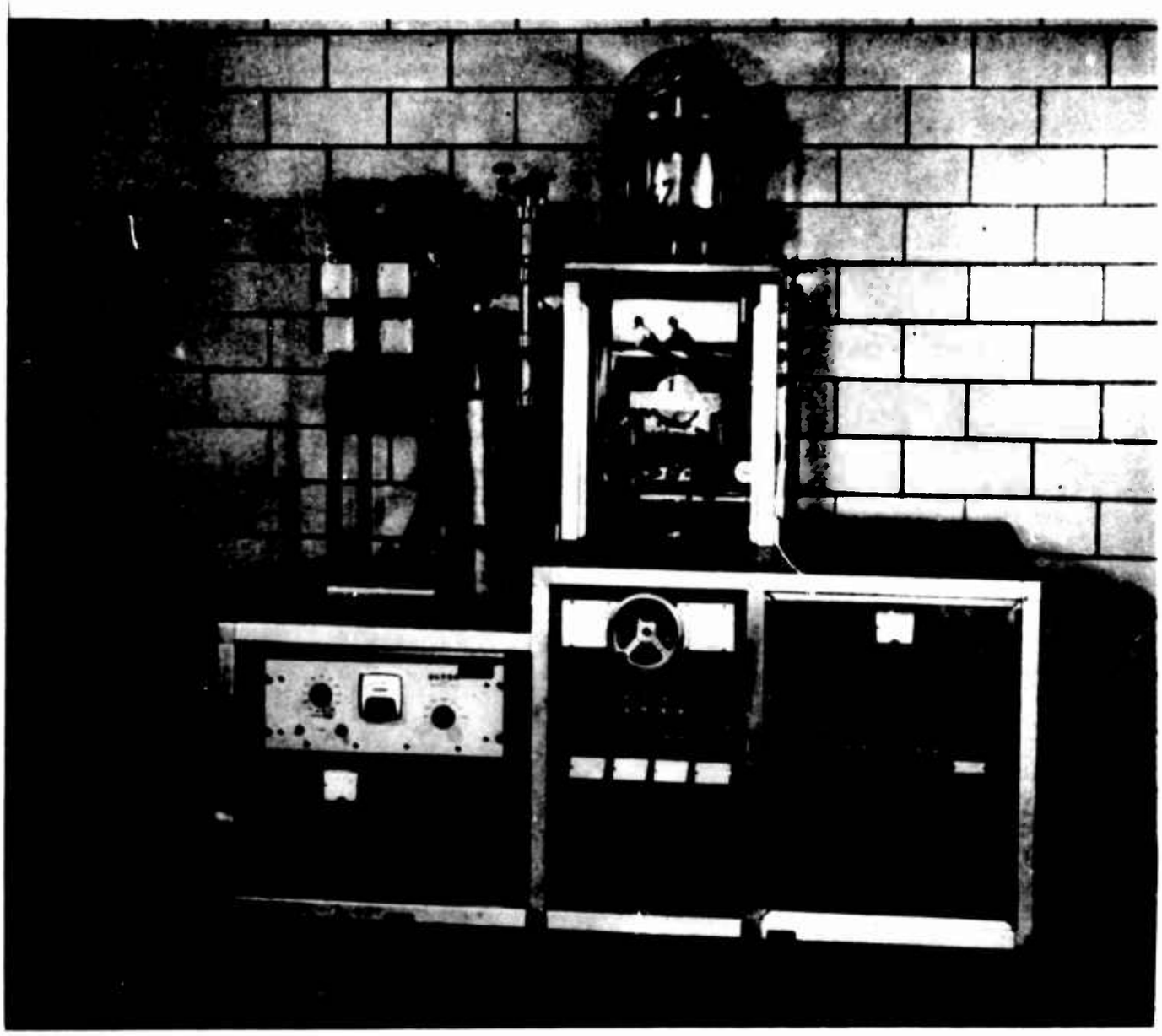

FIG. 6.3 ELECTRON BEAM ANALYZER ASSEMBLY.

wheel above the filament supply is the gear drive control for the z-motion of the mechanical stage.

Figure 6.4 is a close-up view of the special necked-down bell jar design which allows the magnet pole piece gap to be kept to a reasonable value. The normal spacing is 6-1/2 inches for which magnetic fields in excess of 700 gauss are easily achieved.

Figure 6.5 illustrates the relationship between the mechanical stage, flexible bellows and base enclosure. The x- and y-translation controls and tilting mechanism are clearly displayed. The two 7-pin feed throughs located in the front side of the base are also visible.

Figure 6.6 is a photograph of the tube and grid wire assembly. The tube, which consists of an extended Kino short gun and planar anode-sole region, is bolted to the stationary base plate. The anode and sole electrodes are connected by four ceramic rods which are also attached to the top and bottom supporting plates. The original anode-sole spacing was 0.128 inch but later was increased to 0.188 inch for the aperture measurements. The sole electrode included two 0.030 inch rails spaced 0.690 inch apart. These rails help in preventing the beam from spreading in the x-direction and moving out of the interaction region. The collector is a V-shaped copper block which is connected to the other components by two ceramic plates.

The grid assembly, which is illustrated in Fig. 6.7, consists of ten parallel 0.003 inch diameter tungsten wires stretched across a frame which is mounted on the movable center pedestal. The wires are positioned in grooves cut into ceramic supports located at each end of the wires. Each wire is terminated by welding to a thicker L-shaped wire which acts as a spring to maintain the grid wires under tension. The other end of

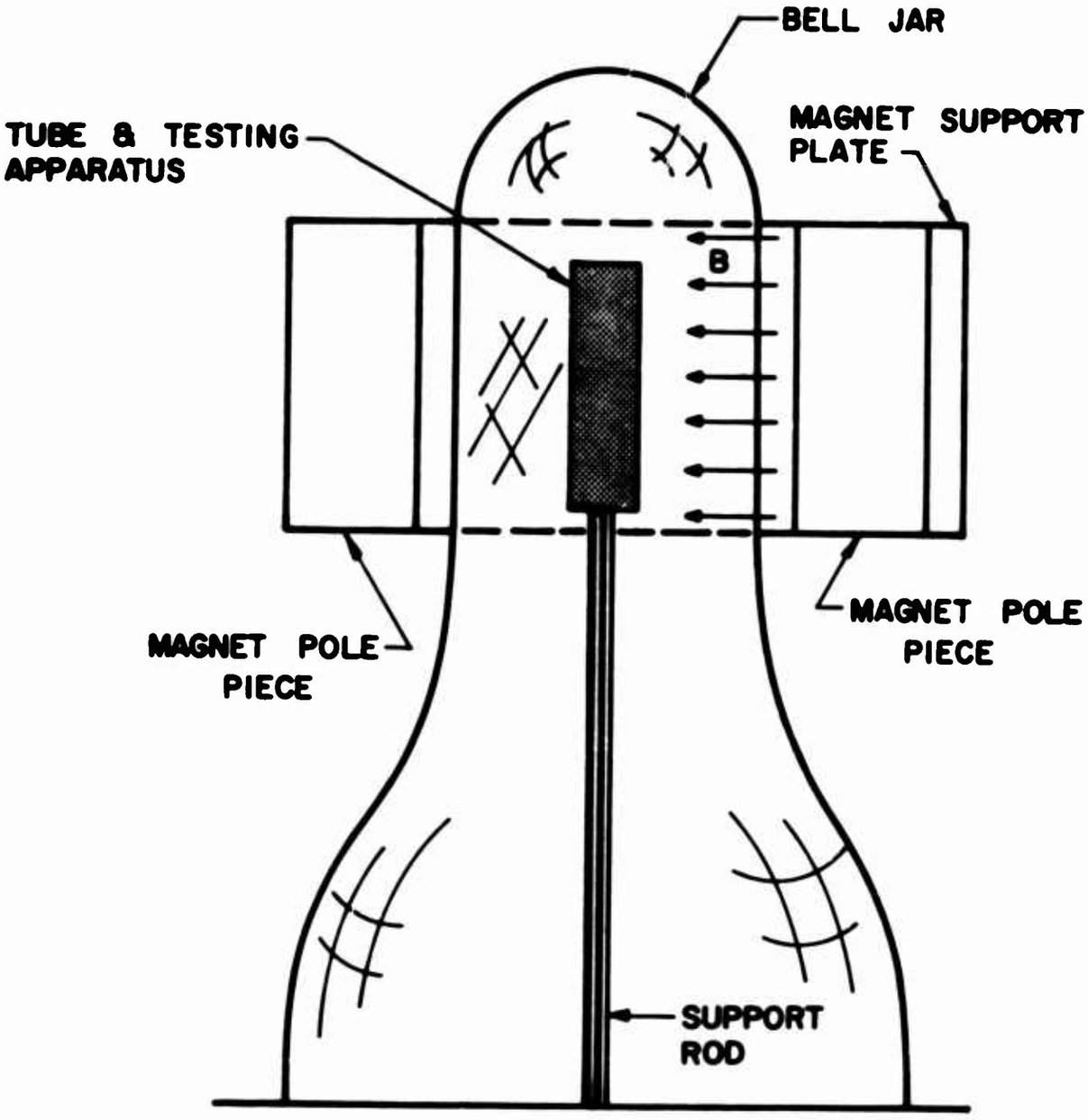

FIG. 6.4 ILLUSTRATION OF COMPONENTS OF THE CROSSED-FIELD BEAM ANALYZER.

FIG. 6.5 MECHANICAL MOVEMENT STAGE .

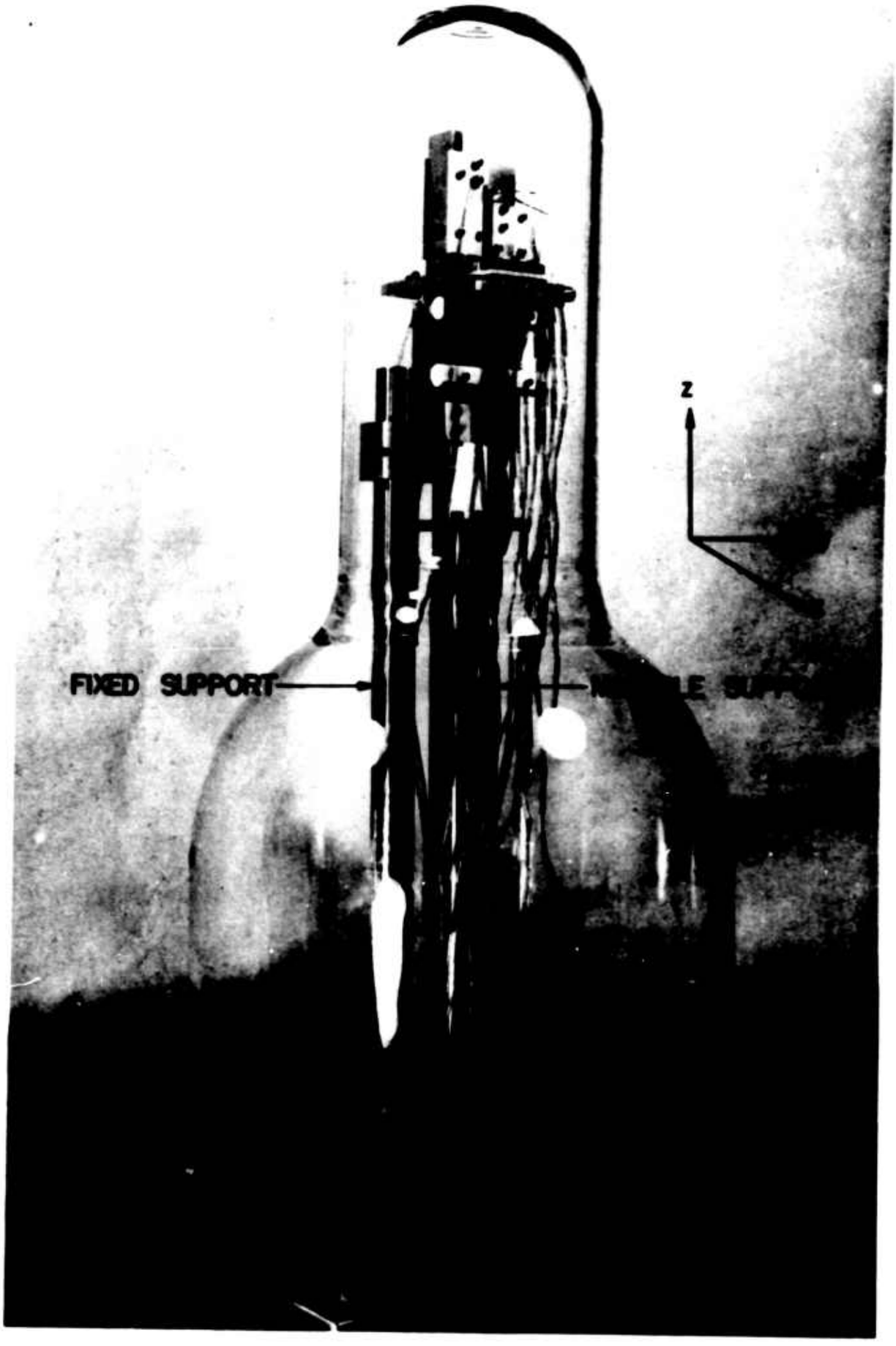

FIG. 6.6 CROSSED-FIELD DEVICE LOCATED WITHIN THE SPECIAL BELL JAR OF THE BEAM ANALYZER.

FIG. 6.7 GRID WIRE ASSEMBLY FOR INTERCEPTING THE ELECTRON BEAM.

each wire is connected to one of the terminals on the 7-pin feed throughs. Thus the application of voltages to the various wires can be easily performed on the external base plate panel.

Figure 6.8 provides a view of the grid wires located in the anode-sole region and in position to intercept the electron beam. For the crossed-field investigations the motion of the grid wires was restricted to the z-direction (i.e., parallel to the anode and sole electrodes). The grid was capable of approximately 1.2 inches of motion through the interaction region starting at the gun exit plane. The grid wires were biased at different potentials by connecting them to a resistance network as illustrated in Fig. 6.9.

The aperture system, which is not shown in the above photographs, is located approximately 0.005 inch behind the grid wires as indicated in Fig. 6.10. The system is composed of a 0.010 inch molybdenum beam intercepting aperture plate and a parallel molybdenum deflection plate spaced 0.020 inch away. A 0.004 inch diameter opening in the aperture plate allows a small portion of the beam to enter the deflection region. The motion of the electrons in this region is controlled by the voltage difference between the two plates. In particular, the capability of the electrons in reaching the deflection plate depends on their entrance velocities and the voltage difference between the two plates. These relationships are discussed in more detail in Appendix F.

6.3 Extended Kino Short Gun Design

Figure 6.11 illustrates the extended Kino short gun assembly. The configuration is identical to that which was analyzed on the Poisson cell and described in Chapter III. The extension of the gun beyond the usual cut-off plane was motivated by the experimental results of Midford

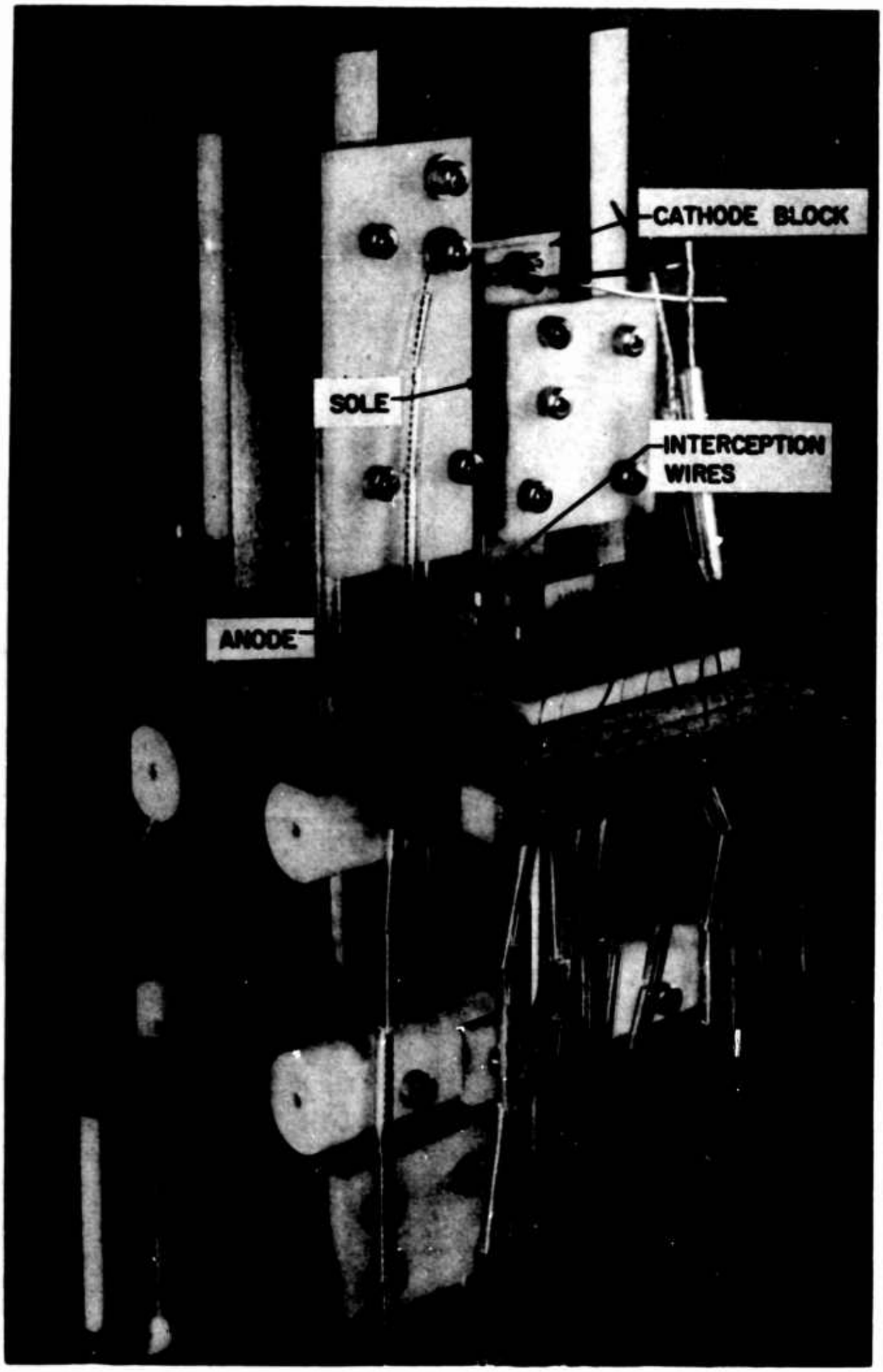

FIG. 6.8 GRID WIRE ASSEMBLY LOCATED IN POSITION TO INTERCEPT THE BEAM.

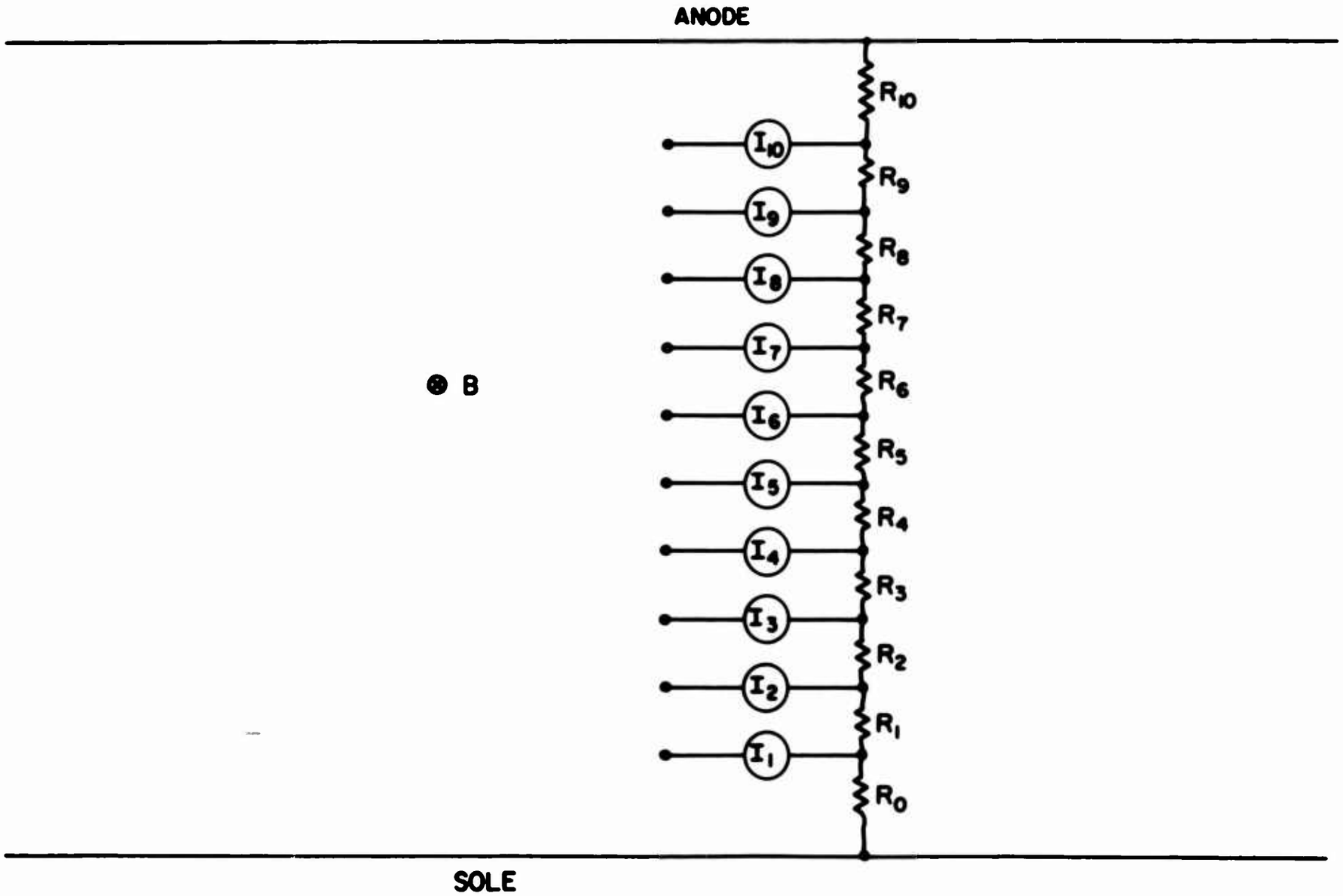

FIG. 6.9 GRID WIRE CONNECTIONS TO THE RESISTANCE NETWORK.

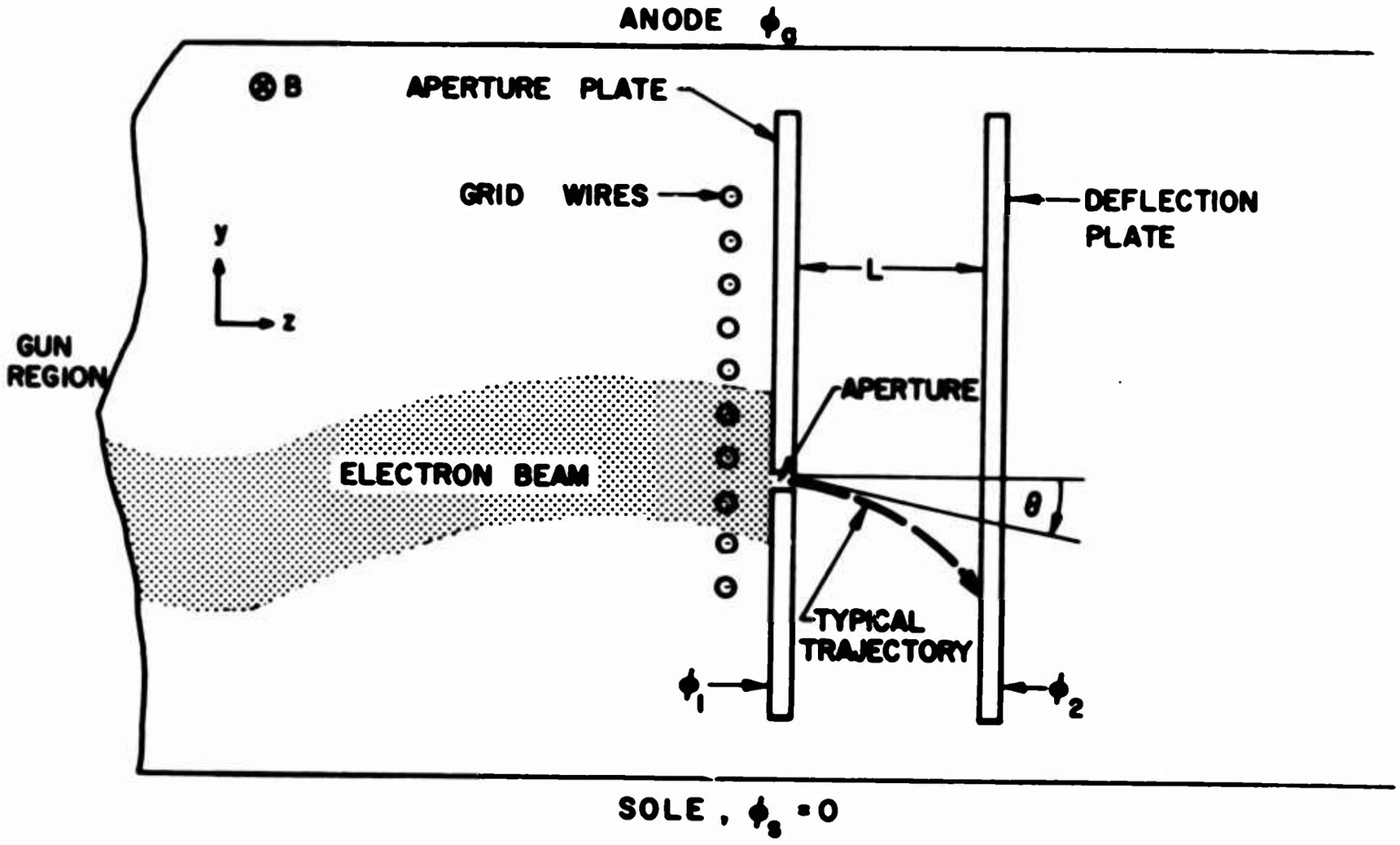

FIG 6.10 APERTURE SYSTEM FOR THE CROSSED-FIELD BEAM ANALYZER INVESTIGATION.

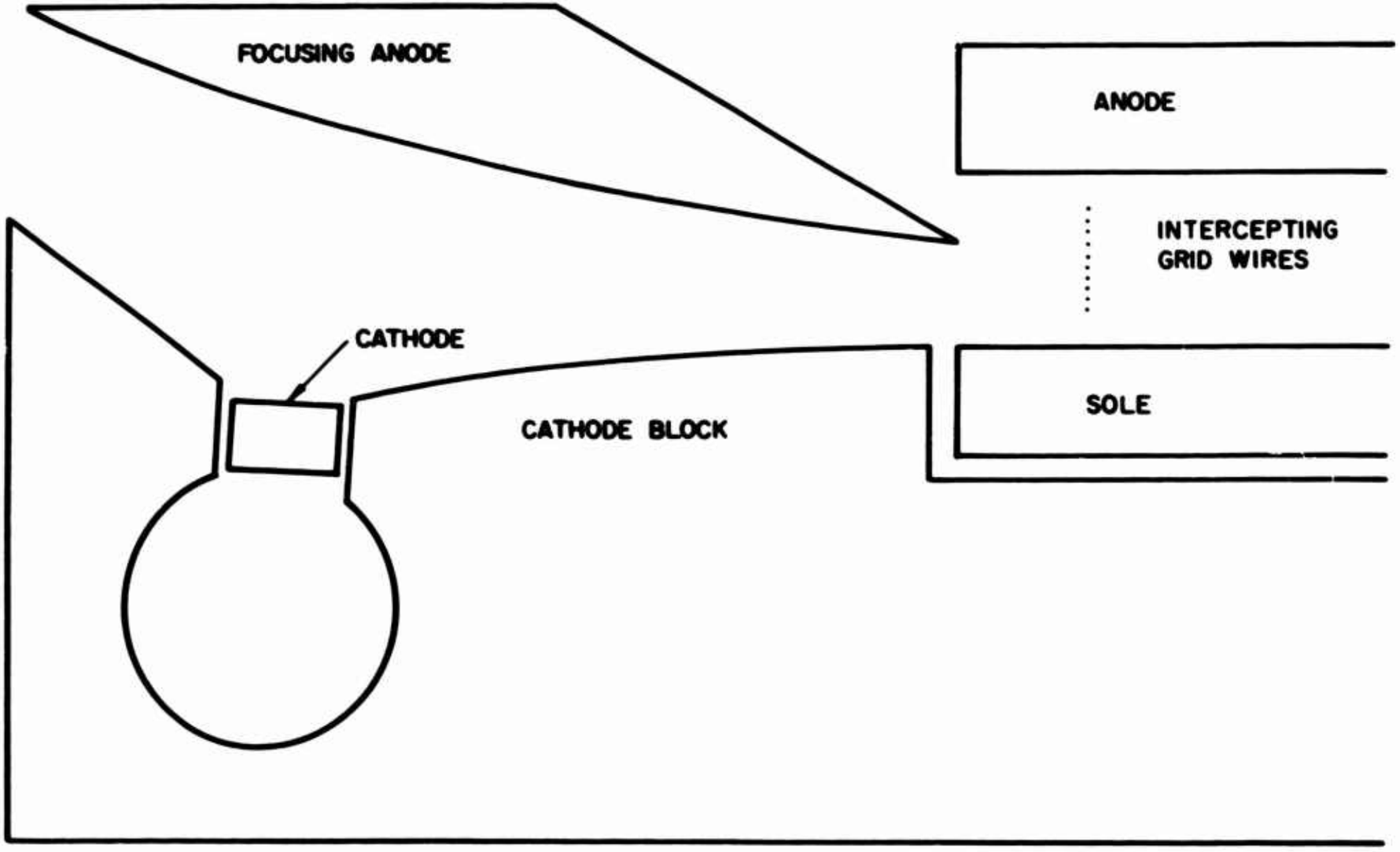

FIG. 6.11 DRAWING OF KINO GUN GEOMETRY WITH THE BEAM INTERCEPTING GRID WIRES PLACED IN THE INTERACTION REGION.

which indicated that such a change was capable of improving the beam characteristics.

The focusing anode, which is located along the theoretical $\Phi_f = 25$ equipotential, is made of molybdenum. It is attached to a copper block which is connected to the anode and top support structure by means of two ceramic plates.

The contour of the upper portion of the cathode block is a reproduction of the zero equipotential curve from the Kino theory. These two curved surfaces are referred to as the front and rear cathode ramp electrodes. The block is made of oxygen-free-high-conductivity (OFHC) copper just as are the sole, anode and collector electrodes. The cathode block is attached to the sole and bottom supporting structure by ceramic plates in exactly the same manner as the focusing anode is connected to the anode and top support plate.

The cathode-heater assembly for the extended gun is illustrated in Fig. 6.12. The design has been quite successful in allowing relatively troublefree operation of the cathode over a long period of time. A sapphire rod is passed through the center opening of the helical heater filament to keep it properly aligned with respect to the cathode. The cathode itself is an impregnated tungsten bar (0.050 inch square by 0.400 inch long) which is welded to the molybdenum shield by means of two tungsten wires. The heater and sapphire rod lie within the shield so that the proper operating temperature of 1100°C can be achieved at a reasonable heater power of approximately 25 watts.

The two tungsten wires which support the cathode and shield, as well as the sapphire rod and heater leads are fitted through appropriate holes in 0.030 inch thick ceramic wafers mounted on the two ends of the

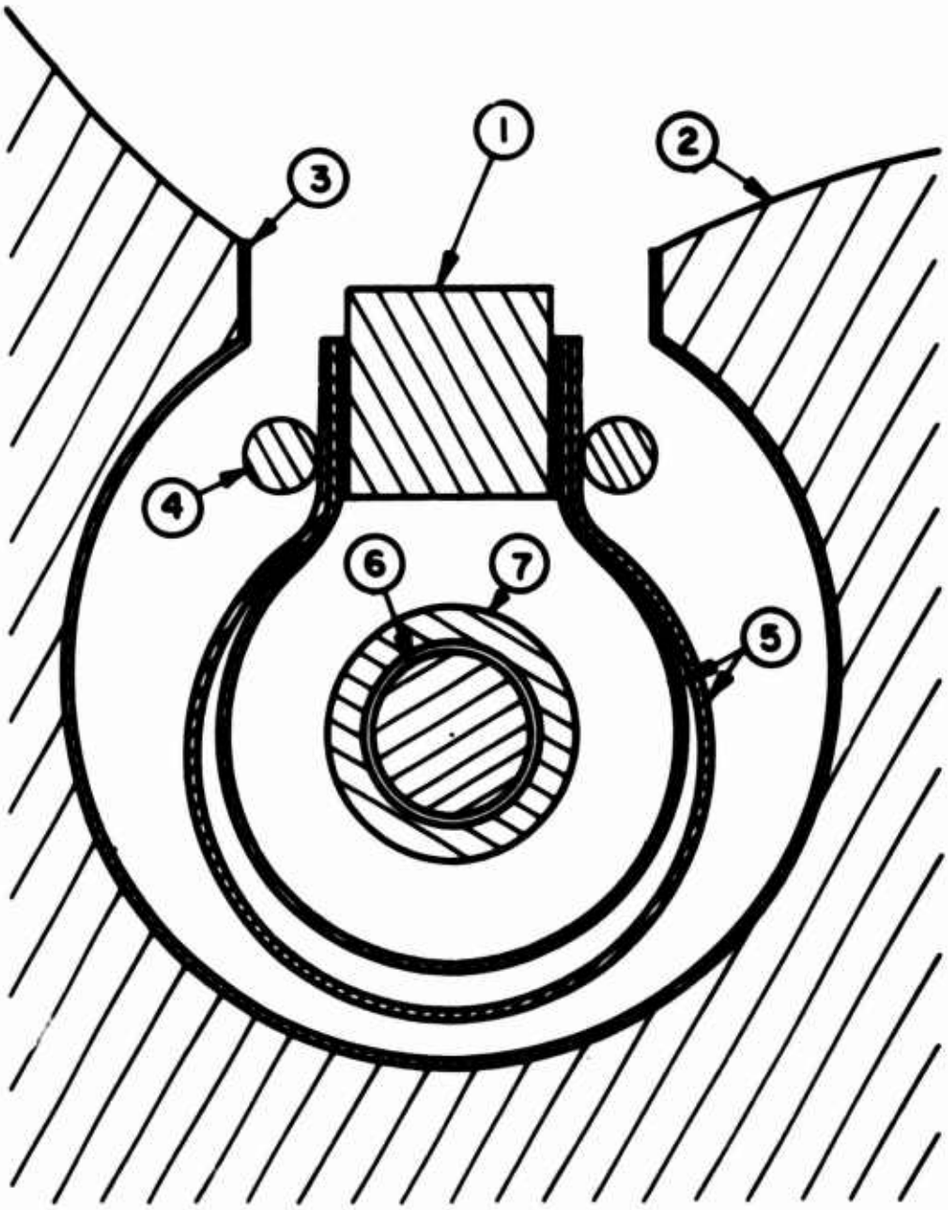

1. Cathode
2. Cathode Block
3. Molybdenum Lining
4. Tungsten Wires for Supporting Cathode and Shields
5. Molybdenum Shield
6. Sapphire Support Rod for Heater Filament
7. Uncoated Heater Filament.

FIG. 6.12 CROSS-SECTIONAL VIEW OF CATHODE ASSEMBLY.

cathode block. This method of supporting the components allows them to expand freely through the holes as the assembly heats up and yet maintains them in the proper position relative to the cathode block. The problem of electrical shorts between various components has been successfully eliminated by this design.

The experimental operating characteristics of the gun are described in the next chapter. This is followed by the discussion and interpretation of the anode-sole region beam interception data.

CHAPTER VII. EXPERIMENTAL INVESTIGATIONS

7.1 Introduction

The experimental investigation of crossed-field space-charge flows can be separated into two general classifications:

1. Evaluation of the electron gun behavior under various operating conditions.

2. Determination of the beam characteristics in the anode-sole region.

The two investigations, however, are not completely independent since the space-charge characteristics in the anode-sole region are determined to a great extent by the quality of the beam which is ejected from the gun.

The electron gun investigation is primarily concerned with an evaluation of the effects of the magnetic field and focusing-anode voltage on the cathode current, focusing-anode current, high-voltage anode current, and collector current. The experimental results are discussed and compared with the predictions of the Kino theory.

The investigations of the beam in the anode-sole region are concerned with two general areas of interest. One deals with the gross behavior of the beam during its anode-sole journey which involves a consideration of the general characteristics of the space-charge flow. In particular, the beam location, thickness and average space-charge density are investigated as a function of the z-position. This information is quite useful in optimizing the design of crossed-field electron devices.

The other area of interest is concerned with the microscopic description of the space-charge flow. In this case a small section of

the beam is examined in more detail with the intention of determining the velocity distribution of the electrons. These investigations also provide information concerning the space-charge density and current density in the beam as a function of position.

The experimental investigations were all carried out utilizing the beam analyzer described in the previous chapter. In a majority of the work the extended Kino short gun was used as the beam injection system.

7.2 Experimental Behavior of the Extended Kino Short Gun

The basic gun geometry indicating the voltages applied to the various electrodes is illustrated in Fig. 7.1. The anode and collector are held at ground potential while the cathode and sole are pulsed between ground and a negative voltage V_c. The pulser generates a 100 μ second pulse at a repetition rate of 100 pulses per second. The focusing anode is biased to V_f by means of a d-c supply.

The cathode current (I_k), focusing-anode current (I_f), anode current (I_a), and collector current (I_c) are plotted as a function of the magnetic field in Fig. 7.2a. The focusing-anode voltage and cathode voltage were fixed at -500 volts and -1430 volts respectively. The cathode current remains fairly constant for low magnetic field values bur decreases quite rapidly as the magnetic field is increased. This type of behavior is quite well-known and is the result of reduced emission from the front portion of the cathode. In other words, as the magnetic field is increased the electrons leaving the left-hand section of the cathode pass closer to the front section thus increasing the space-charge density in this region and decreasing the emission.

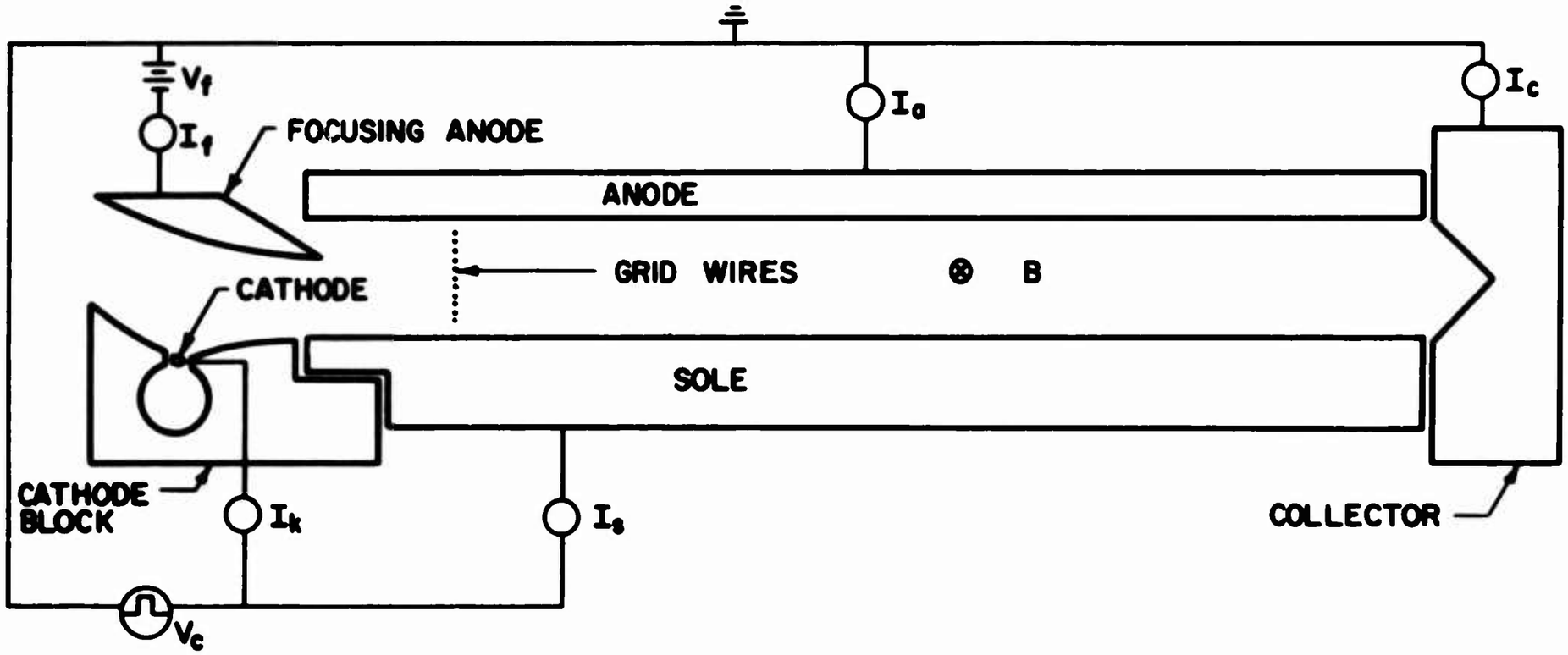

FIG. 7.1 SCHEMATIC DIAGRAM OF THE EXTENDED KINO GUN CROSSED-FIELD DEVICE.

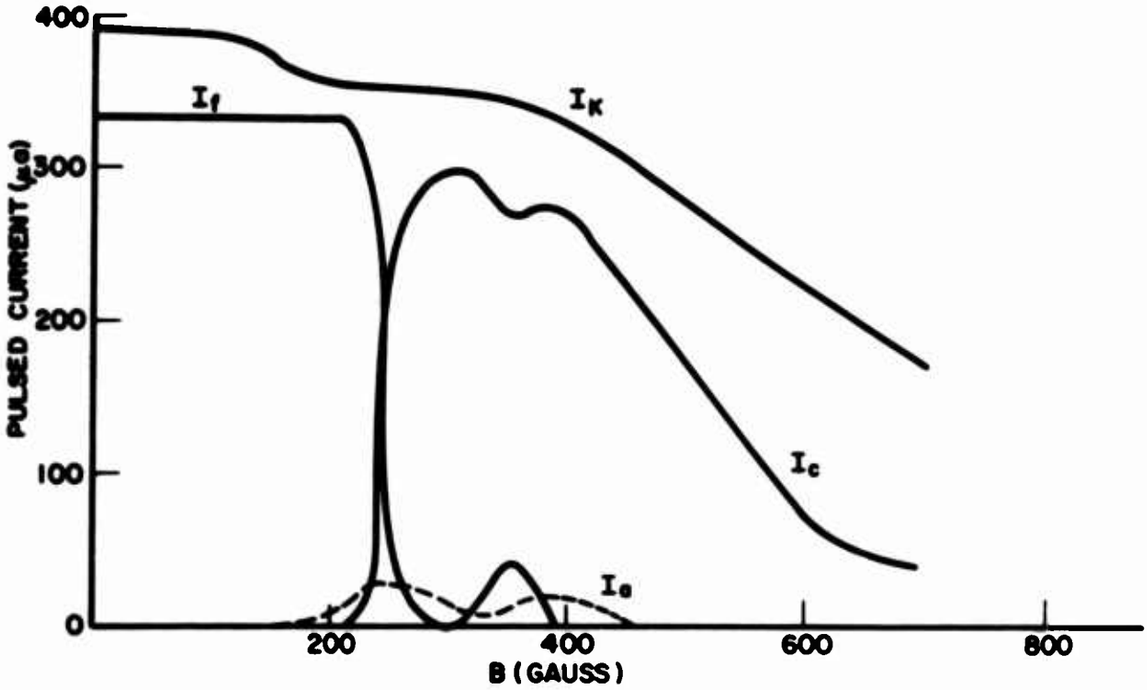

a.) CURRENT VARIATIONS

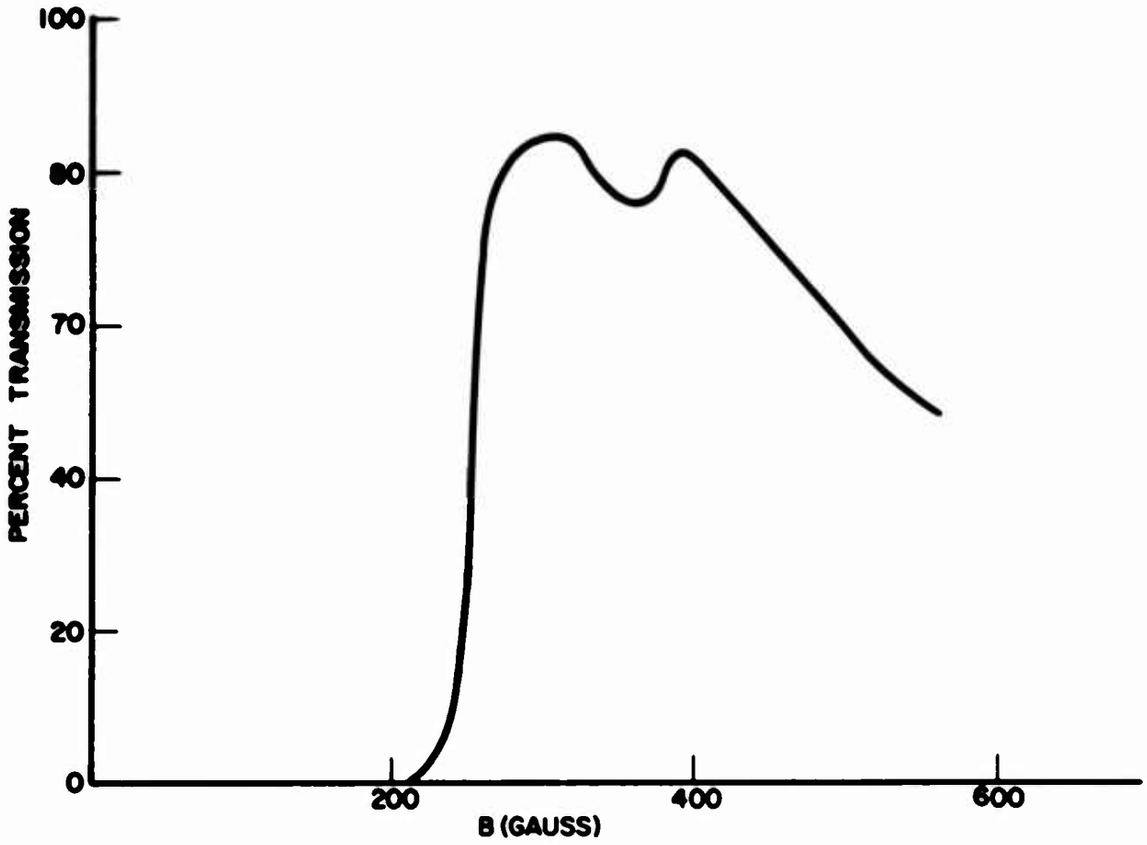

b.) PERCENT TRANSMISSION

FIG. 7.2 EXPERIMENTAL VARIATION OF CURRENTS WITH MAGNETIC FIELD. (V_c = -1430, V_f = -500)

I_f remains essentially constant until the cut-off magnetic field is reached at which point it decreases sharply to zero. This, of course, is a direct consequence of the increased magnetic field causing the beam to bend until it is no longer intercepted by the focusing anode. Simultaneously with the decrease in I_f the collector current rises abruptly as indicated in Fig. 7.2a. The expected behavior of I_c would be a smooth increase to a maximum value before decreasing as a result of the reduction in I_k. This is essentially the pattern followed by I_c except for a slight depression which occurs shortly beyond the maximum I_c value (i.e., at approximately B = 375 gauss in Fig. 7.2a). At this same point, I_f rises abruptly to a relative maximum before decreasing again as the magnetic field is increased.

The above phenomenon can be explained by considering the cycloidal nature of the electrons in the gun region. As the magnetic field is increased, the curvature of the beam increases until eventually some of the electrons strike the front ramp electrode while others reach a position very close to that electrode. Those which strike the ramp cause secondary electrons to be emitted and these are immediately drawn to the focusing anode. Those electrons which do not strike the ramp can also reach the focusing anode on their subsequent upward trajectory. In either case, I_f has a relative maximum and I_c a corresponding relative minimum.

Figure 7.2b illustrates the percentage of cathode current which reaches the collector as a function of magnetic field for the above conditions. The maximum transmission is approximately 87 percent at 350 gauss. This value was typical of the optimum results found for most magnetic field conditions. However, for a given magnetic field the transmission is obviously also a function of V_c and V_f.

The current variations for higher velocity beams were similar to the preceding results. Figure 7.3a illustrates the curves obtained for $V_f = -900$ volts and $V_c = -2400$ volts. The relative I_f maximum occurs at a higher magnetic field, approximately 470 gauss, which is consistent with the fact that the electric field is greater; i.e., the scaling constant $(V_f - V_c)/B^2$ which maintains the trajectories constant is 6.62×10^5 at the relative I_f maximum point in Fig. 7.2a and 6.82×10^5 in Fig. 7.3a. This implies that the relative increase in focusing-anode current beyond cut-off occurs under conditions for which the electron trajectories are essentially the same. Figure 7.3b shows the transmission as a function of magnetic field with the maximum value being 90 percent.

The dependence of the various currents on the voltage difference between the cathode and focusing anode $(V_f - V_c)$ is illustrated in Figs. 7.4 and 7.5 where each case involves different values of V_f and B. The cathode current appears to vary as $(V_f - V_c)^2$. This is demonstrated by the parabolic curves in the figures which were plotted according to the equation

$$I = C + K \frac{(V_f - V_c)^2}{B} , \qquad (7.1)$$

where C and K are constants. This variation agrees with the results of other experimenters[17,38] who used simpler electron injection systems. Midford[11] has stated that I_k varies linearly with $(V_f - V_c)$ for the Kino short gun, although this relation appears to be valid only in the vicinity of the design value of $(V_f - V_c)$. On the other hand he shows that the long gun cathode current has a $(V_f - V_c)^2/B$ variation.

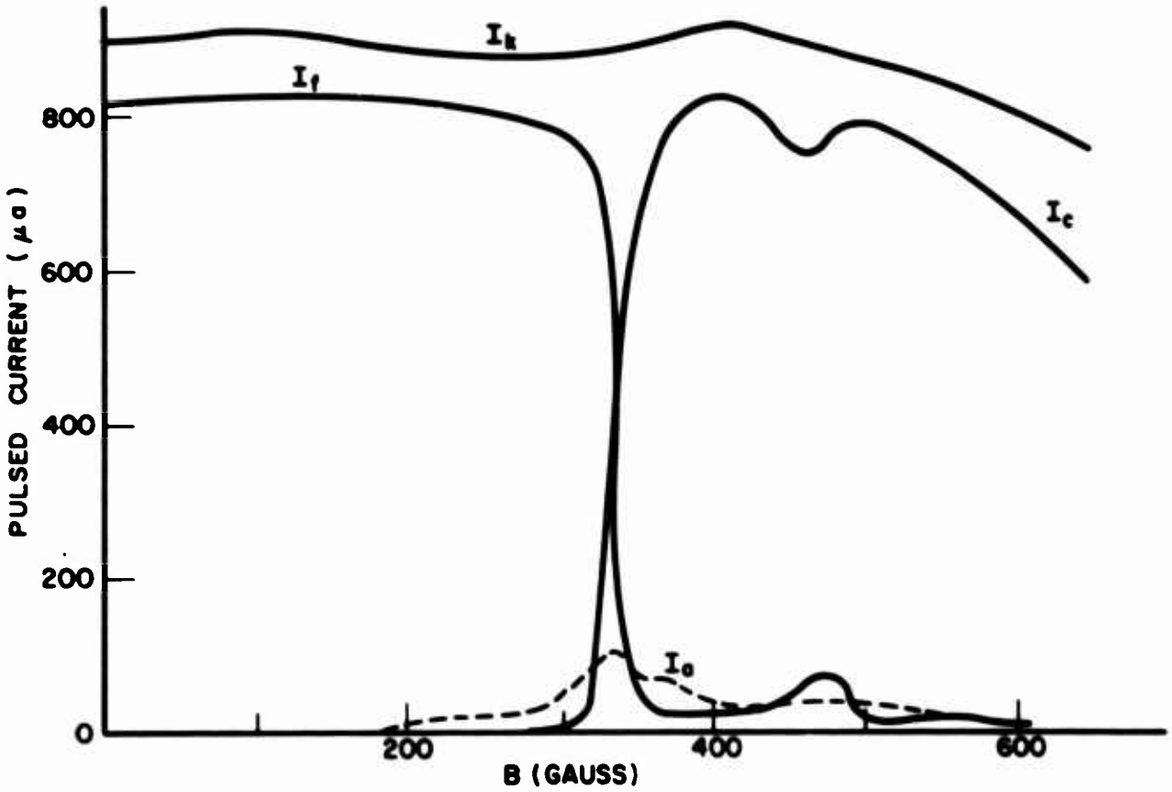

a.) CURRENT VARIATIONS

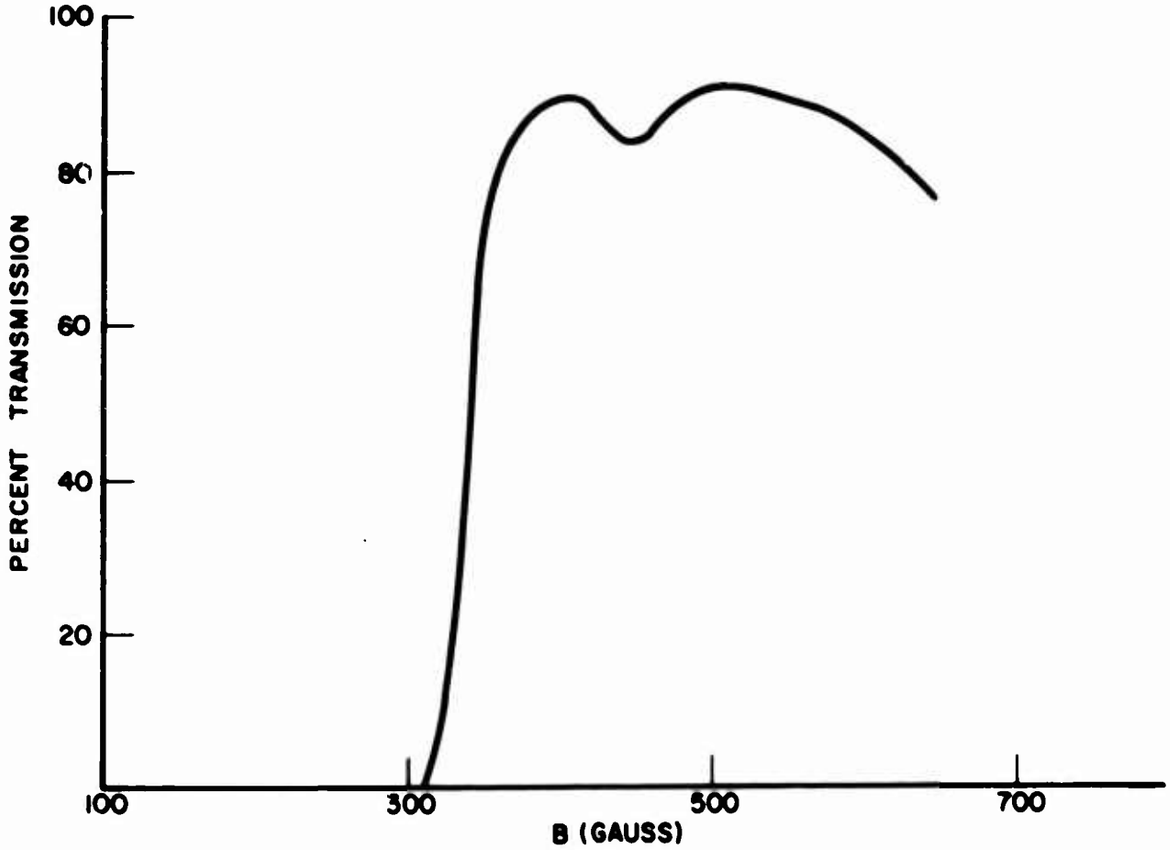

b.) PERCENT TRANSMISSION

FIG. 7.3 EXPERIMENTAL VARIATION OF CURRENTS WITH MAGNETIC FIELD. (V_c = -2400, V_f = -900)

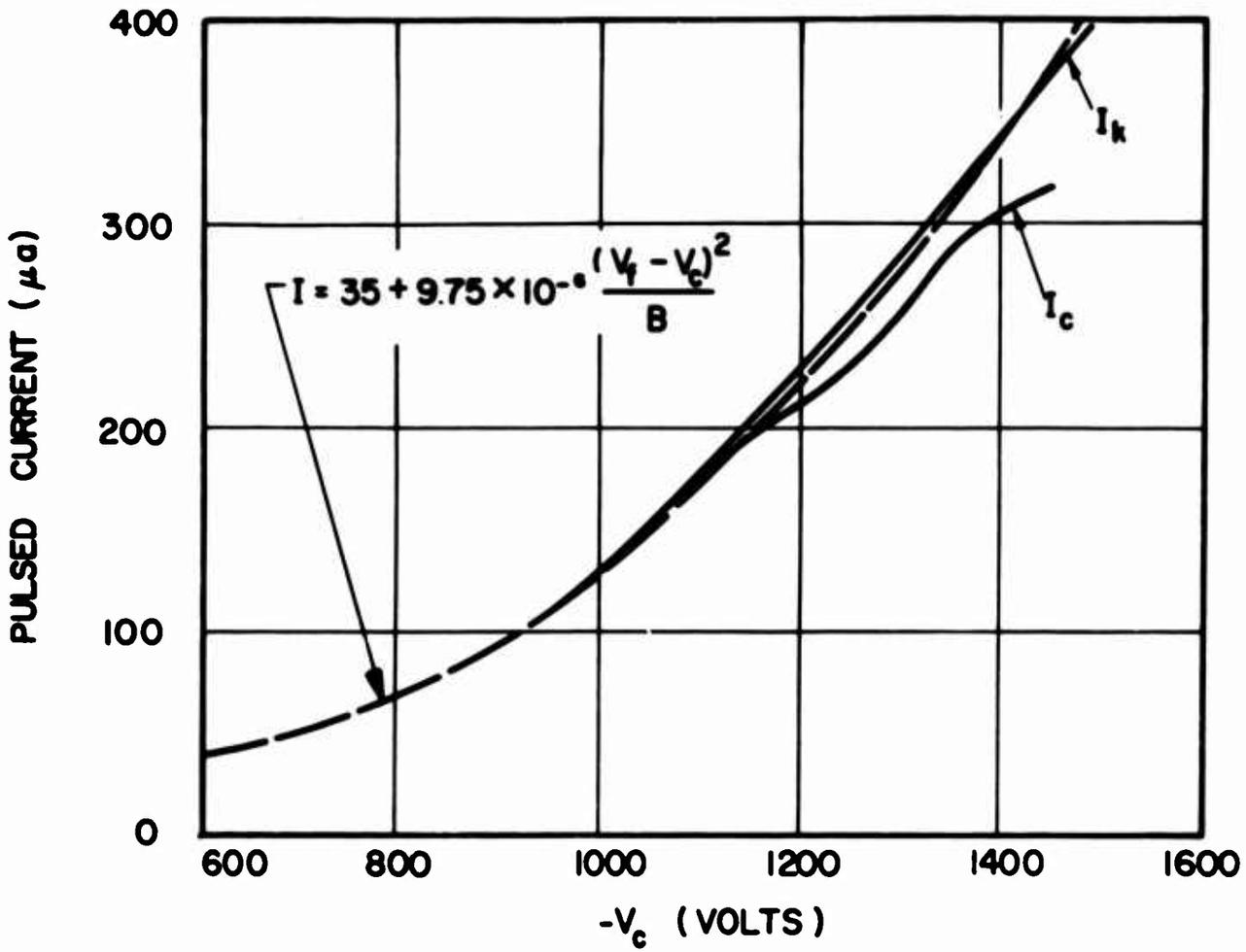

FIG. 7.4 VARIATION OF CURRENTS WITH V_c. NO GRID WIRES. (V_f = - 500, B = 256 GAUSS)

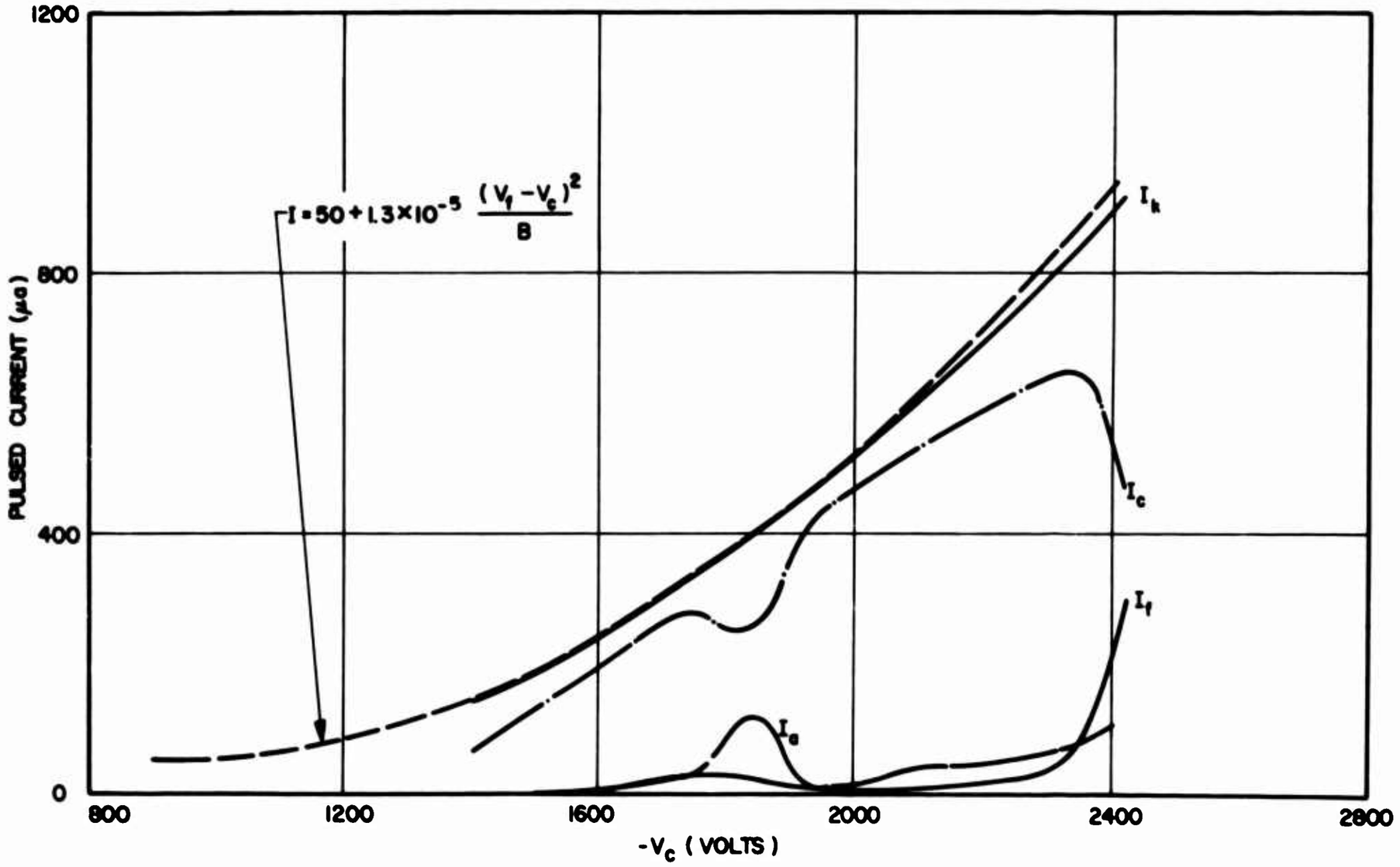

FIG. 7.5 VARIATION OF CURRENTS WITH V_c. NO GRID WIRES.

(V_f = - 900, B = 335)

The constants C and K in Eq. 7.1 were selected to fit the experimental data points in Figs. 7.4 and 7.5 and there is no indication of the magnetic field range for which they apply. However, Figs. 7.6 and 7.7 provide some idea of the region of validity of Eq. 7.1. The operating conditions are identical to those of Fig. 7.4 except that B has been increased from 256 gauss to 315 gauss and 387 gauss respectively. The agreement between the theoretical parabolas and the experimental curves is quite reasonable and suggests that the $(V_f - V_c)^2/B$ variation of the cathode current is valid over a rather wide range of magnetic field values.

The focusing anode in the experimental Kino gun is located along the theoretical curve for the normalized potential of $\Phi_f = 25$. The Kino flow conditions require that the y-component of current density at any point be given by

$$J_y = \frac{\epsilon_o \omega_c^2}{(\eta)^{1/2}} (\varphi/\Phi)^{1/2} = \text{constant} \quad , \qquad (7.2)$$

where φ is the actual potential at the point and Φ is the normalized value. Using this equation it is possible to compare the experimental currents with the theoretical predictions. However, this requires a knowledge of the voltage at a given point in the beam.

The following procedure can be used to obtain an approximate solution for J_y. Starting with B = 0 the magnetic field is increased until I_f goes to zero which corresponds to the situation where the beam passes adjacent to the focusing anode but is not intercepted. Consequently the voltage at the top of the beam is approximately φ_f which allows J_y to be computed from Eq. 7.2. For each φ_f value a different cut-off magnetic field (B_{co}) is required and hence also a different J_y. At the

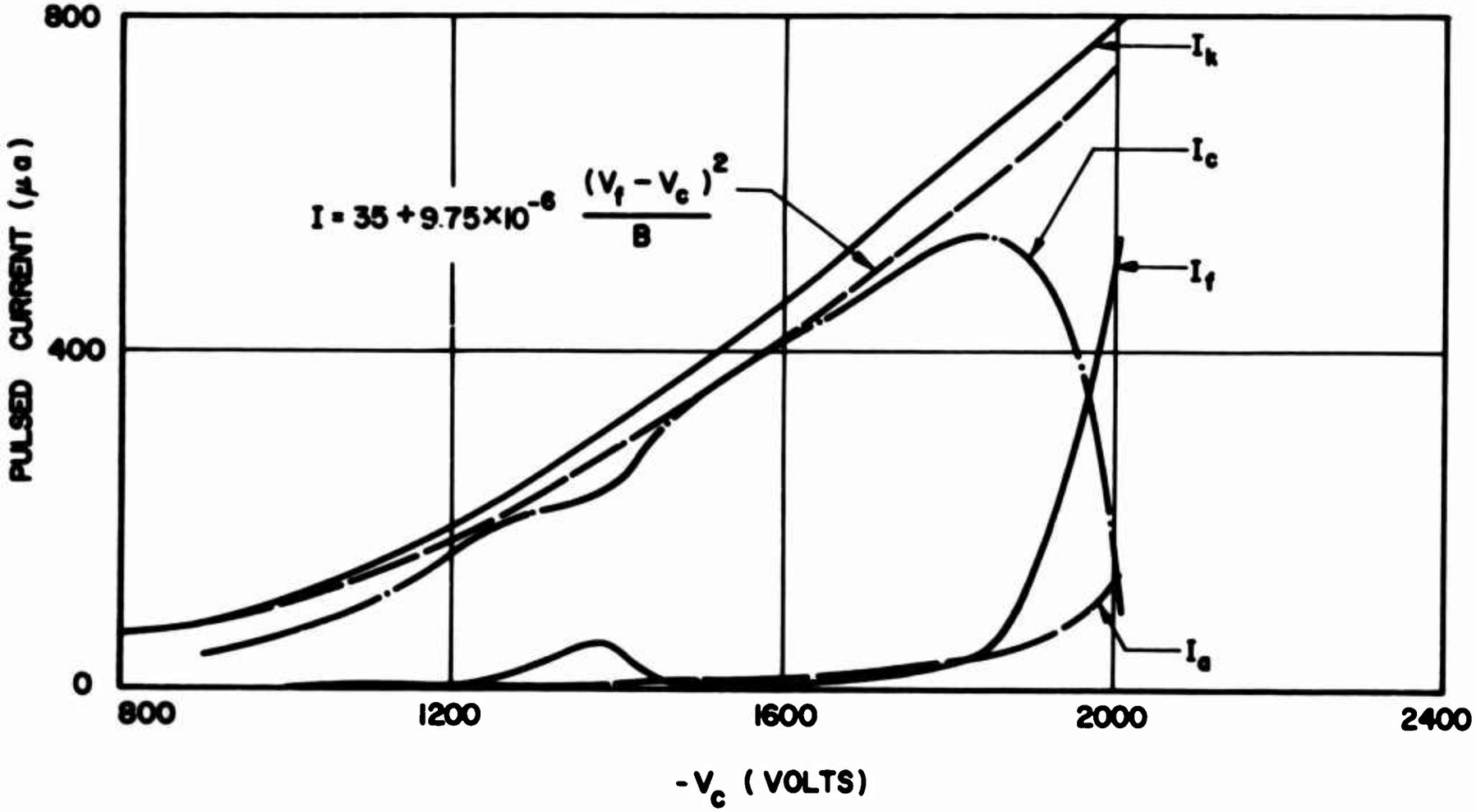

FIG. 7.6 VARIATION OF CURRENTS WITH V_c. NO GRID WIRES. (V_f = - 500, B = 315)

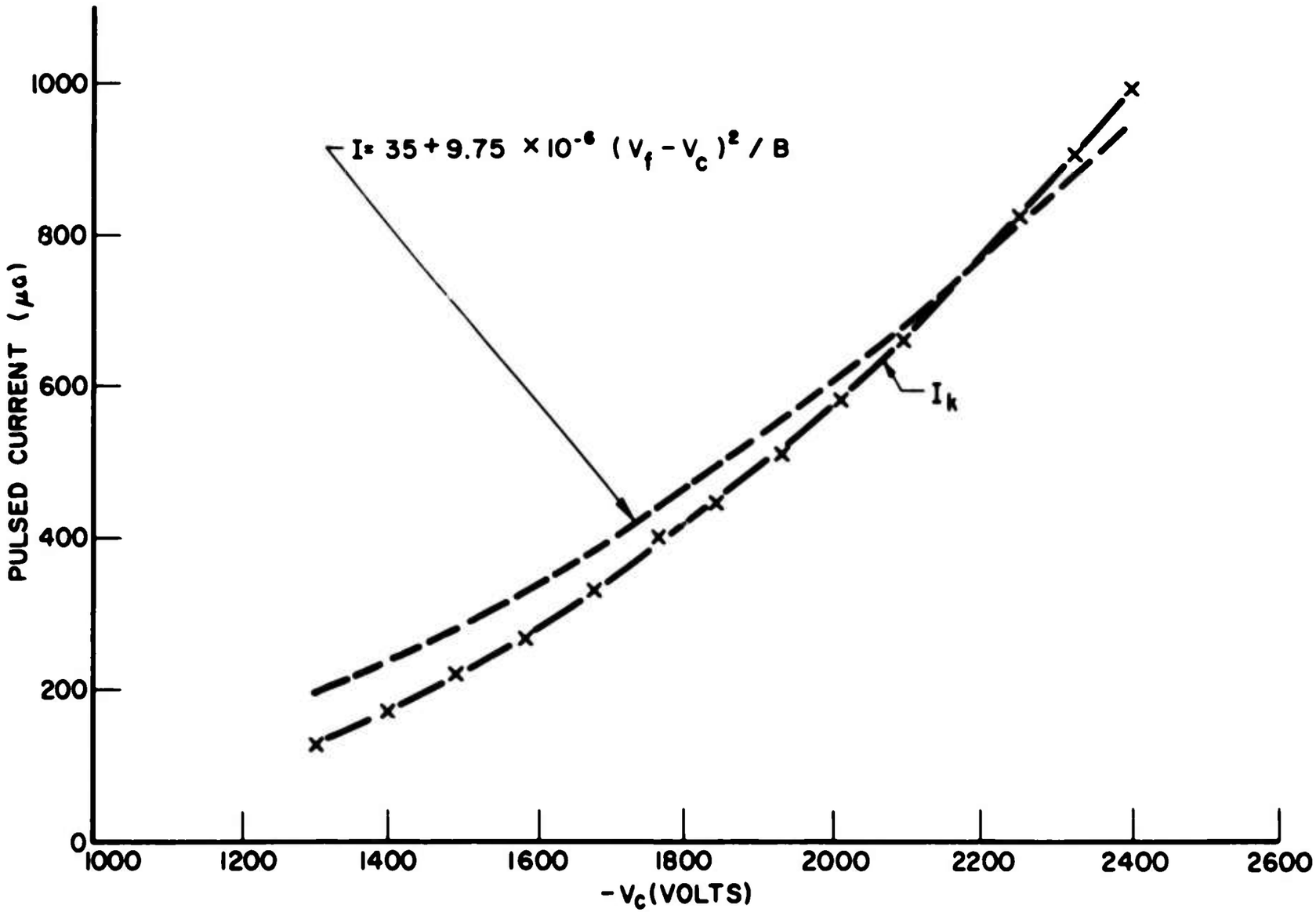

FIG. 7.7 VARIATION OF CATHODE CURRENT WITH V_c. (V_f = -500, B = 387)

same time the experimental cathode current densities (J_k) can be determined from the total emission. Figure 7.8 illustrates the theoretical J_y and experimental J_k variations as a function of B_{co}. The curves are very similar although the experimental J_k values do drop off somewhat at higher B_{co} values. Nevertheless the results indicate that in general the average cathode emission behaves according to the theoretical relationship expressed by Eq. 7.2.

The space-charge-limited Poisson cell analysis of the extended Kino short gun described in Chapter III resulted in an average cathode current density of 0.79 amp/cm^2 for φ_f = 1540 volts and B = 368 gauss. A few of the experimental studies were conducted under similar conditions and are listed below for comparison:

(a) φ_f = 1500 volts, B = 352 gauss, average cathode current density = $\bar{J}_k$ = 0.74 amp/cm^2;

(b) φ_f = 1500 volts, B = 370 gauss, $\bar{J}_k$ = 0.75 amp/cm^2; and

(c) φ_f = 1500 volts, B = 387 gauss, $\bar{J}_k$ = 0.72 amp/cm^2.

Thus the experimental cathode emission is generally within 10 percent of the Poisson cell value.

The beam analyzer investigations described in the following section allow the determination of the beam profile in the interaction region. Figure 7.9 illustrates such a profile where 90 percent of the beam current flows between the boundaries indicated by the triangles. The beam outline in the gun region was obtained from a Poisson cell analysis in which the scaling parameter $\varphi_f/B^2 = 9.76 \times 10^5$ was nearly the same as the 9.97×10^5 experimental value. These results indicate that the electron beam formed by the experimental gun is essentially the same as was predicted by the Poisson cell investigation.

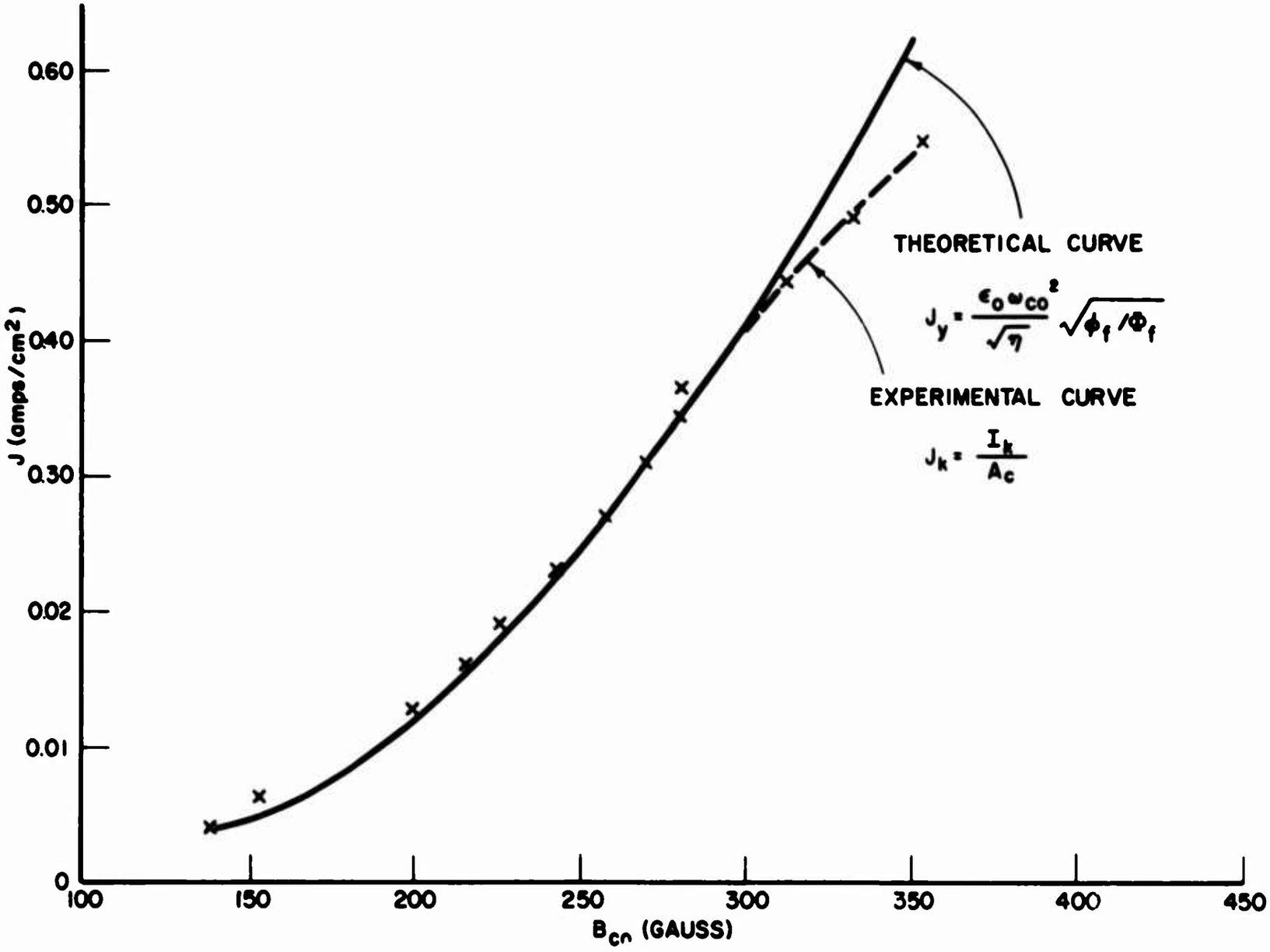

FIG. 7.8 COMPARISON OF THEORETICAL AND EXPERIMENTAL CATHODE CURRENT DENSITIES. (Φ_f = 25)

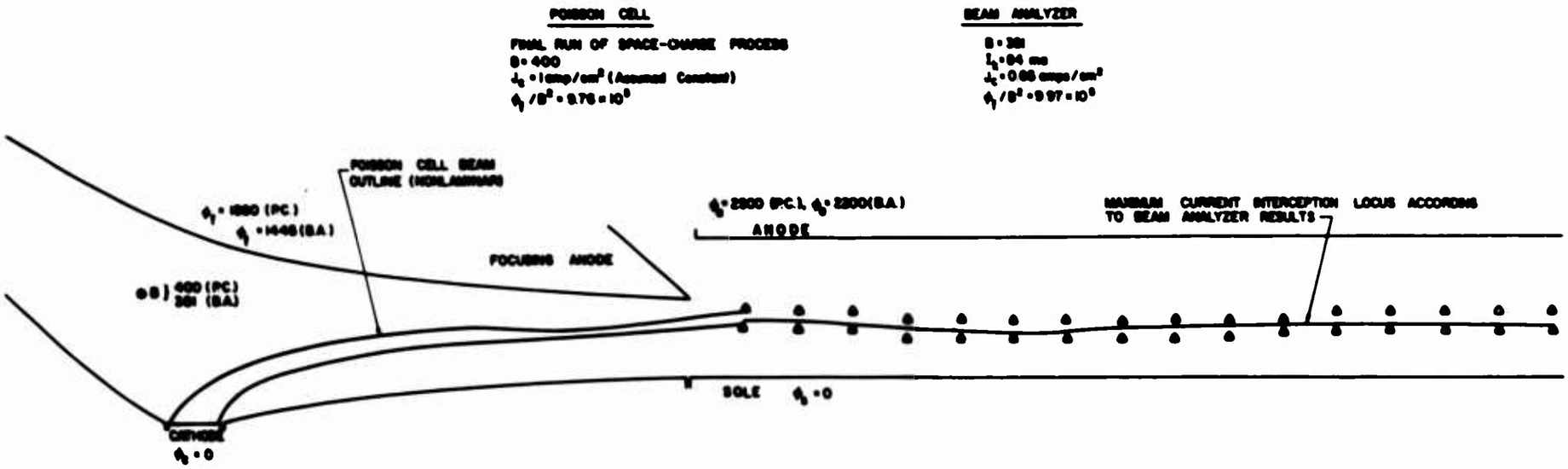

FIG. 7.9 EXTENDED KINO SHORT GUN RESULTS. THE BEAM IN THE GUN REGION IS OBTAINED FROM THE POISSON CELL INVESTIGATION WHILE THE LOCATION OF THE BEAM IN THE ANODE-SOLE REGION IS DETERMINED FROM THE BEAM ANALYZER EXPERIMENTS.

7.3 Gross Characteristics of Electron Beams

The grid wire assembly is located so that the ten wires lie in a plane which is transverse to the general direction of electron flow. A voltage is applied to each wire by connection to the eleven resistor network as indicated in Fig. 7.10. The currents intercepted by the various wires provide a description of the gross characteristics of the space-charge flow in the anode-sole region. As described previously, the grid assembly is mounted on the movable center pedestal of the beam analyzer thus allowing investigation of the beam over a z-interval of 1.2 inches.

The magnitude of current intercepted by a given wire depends on the current density at that point in the beam as well as on the potential difference between the wire and the corresponding location in the beam. If it is assumed that this potential difference is relatively small, then the currents intercepted by the wires provide a description of the beam profile. The variation of the beam profile throughout the interaction region can be observed by moving the grid system and monitoring the current interceptions at the various cross sections.

Figure 7.11a illustrates the profile variations obtained for $V_c = -1425$ volts, $V_f = -500$ volts and $B = 352$ gauss. It is obvious from this figure that the beam is undergoing periodic variation as it proceeds through the anode-sole region. The behavior is illustrated in Fig. 7.11b where the y-location of the maximum current interception has been plotted for each z-position of the grid wires. The result indicates a distance of approximately 0.48 inch between successive maxima and 0.46 inch between minima. The theoretical variation in a planar anode-sole region can be written as

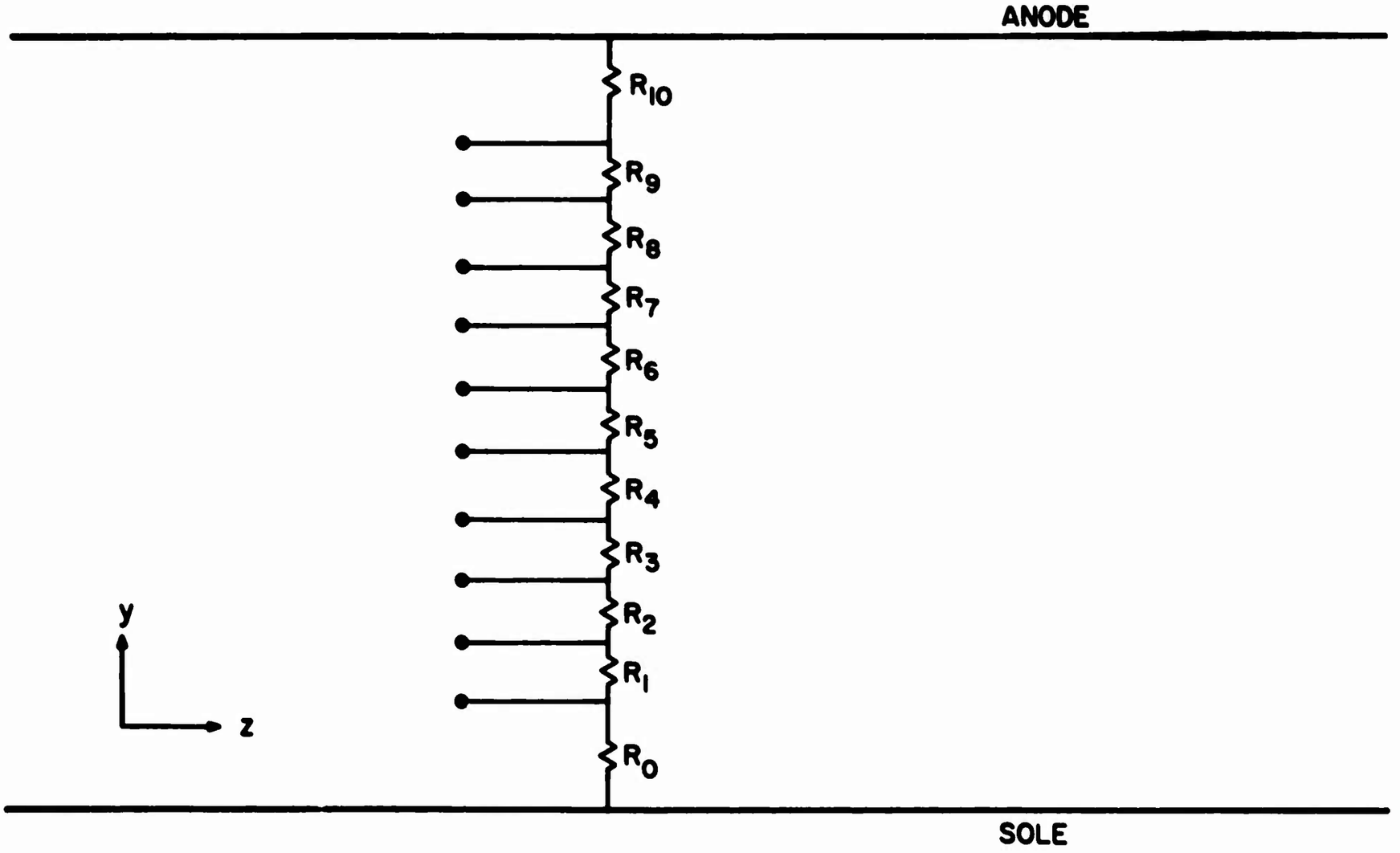

FIG. 7.10 GRID WIRES FOR INTERCEPTING THE ELECTRON BEAM.

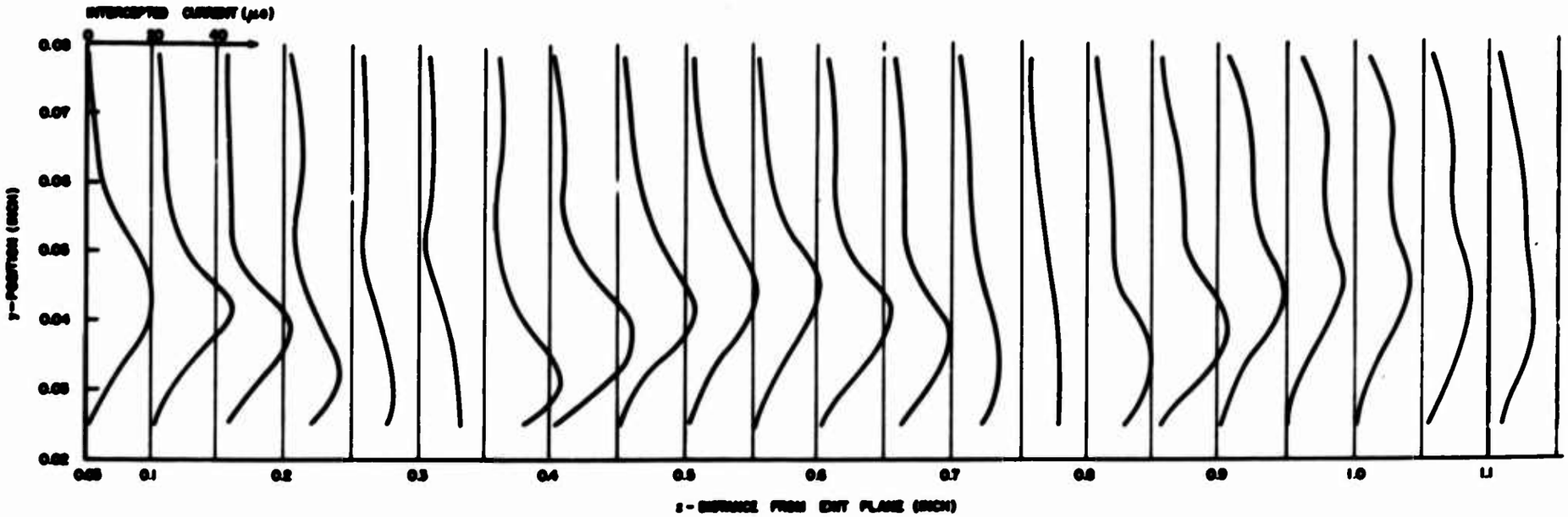

FIG. 7.11a CURRENTS INTERCEPTED BY THE GRID WIRES AT VARIOUS CROSS SECTIONS IN THE INTERACTION REGION. (V_c = -1425, V_f = -500, B = 352 GAUSS)

$$L_{th} = \frac{2\pi V_{a-s}}{\eta d B^2} , \qquad (7.3)$$

where V_{a-s} = potential difference between the anode and sole, and d = anode-sole spacing. Substituting the appropriate values of Fig. 7.11 into Eq. 7.3 results in L_{th} = 0.496 inch which is in reasonable agreement with the experimental values.

Figure 7.12a illustrates the profiles at various z-locations for V_c = -1890 volts and B = 409 gauss. The solid curves represent V_f = -1100 volts while the broken curves are for V_f = -1000 volts. Figure 7.12b is a plot of the y-location of the maximum current interception as a function of the z-position of the grid assembly. The reduction in focusing-anode voltage from -1100 to -1000 volts has resulted in a more nearly laminar beam as indicated by the reduced amplitude of the maximum interception curve. In each case the experimental and theoretical periods are in good agreement as indicated on the figure.

The undulation of the beam under high magnetic field conditions is illustrated in Fig. 7.13a and 7.13b where V_c = -2210 volts, V_f = -850 volts and B = 590 gauss. Obviously the strong magnetic field has caused the beam to travel rather close to the sole such that at its minimum location very little current strikes the grid wires. Once again there is good agreement between the theoretical and experimental values of the period. The figure also seems to imply that the amplitude of the beam undulation decreases as the beam moves away from the gun exit plane. At the same time the maximum current intercepted at any cross section is observed to increase with z. This implies either an increase in the space-charge density or in the beam velocity. However, the behavior is not

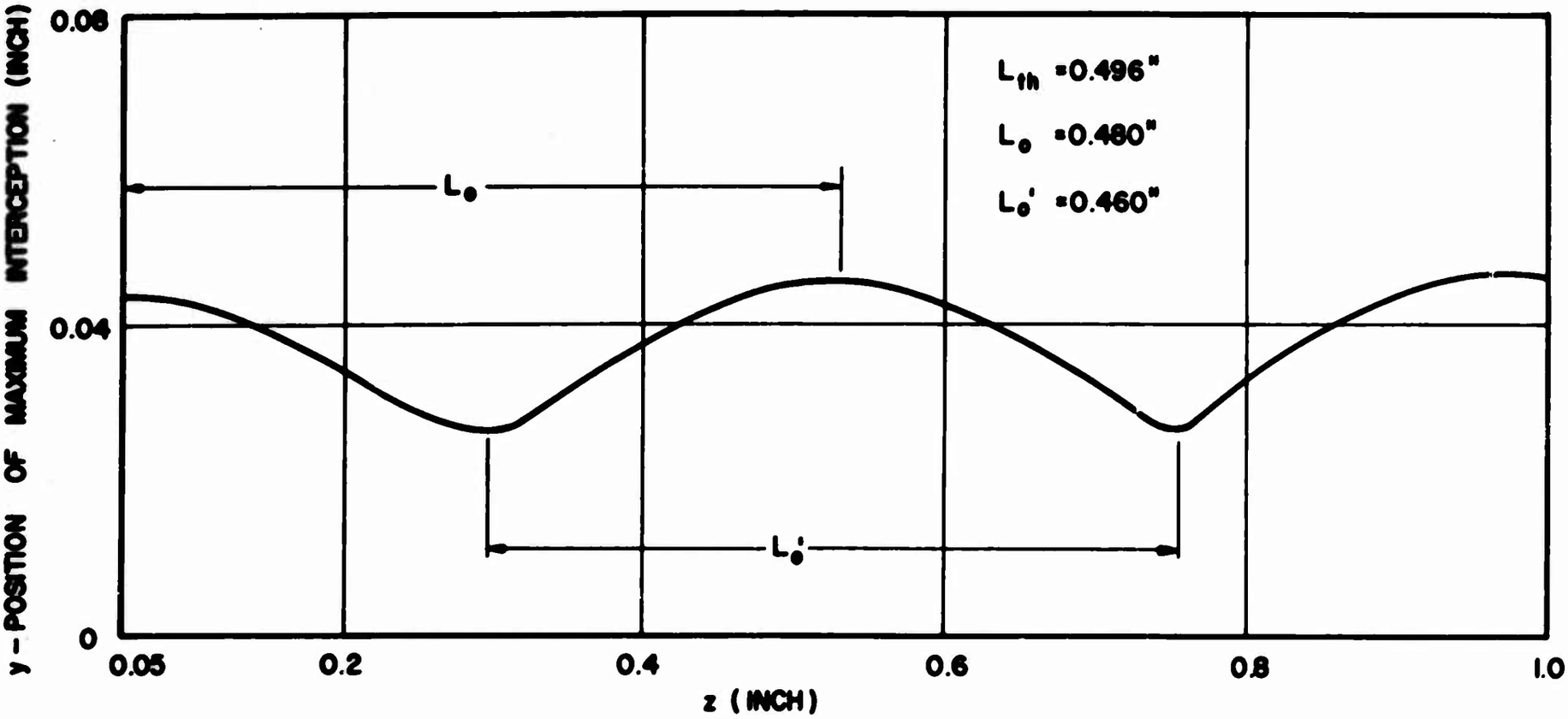

FIG. 7.11b LOCATION OF MAXIMUM CURRENT INTERCEPTION AT VARIOUS z-POSITIONS.

(V_c = -1425, V_f = -500, B = 352 GAUSS)

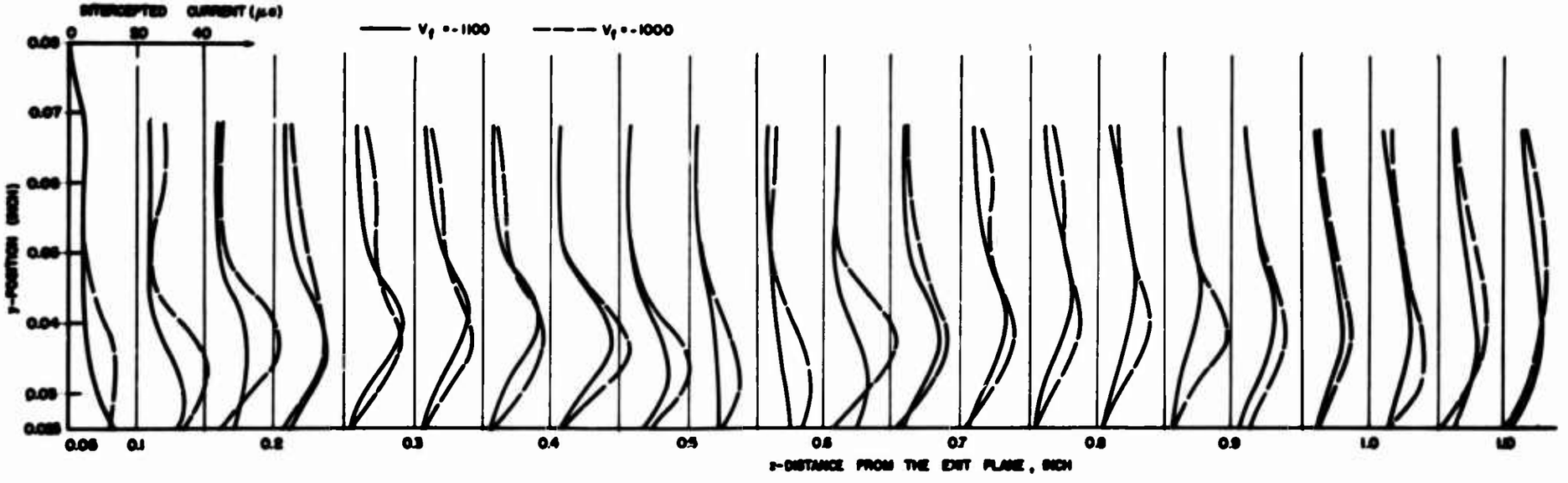

FIG. 7.12a CURRENTS INTERCEPTED BY THE GRID WIRES AT VARIOUS CROSS SECTIONS IN THE INTERACTION REGION. (V_c = - 1890, B = 409 GAUSS)

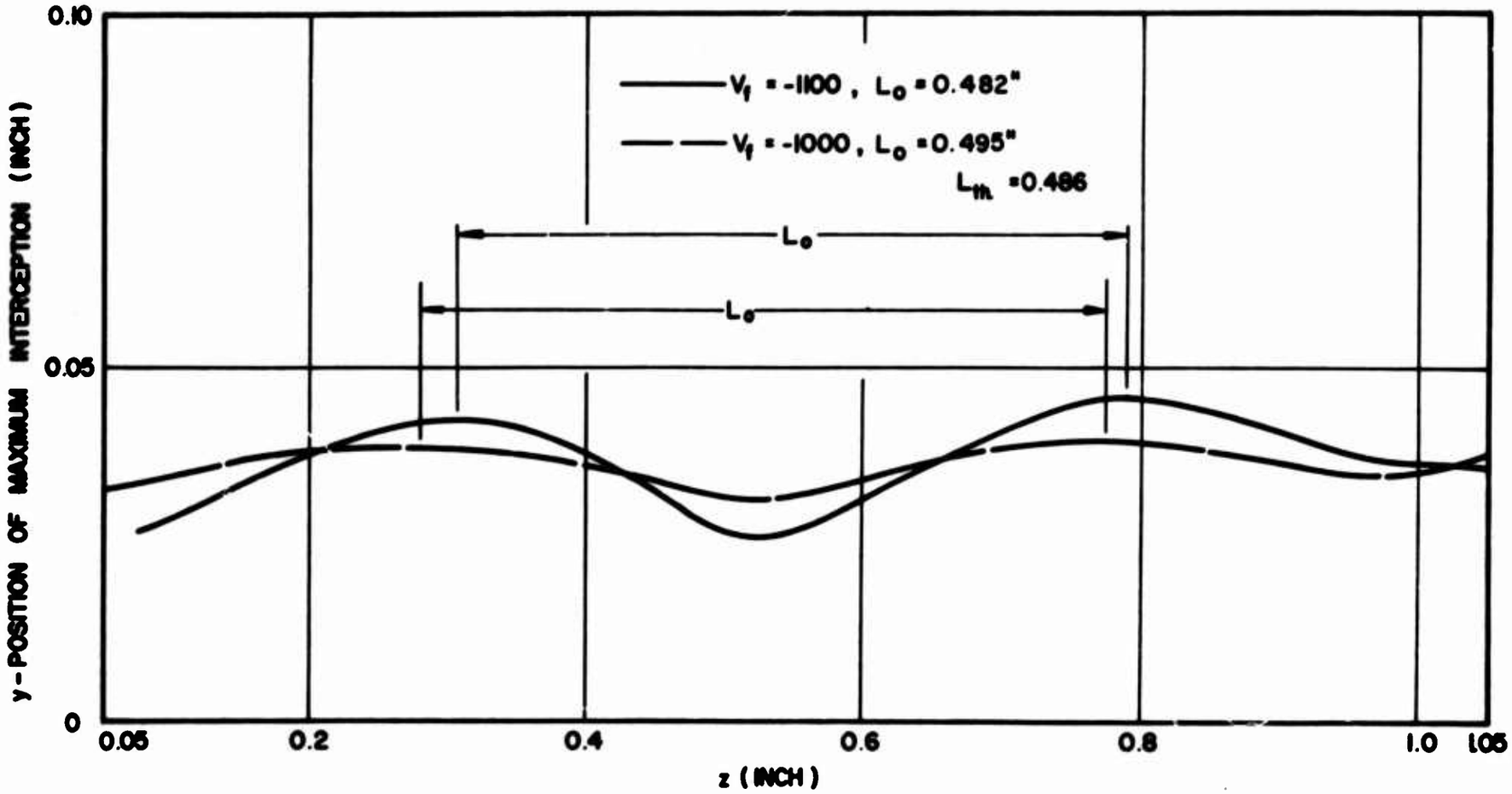

FIG. 7.12b LOCATION OF MAXIMUM CURRENT INTERCEPTION AT VARIOUS z-POSITIONS. (V_c = - 1890, B = 409 GAUSS)

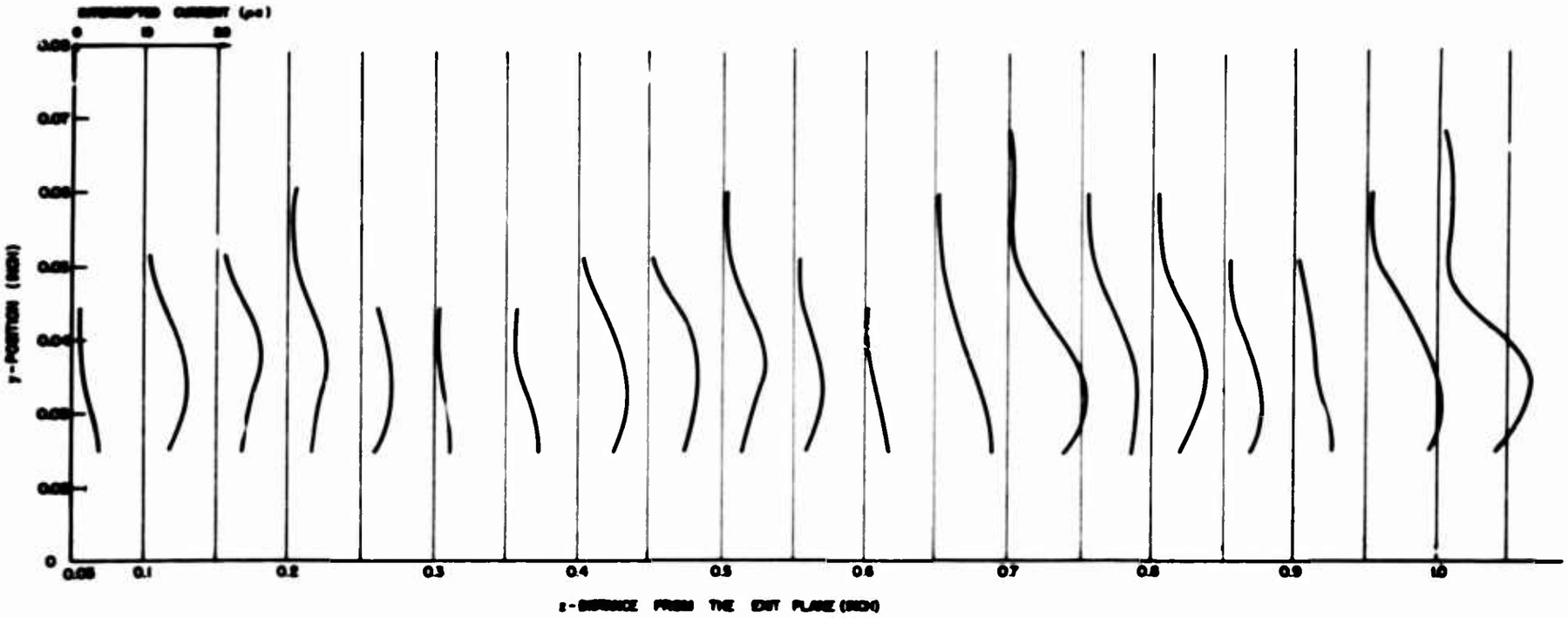

FIG. 7.13a CURRENTS INTERCEPTED BY THE GRID WIRES AT VARIOUS CROSS SECTIONS IN THE INTERACTION REGION. (V_c = - 2210, V_f = - 850, B = 590 GAUSS)

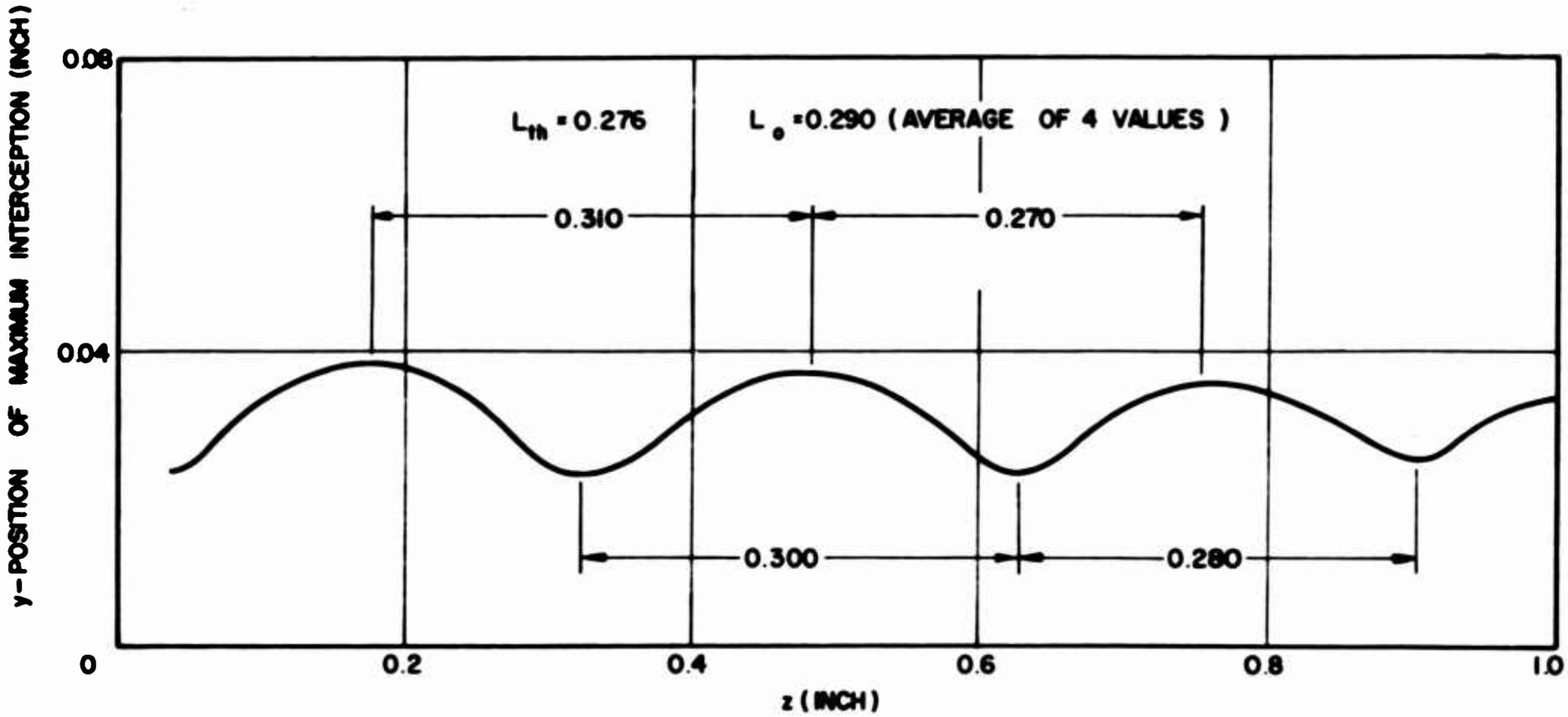

FIG. 7.13b LOCATION OF MAXIMUM CURRENT INTERCEPTION AT VARIOUS z-POSITIONS. (V_c = - 2210, V_f = -850, B = 590 GAUSS)

sufficiently consistent to allow definite conclusions to be formed. For example, in Fig. 7.11 the exact opposite behavior was observed such that the maximum current interception decreased with z while simultaneously the beam became wider and less clearly defined.

Figure 7.14a (V_c = -1450, V_f = -500, B = 335) presents a rather interesting situation wherein the beam moves through the interaction region at a nearly fixed location and with approximately the same profile at each cross section. The variation of the maximum profile point illustrated in Fig. 7.14b shows that the beam undulation is extremely small. The above results imply that the transition from the gun to the interaction region is fairly smooth and furthermore that the electron velocities at the gun exit plane are nearly equal to E/B, the value required for linear flow. Assuming a narrow beam with negligible space charge located as illustrated in Fig. 7.14b, the electric fields in the two regions are given by

$$E \text{ at gun exit} = 4.85 \times 10^5 \text{ volts/m}$$

and

$$E \text{ in anode-sole region} = 4.45 \times 10^5 \text{ volts/m.}$$

The velocity of the electrons is found to be

$$v = 1.23 \times 10^7 \text{ m/sec} ,$$

whereas the E/B in the interaction region is

$$E_{a-s}/B = 1.33 \times 10^7 \text{ m/sec} .$$

Although the velocity of the electrons entering the anode-sole region is slightly less than the desired value, the tendency of the beam to move up because of this condition is counteracted by the fact that $E_{a-s} < E_{exit}$ which tends to move the beam down. Thus the net result is an approximate

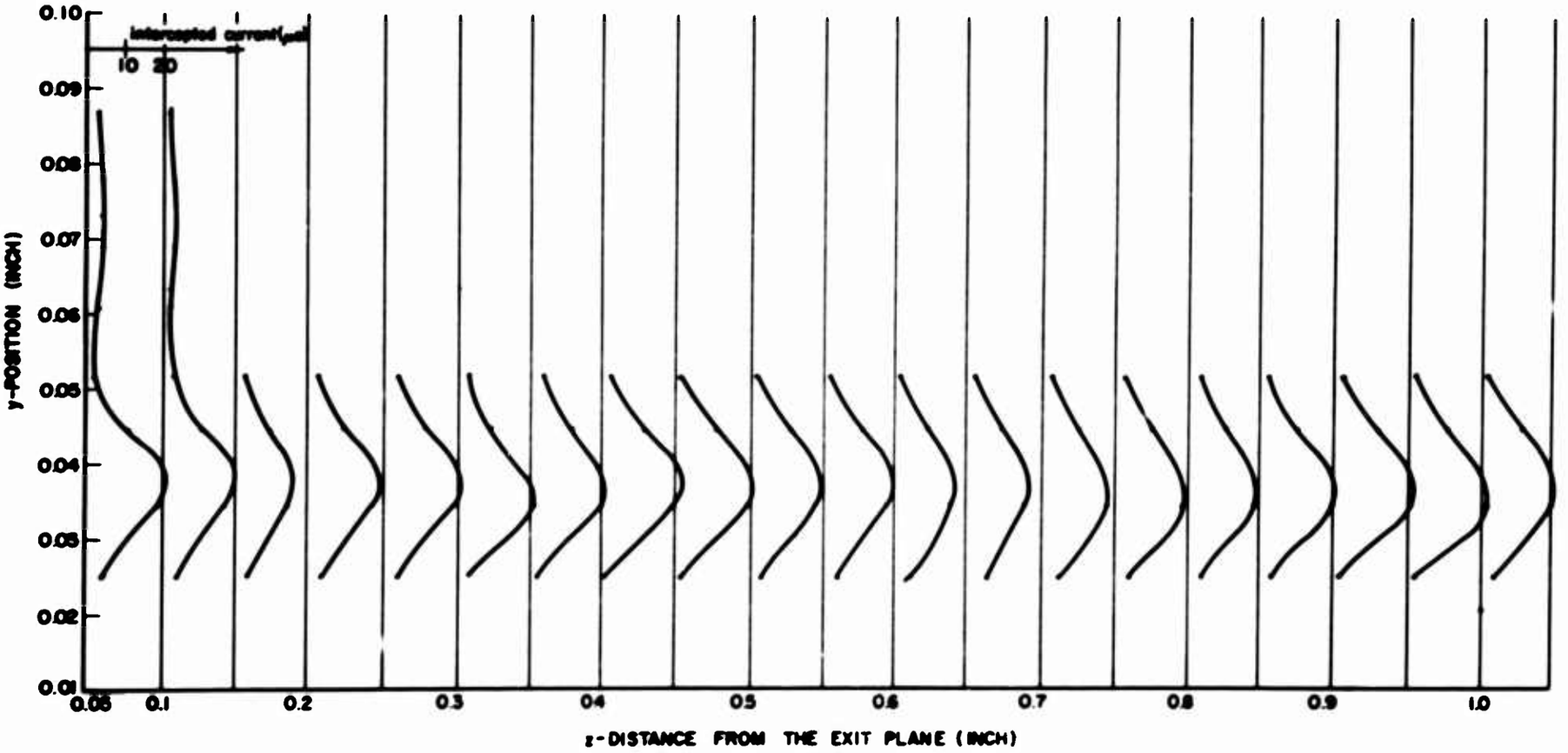

FIG. 7.14a CURRENTS INTERCEPTED BY THE GRID WIRES AT VARIOUS CROSS SECTIONS IN THE INTERACTION REGION. (V_c = -1450, V_f = -500, B = 335)

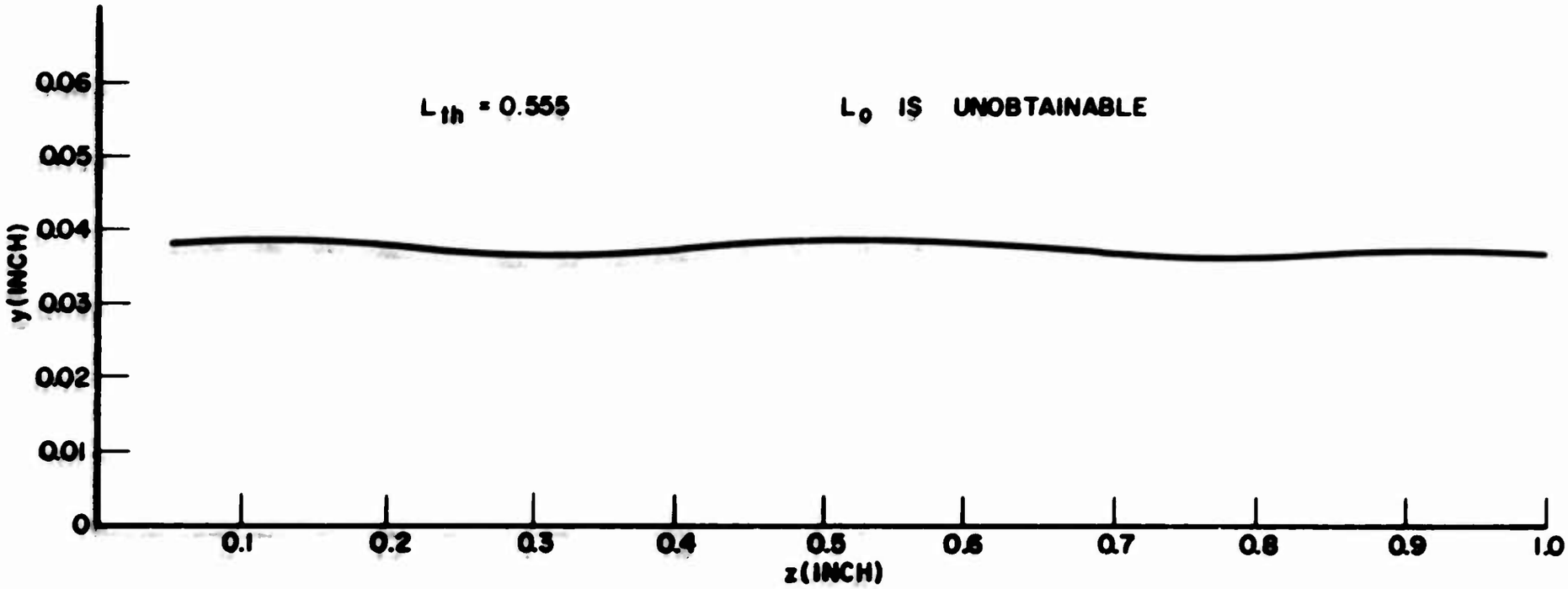

FIG. 7.14b LOCATION OF MAXIMUM CURRENT INTERCEPTIONS AT VARIOUS z-POSITIONS.

(V_c = -1450, V_r = -500, B = 335)

balance between the electric and magnetic forces so that the beam undulation is relatively small.

The results of Fig. 7.15a were obtained when the voltages and magnetic field were increased to $V_c = -1765$, $V_f = -660$ and $B = 465$. The beam experiences a pronounced undulation during its motion through the anode-sole region as indicated in Fig. 7.15b. Performing the same calculations as above results in

$$E_{exit} = 5.15 \times 10^5 \text{ volts/m},$$

$$E_{a-s} = 5.42 \times 10^5 \text{ volts/m},$$

$$v = 1.02 \times 10^7 \text{ m/sec, and}$$

$$E_{a-s}/B = 1.16 \times 10^7 \text{ m/sec.}$$

The reason for the undulation is immediately obvious. The velocity of the incoming electrons is less than the desired value while at the same time the anode-sole region electric field exceeds the exit plane value. Both of these conditions cause the entering electrons to move in an upward direction, a result which is substantiated by Fig. 7.15b.

Figures 7.16a and b illustrate the results when the voltages and magnetic field were increased still further to $V_c = -2000$, $V_f = -750$, and $B = 578$. The behavior of the beam is similar to that of Fig. 7.15 insofar as the undulatory nature of the motion is concerned. As in most cases the experimental and theoretical cycloidal periods are approximately the same.

The above experimental results have been interpreted without considering the effect which the presence of the grid wires exerts on the beam. This effect can be evaluated qualitatively by referring to Figs. 7.17a and b which indicate the results when grid wire number 4 was disconnected from the resistance network with $V_c = -1490$, $V_f = -500$ and $B = 352$ (although wire 4 draws no current, the profiles are plotted as

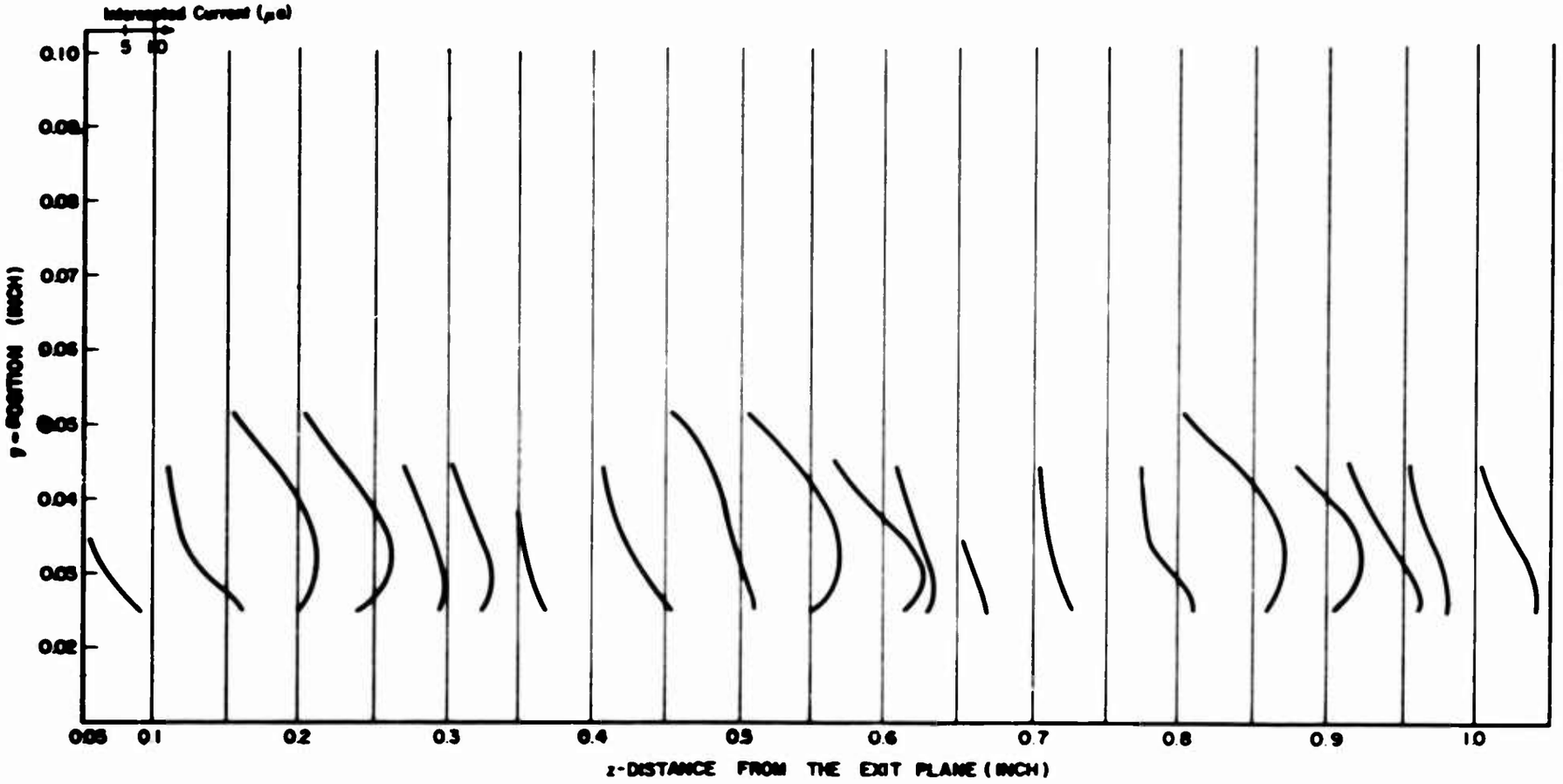

FIG. 7.15a CURRENTS INTERCEPTED BY THE GRID WIRES AT VARIOUS CROSS SECTIONS. (V_c = -1765, V_f = -660, B = 465)

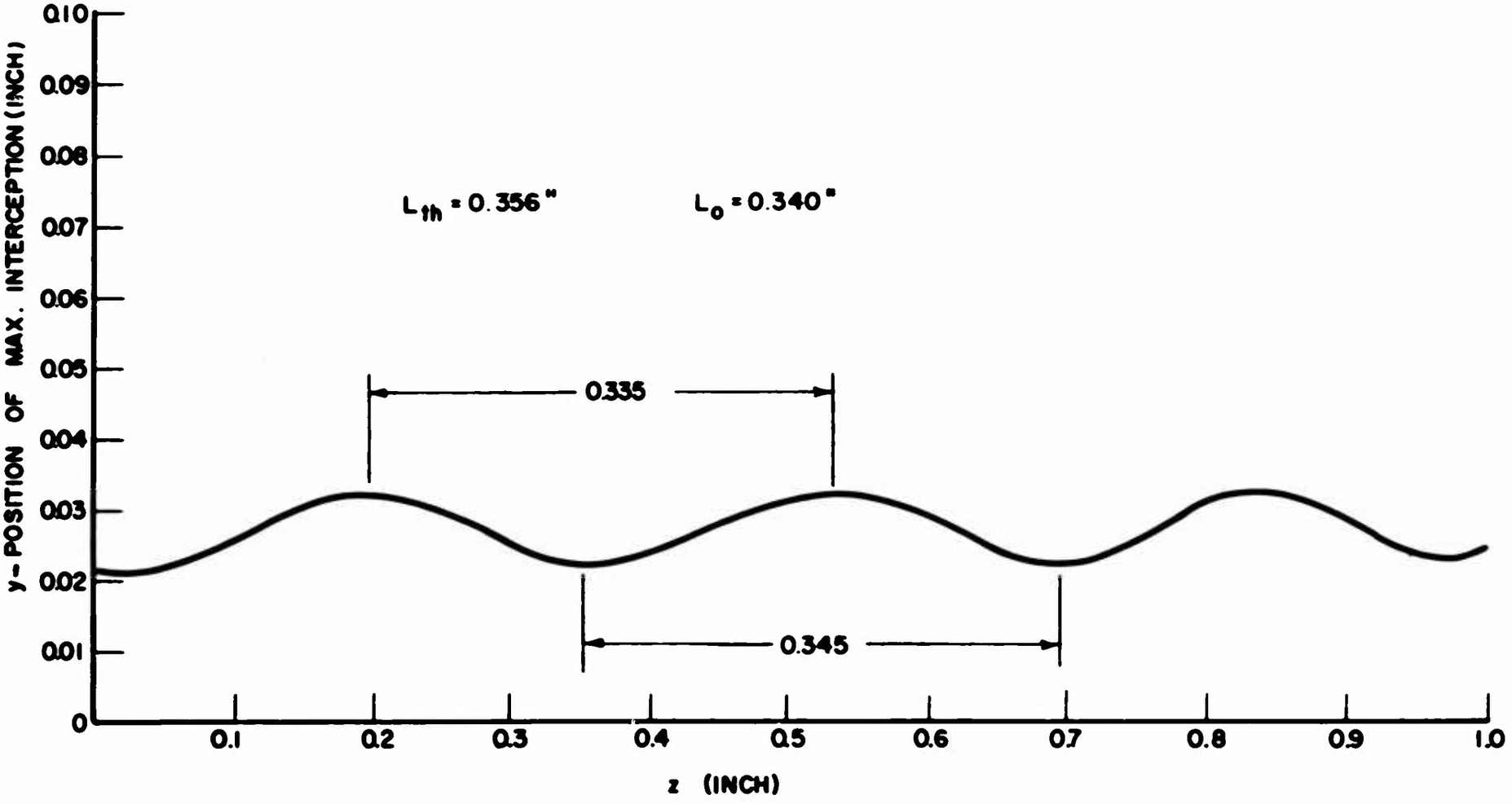

FIG. 7.15b LOCATION OF MAXIMUM CURRENT INTERCEPTION AT VARIOUS z-POSITIONS.

(V_c = -1765, V_f = -660, B = 465)

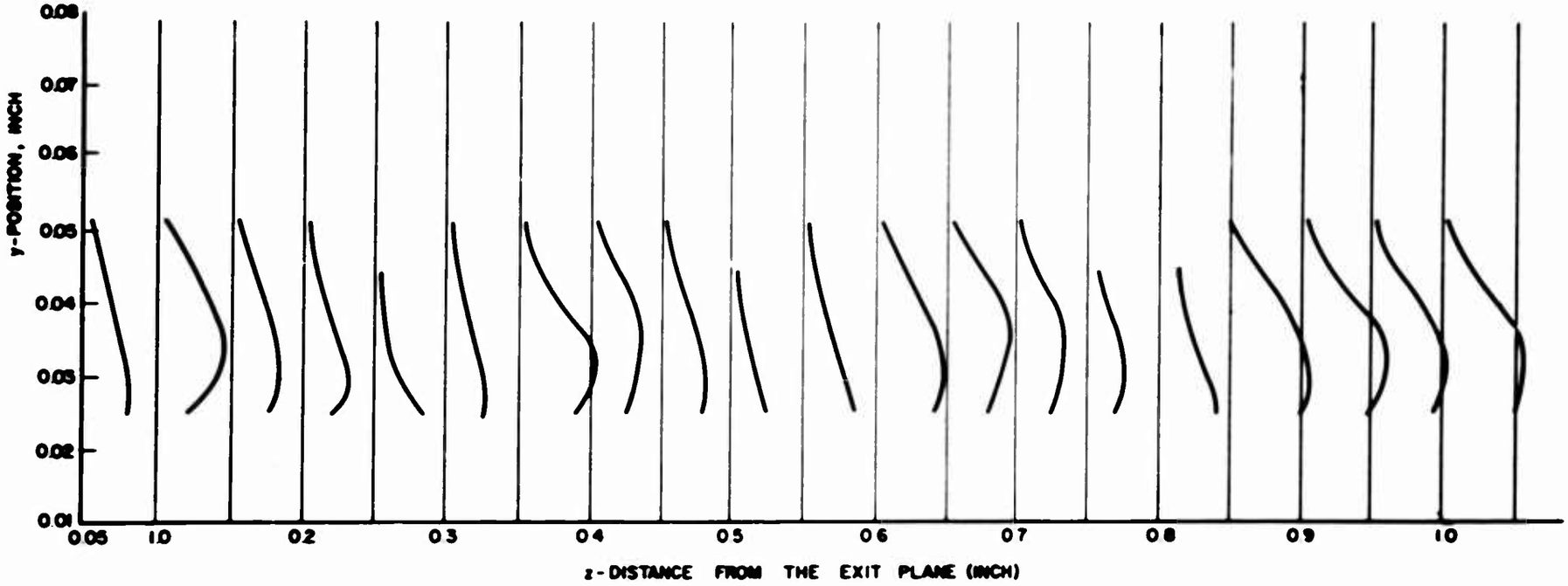

FIG. 7.16a CURRENTS INTERCEPTED BY THE GRID WIRES AT VARIOUS CROSS SECTIONS.

(V_c = -2000, V_f = -750, B = 578)

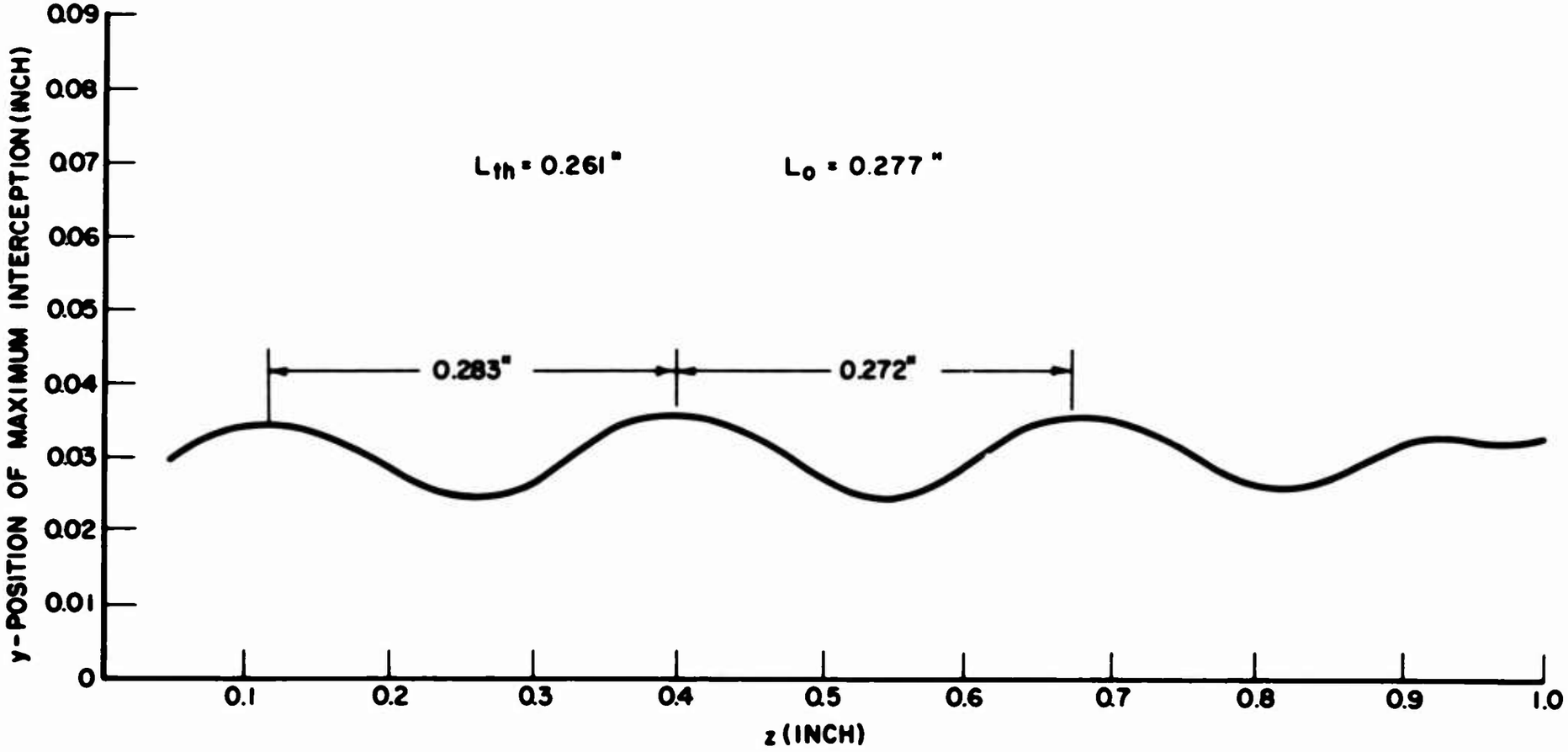

FIG. 7.16b LOCATION OF MAXIMUM INTERCEPTION AT VARIOUS z-POSITIONS.

(V_c = -2000, V_f = -750, B = 578)

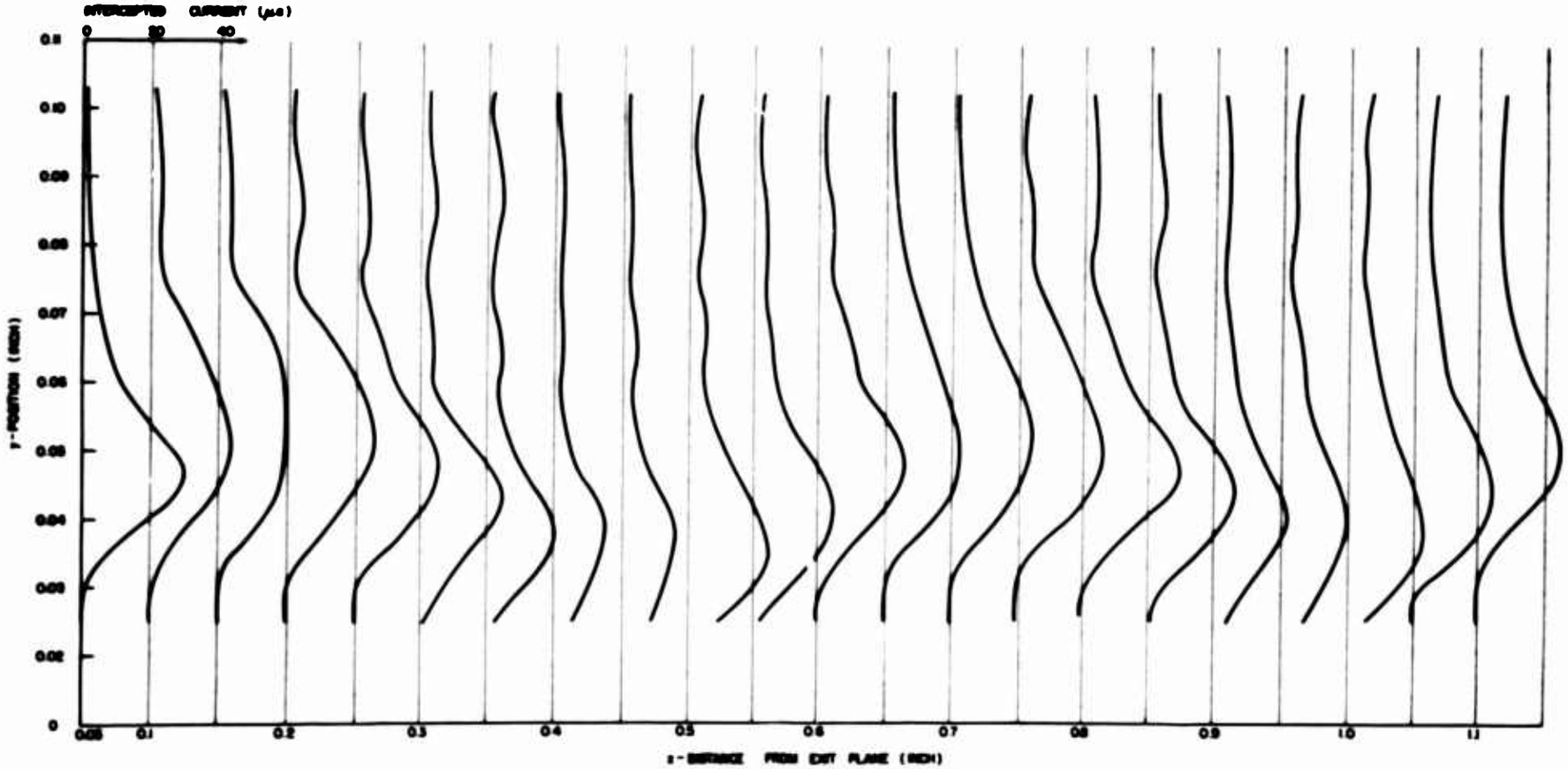

FIG. 7.17a CURRENTS INTERCEPTED BY THE GRID WIRES AT VARIOUS CROSS SECTIONS OF THE INTERACTION REGION WITH WIRE NO. 4 DISCONNECTED. (V_c = - 1490, V_f = - 500, B = 352 GAUSS)

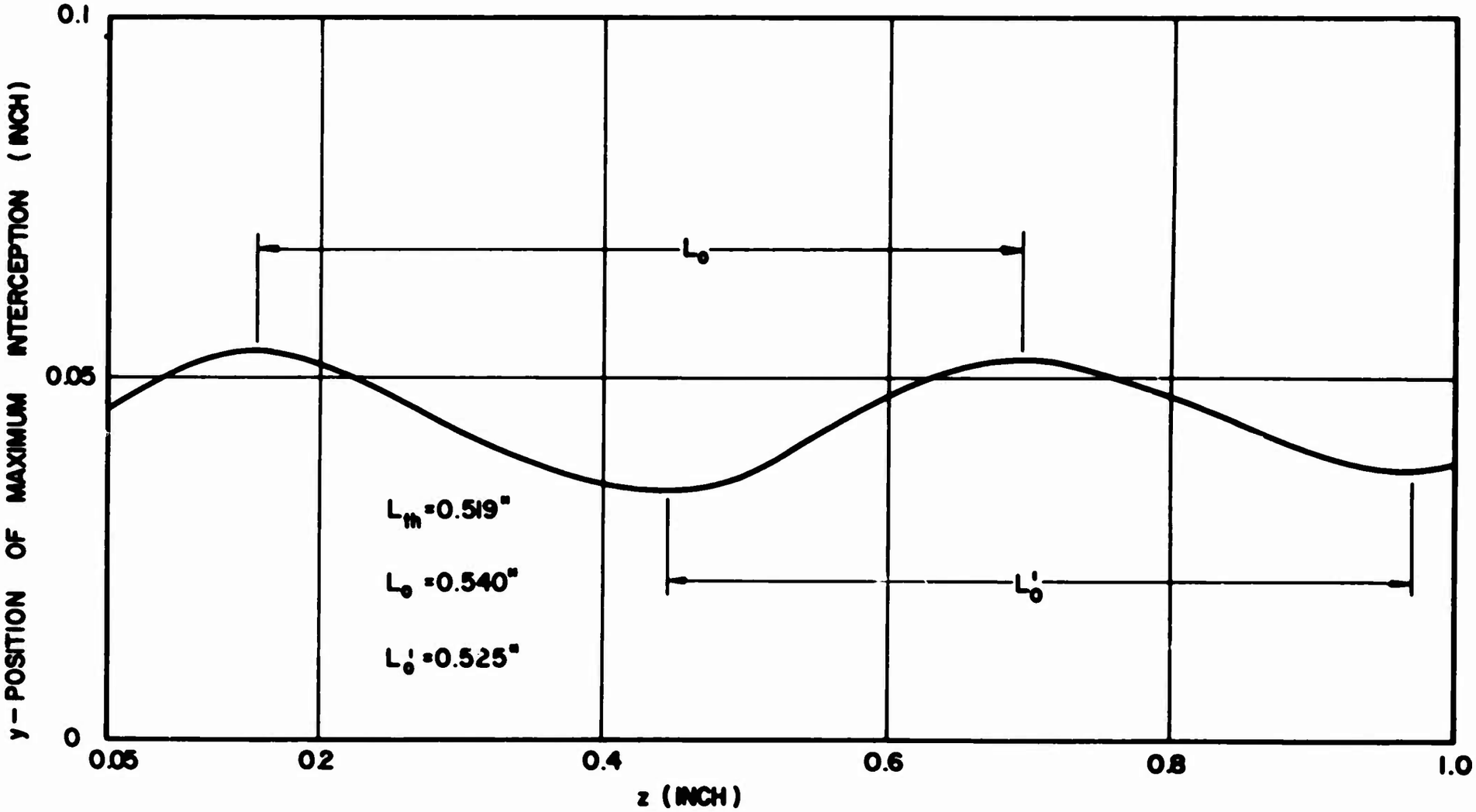

FIG. 7.17b LOCATION OF MAXIMUM CURRENT INTERCEPTION AT VARIOUS z-POSITIONS WITH WIRE NO. 4 DISCONNECTED. (V_c = - 1490, V_f = - 500, B = 352)

if $I_4 \neq 0$. This is simply to improve the appearance of the curves). It is interesting to observe that the same type of behavior occurs as when wire 4 is connected to the circuit in the usual manner.

Figure 7.18 presents a detailed description of the currents intercepted by wire 3 both with wire 4 connected and disconnected. The experimental points were obtained by moving the grid along the z-axis in increments of 0.01 inch. The I_3 variation is the same in each case except that the magnitude of the intercepted current is greater with wire 4 disconnected. This implies that the presence of the grid wires does not distort the beam as far as the general configuration and periodic variation is concerned. The difference in the value of intercepted current comes about as a result of the potential on wire 3 being affected by the disconnection of wire 4. In other words, the magnitude of current interception depends not only on the current density but also on the difference in potential between the wire and the corresponding beam location.

The experimental value of the cycloidal period is obtained by measuring the distance between alternate peaks of Fig. 7.18 rather than adjacent peaks. The necessity of measuring L_o in this manner can be explained by referring to Fig. 7.19. The cycloidal curve describes the variation of the maximum profile point along the z-axis while the shaded area represents the beam configuration. The straight line is the path followed by wire 3 as the grid is moved. Although a complete cycloid corresponds to the distance between A and C, relative maxima of I_3 occur at the three points A, B, and C. Thus the value of L_o is obtained by measuring the distance between the alternate peaks. This type of behavior occurs whenever the maximum point passes through the wire in question.

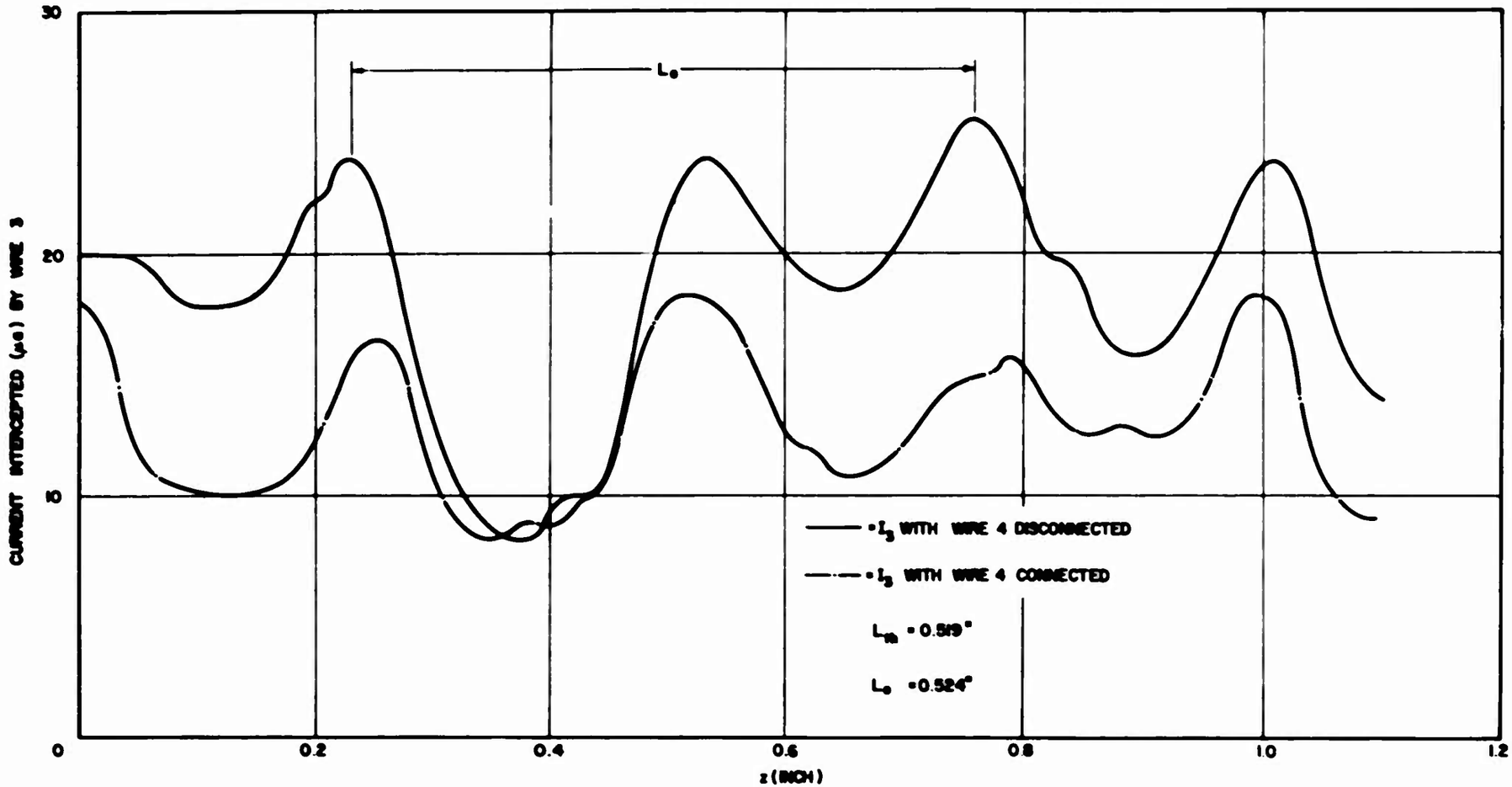

FIG. 7.18 COMPARISON OF THE CURRENTS INTERCEPTED BY WIRE 3 WHEN WIRE 4 IS CONNECTED AND DISCONNECTED. (V_c = - 1490, V_f = - 500, B = 352 GAUSS)

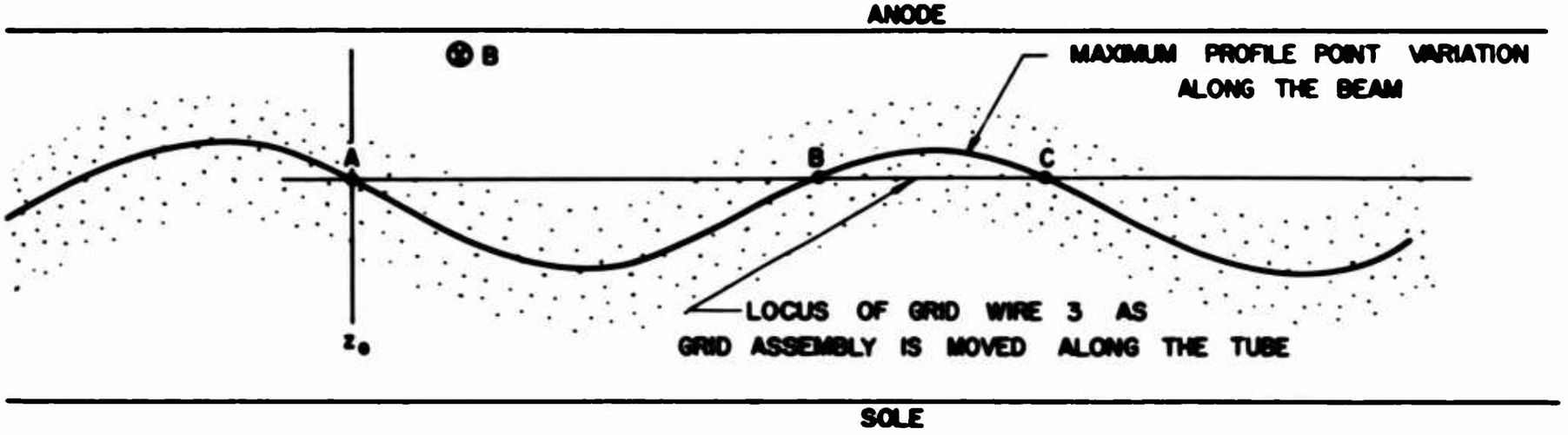

FIG. 7.19 ILLUSTRATION OF THE MANNER IN WHICH A GRID WIRE INTERCEPTS VARIOUS PARTS OF A CYCLOIDING BEAM AS THE GRID ASSEMBLY IS MOVED IN THE z-DIRECTION. THE DISTANCE FROM A TO C CORRESPONDS TO ONE PERIOD OF THE BEAM VARIATION.

However, if the maximum point never reaches a particular wire the distance between two consecutive peaks represents the cycloidal period.

Figure 7.20 is a plot of the currents intercepted by wires 2, 3, 4, 5 and 6 for the case $V_c = -2200$, $V_f = -850$ and $B = 387$. The theoretical cylcoidal length is 0.635 inch. The measurement of the appropriate distances yields L_o values which are in good agreement with L_{th}. Notice that wires 2, 5 and 6 lie outside of the maximum interception region and thus the distance between successive peaks of I_2, I_5, and I_6 represents a complete period. However, the maximum point does pass through wires 3 and 4 so that alternate peaks measurements of I_3 and I_4 yield the correct L_o values.

It is difficult to obtain an exact description of the beam from the experimental data. However, if the beam is defined to lie between those points whose intercepted current is 10 percent of the maximum profile point, then it is possible to plot a beam configuration in the anode-sole region. Figures 7.21 through 7.26 represent typical beam outlines obtained in this manner. Each figure also includes the location and thickness of the Brillouin beam which is compatible with the experimental voltages, current and magnetic field.

In Fig. 7.21 the beam enters the anode-sole region below the corresponding Brillouin beam location. The beam width at the entrance plane is several times the theoretical value. The magnetic field for this case was relatively low (246 gauss) thus resulting in a rather long cycloidal variation. The thickness of the beam remains nearly constant but its location does change slightly. However, the variation is not sufficiently large to allow an accurate experimental evaluation of the period.

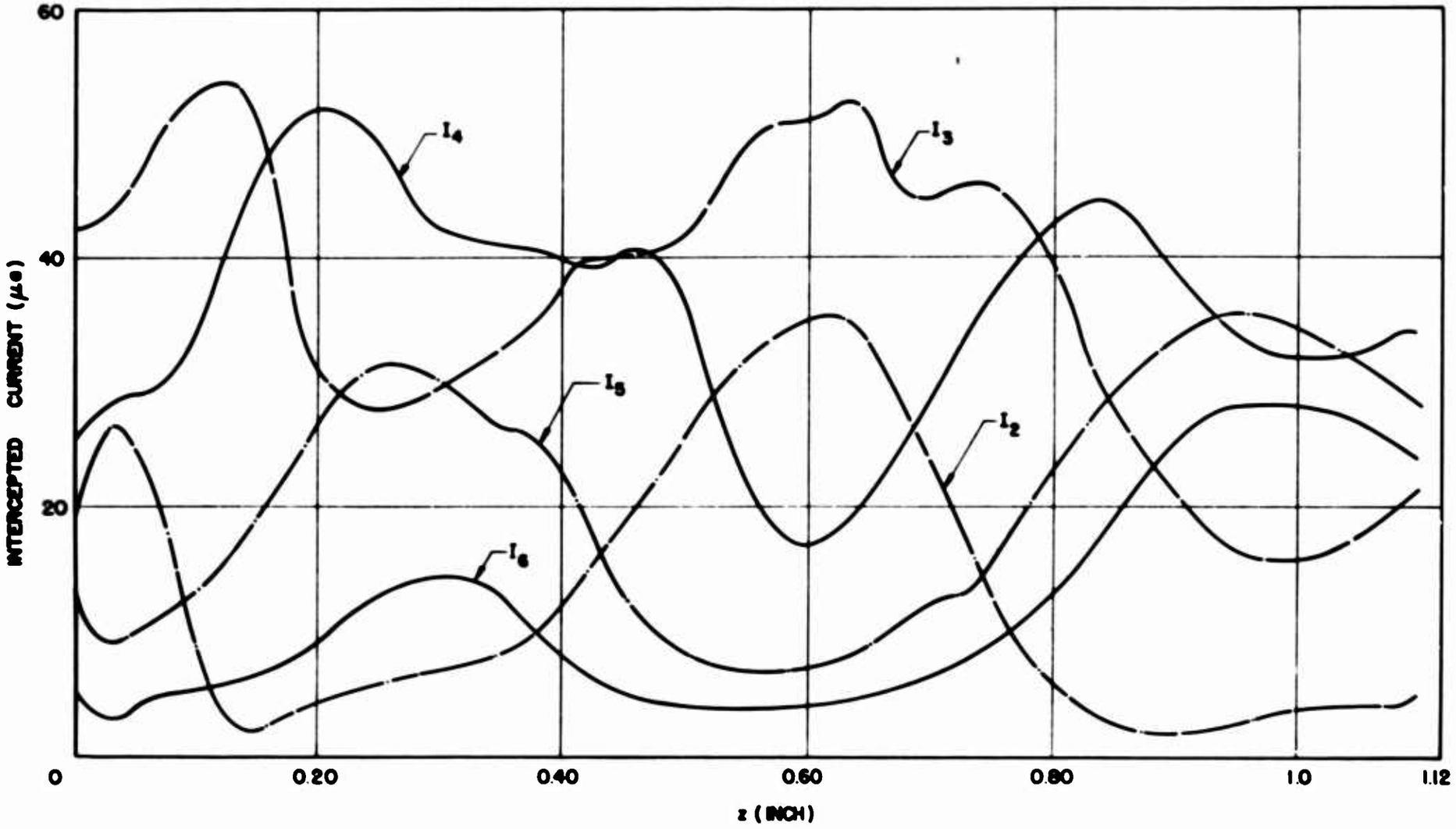

FIG. 7.20 CURRENTS INTERCEPTED BY THE GRID WIRES AT VARIOUS z-LOCATIONS. (V_c = - 2200, V_f = - 850, B = 387 GAUSS)

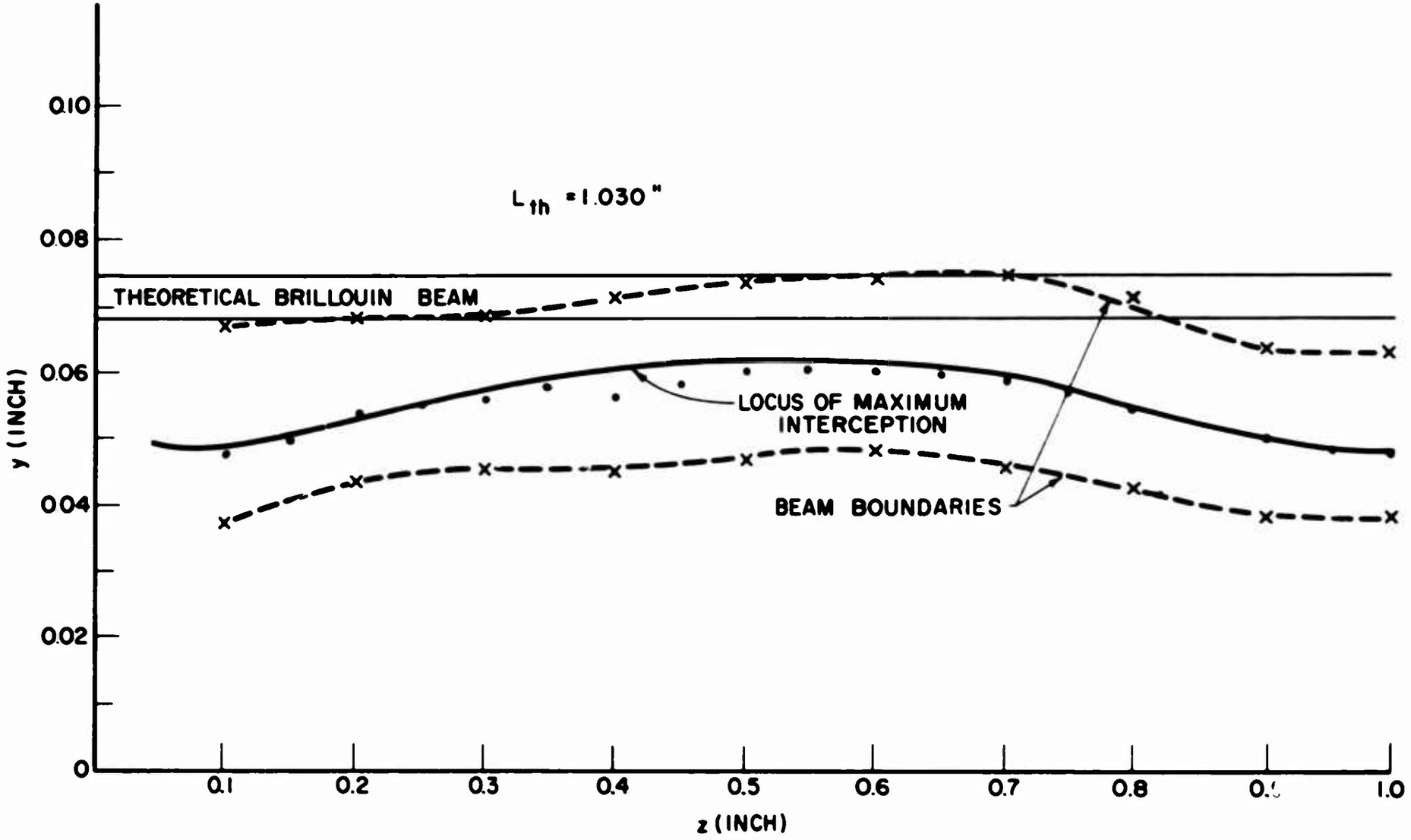

FIG. 7.21 EXPERIMENTAL BEAM CONFIGURATION IN THE INTERACTION REGION.

(V_c = -1450, V_f = -500, B = 246)

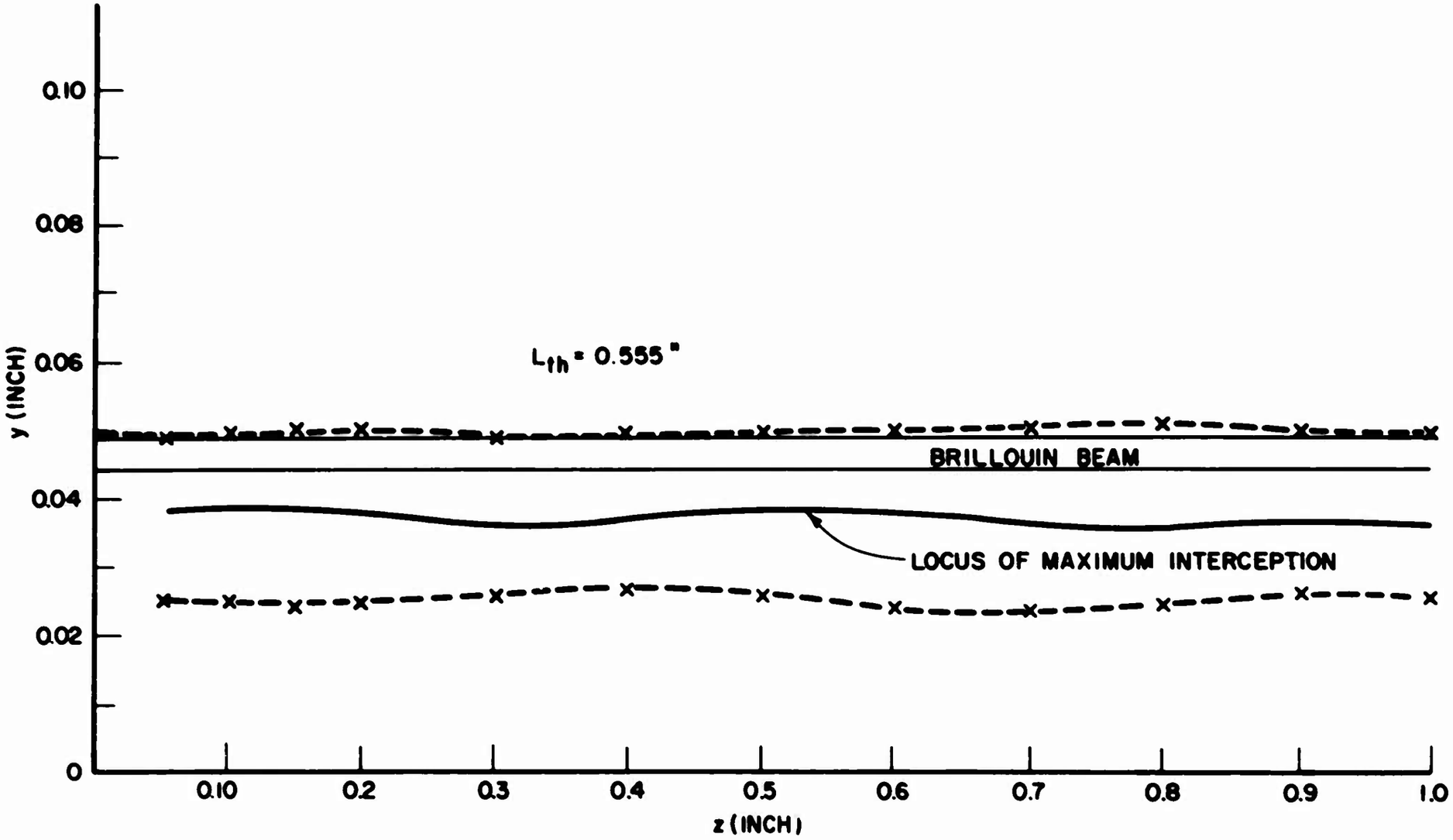

FIG. 7.22 EXPERIMENTAL BEAM CONFIGURATION IN THE INTERACTION REGION.

(V_c = -1450, V_f = -500, B = 335)

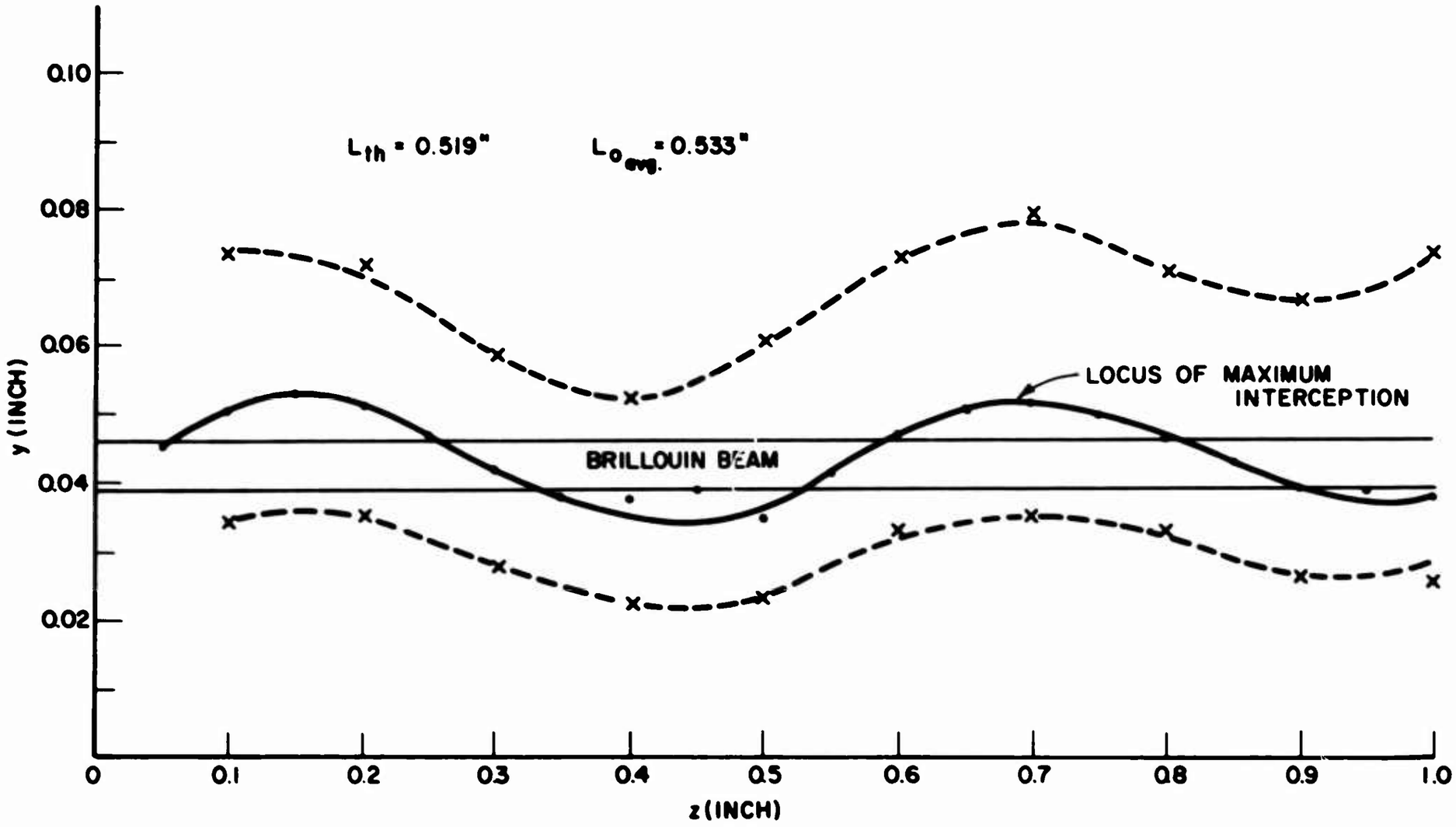

FIG. 7.23 EXPERIMENTAL BEAM CONFIGURATION IN THE INTERACTION REGION.

(V_c = -1490, V_f = -500, B = 352)

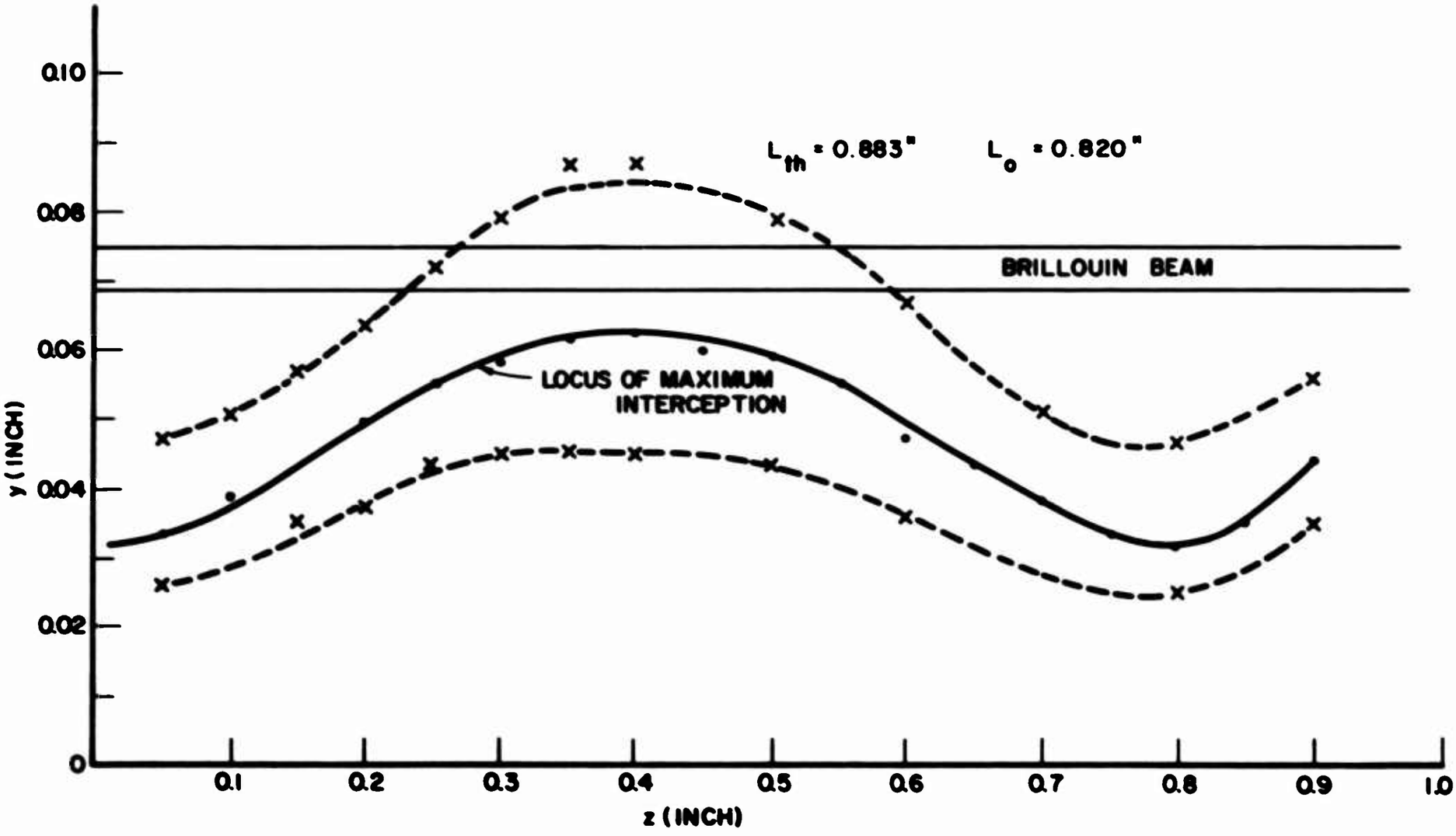

FIG. 7.24 EXPERIMENTAL BEAM CONFIGURATION IN THE INTERACTION REGION.

(V_c = -1765, V_f = -660, B = 295)

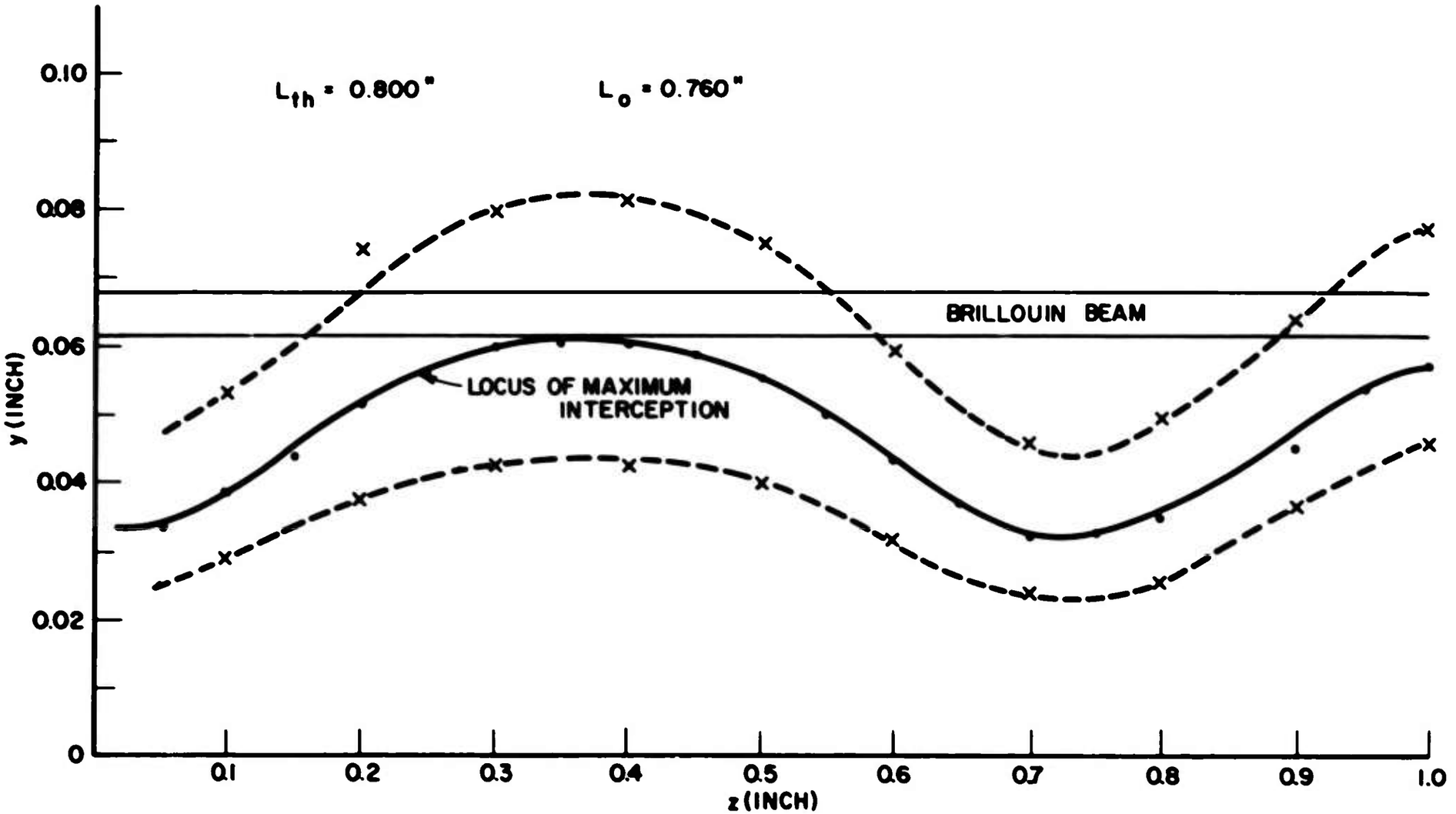

FIG. 7.25 EXPERIMENTAL BEAM CONFIGURATION IN THE INTERACTION REGION.

(V_c = -2010, V_f = -750, B = 330)

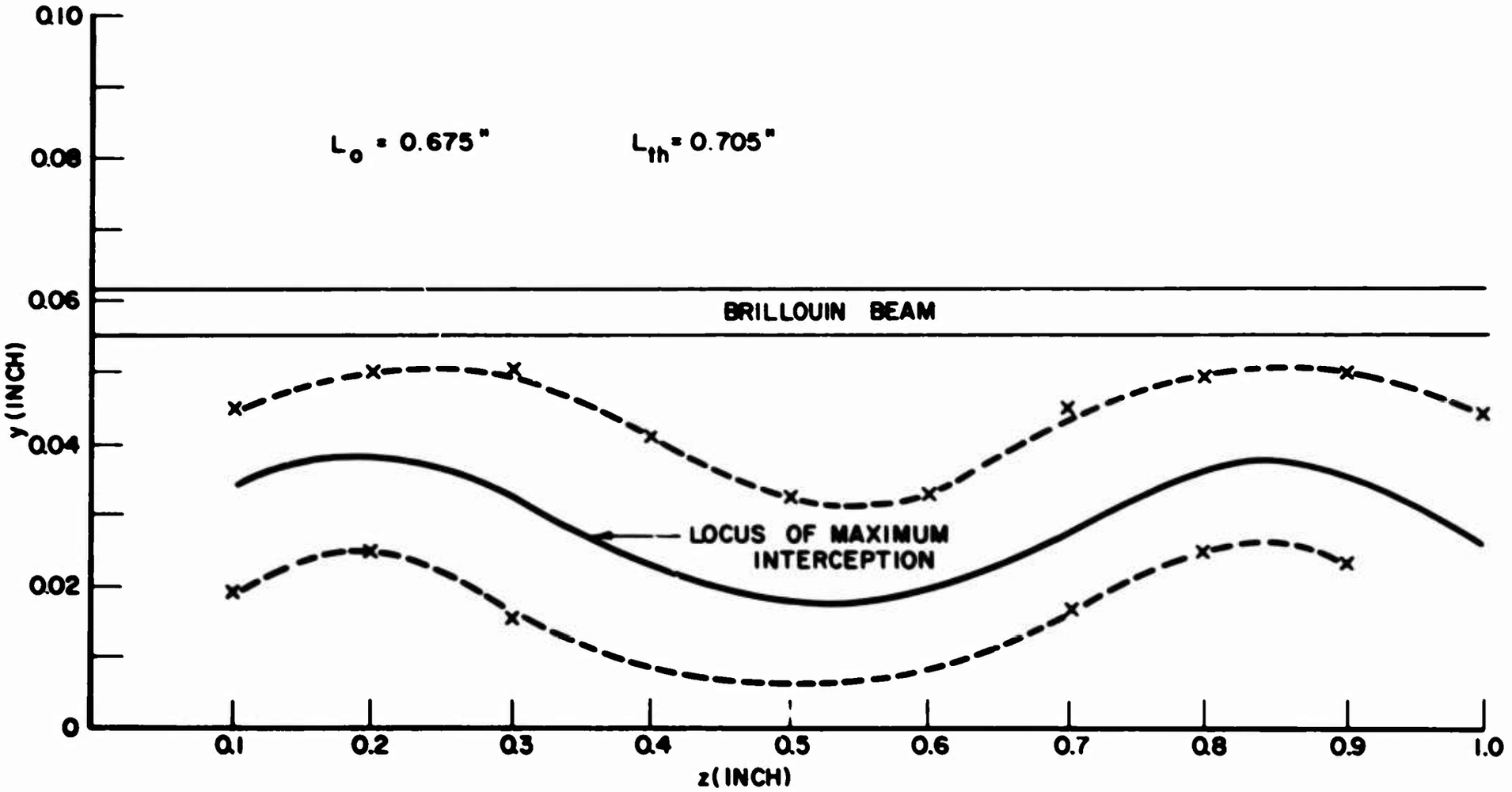

FIG. 7.26 EXPERIMENTAL BEAM CONFIGURATION IN THE INTERACTION REGION.

(V_c = -2010, V_f = -750, B = 350)

Figure 7.22 represents a situation which is similar to the preceding except that the magnetic field was increased to 335 gauss. Once again the beam maintains a nearly constant thickness, which is greater than the corresponding Brillouin value, and experiences only a slight undulation during its motion.

Figure 7.23 illustrates the situation of a pronounced beam undulation under the conditions V_c = -1490 volts, V_f = -500 volts and B = 352 gauss. The beam is much wider than for Brillouin flow. The thickness also undergoes variation as the beam travels through the anode-sole region. It is interesting to observe that the variation of the maximum beam profile location is nearly symmetrical with the theoretical Brillouin beam. This indicates that the beam enters the interaction region at the correct location but with nonideal conditions: e.g., the beam thickness and direction of motion at the entrance plane do not fulfill the proper matching conditions for laminar flow. Consequently the beam undulates about the ideal Brillouin position.

Figure 7.24 demonstrates the behavior of a beam which enters the anode-sole region far below the Brillouin location. The effect of such an entrance is to produce a greater electric field on the top edge of the beam thus resulting in the sharp upward curvature of the electron. This is followed by the usual cycloidal variation of the beam location. There is also a pronounced beam thickness variation with the largest value occuring when the beam is at its maximum height above the sole. The operating conditions for this situation were V_c = -1765, V_f = -660 and B = 295.

Figure 7.25 illustrates a similar behavior for V_c = 2010, V_f = -750 and B = 330. The beam enters the anode-sole region below the

Brillouin location and is immediately forced up toward the anode. The cycloidal variation of the beam thickness and location is readily apparent from the figure. Again the beam has its maximum thickness when it is farthest from the sole.

The operating conditions for Fig. 7.26 are the same as Fig. 7.25 except that B has been increased to 350 gauss. The larger magnetic field has caused the beam to enter the anode-sole region at a lower position. It is also apparent that the beam always remains well below the theoretical Brillouin location. However, the general configuration is similar to the preceding result.

There are several methods for evaluating the approximate space-charge densities in the beam by using the data obtained from the grid wire current interceptions. Appendix E discusses the various methods one of which will be used here to evaluate the space-charge density variation along the beam. ρ is assumed to be constant across any transverse plane while $\dot{z}$ is considered to vary linearly as in Brillouin flow

$$\dot{z} = \omega_c(y + 2a) \quad . \tag{7.4}$$

Then the average space-charge density at any cross section can be written as

$$\bar{\rho} = \frac{2}{h\omega_c \ell(\ell + 4a)} \; I \quad , \tag{7.5}$$

where h = beam width in the x-direction,

ℓ = beam thickness in y-direction,

a = distance between beam and sole, and

I = beam current.

The values of a and ℓ at each cross section can be obtained from Figs. 7.21-7.26. Calculation of the $\bar{\rho}$ values results in the curves illustrated in Fig. 7.27. The ρ_o values are the Brillouin space-charge densities corresponding to the various magnetic field values.

In every case (except b) the average space-charge density undergoes periodic behavior which is a necessary consequence of the variation of the beam thickness and location. The $\bar{\rho}$ values are usually less than the theoretical Brillouin values (except for case f). The maximum $\bar{\rho}$ for the various cases are:

(a) $\bar{\rho}_{max}/\rho_o = 0.53$,

(b) $\bar{\rho}_{max}/\rho_o = 0.28$,

(c) $\bar{\rho}_{max}/\rho_o = 0.31$,

(d) $\bar{\rho}_{max}/\rho_o = 0.66$,

(e) $\bar{\rho}_{max}/\rho_o = 0.62$, and

(f) $\bar{\rho}_{max}/\rho_o = 1.15$.

These are average values and hence at some point in the beam for a given z the maximum space-charge density could be greater.

In appendix E it is shown that for variable space-charge density across the beam, given by

$$\rho = \rho_m \sin \pi y/\ell \quad , \tag{7.6}$$

the peak space-charge density at any cross section can be written as

$$\rho_m = \frac{\pi}{\hbar\omega_c \ell(\ell + 4a)} I \quad . \tag{7.7}$$

Thus $\rho_m = \pi/2\ \bar{\rho}$ which results in values for the above situations of $\rho_m/\rho_o = 0.83$, 0.44, 0.49, 1.04, 0.97, and 1.8. Since the beam profiles illustrated earlier generally appear to have a maximum near the center

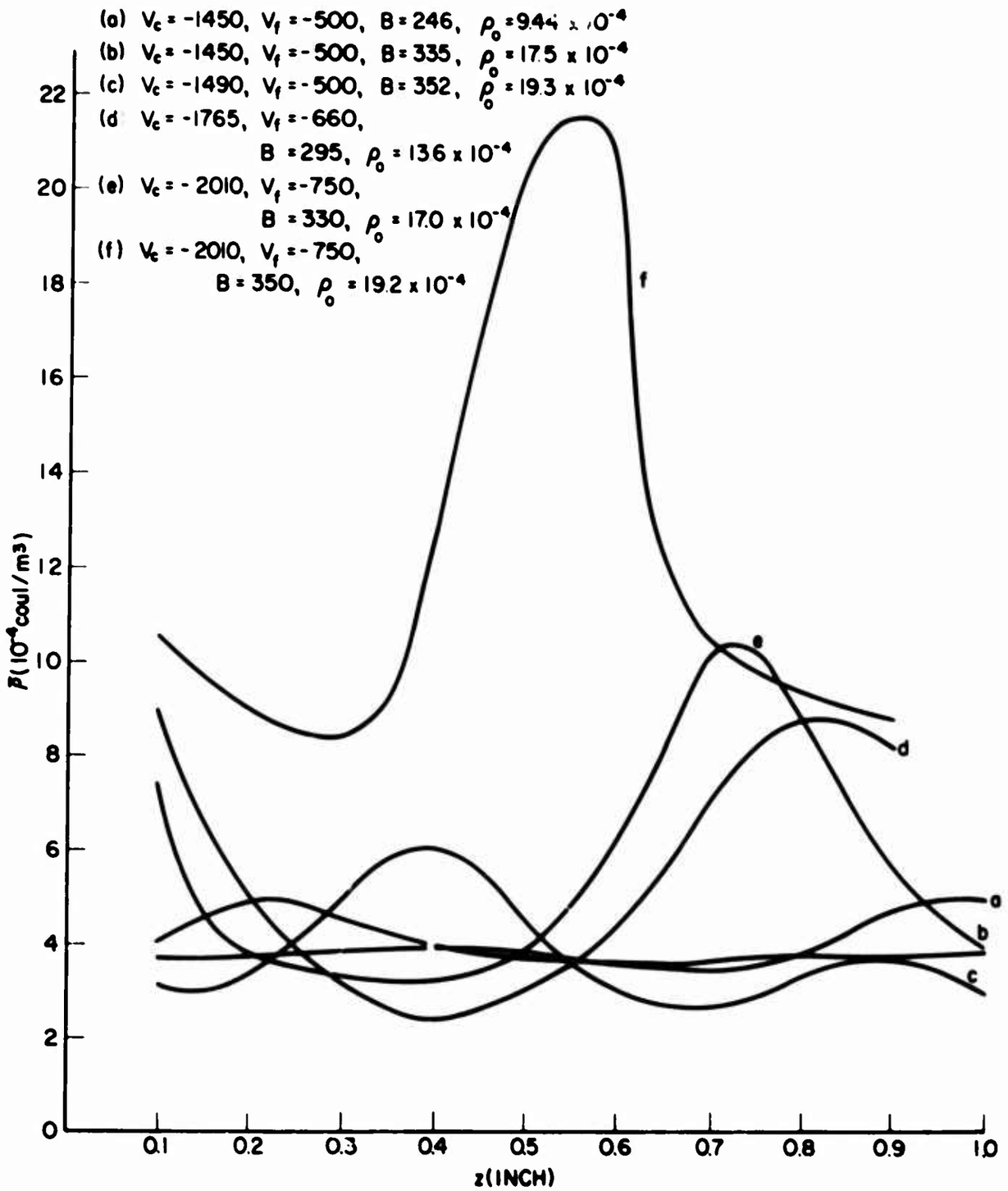

FIG. 7.27 VARIATION OF AVERAGE SPACE-CHARGE DENSITY ALONG THE z-DIRECTION.

of the beam, the sinusoidal variation of Eq. 7.6 is not an unreasonable representation.

Although it is difficult to determine the accuracy of the space-charge densities calculated from the current interception data, the above results appear to be fairly realistic. They indicate that $\bar{\rho}$ is generally less than ρ_o although at the highest density points in the beam the values approach ρ_o. Case f indicates larger $\bar{\rho}$ values but the proximity of the beam to the sole for this case makes the measurements difficult to intrepret and hence leads to some question concerning the validity of the results. In most cases the space-charge density is observed to vary periodically along the beam in much the same manner as the beam thickness and location.

The configuration suggested by Figs. 7.21 through 7.26 indicate that the beam invariably is thicker than the corresponding Brillouin case. The location varies periodically while the thickness either remains approximately constant or varies in a cycloidal manner. Under no conditions was a scalloped beam obtained. This suggests that such a flow cannot exist in the anode-sole region of a device which utilizes the extended Kino short gun as the beam forming system. However, the insertion of an r-f structure (e.g., an interdigital line) into the interaction region could theoretically make it possible to achieve a scalloped d-c electron beam.

The gross beam characteristics provide experimental verification of several fundamental concepts which have been discussed in preceding chapters. That is, the nonlaminar behavior of the beam in the interaction region can be produced by any one of the three conditions:

1. The beam enters the anode-sole region at a location which differs from the theoretical Brillouin position.

2. The electric fields in the gun and anode-sole regions are poorly matched.

3. The fields are matched but the voltages are mismatched.

These last two conditions are a direct consequence of a poor transition region. This emphasizes the fact that the generation of nearly laminar electron beams is critically dependent on the proper matching of conditions at the boundary between the gun region and interaction region.

However, even if the conditions are perfectly matched and the electrons enter at the proper location, the beam will still be somewhat thicker than the Brillouin value. Two of the factors which contribute to this behavior are imperfections in the gun system and initial velocity effects at the cathode. The effect of tangential emission velocities was analyzed in Chapter IV and found to produce significant broadening of the beam. In addition it causes the beam to become "fuzzy" such that space-charge densities near the boundaries are less than in the center of the flow. Such characteristics are typical of the beam profiles indicated by the experimental investigations. Although the undulation of a beam can be minimized by the proper match between the gun and interaction regions, the presence of initial tangential velocities makes it impossible to achieve exact Brillouin flow from any electron injection system.

There is yet another factor which influences the shape of the apparent beam profile. This is the emission of secondary electrons from any surface which is bombarded by primary electrons. Figure 7.28 compares the linear current density distribution in a Brillouin beam with a profile which is typical of the experimental observations. The secondary electrons released from one wire are capable of moving to higher potential wires. Thus if a Brillouin beam strikes the grid the net current reading of the lowest potential wire will be reduced due to its loss of secondary

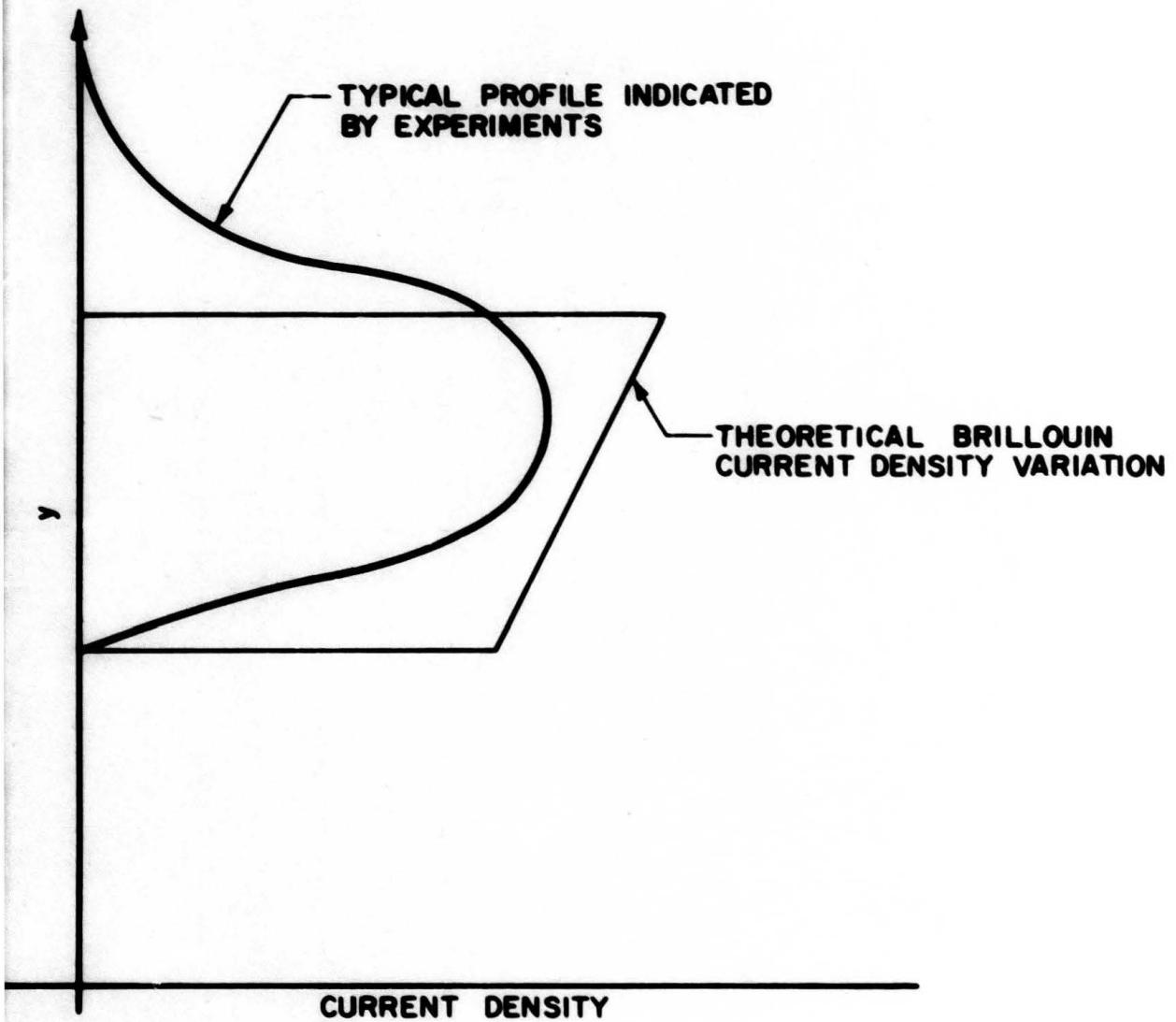

. 7.28 COMPARISON OF THE THEORETICAL BRILLOUIN CURRENT DENSITY DISTRIBUTION WITH A TYPICAL EXPERIMENTAL PROFILE.

electrons. Similarly the uppermost wire which is struck by the beam will eject secondaries which move through the beam boundary and arrive at wires located outside of the space-charge flow. The secondary currents reaching these wires would imply a beam width greater than the actual value. They would also impart a rounded shape to the apparent beam profile as determined from the current interception data. Both of these characteristics are typical of the experimental beam configurations described above.

The results indicate that there are three principal reasons for the shapes of the beam profiles obtained from the experimental investigations. Two of these effects (tangential emission velocity and improper beam focusing) are inherent in the physical operating characteristics of the device. The secondary emission effect, however, comes about because it is necessary to intercept the beam in order to evaluate its characteristics. Thus the measurement technique introduces a relative uncertainty into the beam profile calculations.

7.4 Aperture System Measurements

7.4.1 Description of System. Figure 7.29 illustrates the basic aperture system design used for analyzing the electron beam characteristics. A small portion of the beam passes through the 0.004 inch diameter opening in the aperture plate and enters the deflection region. The motion of the electrons in this region is dependent on their initial velocities and the voltage difference between the two plates. Measurements of the current reaching the deflection plate for various $\Delta\varphi$ values provides a means for evaluating the velocity distribution of the incoming electrons. The proper interpretation of the data also allows the determination of

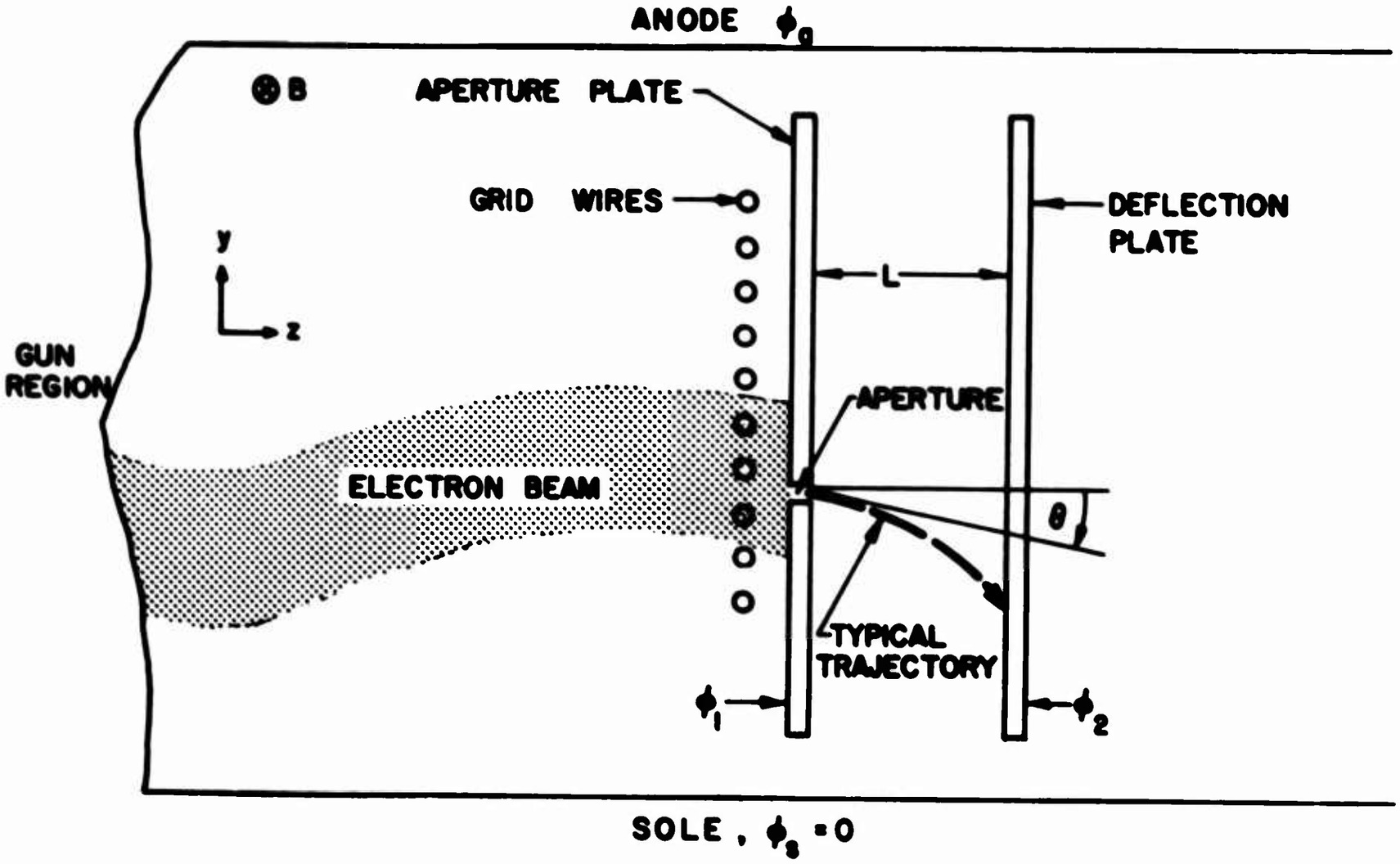

FIG. 7.29 APERTURE SYSTEM FOR THE CROSSED-FIELD BEAM ANALYZER INVESTIGATION.

the average space-charge density. A more detailed discussion of the effect of the grid wires on the electron trajectories and of the measurement capabilities of the aperture system are presented in Appendix F.

7.4.2 Space-Charge-Density Measurements. The determination of the average space-charge density at a given location requires a knowledge of the average electron velocity and current density passing through the aperture. The z-component of current density can be determined from the total current reaching the deflection plate and is given by

$$\langle J_z \rangle = \frac{I_{dp}}{A} , \tag{7.8}$$

where $\langle J_z \rangle$ = average current density passing through the aperture,

I_{dp} = total current reaching the deflection plate, and

A = aperture area.

$\langle J_z \rangle$ is related to the average space-charge density ($\langle \rho \rangle$) and z-component of velocity ($\langle \dot{z} \rangle$) by the equation

$$\langle J_z \rangle = \langle \rho \rangle \langle \dot{z} \rangle . \tag{7.9}$$

The data obtained from the aperture system measurements would provide the necessary information for calculating $\langle \dot{z} \rangle$ and thus would lead to the evaluation of the average space-charge density. However, as will be discussed a little later, there are some technological problems associated with the aperture system measurements which complicate the $\langle \dot{z} \rangle$ calculations.

A simple experiment was carried out to illustrate the importance of matching the fields and voltages between the gun and anode-sole region. The aperture system was positioned quite close to the gun exit plane (approximately 0.050 inch away) and the beam leaving the gun was analyzed under both matched and mismatched conditions. For the matched situation,

V_f, V_a and V_s were selected so that there was no curvature of the equipotential lines in moving from the gun exit plane into the anode-sole region. For these voltages the magnetic field was increased until the current passing through the aperture was a maximum. When this condition is reached it is reasonable to assume that the average velocity of the electrons is essentially only in the z-direction and can be approximated by

$$\langle \dot{z} \rangle \cong \sqrt{2\eta\,\varphi} \quad , \tag{7.10}$$

where φ is the space-charge-free voltage at the aperture location. Using Eqs. 7.8, 7.9 and 7.10 the $\langle\rho\rangle$ values for matched conditions were calculated and plotted in Fig. 7.30. It is apparent that the space-charge densities are quite close to the corresponding Brillouin values for each magnetic field intensity. It should also be realized that the presence of space charge causes the actual potential at the aperture location to be less than the value used in Eq. 7.10. This means that $\langle \dot{z} \rangle$ is smaller and hence the actual $\langle\rho\rangle$ is greater than indicated. Thus it can be concluded that for the proper magnetic field the gun is capable of generating a beam whose space-charge density is approximately the Brillouin value as long as the voltages and electric fields between the two regions are matched.

The deliberate mismatch of the conditions at the exit plane resulted in the other curve illustrated in Fig. 7.30. Again B was selected for maximum I_{dp}. For this case the experimental points lie well below the Brillouin curve. This suggests that either the space-charge densities are reduced or the electrons have picked up appreciable y-components of velocity. Since the voltages are definitely mismatched,

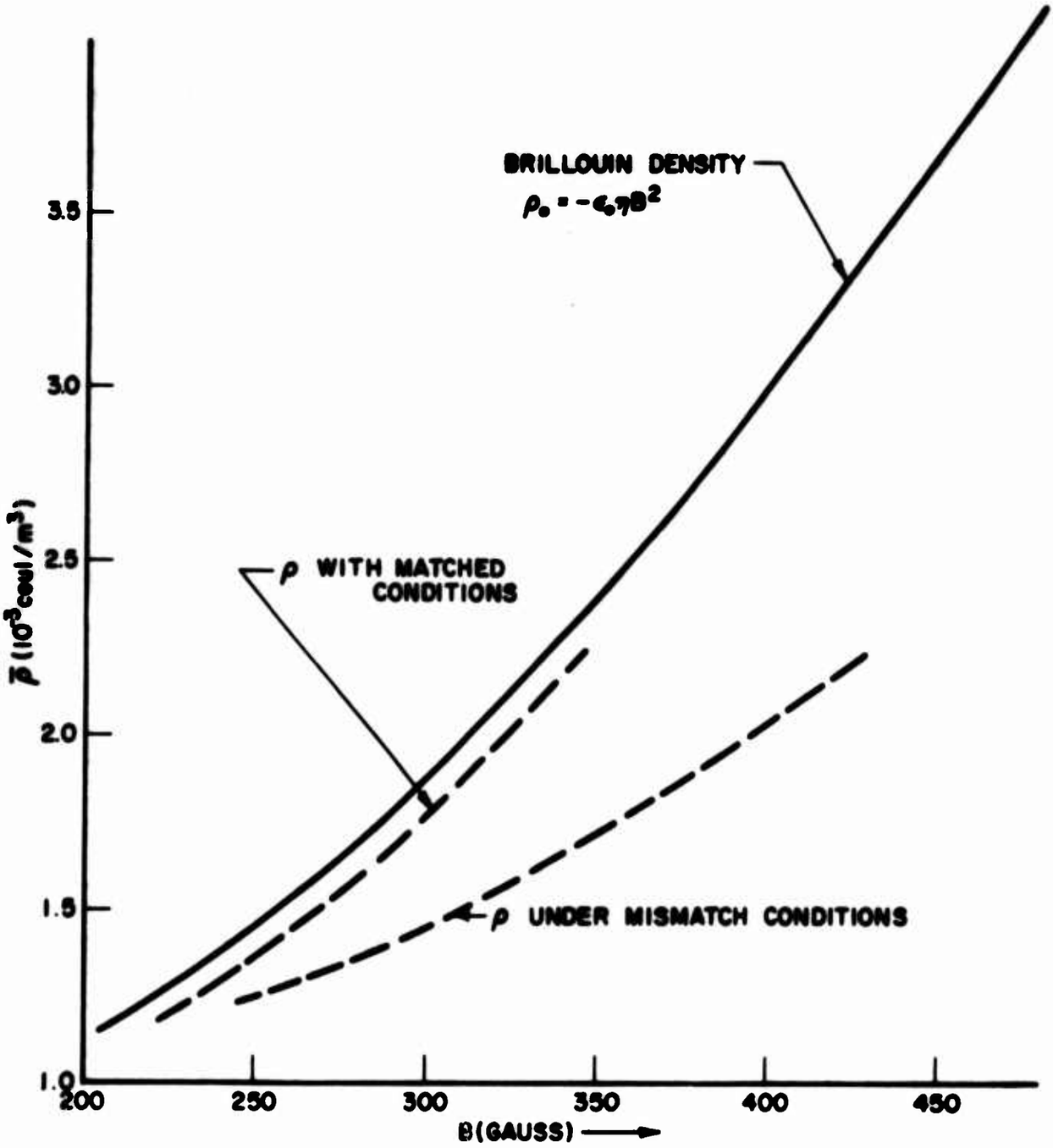

FIG. 7.30 SPACE-CHARGE DENSITY AS A FUNCTION OF MAGNETIC FIELD.

this latter effect is the more probable. This means that the $\langle \dot{z} \rangle$ values are less than those indicated by Eq. 7.10 so that the $\langle \rho \rangle$ values are greater. However, the beam is experiencing a rather sudden downward acceleration thus indicating subsequent nonlaminar flow. This behavior is substantiated by the following discussion.

Figure 7.31 illustrates the variation of deflection plate current as the aperture system is moved away from the gun exit plane. For the matched conditions the current which passes through the aperture (I_o) varies periodically with distance. This is to be expected since the magnetic field and anode voltage were not properly selected to give Brillouin flow. There is a reduction in the I_o value at the second peak as compared to the first maximum value. This can be explained in either of two ways:

1. Since the anode-sole spacing has been increased from 0.128 inch to 0.188 inch to facilitate insertion of the aperture system, it is possible that the 0.030 inch sole hats are no longer capable of confining the beam. In this case the beam would spread in the x-direction and hence would reduce the current density passing through the aperture.

2. The thickness (ℓ) may be increasing as the beam proceeds down the tube.

Although the beam configurations encountered in the investigations described in Section 7.3 did not generally indicate increasing thickness in the z-direction, it is possible that with the increased anode-sole spacing the situation has become more conducive to such behavior. It is felt that both of the above conditions exist to some extent and contribute to the reduction in current density.

The current variation under mismatched conditions resulted in extremely large variations of I_o, especially near the two peaks. The

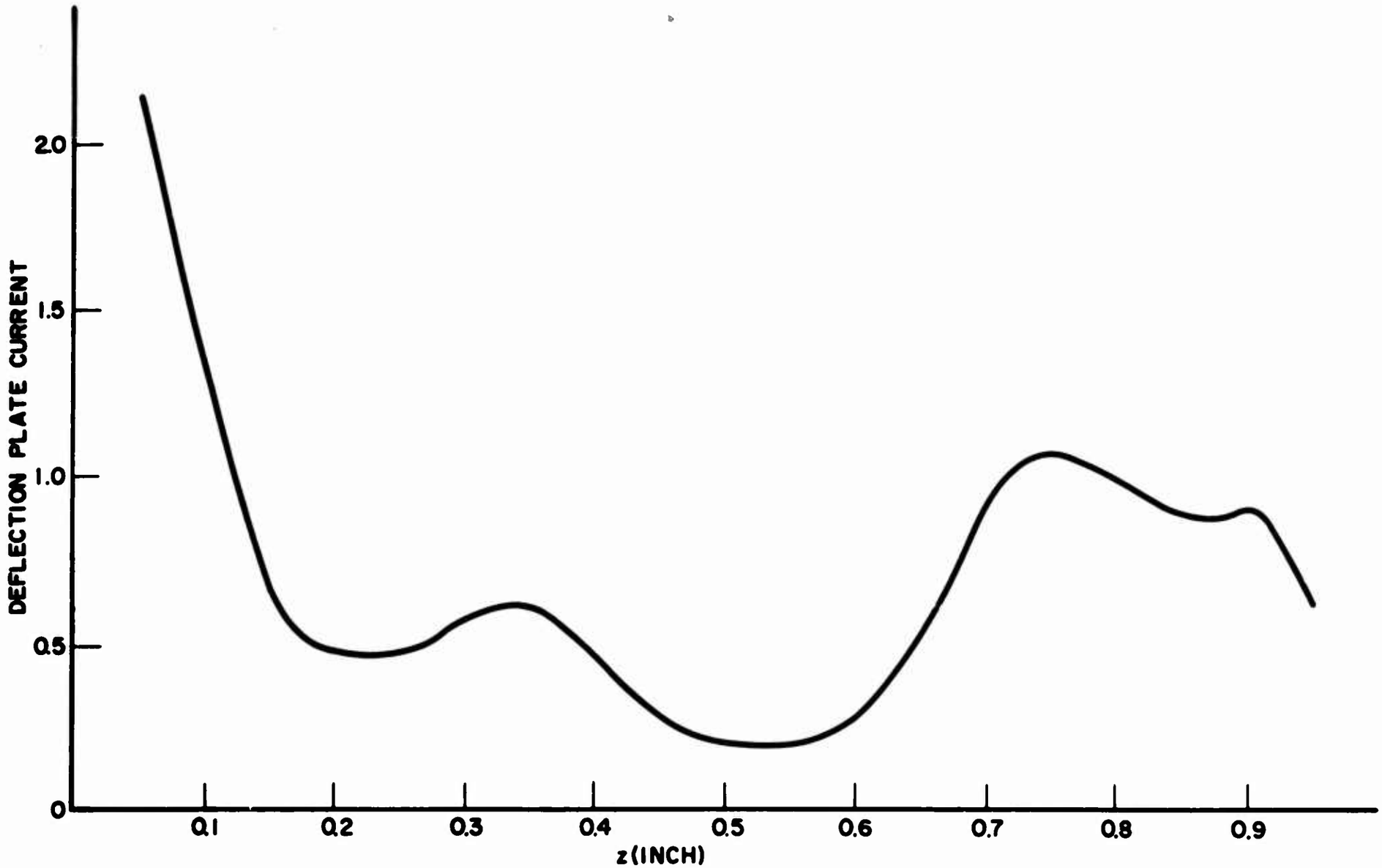

FIG. 7.31 VARIATION OF DEFLECTION PLATE CURRENT WITH z-POSITION.

(V_c = -1500, V_f = -770, V_s = -1785, B = 280)

explanation for this behavior is that the mismatch conditions at the exit plane disturb the beam to such an extent that it undergoes extreme undulation in the anode-sole region. The undulation is so great that the electrons are capable of slipping around the aperture plate (either below or above it) and reach the deflection plate. Thus the peak I_o values are not caused by the electrons which pass through the aperture but rather by those which bypass the aperture plate. This is additional confirmation of the conclusion that the transition between the gun and interaction region is extremely critical in producing decent beam configurations.

7.4.3 Analysis of Deflection Plate Data. Ideally the current intercepted by the deflection plate should vary with $\Delta\varphi$ as described in Appendix F and illustrated in Fig. 7.32. As $\Delta\varphi$ is decreased from large positive values, I_{dp} remains constant at I_o until the lowest velocity class of electrons is cut off and unable to reach the deflection plate. I_{dp} starts decreasing at this point and continues doing so until it becomes zero when the cut-off condition for the highest velocity electrons is reached.

Unfortunately, the application of this procedure to measure the characteristics of an electron beam encounters some complications. The relatively small dimensions which are required force the $\Delta\varphi$ values to become negative in order to cut off any electron entering with an angle $\theta > -45°$. Thus the electrons which strike the deflection plate when $\Delta\varphi < 0$ cause the emission of secondaries which move across to the aperture plate rather than returning to the deflection plate. As $\Delta\varphi$ changes from positive to negative, I_{dp} decreases abruptly to negative values. The magnitude of the negative current is dependent on the secondary emission coefficient of the deflection plate which in turn is dependent on the cleanliness of the surface, the energy of the primary electrons, and the

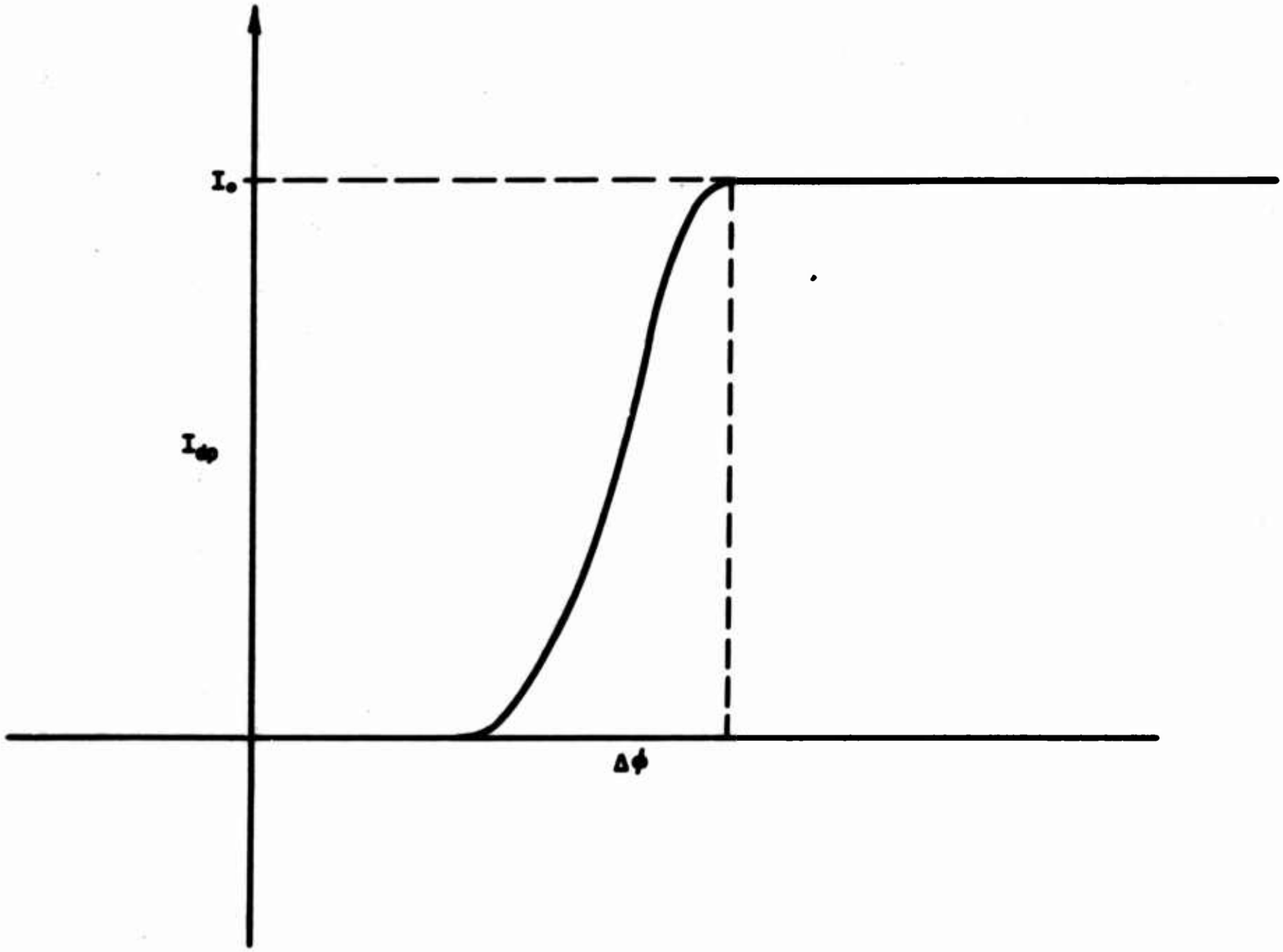

FIG. 7.32 THEORETICAL VARIATION OF DEFLECTION PLATE CURRENT WITH $\Delta\varphi$.

angle at which they strike the plate. Some typical I_{dp} curves are illustrated in Fig. 7.33. The application of a graphite coating to reduce the secondary emission was found to be of very little benefit.

Even though secondary emission is present, it is still possible to analyze the data and obtain qualitative results. For example, each curve in Fig. 7.33 reaches a minimum at some $\Delta\varphi$ value and then gradually returns to zero. The data can be interpreted such that the region of increasing I_{dp} corresponds to that interval in which the various velocity classes of electrons are being cut off.

The shape of the I_{dp} vs. $\Delta\varphi$ curve is dependent on the characteristics of the electrons which pass through the aperture. The analyses of Appendix F indicate that there are three situations which are particularly interesting.

1. The electrons pass through the aperture with the same energy ($q\varphi_o$) but at different angles (θ). Each θ class of electrons requires a different $\Delta\varphi$ value in order to be cut off. The relationship is expressed by the equation

$$\sin\theta = \frac{\omega_c L}{\sqrt{2\eta\varphi_o}} \pm \sqrt{1 + (\Delta\varphi/\varphi_o)} \quad . \tag{7.11}$$

2. Electrons enter with different energies but in the same direction. Equation 7.11 applies here also but for this case θ is fixed and each φ_o class of electrons requires a different $\Delta\varphi$ value for cut off.

3. Electrons pass through the aperture with a distribution in both energy and direction.

Although this last situation probably is closest to the actual physical conditions in most cases, the complexity of the required measurement system

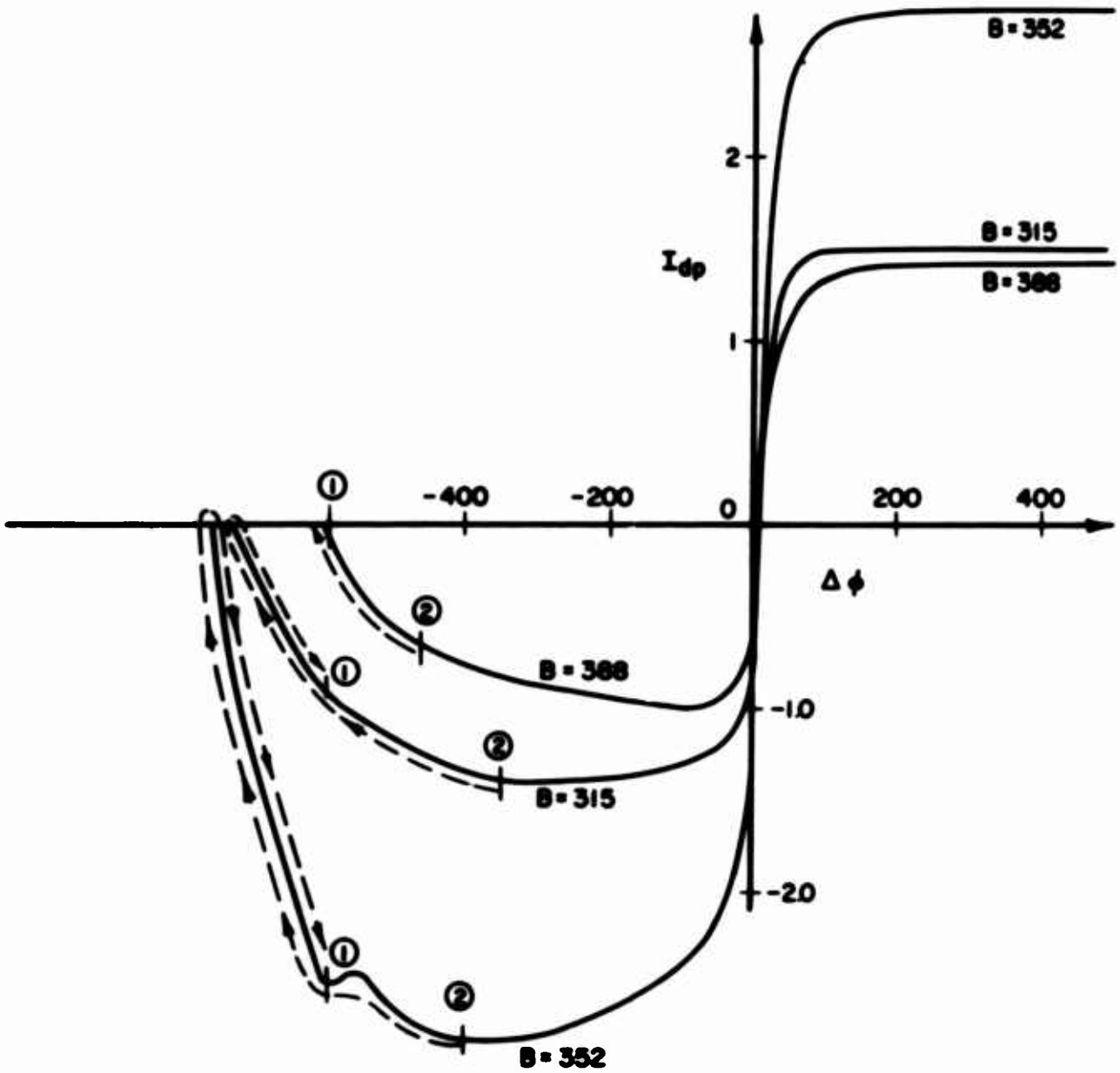

FIG. 7.33 EXPERIMENTAL RESULTS OF I_{dp} VARIATION WITH $\Delta\varphi$ FOR VARIOUS MAGNETIC FIELDS. (V_c = -1600, V_f = -500, z = 0.05")

precludes its investigation at this time. Consequently the experimental data will be analyzed on the assumption that either one of the first two conditions exists as the electrons pass through the aperture.

Consideration of Fig. 7.33 in more detail makes it possible to compare the results when there is only an angular distribution of electrons ($\Delta\theta$) with those when there is only an energy distribution ($\Delta\varphi_o$). For B = 388 gauss, the assumption of uniform energy requires that the electrons pass through the aperture with angles varying from $\theta_1 = 0°$ to $\theta_2 = -14°$. These angles correspond to the points labeled 1 and 2 on the curve. If it is assumed that the electrons all enter with $\theta = -7°$, the resulting energies fall between $\varphi_{o1} = 680$ volts and $\varphi_{o2} = 585$ volts. Thus even with the relatively sharp break of this particular curve the corresponding energy difference is nearly 100 volts which is rather large. For most of the data the difference in energy would be even greater thus suggesting that the angular distribution of the electrons at the aperture is a more reasonable explanation for the shape of the I_{dp} curves.

The above results indicate that the beam is nonlaminar. However, it is possible to calculate the average space-charge density of the electrons which pass through the aperture. This can be done by using the average angle at which the electrons enter, their average energy ($\langle\varphi_o\rangle$) and the total current passing through the aperture. For the 388 gauss curve in Fig. 7.33 these values are $\langle\theta\rangle = -7°$, $\langle\varphi_o\rangle = 680$ volts, and $I_o = 1.42 \times 10^{-4}$ amp. Equation 7.9 can be written

$$\langle\rho\rangle = \frac{\langle J\rangle}{\langle v\rangle} = \frac{I_o}{A(2\eta\langle\varphi_o\rangle)^{1/2}\cos\langle\theta\rangle}, \qquad (7.12)$$

where A = aperture area = 0.812×10^{-8} m^2. Using the above data in Eq. 7.12 results in $\langle\rho\rangle = 1.11 \times 10^{-3}$ coul/m^3 which is approximately half the Brillouin value of $\rho_o = 2.34 \times 10^{-3}$ coul/m^3.

The same calculations can also be made for the other magnetic field conditions. The results are illustrated in Table 7.1 which also includes the calculations based on the curves of Fig. 7.34 and 7.35. The tabulated values of $\langle\rho\rangle/\rho_o$ for Fig. 7.33 indicate that the flow is quite nonlaminar. The incoming electrons are observed to lie within the angular intervals $-14° < \theta < 0°$, $-19° < \theta < 39°$, and $-25° < \theta < 36°$ for B = 388, 352 and 315 gauss respectively. The lowest magnetic field condition results in a beam whose average velocity is most nearly parallel to the z-axis ($\langle\theta\rangle = 5.5°$). However, the 352 gauss situation results in the highest relative space-charge density ($\langle\rho\rangle/\rho_o = 1.16$). The difficulty in interpreting the data comes about because changes in the magnetic field modify the electron trajectories everywhere in the gun region. Furthermore, the extreme length of the gun also introduces certain nonlaminarities as indicated in Chapter III. In general, however, the space-charge densities are found to agree at least qualitatively with the results obtained in the earlier part of this chapter; i.e., $\langle\rho\rangle/\rho_o$ calculations usually result in values somewhere in the range between 0.5 and 1.5.

The space-charge densities calculated from the curves of Fig. 7.34 are of the same order of magnitude as the above results. These curves also seem to follow a more consistent pattern as the magnetic field is varied. In particular the average angle at which the electrons pass through the aperture is observed to become more negative as B is increased. These angles vary from -4° at B = 258 gauss to -16.5° at

Table 7.1

Average Space-Charge Densities Calculated from the Experimental Data

	V_c	V_f	B	$\langle\varphi_o\rangle$	θ_1	θ_2	$\langle\theta\rangle$	$\langle\dot{z}_o\rangle \times 10^{-7}$	$I_o \times 10^4$	$\langle\rho\rangle \times 10^3$	$\rho_o \times 10^3$	$\langle\rho\rangle/\rho_o$
Fig. 7.33	-1600	-500	388	682	0°	-14°	-7°	1.53	1.32	1.06	2.34	0.45
	-1600	-500	352	682	39°	-19°	+10°	1.52	2.80	2.26	1.94	1.16
	-1600	-500	315	682	36°	-25°	+5.5°	1.54	1.35	1.08	1.54	0.70
Fig. 7.34	-1100	-500	315	468	-4°	-29°	-16°	1.23	0.72	0.72	1.54	0.47
	-1100	-500	295	468	+3°	-29°	-13°	1.25	0.62	0.61	1.35	0.45
	-1100	-500	277	468	+15°	-24°	-4.5°	1.28	1.50	1.44	1.20	1.20
	-1100	-500	258	468	+20°	-28°	-4°	1.28	0.81	0.78	1.03	0.75
	-1100	-500	242	468	+20°	-28°	-4°	1.28	0.92	0.88	0.91	0.97
Fig. 7.35	-1400	-660	278	596	-2°	-26°	-14°	1.40	1.93	1.70	1.20	1.41
	-1300	-660	253	553	-12°	-30°	-21°	1.30	1.50	1.42	1.00	1.42
	-1200	-660	235	511	-15°	-37°	-26°	1.21	1.10	1.12	0.86	1.30
	-1100	-660	221	468	-26°	-38°	-32°	1.09	0.70	0.80	0.76	1.05

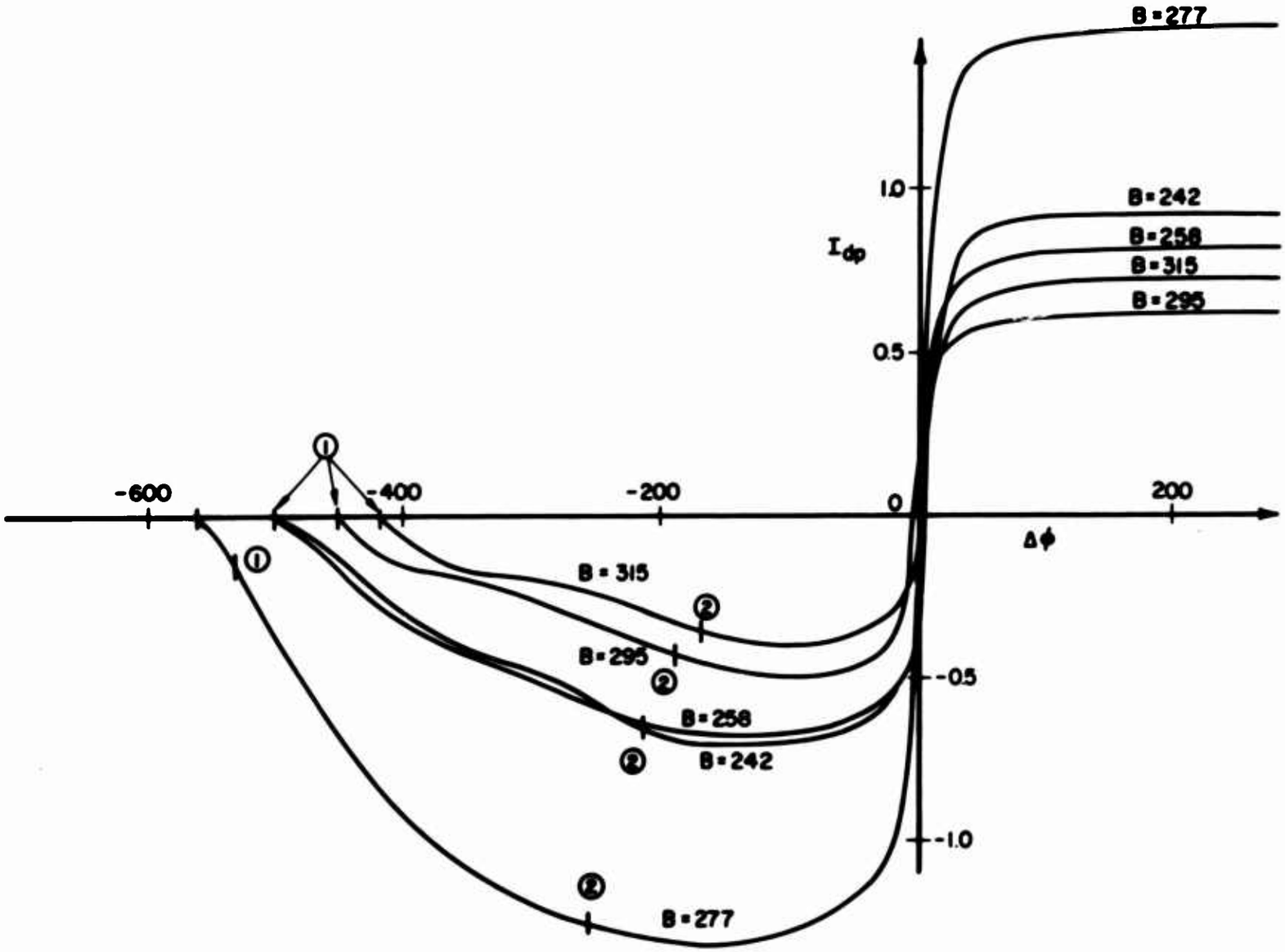

FIG. 7.34 EXPERIMENTAL VARIATION OF I_{dp} WITH $\Delta\phi$ FOR VARIOUS MAGNETIC FIELDS. (V_c = -1100, V_f = -500, z = 0.05")

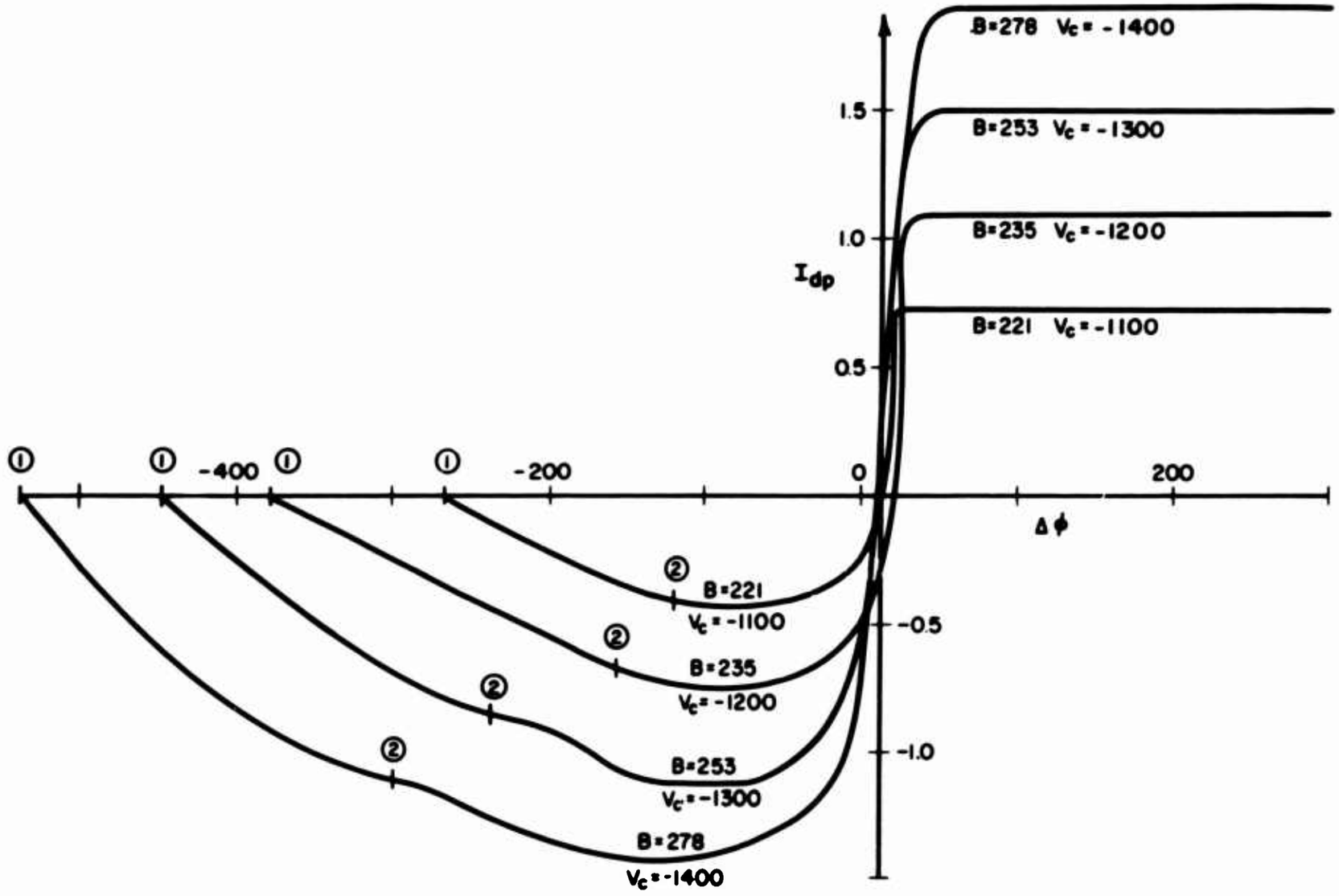

FIG. 7.35 EXPERIMENTAL VARIATION OF I_{dp} WITH $\Delta\varphi$ FOR VARIOUS B AND V_c COMBINATIONS. (V_f = -660, z = 0.05")

B = 315 gauss. The results imply that the larger magnetic field values exert a greater downward force on the beam as it leaves the gun region.

Comparison of the 315 gauss curves in Fig. 7.33 and 7.34 indicates that the electrons leave the gun in a more negative direction for V_c = -1100 volts. This behavior should be expected since the change in V_c from -1600 volts to -1100 volts results in the electron velocities being smaller by a factor of only 1.21 whereas the electric field is reduced by the factor 1.46. Thus the magnetic force is increased relative to the electric force when V_c is reduced to -1100 volts and the average angle changes from -7° to -16°.

The results of Fig. 7.35 indicate $\langle\rho\rangle$ values which are greater than the Brillouin densities. However, in contrast to the preceding data, the parameters for these curves were selected to optimize $\langle\rho\rangle$ and hence the values should correspond approximately with the maximum $\langle\rho\rangle/\rho_o$ values obtained from Figs. 7.33 and 7.34. This is essentially true since the $\langle\rho\rangle/\rho_o$ values in Fig. 7.35 vary between 1.05 and 1.42 whereas the maximum values in the preceding two cases were 1.16 and 1.2 respectively.

The V_f and V_c values in Fig. 7.35 were selected so that for each B value the ratio $(V_c-V_f)/B^2$ remained essentially constant varying only between 0.9 and 1.0. Maintaining this scaling parameter constant would result in the same trajectories and beam configurations in the gun region for each B value. As the magnetic field is reduced it is apparent from Table 7.1 that $\langle\theta\rangle$ decreases. This, of course, is in direct opposition to the type of behavior one would expect as B is varied. However, the apparent anomaly can be explained by referring to Fig. 7.36 which illustrates the location of the equipotential corresponding to the focusing-anode voltage for the various cases. As B is decreased the voltages are

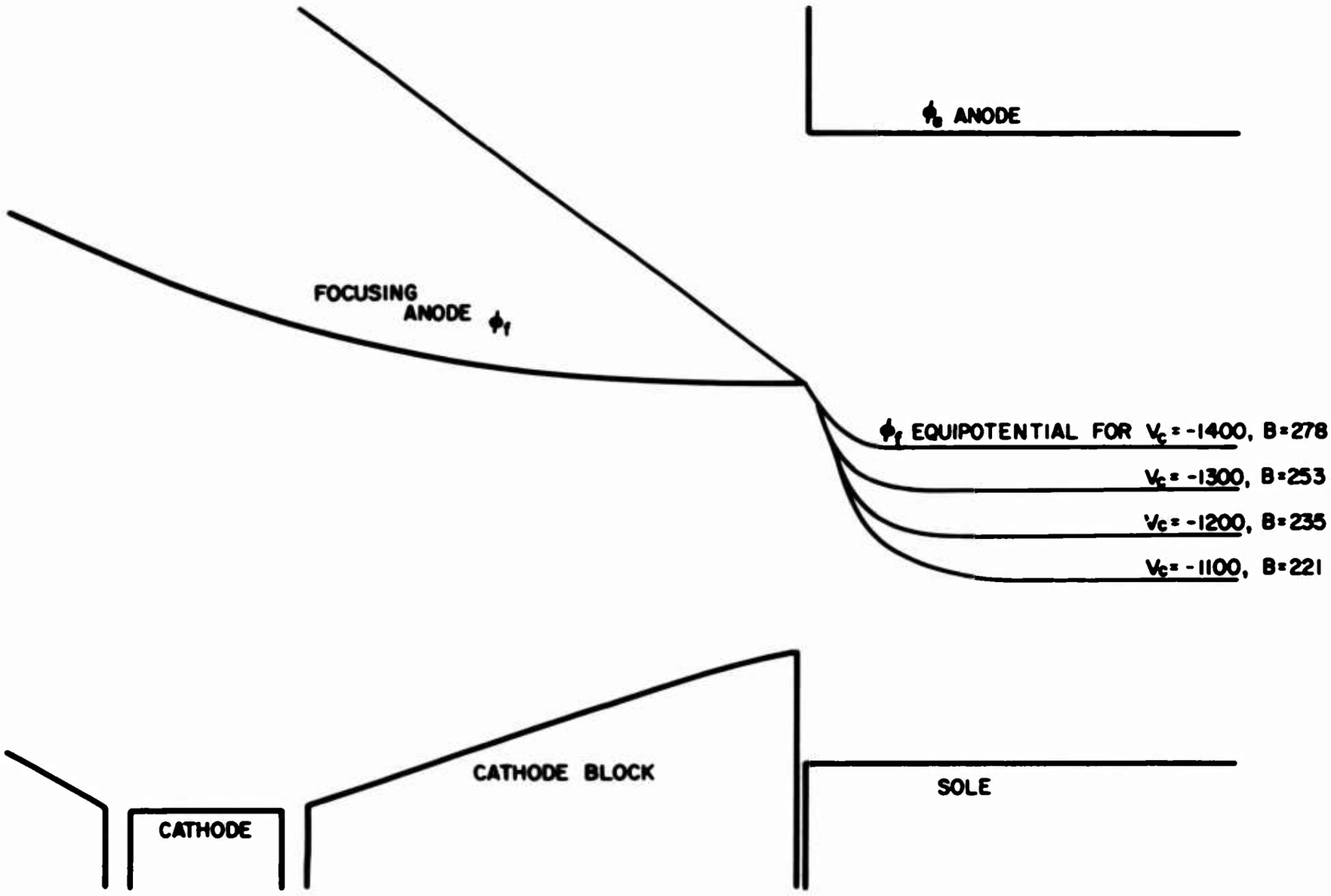

FIG. 7.36 LOCATION OF φ_f EQUIPOTENTIAL FOR VARIOUS V_c AND B VALUES.

also decreased so that the location of the equipotential in the anode-sole region is forced down toward the sole. Since electrons in crossed electric and magnetic fields tend to flow along equipotential lines, the lowering of the φ_f/φ_a equipotential forces the beam in a more downward direction as it leaves the gun. This is the reason that $\langle\theta\rangle$ decreases as B and V_c are reduced. The results again emphasize the necessity of proper matching at the exit plane in order to reduce the undulation and nonlaminarity of the beam.

The angular distribution of the electrons indicated by the experimental data appears to be rather large in some cases. In order to evaluate the $\Delta\theta$ intervals which might be expected for a given problem, the space-charge-free behavior of the electrons will be considered. The beam is assumed to be composed of identical trajectories as illustrated in Fig. 7.37. Thus at a given point (e.g., A) the electrons will have directions distributed between the limiting values of $\pm\,\theta_m$. θ_m can be obtained by solving the equations of motion which result in

$$y = \left(\frac{\eta\varphi_a}{d\omega_c^2} - \frac{\dot{z}_o}{\omega_c}\right)(1 - \cos\omega_c t) \tag{7.13}$$

and

$$z = \frac{\eta\varphi_a}{d\omega_c^2}(\omega_c t - \sin\omega_c t) + \frac{\dot{z}_o}{\omega_c}\sin\omega_c t \quad , \tag{7.14}$$

where $\dot{z}_o = (2\eta a\varphi_a/d)^{1/2}$ is the velocity of the electron at its minimum y-location. From these equations the slope of the trajectory at any point is found to be

$$\tan\theta = \frac{dy}{dz} = \frac{(\eta\varphi_a/d\omega_c - \dot{z}_o)}{(\omega_c y + \dot{z}_o)}\sin\omega_c t \tag{7.15}$$

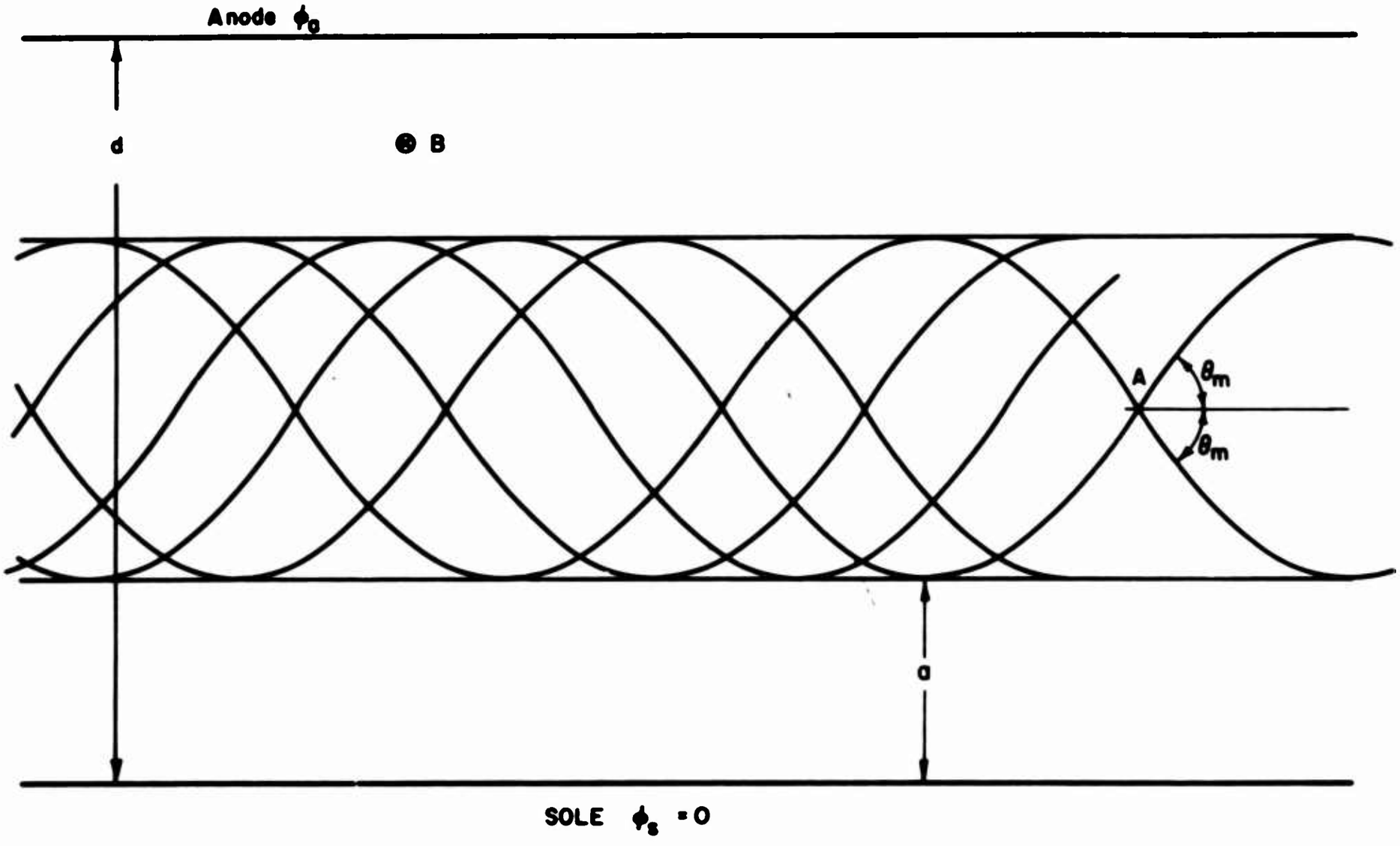

FIG. 7.37 ELECTRON BEAM COMPRISED OF ELECTRONS HAVING SIMILAR TRAJECTORIES.

which assumes a maximum value at $\omega_c t = \pi/2$ given by

$$\tan \theta_m = 1 - \frac{dB\dot{z}_o}{\varphi_a} \quad . \tag{7.16}$$

The thickness for this bundle of trajectories can be written as

$$l = \frac{2}{\omega_c} \left(\frac{\eta\varphi_a}{d\omega_c} - \dot{z}_o \right) \quad . \tag{7.17}$$

Some typical values of the various parameters would be

$$d = 3.25 \times 10^{-3} m,$$

$$B = 335 \text{ gauss},$$

$$\varphi_a = 1450 \text{ volts, and}$$

$$\dot{z}_o = 1 \times 10^7 \text{ m/sec.}$$

These values, which are those of Fig. 7.14, result in $\theta_m = 14°$ so that the trajectories passing through a given point may have an angular interval as large as $\Delta\theta = 28°$. Although the value of $\Delta\theta$ is dependent on the operating conditions, it is quite obvious that large values of $\Delta\theta$ would not be unusual. This becomes especially true when the conditions at the exit plane are badly mismatched.

Figures 7.38 and 7.39 illustrate the deflection plate current variations as the aperture system is moved along the z-axis. The first figure corresponds to the operating conditions of $V_c = -1200$, $V_f = -500$ and $B = 295$ gauss while the second has $V_c = -1400$, $V_f = -500$ and $B = 315$ gauss. In many cases the data is impossible to analyze and hence provides very little useful quantitative information.

From Fig. 7.38 the average entrance angle of the electrons at the z = 0.20, 0.40, and 0.98 inch planes are calculated to be $\langle\theta\rangle = -13°$, $-5°$ and $-18°$ respectively. Similar calculations for Fig. 7.39 result in

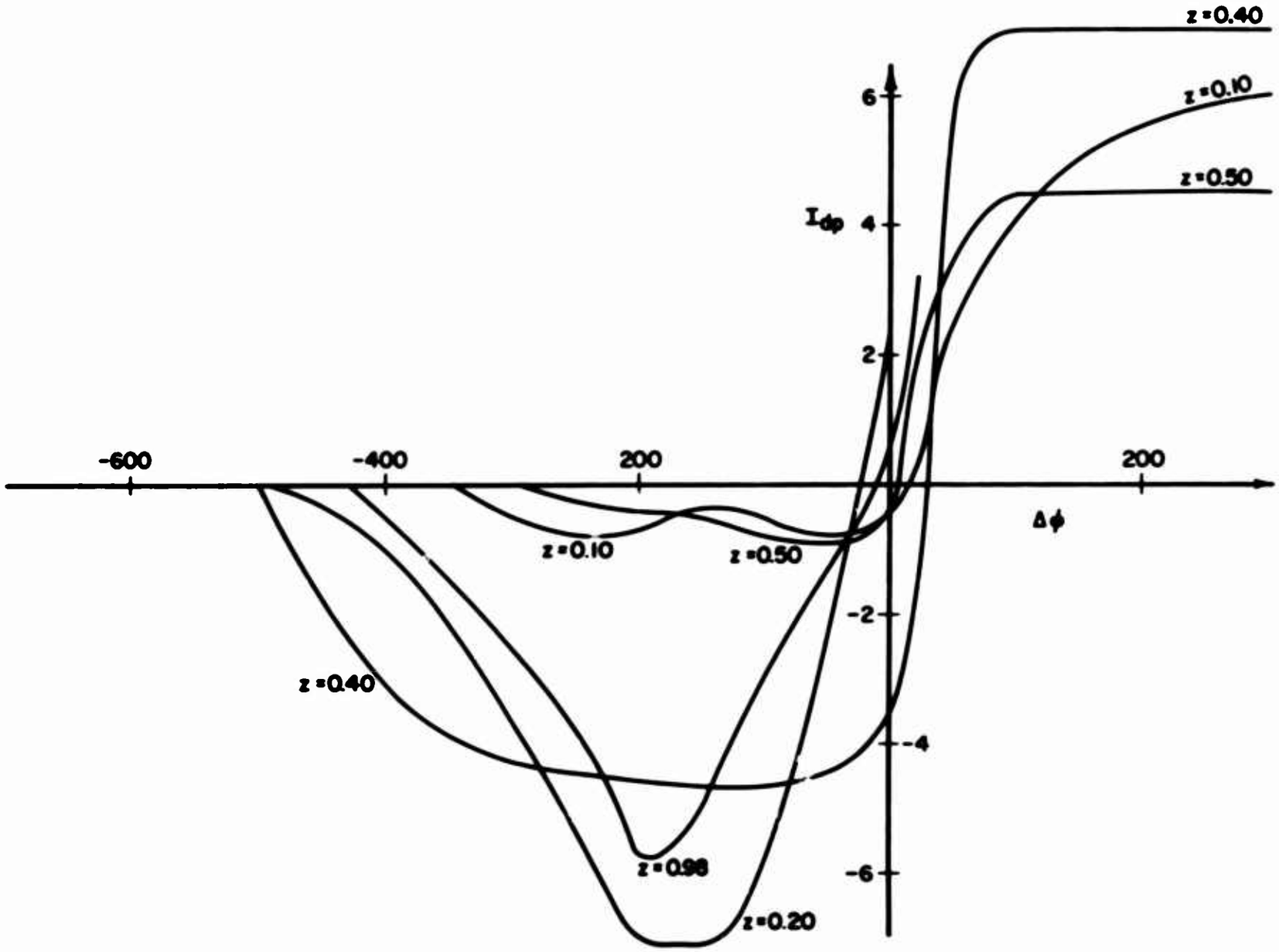

FIG. 7.38 VARIATION OF I_{dp} WITH $\Delta\varphi$ AT VARIOUS z-LOCATIONS. (V_c = -1200, V_f = -500, B = 295)

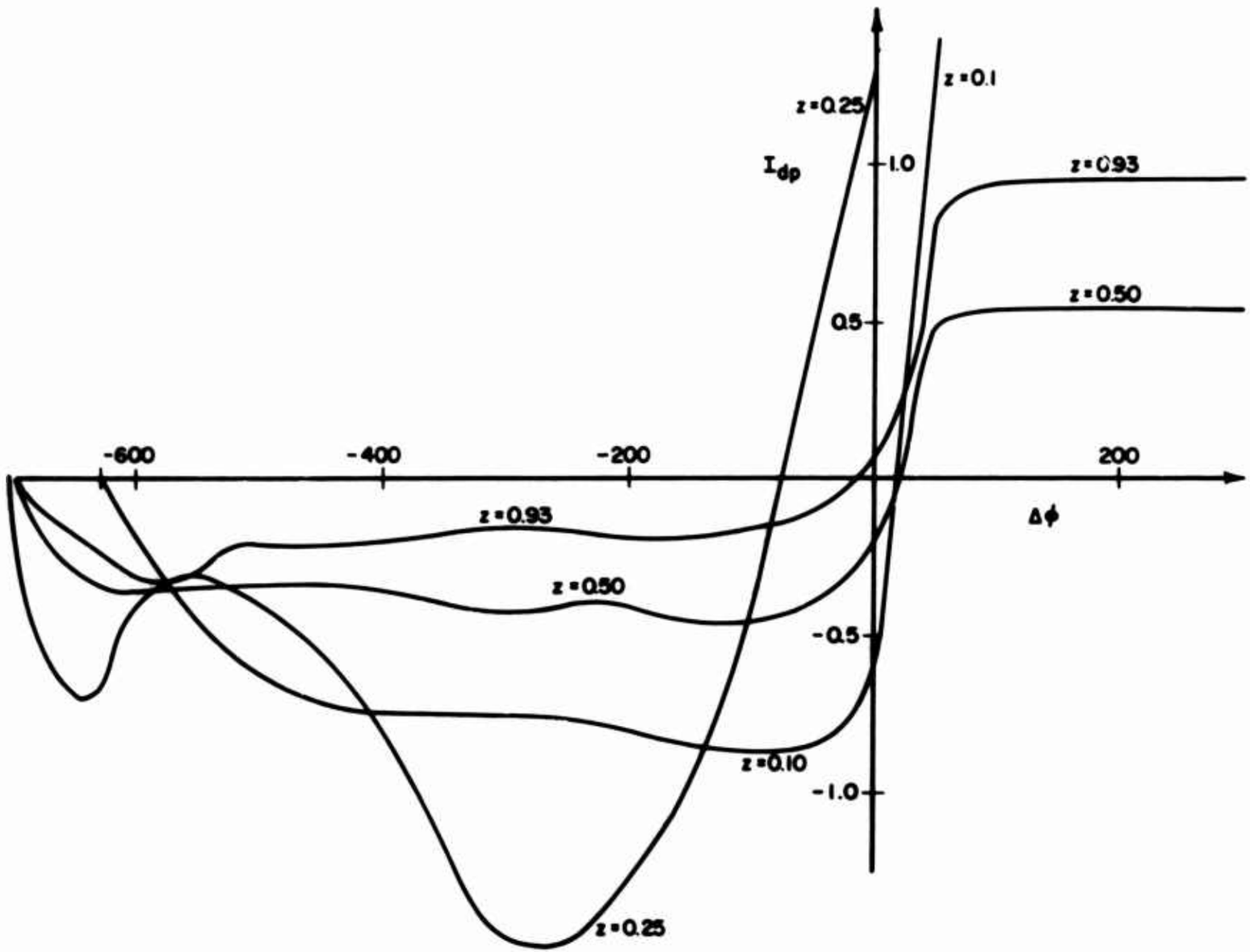

FIG. 7.39 VARIATION OF I_{dp} WITH $\Delta\varphi$ AT VARIOUS z-LOCATIONS. (V_c = -1400, V_f = -500, B = 315)

$\langle\theta\rangle$ values of -10°, 10°, 6° and 4° at z = 0.10, 0.25, 0.50 and 0.93 inch. In neither figure is there a discernible pattern to the experimental curves. It is difficult to say much more than that the beam is quite nonlaminar and the electrons have greater $\Delta\theta$ intervals at some z-locations. As the aperture system is moved away from the gun exit plane the beam undulations become more severe especially if the matching conditions are poor. Such extreme variations of the beam also complicate attempts to measure its characteristics.

7.5 Double Beam Investigations

It was suggested by Gandhi[3] that there would be certain advantages gained by operating with two thin streams rather than a single thick stream. It is thus interesting to investigate the feasibility of forming two beams which are essentially laminar in the anode-sole region. The configuration illustrated in Fig. 7.40 was used to study the characteristics of the beams which are emitted from separate cathodes located within a magnetically shielded enclosure. The cathode assemblies were isolated in order to allow each to operate at a different potential. However, this isolation required a rather wide separation of the cathodes and hence complicated attempts to form reasonably laminar electron beams.

The experimental investigations indicated that it was extremely difficult to inject simultaneously both beams into the anode-sole region. In particular, the focusing anode was observed to receive a significant amount of current under all conditions. This indicated that when conditions were favorable for one of the beams to enter the anode-sole region they were unfavorable for the other. Thus it was concluded that both beams could not be simultaneously injected into the anode-sole region without a portion of either or both of the beams being intercepted.

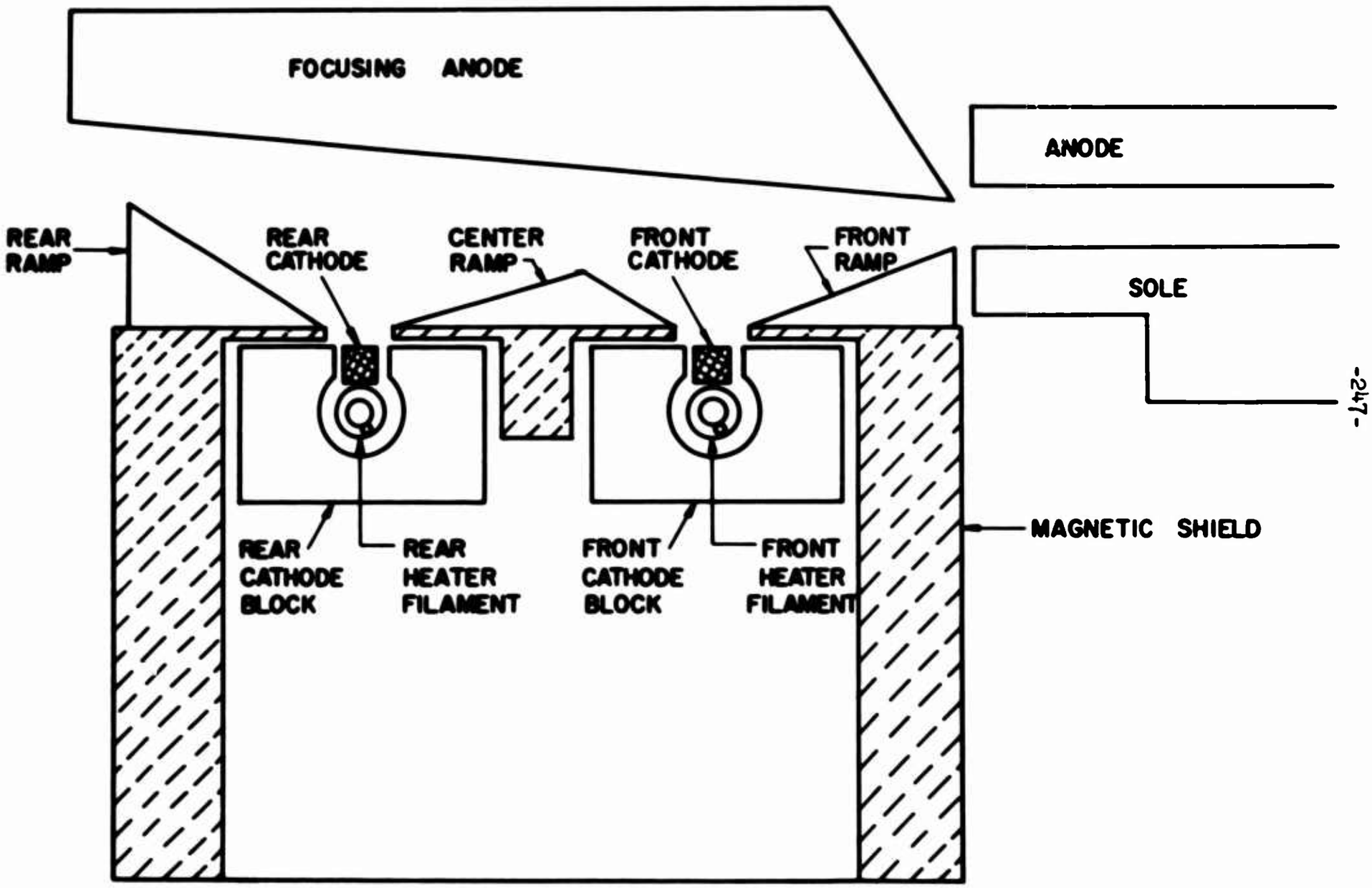

FIG. 7.40 DOUBLE CATHODE SHIELDED GUN CONFIGURATION.

This behavior is indicated in Fig. 7.41 which illustrates the anode-sole region beam profile for V_c = -1300 volts, V_f = -1000 volts and B = 400 gauss. The total emitted current is 132 ma with the front and rear cathodes contributing 96 and 36 ma respectively while the focusing anode is intercepting 45 ma. The profile indicates that there is a non-uniform beam moving through the anode-sole region. For every set of operating conditions investigated the results were essentially the same; i.e., I_f was always quite large and the intercepted grid wire currents indicated the presence of a single beam.

The above data indicate that the front cathode has greater emission than the rear cathode when they are operated at the same potential. This is partially due to the fact that the front cathode region is subjected to a greater electric field intensity. However, the extreme differences in the emissions indicate also that the front cathode is probably more active.

Again the investigations point out very emphatically the sensitive nature of crossed-field electron injection systems. That is, the achievement of a gun configuration which is capable of forming a well defined beam from a single cathode is an extremely difficult task in itself. The possibility of developing a system capable of forming two beams from separate cathodes appears to be extremely unlikely. This is especially true when the spacing between cathodes is rather large.

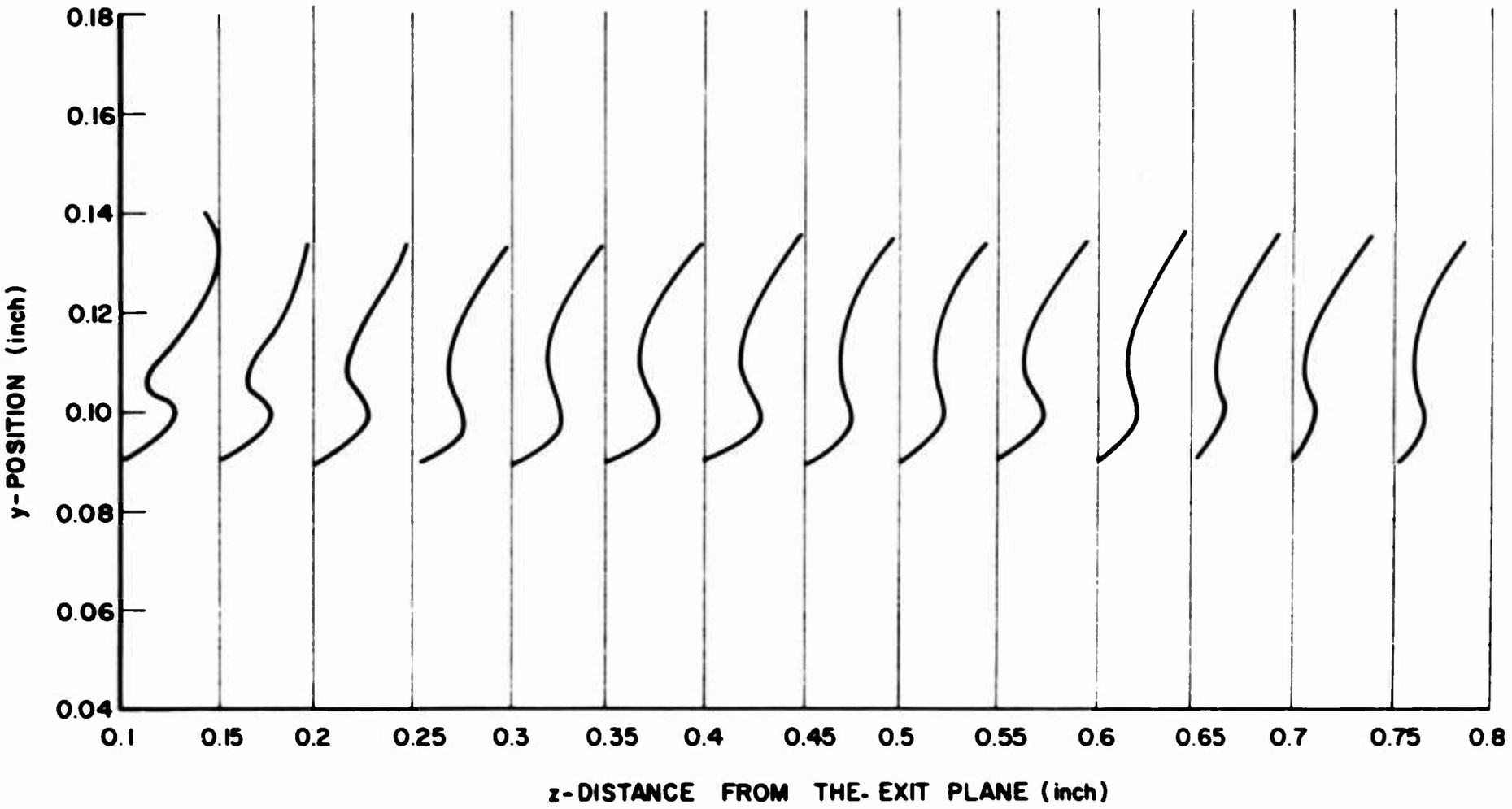

FIG. 7.41 ANODE-SOLE REGION PROFILES OF BEAM FORMED BY SHIELDED GUN. (V_c = -1300, V_f = -1000, B = 400)

CHAPTER VIII. SUMMARY, CONCLUSIONS AND SUGGESTIONS FOR FURTHER STUDY

8.1 Summary and Conclusions

This dissertation has attempted to provide a better understanding of the space-charge flow in injected-beam crossed-field devices. The investigations have been concerned with the problems associated with the formation of laminar electron beams and the experimental evaluation of the beam characteristics.

It has been demonstrated that the achievement of Brillouin flow in a planar anode-sole region involves a unique beam location and thickness for a given set of operating conditions. These restrictions result in a limitation of the maximum perveance and electronic efficiency which can be obtained for the condition of laminar space-charge flow. Furthermore, there is also a limitation to the maximum convergence which the electron gun system can impose on the beam. The operating characteristics of various theoretical guns, such as the Kino short gun, were investigated and found to be different in many respects from the Brillouin flow requirements.

The Poisson cell investigations indicated that the Kino gun did not behave exactly according to theory although the general beam configurations were essentially as predicted. The major discrepancies from the theory were the nonuniform emission of electrons from the cathode and the nonlaminar trajectories within the beam. These results were also substantiated by the digital computer investigations of similar Kino injection systems.

The digital computer analysis of an abbreviated Kino gun indicated the possibility of achieving desirable beams by modifying the ramp electrode configurations. In particular it was observed that one could achieve either laminar flow or uniform emission (although not simultaneously) by changing the slopes of the ramp electrodes. The attainment of uniform cathode emission and laminar trajectories simultaneously (if possible) would require modifications in the focusing anode configuration.

The effect of initial velocities on the electron trajectories was also evaluated by means of the digital computer program. The results indicated that variations in the normal emission velocity component produced essentially no change in the electron trajectories although it did modify the time required for the electrons to proceed along the trajectory. However, the consideration of tangential emission velocity components indicated a rather significant influence on the electron trajectory. In particular, those electrons emitted with a negative z-component of velocity were capable of reaching higher potential regions than those reached by electrons emitted in the positive z-direction. Thus the tangential emission velocity components provide a mechanism whereby electrons can reach the anode of a cut-off magnetron. For injected-beam devices these initial velocities are also responsible for wider beam configurations.

The configurations which electron beams can assume in the anode-sole region of a crossed-field device were investigated under d-c conditions. The establishment of irrotational flow was found to preclude the existence of certain configurations such as the scalloped beam pattern. The condition of irrotationality also requires that the velocity slip across the beam always be given by $\partial v/\partial n = \omega_c$. Furthermore, the only

constant space-charge density beam which can exist is one whose density is everywhere equal to the Brillouin value. Thus for an undulating beam the thickness must be less at the higher velocity cross sections of the beam.

The experimental investigations have resulted in numerous interesting observations. The volt-ampere behavior of the Kino gun was observed to follow very closely the pattern predicted by the Kino theory. The cathode emission was found to vary as $(V_f - V_c)^2/B$ for a fixed magnetic field. This variation was found to be valid over a rather wide range of magnetic field values. The average experimental cathode current densities were also found to be in good agreement with the theory.

The investigations of the gross properties of the beam in the anode-sole region indicated variations which were repeatable over distances corresponding to the cycloidal period. In general the entire beam was observed to undulate with this period. In some cases the beam thickness was observed to remain fairly constant while in others it also underwent periodic variations. The average space-charge densities were found to have values in the range of 0.5 to 1.5 times the Brillouin densities. The beam thicknesses were generally wider than the corresponding Brillouin thicknesses and under no conditions did the beam assume a scalloped configuration.

The beam characteristics in the anode-sole region were found to be critically dependent on the matching conditions between the gun and the interaction region. In addition to matching the voltages (and hence also the electric fields) at the gun exit plane, it is also necessary to match the beam which leaves the gun to the theoretical Brillouin beam which can be maintained in the anode-sole region. This requires that

the injection system form a beam whose thickness and location at the exit plane correspond to the Brillouin conditions and whose velocity variation across the beam is given by ω_c. Deviations from any of these matching conditions will result in the undulation and nonlaminar behavior of the beam in the anode-sole region.

The introduction of the aperture system allowed additional data to be taken for calculation of the space-charge densities in the beam. With the voltages matched at the gun exit plane, the magnetic field was varied and the average space-charge densities were calculated. These results were found to be in good agreement with the theoretical variations. However, when conditions were mismatched at the exit plane the beam experienced a large perturbation as it left the gun. The beam was then observed to undergo large amplitude undulatory motion such that in certain regions the electrons were capable of swarming around the aperture plate and thus making the measurements invalid.

The evaluation of the deflection plate current interception data as $\Delta\varphi$ was varied encountered some difficulties due to secondary emission effects. However, by careful examination of the data it was possible to evaluate at least qualitatively the average direction of the electrons as they passed through the aperture. The space-charge densities which were obtained from the experiments again indicated values in the range of 0.5 to 1.5 times the Brillouin values. In every case, however, the beam appeared to be quite nonlaminar.

In summary, these investigations have provided a better understanding of the space-charge flow in injected-beam crossed-field devices. The work has analyzed the limitations of various injection systems especially with respect to the achievement of laminar flow. The Poisson

cell and digital computer investigations were compared and found to be in good agreement. These results were also used to further the understanding of the experimental results. In general the experimental cathode current densities were found to be in agreement with the Poisson cell and digital computer results. Furthermore, the beam configurations in the anode-sole region (see Fig. 7.9) correspond to the results predicted by the Poisson cell investigation. Finally, the transition between the gun and the anode-sole region was demonstrated to exert a tremendous influence on the subsequent motion of the beam through the anode-sole region.

8.2 Suggestions for Further Study.

There are numerous areas of investigation which could be advantageously studied in more detail. One possibility would be a digital computer investigation of the space-charge flow which results when electrons are emitted from the cathode according to a prescribed velocity distribution function. Historically, the problem of determining the paths of electrons was first involved with attempts to obtain individual electron trajectories when space-charge effects were negligible. Various analog systems were soon developed which allowed the solution of these relatively simple problems. The next step was the solution of trajectories when space-charge forces were significant. These problems were solved after the evolution of space-charge simulating analog systems, such as the Poisson cell, and by various digital computer methods. However, the solution invariably required certain assumptions at the cathode such as space-charge-limited emission with zero initial velocities. These are the types of problems which have been handled in this dissertation. However, it was indicated in Chapter IV that the presence of initial

emission velocities causes a change in the electron trajectories. Since thermionic emission involves electrons leaving the cathode with a distribution of initial velocities, it would be extremely valuable to be able to consider such initial conditions. This would allow a more accurate representation of the thermionic emission phenomenon and thus would provide a better opportunity for understanding the experimental observations. At the present time a digital computer program based on the Monte Carlo technique seems to offer a possibility for handling the problem.

The experimental investigations described in Chapter VII could be extended in several different directions. One immediate possibility is the redesign of the Kino electrode configuration to allow grid wire measurements in the gun region. This would provide information concerning the uniformity of emission from the cathode as well as indicating more about the beam configuration in the gun region.

The abbreviated Kino gun described in Chapter IV would prove an interesting experimental model to investigate. Since the digital computer studies indicated such highly desirable characteristics, it would be important to evaluate whether the true behavior is that good. The matching of conditions at the exit plane would be especially interesting to investigate.

Finally the insertion of an r-f structure in the anode-sole region would allow the investigation of the beam characteristics when subjected to the presence of a propagating r-f wave. This would provide a great deal of useful information concerning the response of the beam when interacting with an r-f wave. Such knowledge could lead to improvements in the operation of crossed-field devices.

APPENDIX A. BRILLOUIN ANALYSIS

Figure A.1 illustrates an electron beam moving through the planar anode-sole region of a crossed-field device. In regions 1 and 3 Laplace's equation

$$\nabla^2\varphi\,(y,z) = 0 \tag{A.1}$$

must be satisfied while in the space-charge region 2 the potential distribution is given by Poisson's equation

$$\nabla^2\varphi\,(y,z) = \frac{-\rho(y,z)}{\epsilon_0} \quad . \tag{A.2}$$

The condition of rectilinear laminar flow requires that the electrons have only a z-component of velocity. The transverse electric and magnetic forces acting on the individual electrons will be balanced if

$$\dot{z} = \frac{d\varphi/dy}{B} \quad . \tag{A.3}$$

Conservation of energy also requires that

$$\dot{z} = \sqrt{2\eta}\,\sqrt{\varphi} \quad , \tag{A.4}$$

where the electrons are assumed to have originated from a zero potential cathode with zero initial velocity. Combining equations A.3 and A.4 and integrating gives

$$\varphi = \frac{\omega_c^2}{2\eta}(y + C_1)^2 \quad , \tag{A.5}$$

where C_1 is a constant.

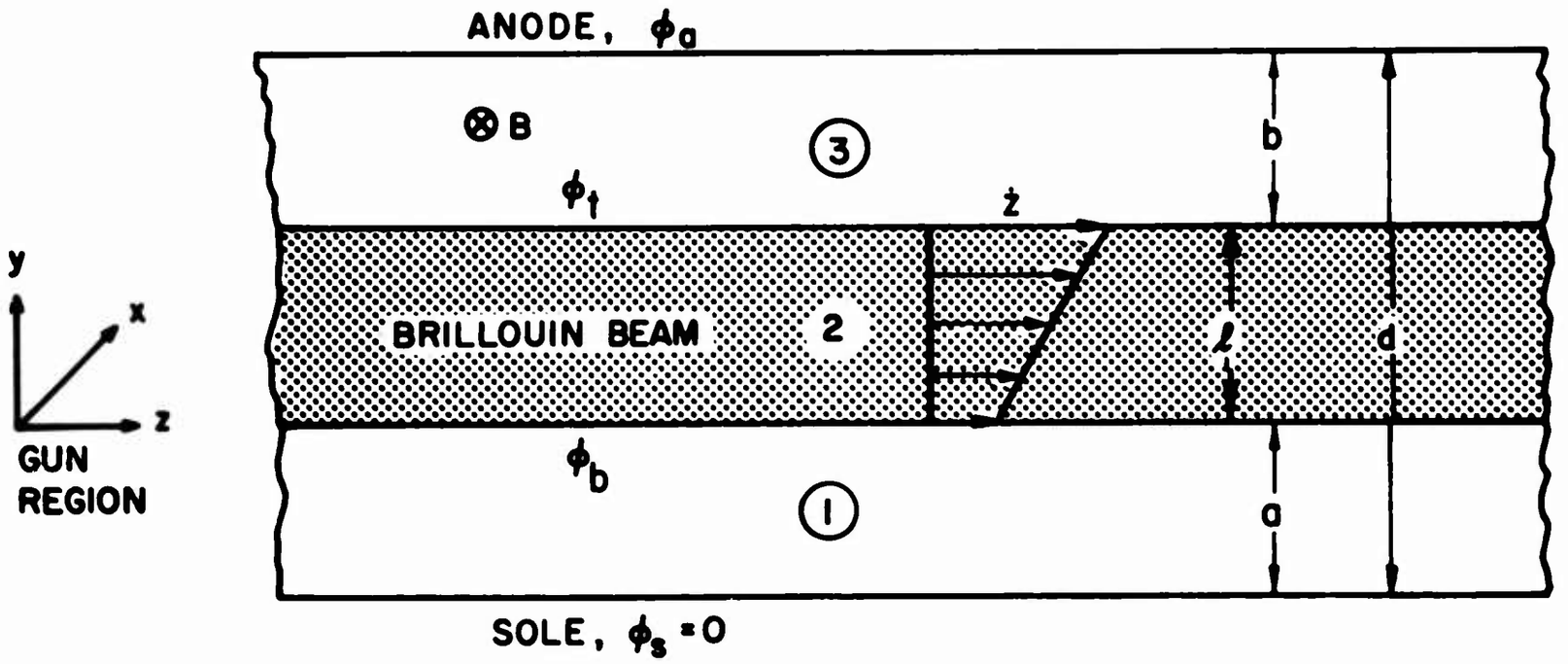

FIG. A.1 BRILLOUIN BEAM MOVING THROUGH THE ANODE-SOLE REGION.

The electric field can thus be written as

$$E_y = -\frac{\omega_c^2}{\eta}(y + C_1) \quad . \tag{A.6}$$

The electric field must be continuous across the lower boundary of the beam which results in the equation

$$-\frac{\omega_c^2}{\eta} C_1 = -\frac{\omega_c^2}{2\eta} \frac{C_1^2}{a} \quad . \tag{A.7}$$

This yields $C_1 = 2a$ where a is the distance from the lower edge of the beam to the sole.

The potential and electric field in the beam can thus be written as

$$\varphi = \frac{\omega_c^2}{2\eta}(y + 2a)^2 \tag{A.8}$$

and

$$E_y = -\frac{\omega_c^2}{\eta}(y + 2a) \quad . \tag{A.9}$$

Using this value of φ in Eq. A.2, results in the Brillouin space-charge density as given by

$$\rho_o = -\frac{\epsilon_o}{\eta}\omega_c^2 \quad . \tag{A.10}$$

This density is only a function of the magnetic field.

From Eq. A.3 the velocity becomes

$$\dot{z} = \omega_c (y + 2a) \tag{A.11}$$

which leads to the current density expression

$$J_z = \rho \dot{z} = -\frac{\epsilon_o \omega_c^3}{\eta} (y + 2a) \quad . \tag{A.12}$$

The total current carried by the beam is given by

$$I = h \int_{y=0}^{y=\ell} J_z \, dy = h \int_0^{\ell} \frac{\epsilon_o \omega_c^3}{\eta} (y + 2a) \, dy \quad , \tag{A.13}$$

which upon integration becomes

$$I = \frac{h \, \epsilon_o \omega_c^3}{\eta} \left(\frac{\ell^2}{2} + 2a\ell \right) \quad , \tag{A.14}$$

where h is the width of the beam in the magnetic field direction.

These equations provide a complete description of a rectilinear Brillouin beam located at a distance "a" above the sole of a planar crossed-field device.

APPENDIX B. DETERMINATION OF ELECTRON TRAJECTORIES BY THE USE OF A POISSON CELL AND ANALOG COMPUTER

The determination of an electron trajectory requires the simultaneous evaluation of the equations of motion and Poisson's equation. The ballistics equations are solved by an analog computer while the effects of space charge require the use of a Poisson cell[32]. The complete system is illustrated in Fig. B.1.

The electrode configuration is applied to the Poisson cell with conducting silver paint. The various electrodes are then connected to the appropriate voltages to produce the space-charge-free potential distribution in the cell. The space charge is simulated by the injection of currents into the matrix of dots located on the underside of the Poisson cell. The electric field acting on an electron at any point is determined by a four probe system which measures the voltage differences in the y-and z-directions. The analog computer uses this information to solve the ballistics equations for the electron motion thus providing a series of trajectories. From a given set of trajectories, the space-charge distribution is determined and the corresponding currents are injected to simulate the conditions for the next run. The process is continued until a self-consistent solution is obtained whereby the space-charge distributions for two successive runs are nearly identical.

The electron ballistics equations for crossed-fields are

$$\frac{d^2y}{dt^2} = -\eta \left[E_y + B \frac{dz}{dt} \right] \qquad \text{(B.1)}$$

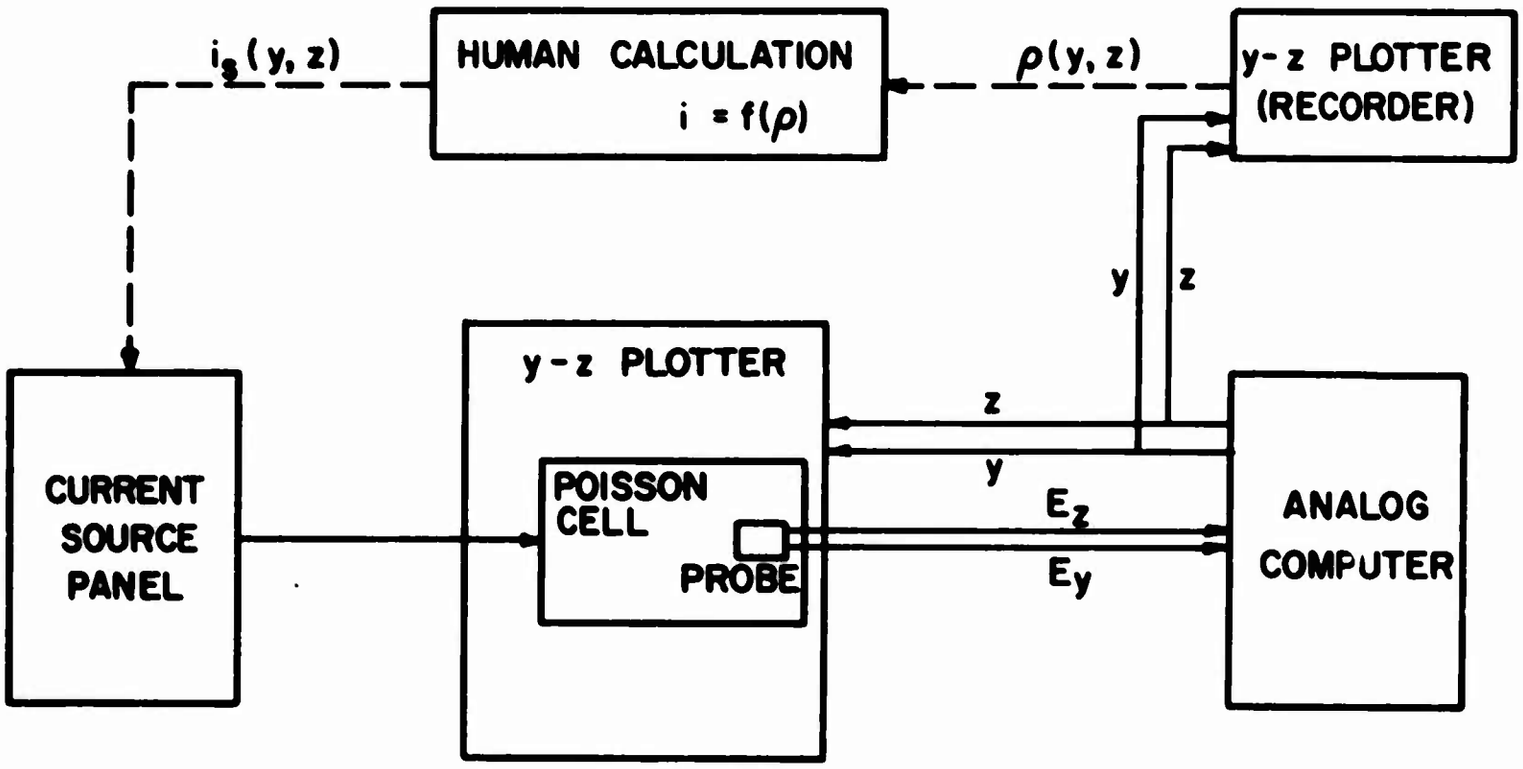

FIG. B.1 ELECTRON TRAJECTORY CALCULATOR AND POISSON CELL.

and

$$\frac{d^2z}{dt^2} = -\eta \left[E_z - B \frac{dy}{dt} \right] \tag{B.2}$$

and can be solved on an analog computer. In computer notation these equations take the form

$$b_1 \frac{d^2y}{dT^2} = C_1 \Delta V_y - C_2 \dot{Z} \tag{B.3}$$

$$b_1 \frac{d^2z}{dT^2} = C_1 \Delta V_z + C_2 \dot{Y} \quad . \tag{B.4}$$

T is computer time while Y, Z, $\dot{Y}$, and $\dot{Z}$ represent amplifier outputs which are proportional to the electron's position and velocity at a given instant. b_1, C_1, and C_2 are appropriate scaling constants while ΔV_y and ΔV_z represent the difference in potentials of the four probes in the y-and z-directions.

The circuitry required for the solution to this problem is illustrated in Fig. B.2. This flow chart can be separated into five basic sections, three of which are necessary for determining the trajectories and two which give an indication of the system accuracy.

The operation performed by each section is fundamental but simple. The voltages picked up by the four probes as they move across the surface of the Poisson cell are first fed into the unloading amplifiers. These signals are then transmitted tc the gradient circuit wherein the magnitudes of the electric field components are determined. These components and a constant magnetic field are simultaneously fed into the ballistics circuit which solves the equations of motion and determines the velocity and position of the electron.

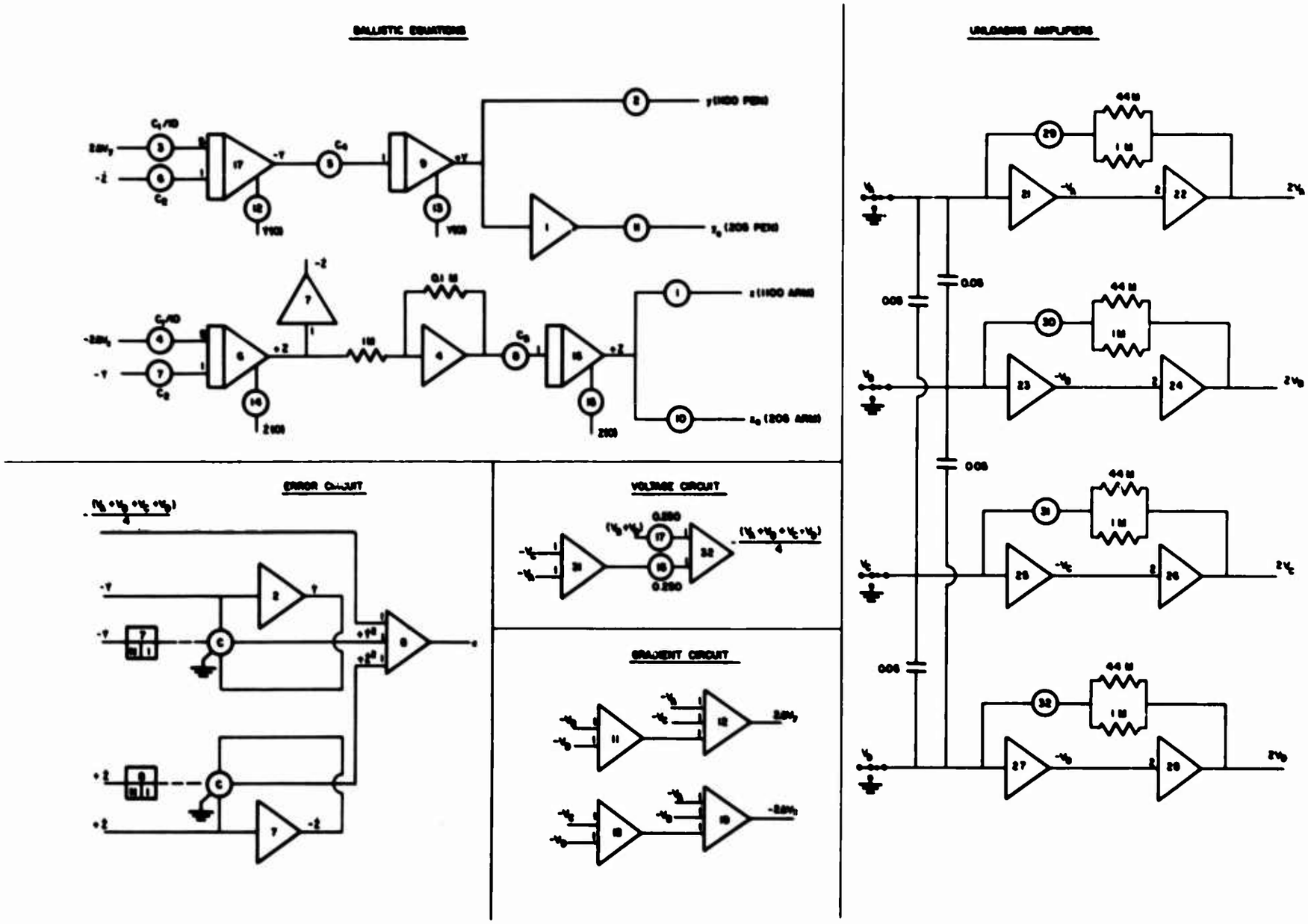

FIG. B.2 ANALOG COMPUTER FLOW CHART ILLUSTRATING THE CIRCUITRY REQUIRED TO DETERMINE THE ELECTRON TRAJECTORIES IN CROSSED-FIELD DEVICES.

The position signals are transmitted to the servo-mechanisms which control the y-and z-motion of the probe carriage on the 205 K variplotter. The probes are thus moved to the correct position at which the voltages are picked up and sent into the unloading amplifiers to complete the operating cycle. The entire process is continuous with all operations occurring simultaneously and results in the trajectory plots illustrated in Chapter III.

The voltage circuit determines the average voltage of the four probes which is then fed into the error circuit where it is compared with the voltage equivalent of the electron velocity. The difference between these two voltages is a direct measure of the error accumulation during the trajectory. When the system is operating properly the error is less than one percent.

APPENDIX C. THEORY OF THE ABBREVIATED KINO SHORT GUN

Figure C.1 illustrates the theoretical Kino short gun trajectories and the equipotentials which exist outside of the space-charge region. The relations between the normalized parameters (Z,Y,Φ) and the actual quantities (z,y,φ) are given by

$$z = \frac{\eta J_y}{\epsilon_o \omega_c^3} Z \quad , \tag{C.1}$$

$$y = \frac{\eta J_y}{\epsilon_o \omega_c^3} Y \quad , \tag{C.2}$$

and

$$\varphi = \frac{\eta J_y^2}{\epsilon_o^2 \omega_c^4} \Phi \quad . \tag{C.3}$$

It is assumed that the normalized cathode width of $W = 3$ corresponds to an actual value of $w = 0.100$ inch. Thus specification of the magnetic field determines both the cathode current density J_y and the voltage ratio φ/Φ. If $B = 300$ gauss, the constant J_y becomes 0.628 amp/cm^2 and the normalized focusing anode voltage of $\Phi = 25$ corresponds to an actual value of $\varphi_f = 2850$ volts.

The theoretical gun is terminated at plane B-B as indicated in Fig. C.1. This eliminates the difficulties associated with the theoretical infinite space-charge density at the $\omega_c t = 2\pi$ point along a trajectory. At the top of the exit beam

$$\omega_c t_+ = 280° \quad ,$$

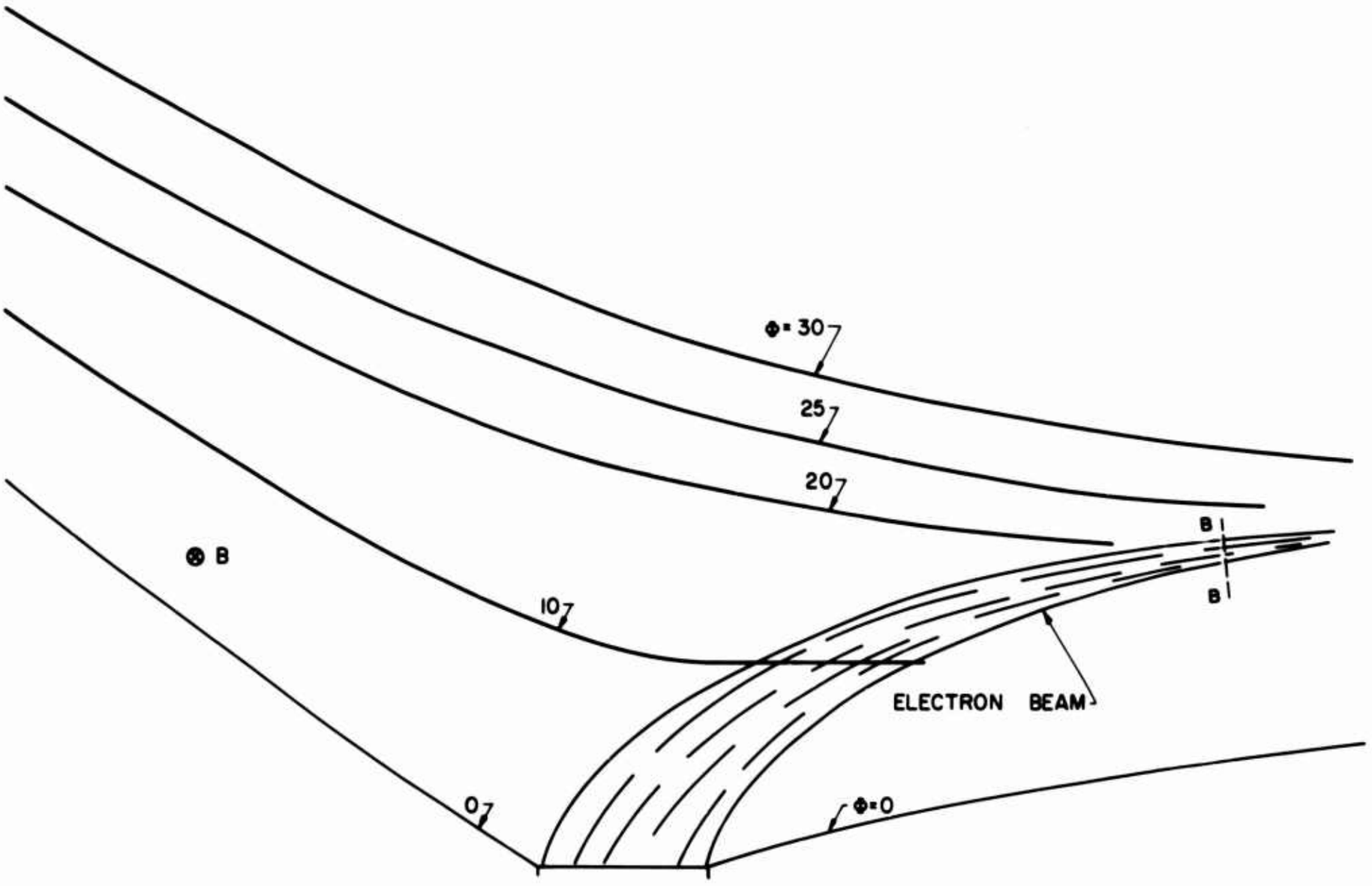

FIG. C.1 ELECTRON BEAM AND EQUIPOTENTIAL CURVES FOR THE THEORETICAL FLOW OF THE KINO SHORT GUN.

$$\varphi_+ = 2000 \text{ volts}$$

and

$$\rho_+ = 1.2\ \rho_o$$

while on the lower boundary

$$\omega_c t_- = 242° \ ,$$

$$\varphi_- = 1690 \text{ volts}$$

and

$$\rho_- = 0.74\ \rho_o \ .$$

The anode-sole region illustrated in Fig. C.2 has been selected so that the Brillouin beam which is compatible with this region matches the above conditions as closely as possible. The location of the Brillouin beam above the sole is given by

$$a = \frac{\eta\ J_c}{\epsilon_o \omega_c^3} \left(\frac{w}{2\ell} \right) - \frac{\ell}{4} \ . \qquad (C.4)$$

Using the theoretical beam thickness $\ell = 4.5 \times 10^{-4}$ meter obtained from Fig. C.1, the above equation can be solved to give

$$a = 2.28 \times 10^{-3} \text{ meter} \ .$$

The potential variation in the Brillouin beam is

$$\varphi = \frac{\omega_c^2}{2\eta} (y + 2a)^2 \qquad (C.5)$$

so that at the upper and lower boundaries

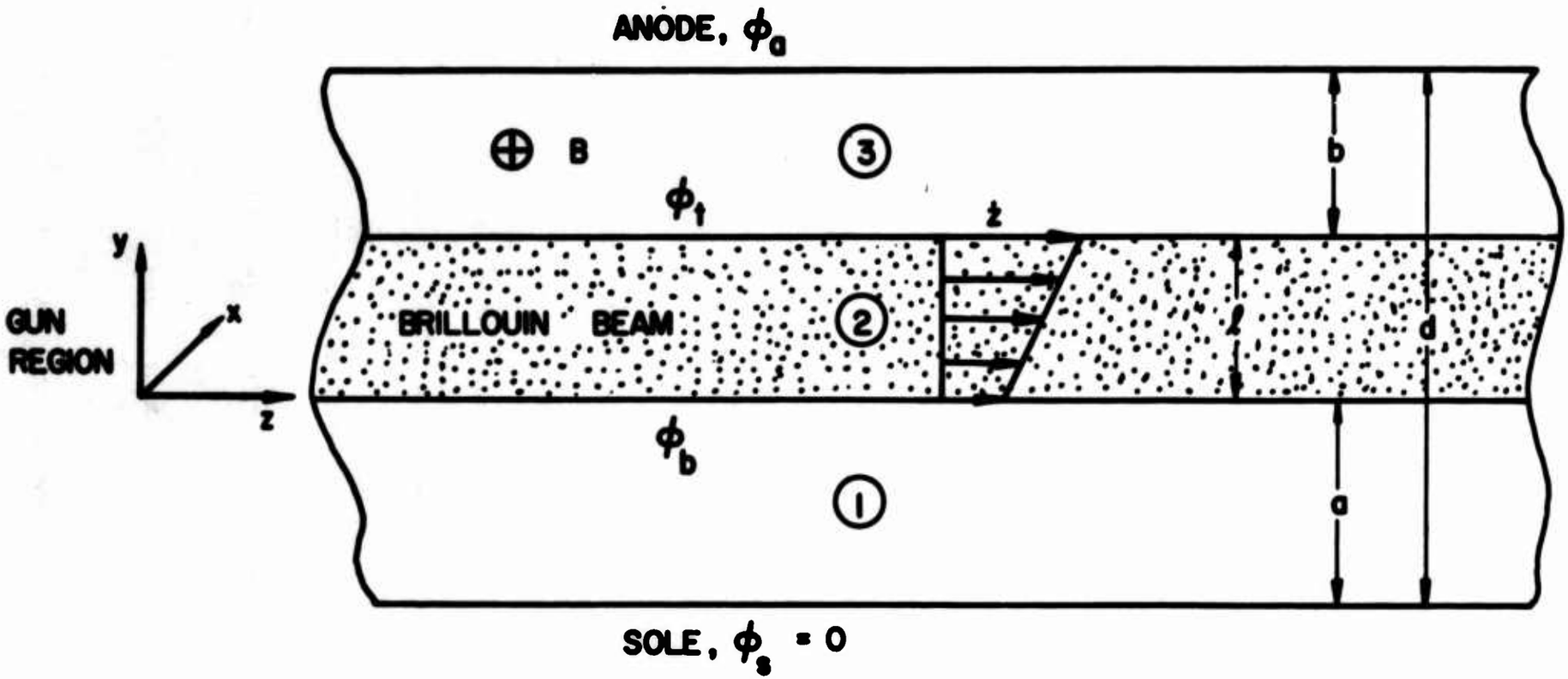

FIG. C.2 BRILLOUIN BEAM MOVING THROUGH THE ANODE-SOLE REGION.

$$\varphi_+ = 1990 \text{ volts} ,$$

and

$$\varphi_- = 1660 \text{ volts} .$$

Thus the beam thickness and potentials are nearly the same in the two regions. However, since the space-charge density in the theoretical Kino flow is not uniform there is a discontinuity in ρ and hence also in the electric field between the two regions. This is characteristic of the Kino electron beam and cannot be avoided. Thus the above prescribed matching conditions are about as good as can be expected between a short gun electron beam and Brillouin flow.

APPENDIX D. ELECTRON MOTION IN A POTENTIAL MINIMUM REGION

The effect of initial velocity on the motion of an electron through a prescribed potential minimum region can be easily evaluated. Consider the voltage in the potential minimum region to be given by

$$\varphi = \varphi_m + \left(\frac{9J_c}{4\epsilon_o \sqrt{2\eta}} \right)^{2/3} (y_m - y)^{4/3} , \tag{D.1}$$

where φ is assumed to be independent of the z-coordinate. Under these conditions the z-component of the Lorentz force equation becomes

$$\frac{d^2 z}{dt^2} = \omega_c \dot{y} \tag{D.2}$$

which upon integration yields

$$\dot{z} = \omega_c y + \dot{z}_o . \tag{D.3}$$

The electrons are assumed to be emitted from the cathode with an initial velocity v_o which can be written as

$$v_o^2 = \dot{y}_o^2 + \dot{z}_o^2 = 2\eta \varphi_o . \tag{D.4}$$

Conservation of energy requires that the velocity at any point satisfies the equation

$$v^2 = \dot{y}^2 + \dot{z}^2 = 2\eta (\varphi + \varphi_o) . \tag{D.5}$$

Thus at the potential minimum

$$\dot{z}_m = \omega_c y_m + \dot{z}_o \tag{D.6}$$

and

$$\dot{y}_m^2 + \dot{z}_m^2 = 2\eta\,(\varphi_m + \varphi_o) \quad . \tag{D.7}$$

The problem will now be to determine the direction in which an electron of initial energy φ_o can leave the cathode and still be capable of reaching the potential minimum plane.

Those electrons which are barely able to arrive at $y = y_m$ must have $\dot{y}_m = 0$ so that Eqs. D.6 and D.7 can be combined to give

$$\dot{z}_o = \pm \sqrt{2\eta\,(\varphi_m + \varphi_o)} - \omega_c y_m \quad . \tag{D.8}$$

For the problem considered in section 4.3,

$$\varphi_m = -0.05 \text{ volt}$$

and

$$y_m = 1.71 \times 10^{-6} \text{ meter.}$$

Assuming the temperature of the cathode to be 1100°C, which corresponds to a voltage of $\varphi_o = 0.12$ volt, the initial thermal velocity is $v_o = 2.05 \times 10^5$ m/sec. Substituting these values into Eq. D.8 results in

$$\dot{z}_o = \begin{cases} -1.66 \times 10^5 \text{ m/sec.} \\ +1.48 \times 10^5 \text{ m/sec.} \end{cases}$$

which defines the limits of the possible emission angle given by

$$\sin\theta = \frac{\dot{z}_o}{v_o} \quad . \tag{D.9}$$

Evaluation of the above equation indicates that those electrons emitted within the angular interval $-56° < \theta < 46°$ are capable of traversing the potential minimum region. Any electron which is emitted in a direction

outside of the above interval is rejected and returned to the cathode. Electrons which are emitted with $\varphi_o > 0.12$ volt have a wider θ interval for which they are able to reach the $y = y_m$ plane.

The minimum initial energy which an electron must have to reach the potential minimum is 0.05 electron volt which is the value of $|\varphi_m|$. However, any electron which leaves the cathode with this energy can reach the y_m plane only if it is emitted in the optimum direction. The velocity corresponding to $\varphi_o = 0.05$ volt is $v_o = 1.33 \times 10^5$ meters/sec. and from Eq. D.8 $\dot{z}_o = 0.904 \times 10^4$ meters/sec. Thus the angle at which this minimum energy electron must leave the cathode is $\theta = -8.3°$. The general expression for the critical angle can be obtained by placing $\varphi_o = |\varphi_m|$ and using Eqs. D.8 and D.9. The result becomes

$$\sin \theta_{cr.} = -\frac{\omega_c y_m}{(2\eta|\varphi_m|)^{1/2}} \qquad \text{(D.10)}$$

from which it is obvious that the critical angle depends on the potential minimum voltage and location as well as on the magnetic field.

APPENDIX E. AVERAGE SPACE-CHARGE-DENSITY CALCULATIONS FROM EXPERIMENTAL DATA

Figure E.1 illustrates a typical electron beam configuration in the anode-sole region of a crossed-field device. Several methods will be used to estimate the average space-charge density in the beam at various z-positions. The following notation will be used:

φ = voltage at any point,

φ_a = anode voltage,

I = total beam current,

I_j = current intercepted by the jth wire,

d = anode-sole spacing,

ℓ = beam thickness,

h = beam width in the x-direction,

b = distance from anode to upper beam boundary,

a = distance from sole to lower beam boundary, and

D = grid wire diameter.

There are numerous ways of interpreting the beam interception data and some of the more obvious possibilities will be considered here.

<u>Case 1</u>: For this situation the current density at a given wire location will be evaluated from the current intercepted by that wire

$$J_j = \frac{I_j}{hD} . \tag{E.1}$$

Combining this result with

$$J_j = \rho_j v_j \tag{E.2}$$

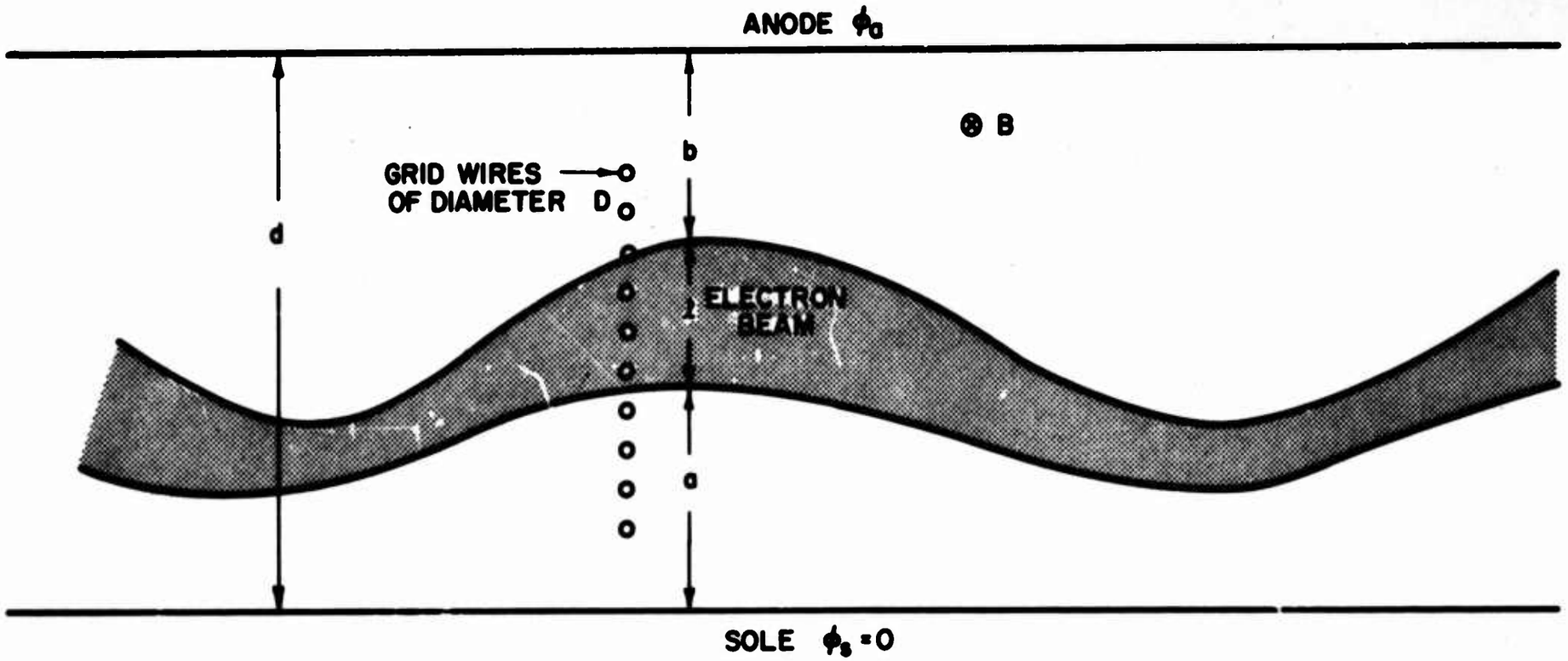

FIG. E.1 ELECTRON BEAM CONFIGURATION IN PLANAR ANODE-SOLE REGION.

results in the space-charge density

$$\rho_j = \frac{I_j}{hD\sqrt{2\eta\varphi_j}} \quad . \tag{E.3}$$

However, use of Eq. E.3 to calculate ρ_j generally results in values much smaller than expected. The principal weakness of this method is the fact that it ignores the potential of the wire. As mentioned in the text, the current intercepted by a given wire is not only a function of the current density in the beam but also of the potential difference between the wire and corresponding beam location.

Case 2: The voltage in the beam is assumed to be only a function of the y-coordinate at any cross section. Poisson's equation can thus be written

$$\frac{d^2\varphi}{dy^2} = -\frac{\rho}{\epsilon_o} \quad . \tag{E.4}$$

If ρ is assumed constant across the beam, then it can be written as

$$\rho = -\frac{\epsilon_o}{\ell}(\varphi'_+ - \varphi'_-) \quad , \tag{E.5}$$

where $\varphi' \triangleq d\varphi/dy$ and the φ'_+ and φ'_- refer to the values at the upper and lower beam boundaries respectively. These values can be determined by plotting the voltages on the wires as a function of y and measuring the appropriate slopes of the curve.

Case 3: The continuity of current equation can be written as

$$I = h \int_{y=0}^{y=\ell} \rho \dot{z} dy \tag{E.6}$$

which must be valid at any z-cross section. The following assumptions are then made:

1. ρ = constant across the beam, and

2. $\dot{z}$ varies precisely as in Brillouin flow so that

$$\dot{z} = \omega_c(y + 2a) \quad . \tag{E.7}$$

Under these restrictions Eq. E.6 becomes

$$I = h\rho\omega_c \int_0^{\ell} (y + 2a)\, dy \tag{E.8}$$

which is integrated to give

$$\rho = \frac{2}{h\omega_c \ell(\ell + 4a)} I \quad . \tag{E.9}$$

<u>Case 4</u>: The same assumptions are made as in Case 3 except that ρ is no longer considered constant across the beam but rather is assumed to vary as

$$\rho = \rho_m \sin \frac{\pi y}{\ell} \quad . \tag{E.10}$$

This implies a maximum density at the center of the beam ($y = \ell/2$). On this basis Eq. E.6 becomes

$$I = h\rho_m\omega_c \int_0^{\ell} (y + 2a) \sin \frac{\pi y}{\ell}\, dy \tag{E.11}$$

which results in

$$\rho_m = \frac{\pi}{h\omega_c \ell(\ell + 4a)} I \quad . \tag{E.12}$$

Thus ρ_m is $\pi/2$ times the result given by Eq. E.9. Any one of the preceding methods could be used to obtain qualitative values of

space-charge density from the experimental grid wire interception data. The values obtained in Chapter VII were calculated by the methods described in cases 3 and 4.

APPENDIX F. INTERPRETATION OF THEORETICAL APERTURE SYSTEM BEHAVIOR

Figure F.1 illustrates the trajectory of an electron as it moves between the grid wires and passes through the aperture into the deflection region. A space-charge-free Poisson cell analysis of the motion was performed in order to evaluate the effect of the aperture plate and grid wires on the electron trajectory. The design voltage for the aperture plate is φ_1 which is intermediate between the potentials of the two wires which are located above and below the aperture. As φ_1 was changed by ± 10 percent, the trajectory angle (θ_o) of the electron at the aperture plane was found to differ by less than one degree from the φ_1 case; i.e., for a design value of 500 volts the aperture plate can be operated between 450 and 550 volts without significantly changing θ_o. The reason, of course, is that the grid wire potentials provide the correct electric field for the electrons until they pass the grid wires plane. Beyond this plane the electrons experience some effect due to the aperture plate. However, the distance between the grid wires and the aperture is so small and the electron velocity so great that the electrons reach the aperture plate before any significant change in trajectory can occur.

This behavior has also been verified analytically by considering the electron to experience zero E_y in the region between the grid wires and the aperture and comparing this trajectory with that obtained when E_y is the usual value in a planar crossed-field region. The trajectories for each situation were found to be essentially the same (less than 4

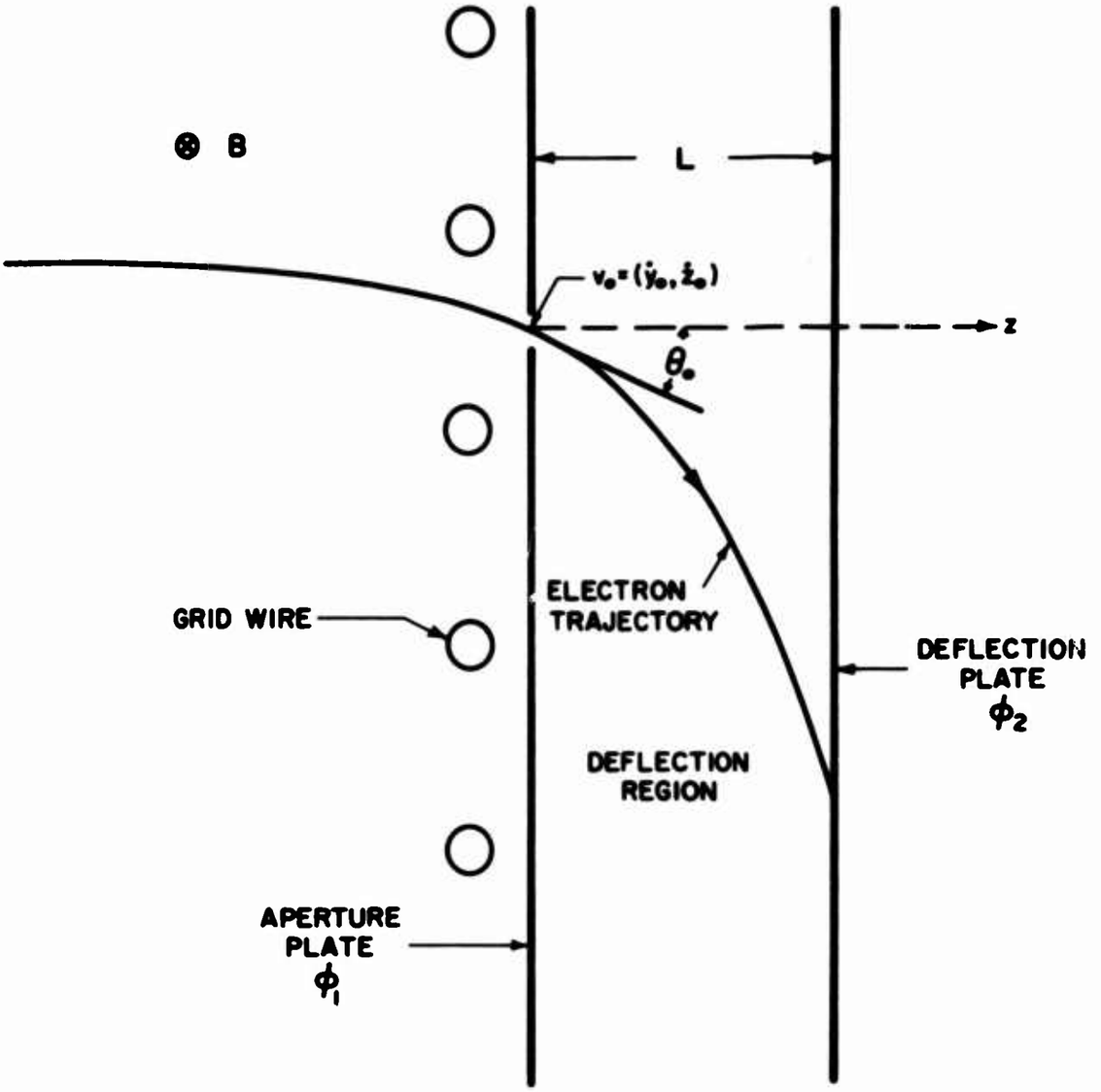

FIG. F.1 ELECTRON TRAJECTORY IN THE DEFLECTION REGION OF THE APERTURE SYSTEM.

degrees difference in θ_o) thus indicating that the aperture plate does not distort the motion to any great extent.

The motion of the electron in the deflection region can be analyzed by again referring to Fig. F.1. The electron is assumed to pass through the aperture with a kinetic energy $mv_o^2/2 = |q|\varphi_o$ and at an angle θ_o with respect to the z-axis. The aperture and deflection plates are biased at potentials φ_1 and φ_2 respectively. The ballistics equations in the deflection region can be written as

$$\frac{d^2y}{dt^2} = -\omega_c\dot{z} \tag{F.1}$$

and

$$\frac{d^2z}{dt^2} = \frac{\eta\Delta\varphi}{L} + \omega_c\dot{y} \quad , \tag{F.2}$$

where $\Delta\varphi \triangleq \varphi_2 - \varphi_1$ and L is the spacing between the aperture and deflection plates. The kinetic energy of the electron at any point along the trajectory is given by

$$\dot{z}^2 + \dot{y}^2 = \dot{z}_o^2 + \dot{y}_o^2 + 2\eta(\varphi - \varphi_1) \quad . \tag{F.3}$$

The above assumes that the energy of the electron is conserved during its motion through the deflection region. As the electron reaches the deflection plate, Eq. F.3 becomes

$$\dot{z}_o^2 + \dot{y}_o^2 = 2\eta\,\varphi_o = \dot{z}_L^2 + \dot{y}_L^2 - 2\eta\Delta\varphi \quad , \tag{F.4}$$

where $\dot{z}_L$ and $\dot{y}_L$ refer to the velocity components at z = L. Under cut-off conditions the electron trajectory is tangential to the deflection plate so that $\dot{z}_L = 0$. Integration of Eq. F.1 gives

$$\dot{y}_L = -\omega_c L + \dot{y}_o \quad , \tag{F.5}$$

which when combined with Eq. F.4 results in

$$\dot{y}_o = \omega_c L \pm \sqrt{2\eta(\varphi_o + \Delta\varphi)} \tag{F.6}$$

and

$$\dot{z}_o^2 = -(\omega_c L)^2 - 2\eta\Delta\varphi \mp 2\omega_c L \sqrt{2\eta(\varphi_o + \Delta\varphi)} \quad . \tag{F.7}$$

The above indicates that an electron entering the aperture with energy $q\varphi_o$ and angle θ will be cut off when $\Delta\varphi$ reaches a value given by

$$\sin\theta_\pm = \frac{\omega_c L}{\sqrt{2\eta\varphi_o}} \pm \sqrt{1 + \Delta\varphi/\varphi_o} \quad . \tag{F.8}$$

Thus there are some $\Delta\varphi$ values which are capable of cutting off electrons which enter in both the θ_+ and θ_- directions. The double sign occurs because those electrons which enter with $\theta_+ > \theta_m$ (where $\sin\theta_m \triangleq \omega_c L/\sqrt{2\eta\varphi_o}$) can be prevented from reaching the deflection plate only if they are forced to curve in a counter-clockwise direction whereas those electrons which enter with $\theta_- < \theta_m$ undergo clockwise rotation as $\Delta\varphi$ reaches the cut-off condition. Consequently the $\Delta\varphi$ values within a certain range are capable of cutting off two classes of electrons corresponding to θ_+ and θ_-. Figure F.2 illustrates a θ vs. $\Delta\varphi/\varphi_o$ plot for typical operating conditions.

In reality, however, things are more difficult than suggested by the above discussion. The difficulty arises because in general neither θ nor φ_o is known for the electrons entering the aperture. Thus it is necessary to make some assumption concerning one of these two quantities. If either θ or φ_o is known it is relatively simple to determine the other. For this reason it will be helpful to consider separately the situation in which electrons enter in the same direction but with a velocity distribution and that in which they enter with the same energy but in different directions.

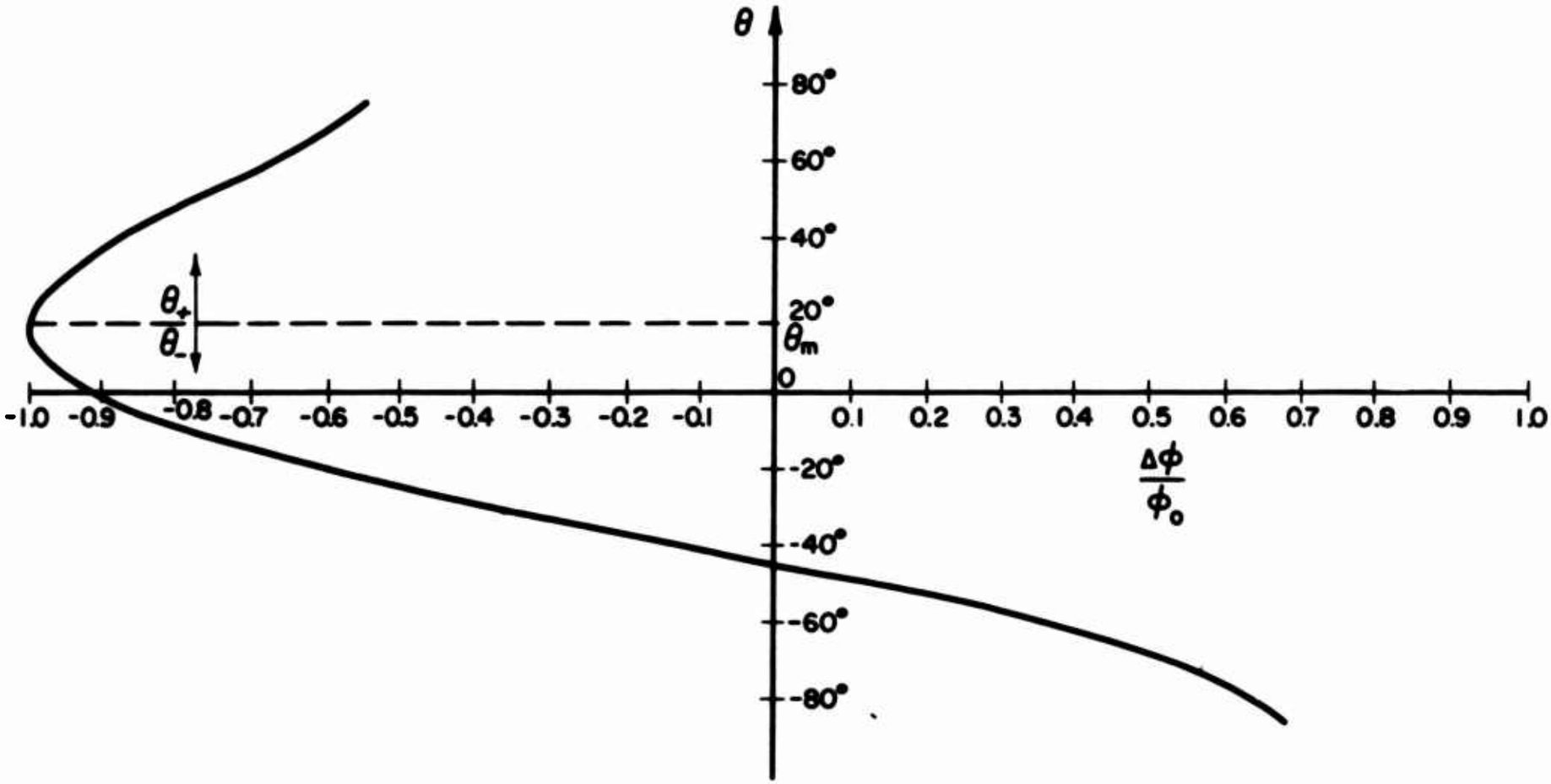

FIG. F.2 ILLUSTRATION OF THE $\Delta\varphi/\varphi_o$ VALUE REQUIRED TO CUT OFF THOSE ELECTRONS ENTERING AT AN ANGLE θ. (V_c = -1200, B = 295)

Case 1. The electrons pass through the aperture in the same direction. The problem can be considered for any arbitrary direction although the analysis is simplified if θ is selected to be 0. In this case the relationship between the entering velocity and the cutoff $\Delta\varphi$ value can be written

$$\dot{z}_o^2 = (\omega_c L)^2 - 2\eta\,\Delta\varphi \quad . \tag{F.9}$$

The incoming electrons are assumed to have a velocity distribution given by $n(\dot{z}_o)$ which is the number of electrons per second per unit area passing through the aperture with a velocity $\dot{z}_o$. The total current carried by the electrons is given by

$$I_o = \int_{\dot{z}_A}^{\dot{z}_B} n(\dot{z}_o)\; q\; A\; d\dot{z}_o \quad , \tag{F.10}$$

where $A \triangleq$ aperture area,

$\dot{z}_A \triangleq$ lowest velocity of the entering electrons, and

$\dot{z}_B \triangleq$ maximum velocity of the electrons.

The entire current will reach the deflection plate until $\Delta\varphi$ becomes small enough to turn back some of the electrons. As $\Delta\varphi$ is reduced the lower velocity electrons are cut off first. For any given $\Delta\varphi$ the current reaching the deflection plate can be written as

$$I_2 = \int_{\dot{z}_o}^{\dot{z}_B} n(\dot{z}_o)\; q\; A\; d\dot{z}_o \quad , \tag{F.11}$$

where the lowest velocity limit is determined from Eq. F.9. Some of the more interesting $n(\dot{z}_o)$ distributions will be considered below for a magnetic field of 267 gauss.

a. <u>All electrons enter with the same $\dot{z}_o$</u>. Assume the electrons enter with $\dot{z}_o = 1.19 \times 10^7$ meters/sec which corresponds to $\varphi_o = 400$ volts. In this case it is found from Eq. F.9 that a cutoff condition will occur at $\Delta\varphi = -364$ volts. Figure F.3 illustrates the situation from which it can be seen that I_2 drops sharply to 0 at -364 volts.

b. <u>$n(\dot{z}_o) = N$ for $\dot{z}_A < \dot{z}_o < \dot{z}_B$</u>. The case in which there is the same number of electrons for each velocity is illustrated in Fig. F.4a. The velocity limits are selected to correspond to $\varphi_A = 225$ volts and $\varphi_B = 625$ volts resulting in the cut-off conditions of $\Delta\varphi_A = -189$ and $\Delta\varphi_B = -589$ respectively. Using Eqs. F.10 and F.11 results in the current expressions

$$I_o = N\,q\,A\,(\dot{z}_B - \dot{z}_A) \tag{F.12}$$

and

$$I_2 = N\,q\,A\,(\dot{z}_B - \dot{z}_o) \quad . \tag{F.13}$$

The graph of I_2/I_o vs. $\Delta\varphi$ results in a parabolic curve as illustrated in Fig. F.4b.

c. <u>$n(\dot{z}_o) = N \sin\,[(\dot{z}_B - \dot{z}_o/\dot{z}_B - \dot{z}_A)\pi]$ for $\dot{z}_A < \dot{z}_o < \dot{z}_B$</u>. The distribution is illustrated in Fig. F.5a indicating that there is an intermediate velocity for which $n(\dot{z}_o)$ has the maximum value N. The current reaching the deflection plate for any $\Delta\varphi$ value assumes the form

$$I_2 = \frac{NqA}{\pi}\,(\dot{z}_B - \dot{z}_A)\left[1 - \cos\frac{(\dot{z}_B - \dot{z}_o)}{(\dot{z}_B - \dot{z}_A)}\pi\right] \quad . \tag{F.14}$$

The graph of I_2/I_o vs. $\Delta\varphi$ is illustrated in Fig. F.5b where

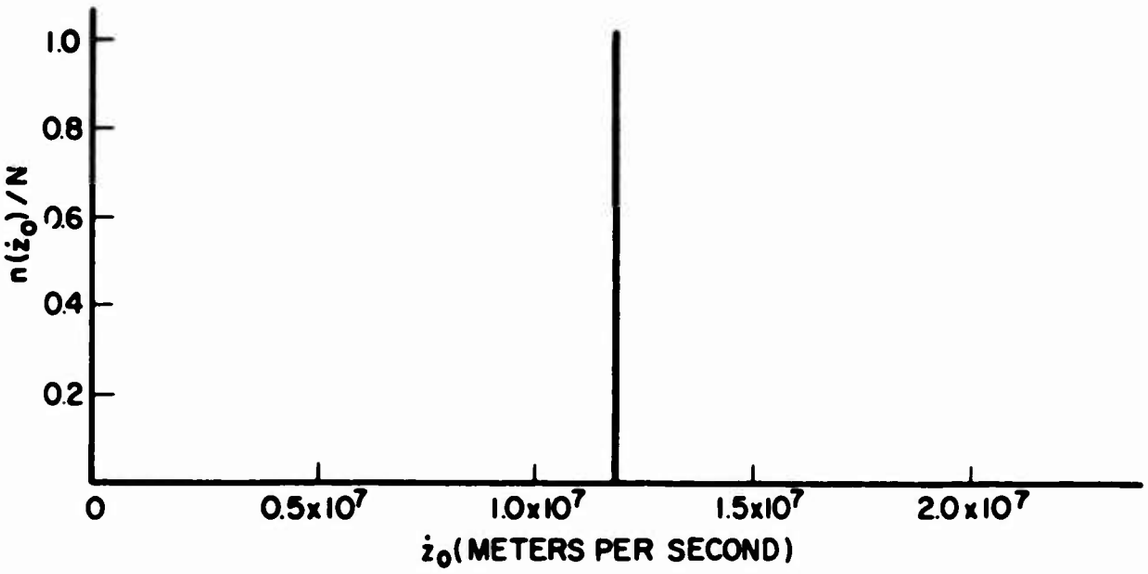

a.) VELOCITY DISTRIBUTION OF ELECTRONS ENTERING THE APERTURE

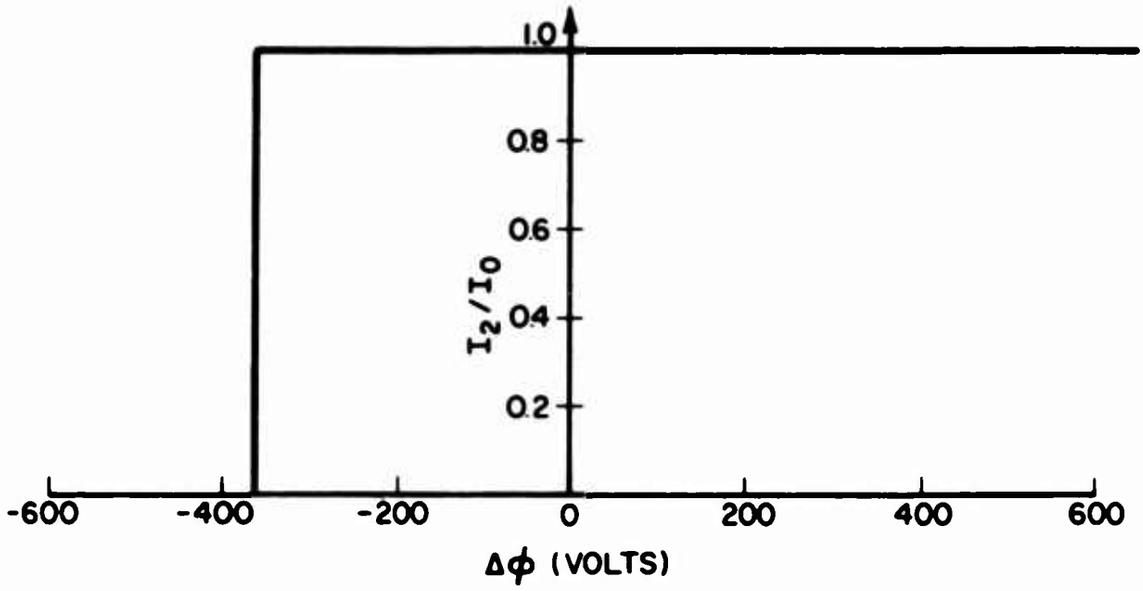

b.) VARIATION OF CURRENT REACHING THE DEFLECTION PLATE

FIG. F.3 ELECTRON VELOCITY DISTRIBUTION AND DEFLECTION PLATE CURRENT VARIATION. (B = 400 GAUSS)

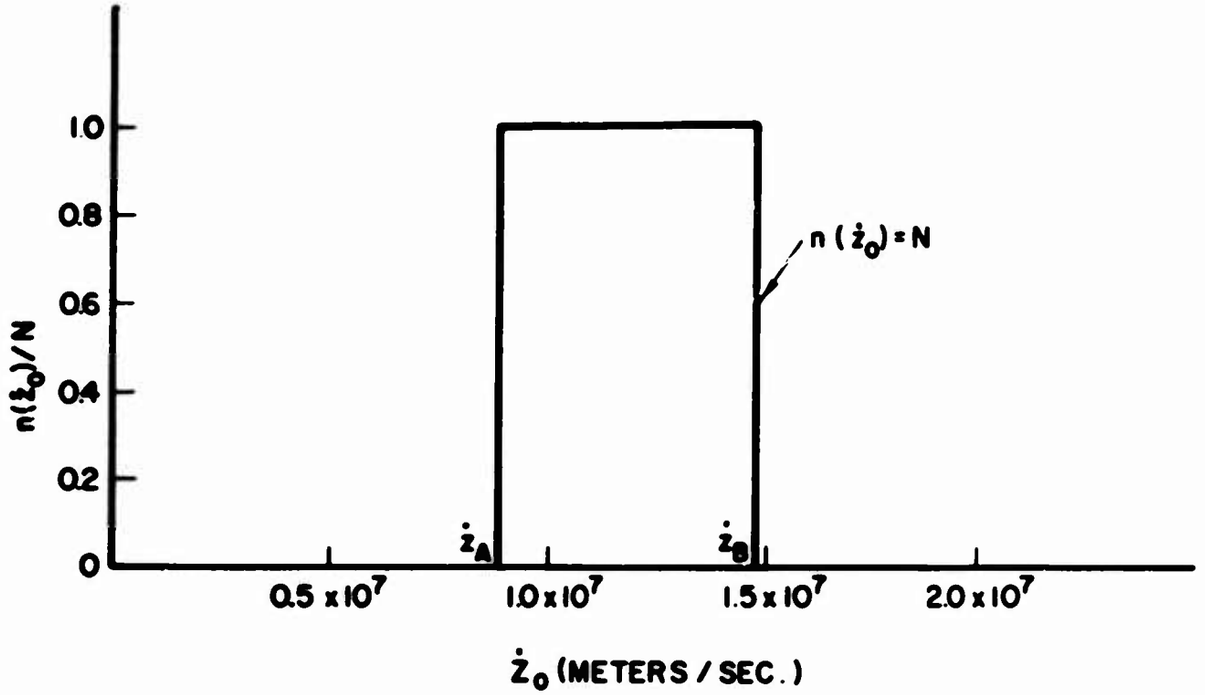

a.) VELOCITY DISTRIBUTION OF ELECTRONS ENTERING THE APERTURE

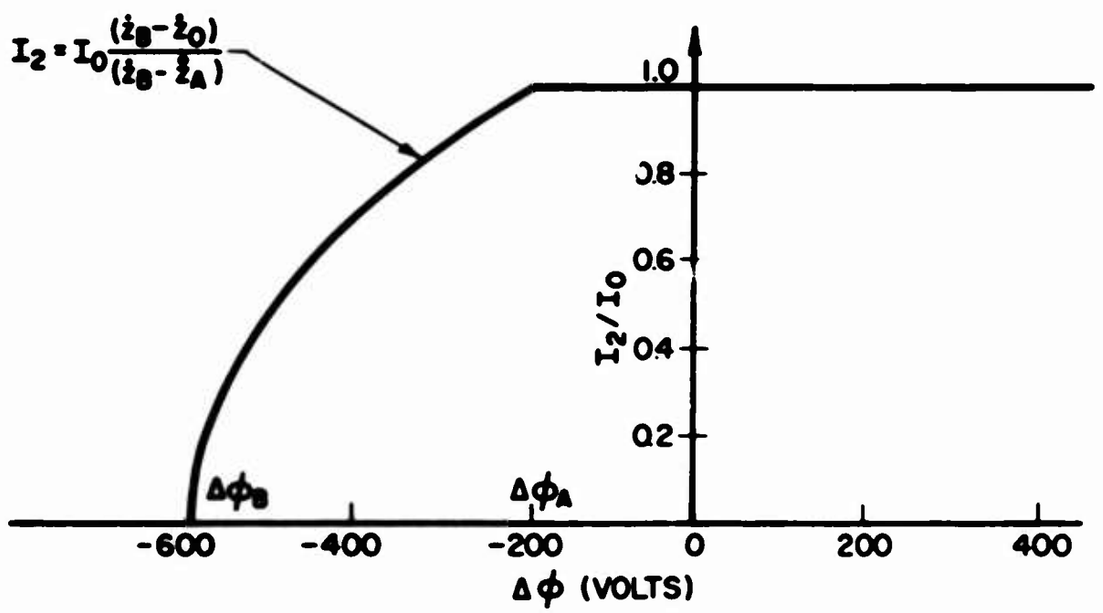

b.) VARIATION OF CURRENT REACHING THE DEFLECTION PLATE

FIG. F.4 ELECTRON VELOCITY DISTRIBUTION AND DEFLECTION PLATE CURRENT VARIATION.(B = 400 GAUSS)

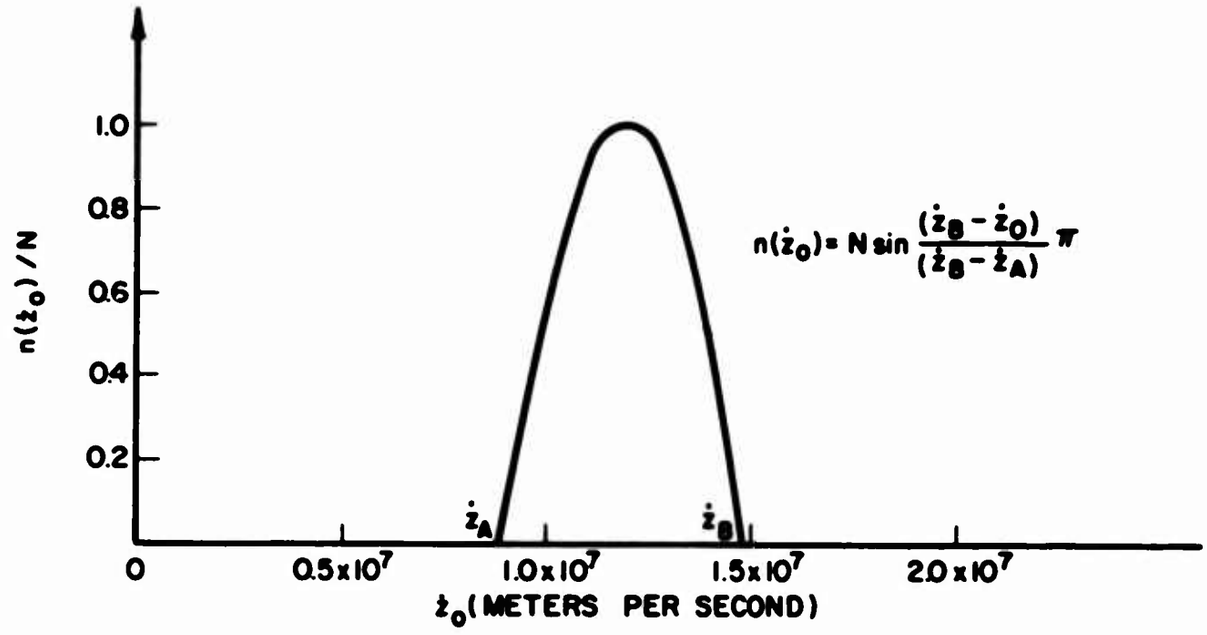

a.) VELOCITY DISTRIBUTION OF ELECTRONS ENTERING THE APERTURE

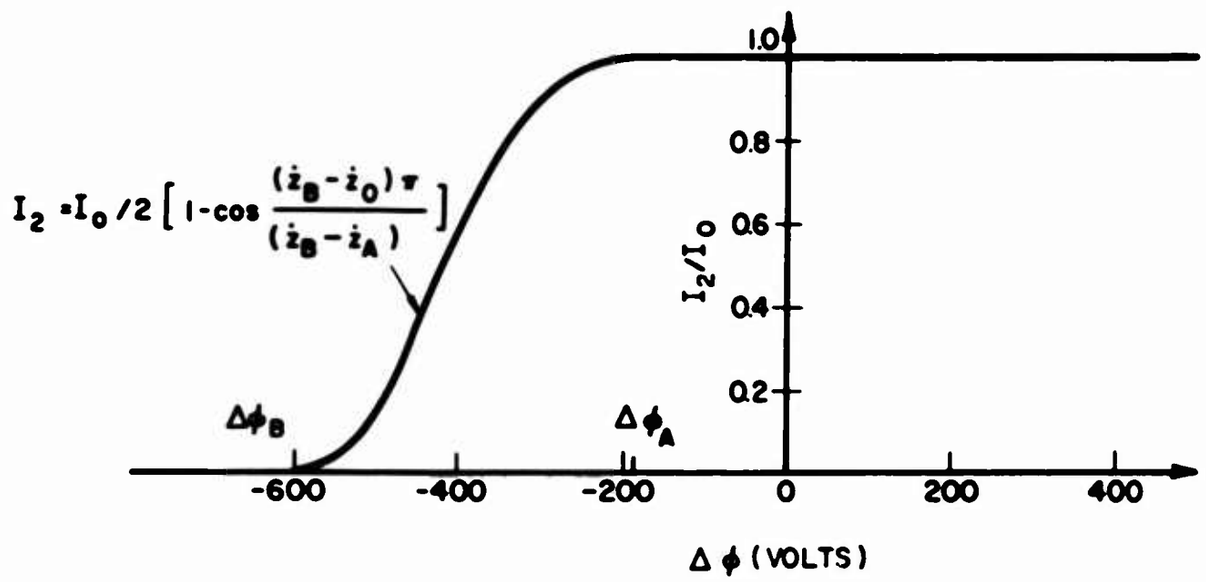

b.) VARIATION OF CURRENT REACHING THE DEFLECTION PLATE

FIG. F.5 ELECTRON VELOCITY DISTRIBUTION AND DEFLECTION PLATE CURRENT VARIATION. (B = 400 GAUSS)

$$I_o = \frac{2NqA}{\pi} (\dot{z}_B - \dot{z}_A) \tag{F.15}$$

is the total current passing through the aperture.

d. $\underline{n(\dot{z}_o) = N \exp\{-k[\dot{z}_o - (\dot{z}_A + \dot{z}_B/2)]^2\} \text{for } \dot{z}_A < \dot{z}_o < \dot{z}_B}$. This case ($k$ = constant) has been included to indicate the great similarity to the previous $n(\dot{z}_o)$ distribution. This distribution is plotted in Fig. F.6 along with the case (c) distribution for comparison. The two curves are fairly similar and thus indicate that the I_2/I_o vs. $\Delta\varphi$ curve for the exponential variation should closely resemble the sinusoidal variation. The current reaching the deflection plate can be expressed in integral form as

$$I_2 = \int_{\dot{z}_o}^{\dot{z}_B} N\, q\, A \exp\left\{-k\left[\dot{z}_o - \left(\frac{\dot{z}_A + \dot{z}_B}{2}\right)\right]^2\right\} d\dot{z}_o \quad . \tag{F.16}$$

The solution to this equation results in an expression for I_o involving the error function of $[\dot{z}_o - (\dot{z}_A + \dot{z}_B)/2]$.

<u>Case 2</u>: <u>The electrons pass through the aperture with the same energy</u>. The energy of the electrons is given by $m(\dot{y}_o^2 + \dot{z}_o^2)/2 = q\,\varphi_o$. For any given φ_o the $\Delta\varphi$ required to cut off those electrons entering at an angle θ can be calculated from Eq. F.8. In the discussion that follows $n(\theta)$ represents the number of electrons per second per unit area which pass through the aperture with energy $q\,\varphi_o$ and angle θ. Thus the evaluation of the total current through the aperture results in

$$I_o = \int_{\theta_A}^{\theta_B} n(\theta)\, q\, A\, d\theta \quad , \tag{F.17}$$

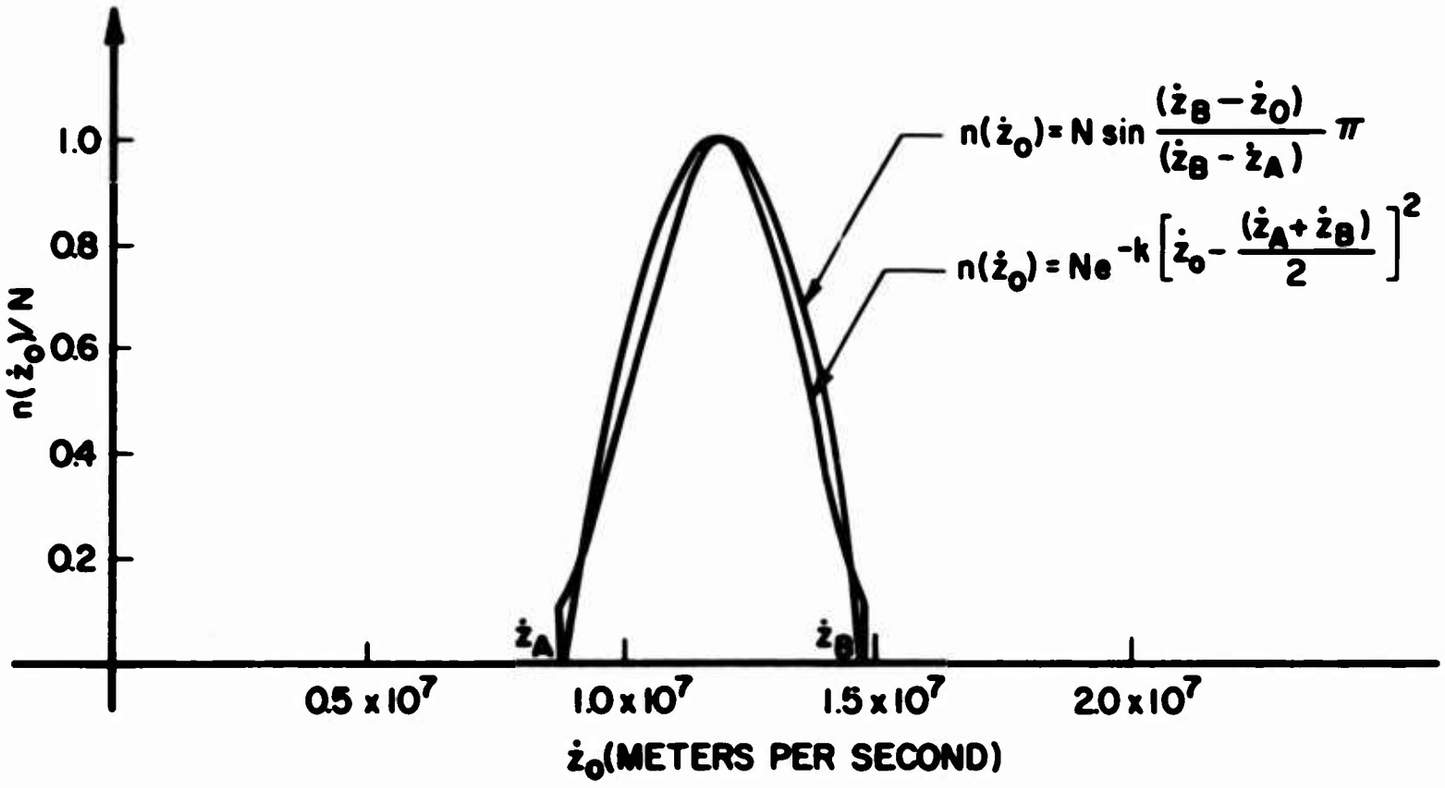

FIG. F.6 COMPARISON OF $n(\dot{z}_o)$ CURVES FOR SINUSOIDAL AND EXPONENTIAL DISTRIBUTIONS.

where θ_A and θ_B represent the extreme angles of the incoming electrons. This integration is not as simple as it appears because of the two possible solutions of Eq. F.8 within certain $\Delta\varphi$ intervals. Thus whenever $\theta_B > \theta_m$ the proper evaluation of Eq. F.17 requires integration along the θ vs. $\Delta\varphi/\varphi_o$ curve. The integration would thus be performed in two steps, the first having θ_A and θ_m as limits and the second having θ_m and θ_B.

The same precaution must be used in evaluating the current reaching the deflection plate when a portion of the electrons are being cut off. Under such conditions the current can be expressed as

$$I_2 = \int_{\theta}^{\theta_B'} n(\theta) q\, A\, d\theta \quad , \tag{F.18}$$

where θ_B' represents either θ_B or the positive angle associated with Eq. F.8.

To illustrate the types of I_2 curves expected for various $\theta_A - \theta_B$ ranges, consider the case where the angular distribution of electrons in the incoming stream can be expressed as

$$n(\theta) = N \sin\left[\frac{(\theta_B - \theta)}{(\theta_B - \theta_A)}\,\pi\right] . \tag{F.19}$$

The distribution is illustrated in Fig. F.7a. The specific values of θ_A and θ_B determine the shape of the deflection plate current curve as illustrated in Fig. F.7b. This figure includes three cases:

1. $\theta_A = 0°$, $\theta_B = 45°$,
2. $\theta_A = -25°$, $\theta_B = 25°$, and
3. $\theta_A = -45°$, $\theta_B = 0°$,

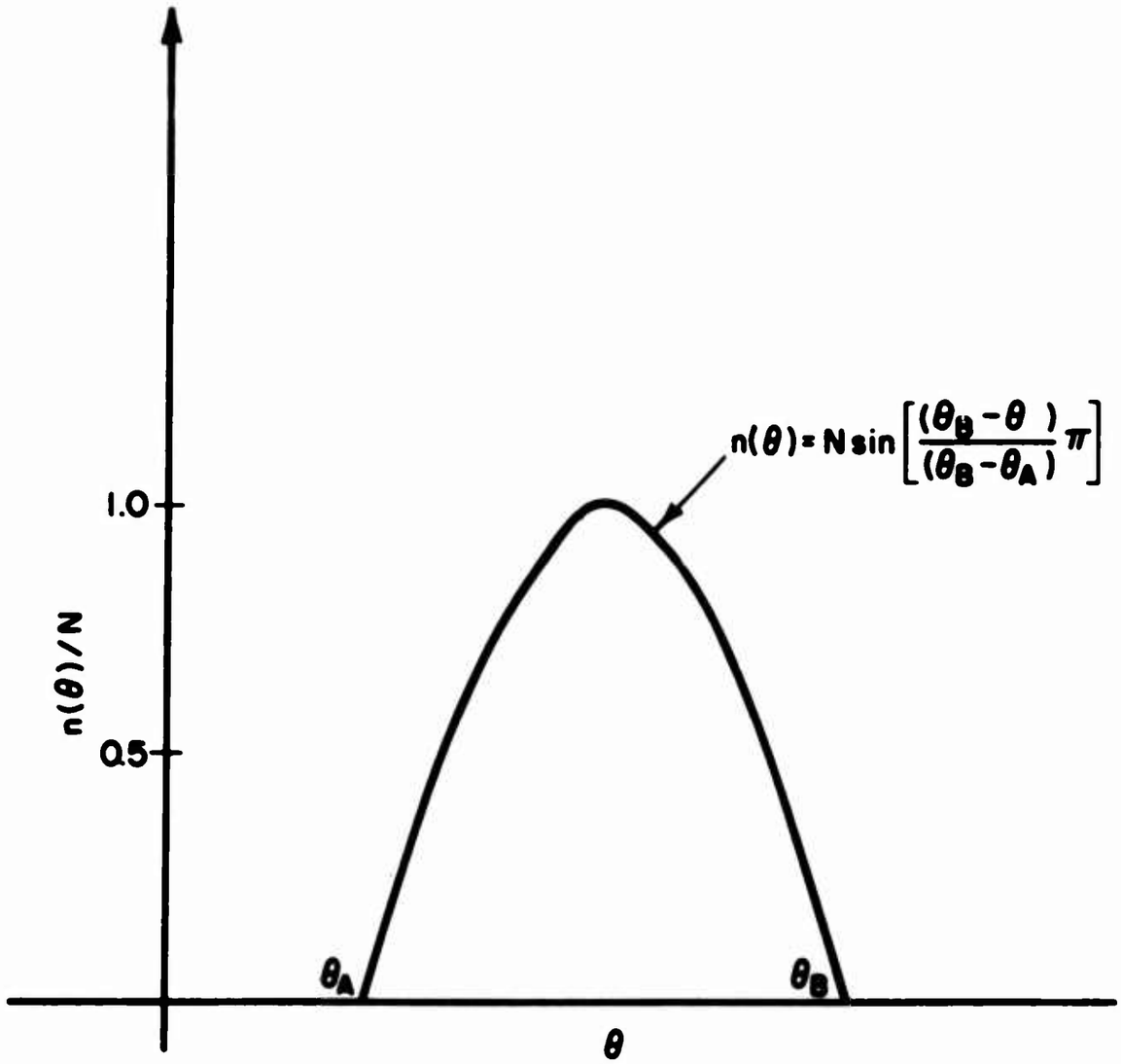

FIG. F.7a DISTRIBUTION FOR ELECTRONS ENTERING THE APERTURE AT DIFFERENT ANGLES.

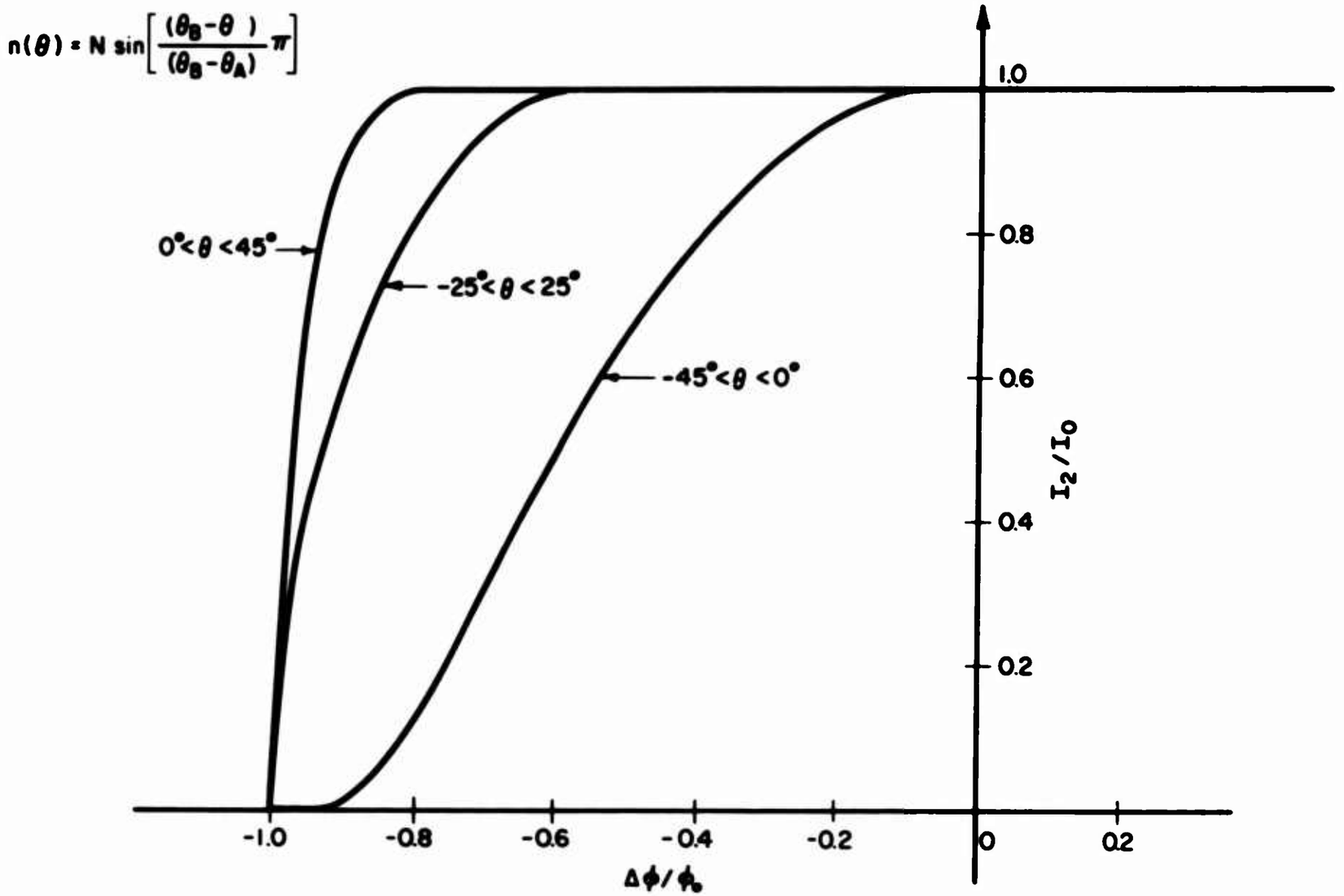

FIG. F.7b VARIATION OF CURRENT REACHING THE DEFLECTION PLATE FOR VARIOUS ANGULAR DISTRIBUTIONS. (V_c = -1400, B = 278, φ_0 = 596)

for the conditions B = 278 gauss, V_c = -1400 volts, and φ_o = 596 volts. The θ vs. $\Delta\varphi/\varphi_o$ curve for this case is illustrated in Fig. F.7c and provides an explanation for the three curves. In the first case the curve drops off sharply because almost every $\Delta\varphi$ value cuts off the two groups of entering electrons as given by Eq. F.8. In the second case the curve decreases more slowly because most of the $\Delta\varphi$ values prevent only one θ group of electrons from reaching the deflection plate. Finally the last case results in a rather slow decrease in I_2 to zero since each $\theta_A < \theta < \theta_B$ requires a different $\Delta\varphi$ to prevent the electrons associated with that angle from reaching the deflection plate.

It is quite apparent that a good picture of the θ distribution of the incoming electrons, and especially of the θ_A and θ_B limits, can be obtained from the shape of the I_2 curve. However, the evaluation of specific experimental data to arrive at a quantitative value for $n(\theta)$ is generally not possible without further information. The difficulty is the lack of knowledge concerning the energy distribution of the electrons as they enter the aperture.

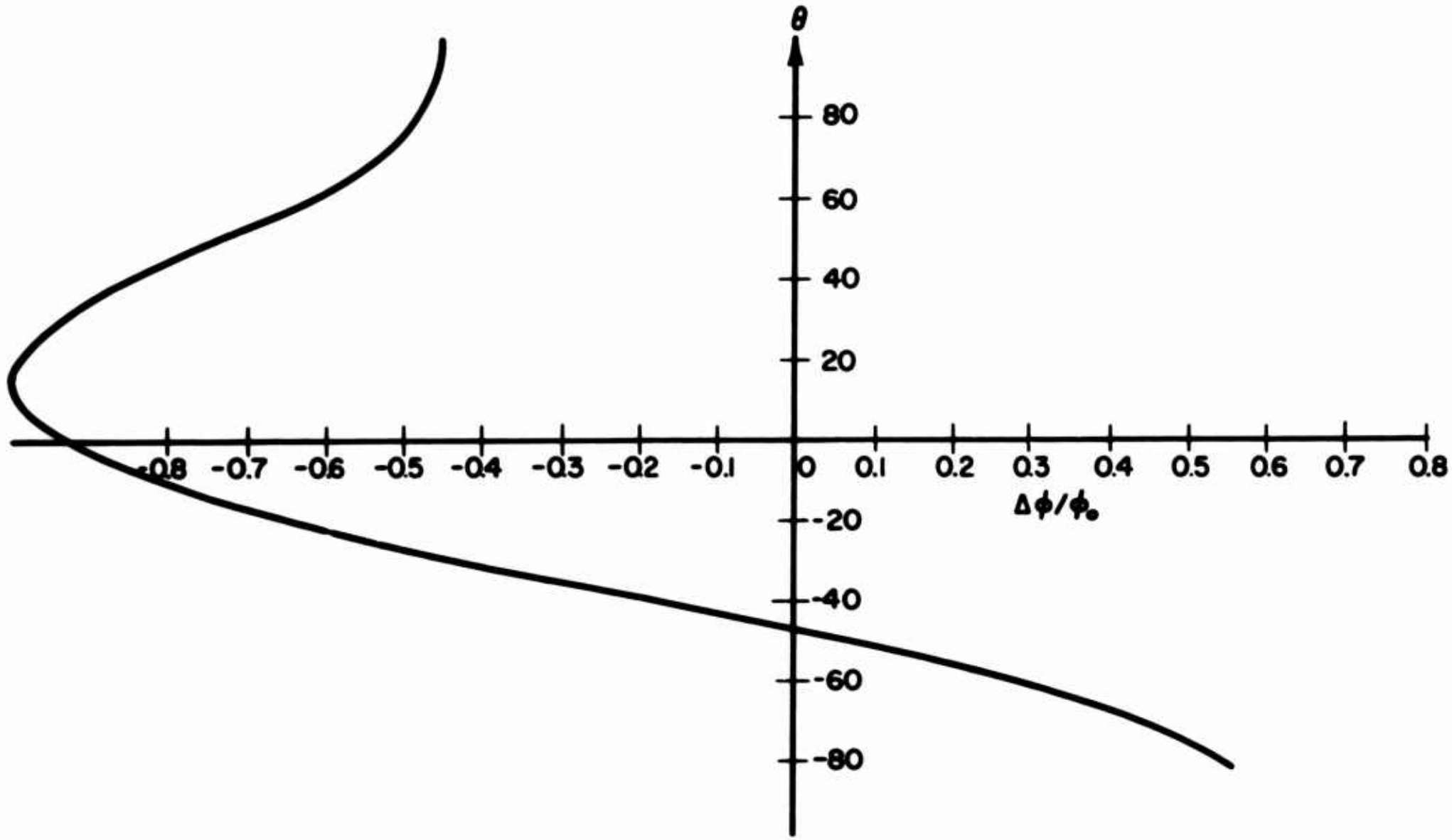

FIG. F.7c ILLUSTRATION OF VARIATION OF θ WITH $\Delta\varphi/\varphi_o$.

BIBLIOGRAPHY

1. Brillouin, L., "Electronic Theory of the Plane Magnetron", Advances in Electronics, vol. 3, pp. 85-141; 1951.

2. Slater, J. C., Microwave Electronics, D. Van Nostrand, New York, pp. 333-345; 1950.

3. Gandhi, O. P., "Nonlinear Electron-Wave Interaction in Crossed Electric and Magnetic Fields", Tech. Rpt. No. 39, Contract No. DA-36-039 sc-78260, Electron Physics Laboratory, The University of Michigan; October, 1960.

4. Doehler, O., "Static Characteristics of Injection Crossed-Field Tubes", Crossed-Field Microwave Devices, Academic Press, New York, Chapter III, pp. 151-163; 1961.

5. Dain, J. and Lewis, D., "Adiabatic Theory of an Electron Gun for Crossed-Field Devices", Proc. Phys. Soc., vol. B67, pp. 449-455; June, 1954.

6. Bartram, R. H. and Pease, M. C., "Theory of a Space-Charge-Limited Crossed-Field Gun", Sylvania Technologist, vol. XI, No. 2; April, 1958.

7. Kino, G. S., "A New Type of Crossed-Field Electron Gun", Crossed-Field Microwave Devices, Academic Press, New York, Chapter III, pp. 164-177; 1961.

8. Kirstein, P. T., "On the Determination of the Electrodes Required to Produce a Given Electric Field Distribution Along a Prescribed Curve", Proc. IRE, vol. 46, pp. 1716-1722; October, 1958.

9. Lomax, R. J., "Exact Electrode Systems for the Formation of a Curved Space-Charge Beam", Jour. Elect. and Control, vol. 3, pp. 367-374; September, 1957.

10. Hoch, O. L. and Watkins, D. A., "A Gun and Focusing System for Crossed-Field Traveling Wave Tubes", Trans. PGED-IRE, vol. ED-6, pp. 18-27; January, 1959.

11. Midford, T. A., "Some Experiments with New Types of Crossed-Field Electron Guns", Microwave Laboratory Rpt. No. 885, Stanford University; February, 1962.

12. Anderson, J. R., "Noise Measurements on an M-Type Backward-Wave Amplifier", Proc. IRE, vol. 49, pp. 946-947; May, 1960.

13. Osepchuck, J. M., "Magnetron Diode Oscillations", Crossed-Field Microwave Devices, Academic Press, New York, Chapter IV, pp. 275-317; 1961.

14. Waters, W. E., "Paraxial Properties of Crossed-Field Electron Sheet Beams", Microwave Laboratory, Rpt. No. 603, Stanford University; May, 1959.

15. Pierce, J. R., "Instability of Hollow Beams", Trans. PGED-IRE, vol. ED-3, pp. 183-189; October, 1956.

16. Alven, H., Lindberg, L., Malfors, K. G., Wallmark, T. and Åstrom, E., "Theory and Applications of Trochotrons", Trans. Roy. Inst. Techn., Stockholm, No. 22; 1948.

17. Miller, M. H., "Study of High-Temperature Electrons Originating in Streams Flowing in Crossed D-c Electric and Magnetic Fields", Tech. Rpt. No. 26, Electron Tube Laboratory, The University of Michigan; July, 1958.

18. Guenard, P. and Huber, H., "Étude expérimentale de l'interaction par ondes de charge d'espace an sein d'un faisceau électronique se déplacant dans des champs électrique et magnétique croises", Annales de Radio-electricité, vol. 7, pp. 252-278; October, 1952.

19. Epsztein, B. and Maillart, D., "Research and Development, Crossed E-H Field Microwave Tubes", QK603 Final Engineering Report, Raytheon Mfg. Co., Waltham, Massachusetts; July, 1958.

20. Warnecke, R., Huber, H., Guenard, P. and Doehler, O., "Amplification par ondes de charge d'espace dans un faisceau électronique se déplacant dans des champs électrique et magnétique croises", C. R. Acad. Sc., vol. 235, pp. 470-472; 1952.

21. Lindsay, P. A. and Sims, G. D., "Electron 'Temperature' in Crossed Fields", Jour. Elect. and Control, vol. 14, No. 3, pp. 273-288; March, 1963.

22. Horsley, A. W. and Sims, G. D., "A Note on the General Steady-State Theory of Linear Magnetrons", Jour. Elect. and Control, vol. 12, No. 3, pp. 243-246; March, 1962.

23. Hok, G., "A Statistical Approach to the Space-Charge Distribution in a Cutoff Magnetron", Jour. Appl. Phys., vol. 23, pp. 983-989; September, 1952.

24. Reverdin, D. L., "Electron Optical Exploration of Space Charge in a Cutoff Magnetron", Jour. Appl. Phys., vol. 22, No. 3, pp. 257-262; March, 1951.

25. Peterson, W. W., "The Trajectron - An Experimental D-c Magnetron", Tech. Rpt. No. 18, Electron Tube Laboratory, The University of Michigan; May, 1954.

26. Mathias, L., "The Space Charge Distribution in the Pre-Oscillation Magnetron", Jour. Electronics, vol. 1, pp. 8-24; January, 1955.

27. Nedderman, H. C., "Space-Charge Distribution in a Static Magnetron", Jour. Appl. Phys., vol. 26, pp. 1420-1430; December, 1955.

28. Dunn, D. A., "Traveling-Wave Amplifiers and Backward-Wave Oscillators for VHF", Trans. PGED-IRE, vol. 4, pp. 246-265; July, 1957.

29. Goudet, G. and Musson-Genon, R., "A Study of Electron Beams with the Electrolytic Tank Taking Account of Space Charge", J. Phys. Radium, vol. 6, pp. 175-195; July, 1945.

30. Hechtel, J. R., "Electron Ray Tracing by Means of Resistor Network and Digital Computer", Trans. PGED-IRE, vol. 9, pp. 62-68; January, 1962.

31. Alma, G. A., Diemer, G. and Groendijk, H., "A Rubber-Membrane Model for Tracing Electron Paths in Space Charge Fields", Philips Tech. Rev., vol. 14, pp. 336-344; May, 1953.

32. Martin, R. J., Masnari, N. A. and Rowe, J. E., "Analog Representation of Poisson's Equation in Two Dimensions", Trans. PGEC-IRE, vol. 9, No. 4, pp. 490-496; December, 1960.

33. Boers, J. E., "Digital Computer Analysis of Crossed-Field Electron Guns", Tech. Rpt. No. 71, Electron Physics Laboratory, The University of Michigan; April, 1964.

34. Twiss, R. Q., "On the Steady-State Theory of the Magnetron", Advances in Electronics, vol. 5, pp. 247-289; 1953.

35. Gabor, D., "Advanced Electron Dynamics and Optics", Colloquium Talks, Massachusetts Institute of Technology; 1951.

36. Buneman, O., "Symmetrical States and Their Breakup", Crossed-Field Microwave Devices, Academic Press, New York, Chapter IV, pp. 209-233; 1961.

37. Hok, G., "Conservation Principles in Multivelocity Electron Flow", Trans. PGED-IRE, vol. ED-6, No. 6, pp. 452-461; November, 1961.

38. Epsztein, B., "Effects de la charge d'espace sur les faisceaux électroniques", Ph.D. Thesis, University of Paris; 1957.

LIST OF SYMBOLS

A	Area of opening in aperture plate.
$\vec{A}$	Magnetic vector potential.
a	Distance between the lower boundary of the beam and the sole.
$\bar{a}$	Normalized distance defined as $\bar{a} = a/d$.
$\vec{B}$	D-c magnetic field vector with components B,0,0 in the x-, y- and z-directions respectively.
b	Distance between the upper boundary of the beam and the anode.
$\bar{b}$	Normalized distance defined as $\bar{b} = b/d$.
D	Diameter of grid wires used in the experimental work.
d	Anode-sole spacing.
$\vec{E}$	Electric field vector.
E_y	y-component of electric field.
E_z	z-component of electric field.
E_{a-s}	Electric field value in the anode-sole region.
E_{exit}	Electric field value at the exit plane of the electron gun.
E_z	Electric field within a Brillouin beam.
H	Hamiltonian function.
h	Beam width in the direction of the magnetic field.
I	Electron beam current.
$\bar{I}$	Normalized current defined as $\bar{I} = \eta I/\epsilon_o \omega_c^3 d^2 h$.
I_a	Anode current.
I_c	Collector current.
I_{dp}, I_z	Deflection plate current.
I_f	Focusing anode current.
I_k	Cathode current.
I_o	Total current passing through the aperture.

I_s	Sole current.
$\vec{J}$	Current density vector.
J_c	Cathode current density.
J_k	Experimental cathode current density, average value.
J_y	Constant y-component of current density as used in the Kino theory.
J_z	z-component of current density.
$\langle J_z \rangle$	Average value of J_z.
K	Beam convergence ratio defined as $K = W/\ell$.
L	Lagrangian function. (Also used as spacing between aperture plate and deflection plate.)
L_o, L_o'	Experimental values of the period of an undulating electron beam.
L_{th}	Theoretical period for electron motion in constant crossed electric and magnetic fields.
L_+, L_-	Average periods associated with the upper and lower boundaries of an undulating beam.
ℓ	Beam thickness (y-direction).
$\bar{\ell}$	Normalized value of beam thickness defined as $\bar{\ell} = \ell/d$. (Also used as the average thickness during one period.)
m	Mass of an electron.
$\hat{n}$	Unit vector in the direction normal to the electron trajectory.
$n(\dot{z}_o)$	Velocity distribution of electrons passing through the aperture.
$n(\dot{\theta})$	Angle distribution of electrons passing through the aperture.
P	Power.
P_{Br}	The total power which is available in a Brillouin beam.
P_o	The total power which is available in the beam at the cathode.
p_i	Generalized momentum in the q_i direction defined as $p_i = \partial L/\partial \dot{q}_i$.
q	Charge of an electron.
q_i	Generalized coordinate.

$\dot{q}_i$	Generalized velocity.
S	Normalized current density defined as $S = (\epsilon_o \omega_c^2/\eta J_y \rho_o)J$.
t	Time coordinate.
U	Normalized velocity defined as $U = (\epsilon_o \omega_c^3/\eta J_y)v$.
u_y, u_z	Velocity components in phase space.
V_a	Anode voltage with respect to ground.
V_{a-s}	Voltage difference between anode and sole.
V_c	Cathode voltage with respect to ground.
V_f	Focusing anode voltage.
V_s	Sole voltage.
$\vec{v}$	Vector velocity of an electron.
W	Cathode dimension in the z-direction.
$\dot{x}$	x-component of electron velocity.
$\hat{x}$	Unit vector in the x-direction.
Y	Normalized distance in the Kino theory defined as $Y = (\epsilon_o \omega_c^3/\eta J_y)y$.
$\dot{y}$	y-component of electron velocity.
$\hat{y}$	Unit vector in the y-direction.
y_m	Distance between cathode and potential minimum.
y_o	Initial y-position of electron.
Z	Normalized z-distance in the Kino theory defined as $Z = (\epsilon_o \omega_c^3/\eta J_y)(z - z_o)$.
$\dot{z}$	z-component of electron velocity.
$\hat{z}$	Unit vector in the z-direction.
$\bar{z}$, $\langle z \rangle$	Average value of z.
z_o	Initial z-position of electron.
$\Delta\varphi$	Potential difference between aperture plate and deflection plate defined as $\Delta\varphi = \varphi_2 - \varphi_1$.

ϵ_o	Dielectric constant of free space.
η	Charge-to-mass ratio of an electron defined as $\eta = \lvert q \rvert / m$.
η_{Br}	Theoretical electronic efficiency for a Brillouin beam.
η_{el}	Electronic efficiency.
θ	Angle variable describing direction of electron travel at any point.
$\langle\theta\rangle$	Average value of θ.
θ_{cr}	Critical angle of emission from the cathode in order for an electron to reach the potential minimum plane.
θ_o	Direction in which an electron passes through the aperture.
ξ	Normalized distance defined as $\xi = 2\pi - Y$.
ρ	Space-charge density.
$\langle\rho\rangle$	Average value of ρ at the aperture.
ρ_o	Brillouin space-charge density defined as $\rho_o = -\epsilon_o \eta B^2$.
Φ	Normalized potential defined as $\Phi = (\epsilon_o^2 \omega_c^4 / \eta J_y^2)\varphi$.
$\bar{\Phi}_a$	Normalized anode potential defined as $\bar{\Phi}_a = 2\eta\varphi_a / \omega_c^2 d^2$.
φ	Electric potential relative to the cathode.
φ_a	Anode potential.
φ_{aux}	Auxiliary electrode potential.
φ_f	Focusing anode potential.
φ_m	Potential minimum plane voltage. (Also used as the mean beam voltage in Eq. 2.25.)
φ_o	Voltage equivalent of electron energy at a specified point.
$\langle\varphi_o\rangle$	Average value of φ_o.
φ_1	Aperture plate potential.
φ_2	Deflection plate potential. (Also used as the potential in a Brillouin beam, Eq. 2.1.)
ψ	Angle of trajectory for Kino flow defined as $\tan\psi = dy/dz$.
ω_c	Cyclotron radian frequency defined as $\omega_c = \eta B$.